Low Cost Monitoring System to Diagnose Problematic Rail Bed: Case Study at a Mud Pumping Site

by

AW, ENG SEW

MEng, Civil and Environmental Engineering (2001)
Imperial College of Science, Technology and Medicine, London, UK

M.S., Civil and Environmental Engineering (2004)
Massachusetts Institute of Technology, Cambridge, MA, USA

Submitted to the Department of Civil and Environmental Engineering
in Partial Fulfilment of the Requirements for the Degree of

Doctor of Philosophy in Civil and Environmental Engineering
at the
MASSACHUSETTS INSTITUTE OF TECHNOLOGY

September 2007

Signature of Author ____
Department of Civil and Environmental Engineering
August 17, 2007

Certified by ____
John T Germaine
Senior Research Associate of Civil and Environmental Engineering
Thesis Supervisor

Certified by____
Andrew J. Whittle
Professor of Civil and Environmental Engineering
Thesis Supervisor

Accepted by ____
Daniele Veneziano,
Chairman, Committee for Graduate Students

Low Cost Monitoring System to Diagnose Problematic Rail Bed: Case Study at a Mud Pumping Site

Aw, Eng Sew

Submitted to the Department of Civil and Environmental Engineering
on August 17, 2007
in Partial Fulfilment of the Requirements for the Degree of
Doctor of Philosophy in the field of Civil and Environmental Engineering

ABSTRACT

This thesis describes the development of low cost sensors and wireless sensor network (WSN) platform aimed at characterizing problematic rail beds (subgrade). The instrumentations are installed at a busy high-speed Northeast Corridor (NEC) railway site that is experiencing recurring mud pumping problems and requires frequent (bi-monthly) track maintenance. The field instrumentation program addresses some of the challenges faced with designing and installing the subgrade sensors: adoption of new low-cost sensor technologies, fabrication for harsh railway environment, ease of installation with minimal traffic disruption; adoption of advances in WSN for remote data gathering, two-way communications, back-end processing, and near real-time viewing of data.

The subgrade sensors consist of piezometers, accelerometers, liquid-based settlement probes, and temperature sensors (thermistors). The piezometers measure the long-term variation in the ground water table and short-term load induced pore pressures. The accelerometers measure the dynamic wheel-induced accelerations at the tie and the top subgrade. The liquid-based settlement probes are designed for long-term settlement measurements although they are not important at this particular site that exhibits greater track vibrations than long-term settlement. The temperature sensors installed at three different levels are able to track the atmospheric, top subgrade, and deep subgrade temperatures.

The field instrumentation installed at the problematic NEC site provides valuable insights into factors causing mud pumping. The field data suggest that water, widely acknowledged one of the causes of mud pumping, is not derived from the in-situ ground water table, perched water table at the top subgrade (that is under hydrostatic matrix suction), or rain (merely replenished the matrix suction in the ground).

An energy-based method, modeled after the Arias Intensity, is used to characterize the response of the track to train loadings based on measured acceleration. This method is able to track the serviceability of the rail track (effect of maintenance and gradual build-up of track deterioration), investigate the damage factor of trains on the track (high-speed Acela is found to be most damaging), and establish that the track is extremely stable during winter due to frozen soil but dramatically deteriorates during ice thaw.

Thesis Supervisor: John T. Germaine
Title: Principal Research Associate in Civil and Environmental Engineering

Thesis Supervisor: Andrew J. Whittle
Title: Professor of Civil and Environmental Engineering

ACKNOWLEDGEMENTS

I would extend my greatest gratitude and appreciation to several people who were involved in the completion of this thesis. They are:

Dr. John Germaine and Professor Andrew Whittle for their invaluable advice, guidance, inspiration and friendship throughout my years at MIT;

Dr. Ted Sussmann and Carl Martland for serving on my thesis committee;

Amtrak for providing for their interest and providing track support in this research project: Mike Trosino, Mike Tomas and colleagues;

Dr. Ivan Stoianov for providing assistance with the wireless sensor networks;

Professor John Burland for first motivating my interest in geotechnical engineering;

Nabi Kartal Toker, Maria A. Nikolinakou , Pei Jianyong , Louis Wong, Anna Agarwal, Sherif Akl, Naeem Abdulhadi and the geotechnical group for the friendship, great company and many spontaneous outings;

Shi Ling and Da Yan for their love and support and my parents for their encouragement and steadfast confidence which provides me with the determination to see this thesis through to a successful completion.

CONTENTS

LIST OF FIGURES

LIST OF TABLES

Chapter 1: Introduction and Objectives

1.1 Introduction

This thesis is divided into two main sections: a) the development of low cost sensors and remote monitoring platform capable of diagnosing railway subgrade problems, and b) the application the monitoring system at a railway site experiencing with problematic subgrade.

1.2 Track Subgrade Problems

The railway track consists of the man-made track superstructure (rails, ties, ballast, and subballast) overlying the in-situ ground (subgrade). The performance and serviceability of the track superstructure is governed by its ability to provide smooth[甲] train rides and inability to do so results in track maintenance[乙]. The performance of the railway track can be compromised by deterioration in the track superstructure (e.g. ballast degradation, bending in rails) and problematic subgrade.

The focus of this thesis is primarily with problematic subgrade affecting the performance of the track superstructure. Problematic subgrade can arise from a variety of mechanisms – mud pumping: migrations of fines from the subgrade into the ballast; progressive shear failure: failure relating to the shear strength of the subgrade; or excessive vertical deformation: compressibility of underlying organics. Table 1-1 lists some of the types, causes, and features of subgrade problems. Sites with chronic subgrade problems and fail rail tolerance safety inspections are faced with frequent track maintenance or costly speed restrictions (slow orders). In more serious cases, problematic subgrade has led to train derailments[丙]. In a recent freight train derailment accident, a CSX train traveling on a stretch of site which has uneven rail elevation (attributed to continuous HAL operations over ponded soft subgrade) resulted in longitudinal rolling in the train carriages. The excessive longitudinal rolling caused the

---

[甲] The recommended rail tolerance is solely based on train speed: the Federal Railroad Administration (FRA) recommends that tracks accommodating trains with speeds up to 256 km/hr (160 mph) – known as class 8 tracks – requires both vertical and horizontal alignment tolerance not exceeding 1.27 cm (0.5 inch) from the mid-chord offset of a 9.4 m (31 feet) chord. Source: (FRA: Track Safety Standards, 2002, Chapter 6).

[乙] Regular maintenance: involves lifting rail to required vertical and horizontal alignment and repacking or refilling ballast stones underneath it

[丙] Problematic soft subgrade contributes to 38 train accidents in year 2004 (or 1.1% of the total train accidents in the year) and causes $3.2 million in damages. The train accidents are defined by incidents causing reportable damage exceed $6700 in year 2004 (FRA 2005).

wheel flange to lift and slide over the rail, thus sending the train carriages over the tracks (National Transportation Safety Board, 1999).

Track operators have two track restoration strategy options at sites with severe rail bed problems: a) low cost standard track geometry realignment and ballast retamping which is, at best, temporary remedial measure; or b) expensive remedial measures such as geotextiles and subgrade strengthening additives aimed at solving the problem. The choice between temporary remedial measures (the former) and fixing the problem (the latter) is often driven by cost. For sites that require expensive remediation schemes such as fly-ash subgrade strengthening and geotextiles, carefully crafted site instrumentation is important because successful selection of appropriate measures depends on reliable diagnosis of the underlying mechanisms controlling subgrade performance.

Discussions with engineers at Amtrak, Volpe National Transportation Systems Center and the Association of American Railways (AAR) have found considerable interest in development of low-cost, modular monitoring systems that can be easily deployed at remote locations. The goal of this research is to develop and test the effectiveness of a prototype monitoring system aimed at characterizing subgrade performance. Successful demonstration of this technology will, hopefully, encourage further development and adoption by other railway operators in diagnosing subgrade problems.

1.3 Outline of Monitoring System

Field instrumentation is currently costly, timely and requires highly specialized personnel endeavor. A remote instrumentation system consists of the three major components: a) sensors, b) data acquisition unit with remote data transfer capability, and c) data storage and processing capability. In general, commercially available sensors such as piezometers, accelerometers and displacement sensors or specialty devices such as strain gages are not suitable for subgrade monitoring (e.g. steel casing which is dangerous in a highly energized environment, unsuitable response and resolution). Similarly, current commercial data acquisition units which allows remote monitoring capabilities are expensive, require high power consumption and are non-scalable (i.e, cost significantly increases with number acquisition channels).

Recent development in wireless monitoring platforms has extended the capability of remote monitoring and such systems have been successfully used for long term monitoring of environment systems (i.e. temperature and pressure) in remote areas (Mainwaring *et al* 2006, Culler *et al* 2004). More recently, a wireless monitoring system developed jointly by MIT and Intel was successfully tested at Boston Water's sewage and water supply pipelines (Stoianov *et al.* 2006).

The three goals of this research project are:

1. to develop a remote monitoring system capable of characterising track with problematic subgrade problems. Sensors will be developed to measure track parameters such as the ground water pressure, track acceleration during passage of trains, and long term track settlement.
2. to further develop and customize the existing Intel Mote wireless sensor network monitoring platform (previously developed at MIT) for railway applications. Data handling, processing and accessibility will be developed to enable users view and download the collected data near real-time.
3. to demonstrate the application of the monitoring system at a problematic railway site near MIT. The system will be used to help diagnose the cause of unsatisfactory track performance.

A site chosen for this research is a high volume passenger rail site at Mansfield, MA which is heavily used by Amtrak’s high speed Northeast Corridor Acela, Regional trains, MBTA commuter trains, and freight CSX cargo trains. Preliminary conversations with Amtrak personnel suggested that the site is experiencing mud pumping problem and requires monthly track maintenance.

1.4 Thesis Organization

Chapter 1 describes the aim and scope for the development and implementation of a remote monitoring system at a problematic busy railway site. Preliminary site investigation and proposed instrumentation strategy are provided in Chapter 2. Preliminary visual site investigation and interviews with Amtrak personnel found that the site undergoes recurring mud pumping problems, prompting further literature investigation in this area (Chapter 3). The development of wireless sensor network used in this research and brief literature review on sensors are presented in Chapter 4. The design and laboratory testing of the specialty sensors are described in Chapter 5. The field installation of the wireless sensor network and sensors are presented in Chapter 6, collected field data and measurements in Chapter 7, and analysis of data in Chapter 8. A track degradation model for capturing the degradation of track over time based on measured acceleration was proposed in Chapter 8. The conclusion is detailed in Chapter 9. The references and appendixes are detailed Chapter 10 and 11.

Table 1-1: Selected subgrade problems and features (adapted from Li & Selig 1994)

Type	***Causes***	***Features***
Subgrade attrition and mud pumping	– repeated loading of subgrade by ballast – contact between ballast and subgrade – clay rich rocks or soils	– muddy ballast – inadequate subballast
Progressive Shear Failure	– repeated over-stressing – fine-grained soils – high water content	– squeezing near subgrade surface – heaves in crib and shoulder – depression under ties
Bridge Approach	– repeated loading – differential stiffness between the bridge and the soft subgrade	– depression of the ballast and subgrade at distance about one half carriage from the abutment of the bridge
Excessive plastic deformation (ballast pocket)	– repeated loading – soft or loose soils	– differential subgrade settlement – ballast pockets
Liquefaction	– repeated loading – saturated silt and fine sand	– large displacement – more severe with vibration
Frost action (heave and softening)	– periodic freezing temperature – free water – frost susceptible soils	– occur in winter/spring period – rough track surface

Chapter 2: Monitoring and Investigative Approach

2.1 Monitoring usage within the railway industry

Problematic subgrade (e.g. soft subgrade, mud pumping) that result in poor track conditions are viewed as a serious safety issue and tracks with historically poor performance are frequently monitored using track alignment-detection vehicles. Recently, there have been attempts at understanding site problematic subgrade mechanisms through field instrumentation. Li (2000) investigated the track performance prior to and after installation of Hot-Mix-Asphalt (HMA) subgrade improvements using pressure cells and Linear-Variable-Displacement-Transducers (LVDT). Konrad et.al, (2007) installed piezometers (by Pressure Systems, Model 735) and wire potentiometers (settlement measurement) at a Canadian National (CN) HAL site overlying 5m of peat. Field measurements and laboratory shear strength measurements (using Direct Simple Shear) suggested peat punching failure at the site. In entirely different project, Wong et al (2006) installed vibrating-wire piezometers for a Canadian Pacific Railway HAL site overlying one to three meters of peat. The site undergoes excessive settlement and form piping holes under repeated HAL loads. The piezometers measured high but short-lived pore pressures in the peat: pore pressure spikes are measured only in the first 80s out of a six-minute train passage. Wong concluded that the generated high pore pressures opened underground channels that led dissipation of subsequent pore pressures and formation of piping holes. Over in Europe, extensive field instrumentation consisting of extensometers, piezometers, accelerometers, and strain gages have used to investigate the performance of lime-cement piles at a site with clay and peat material.

Field instrumentations, as demonstrated by the case studies above, can add value by identifying site-specific failure mechanisms or dispel speculative aggravating factors. This is especially important for tracks where multi-million dollars of remedial measures are being planned; misguided believes on the site mechanisms may lead to ineffective measures.

2.2 Case study: Mansfield site

A problematic subgrade site at Mansfield was chosen for field implementation of the instrumentation and it is ideal because:

a) it has a high track maintenance cycle (one to two months) which is frequent enough to be studied within the timeframe of this research
b) it is heavily used by Amtrak's Northeast Corridor high speed Acela
c) it is in close proximity to MIT to enable easy access for installation and maintenance of the prototype monitoring system
d) it allows convenient track operation support

Conversations with Amtrak field engineers found that the underlying soil foundation migrates upwards onto the ballast, causing formation of cavities beneath the concrete ties. This results in accelerated track deterioration and fails to meet the track geometry safety standards and track maintenance has to be performed in monthly cycles. In addition, the ballast material crushes into fine particles and further clogs the already clogged ballast. The track is particularly vulnerable during summer and fall, and is stable during winter when the ground is frozen. The problem is probably exacerbated by presence of high water table. One of the proposed remedial measures is the installation of drainage system to reduce the high water table.

There are four problematic locations within a range of three hundred meters; three spots on the outbound track 1 and one spot at the bridge approach on the inbound track 2, labeled P1 to P4 (Figure 2-1). These problematic spots typically span six to eleven ties and occur either at track 1 or 2, but not both. Location P2 is selected for the instrumentation program due to its close proximity to the wayside facilities (e.g. on-site power supply, instrumentation box) and appeared to be most visually problematic (i.e. severe track vibrations during passage of trains). The problematic spot (Figure 2-2) is marked with visible patches of dry material (possibly a mixture of crushed ballast material and subgrade silts). During passage of the train, the track is observed to undergo sudden downward jerk as the wheel passed directly over it, suggesting presence of cavities beneath the ties. The ties are held in suspension by the rail under the normal unloaded condition. Interestingly, the area just north of P2 is remarkably stable with little downward displacement component but is subjected to rocking motion in order to accommodate high rail displacements at P2.

The mud pumping spots are a recurring problem, despite bi-monthly track alignments and additions of ballast: the conventional track maintenance exercise (vertical realigning of the track by adding ballast and retamping) is clearly ineffective. This site serves as an excellent test-bed for the prototype instrumentation and further geotechnical analyses.

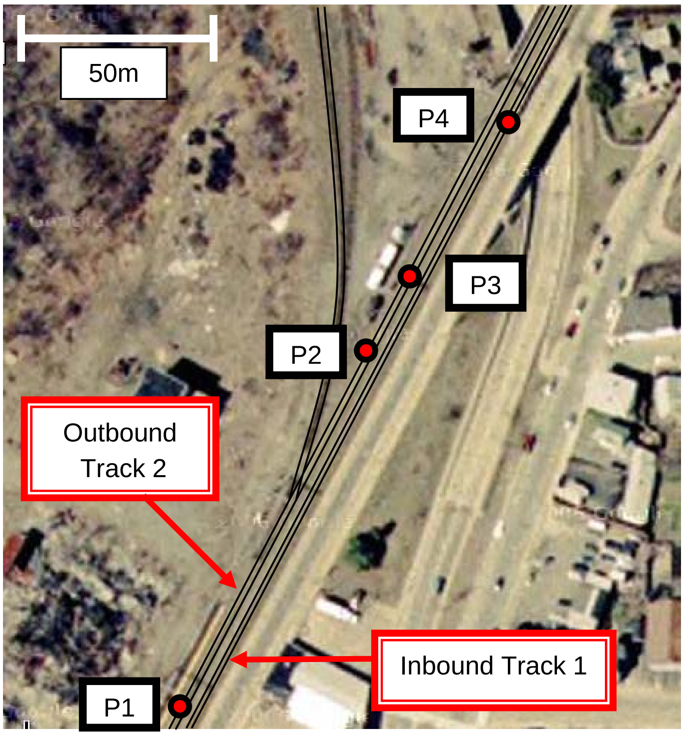

● Mud pumping spots

P1: Mud pumping spot on the outbound track near the station (right of P1).

P2: Sensor installation location. Mud pumping occurs on the outbound track and spans 11 ties.

P3: Mud pumping spans 6 ties on the outbound track

P4: Bridge approach mud pumping site on the inbound track and spans 7 ties.

Daily number of outbound trains 6 Acela, 4 Regionals, 17 Commuter trains

Figure 2-1: Plan view of the Mansfield Site. There are 4 problematic sites within a distance of a few hundred meters (Source: Google Maps). Site P2 is selected for installation of instrumentation.

Figure 2-2: P2 - Mud Pumping Site at Mansfield. The mud pumping spot is visibly marked by white patches on the rails and concrete ties.

2.3 Methodology for diagnosing mud pumping problem

2.3.1 Preliminary desk study

Visual inspection

Preliminary visual inspection of the site was performed and many of the observations have been discussed in the preceding section. In summary, problematic spot P2 can be characterized by high vertical displacements of the rail and ties: a behavior attributed to subgrade losses which result in cavities forming below the ties.

Interviews with Amtrak personnel

Interviews with Amtrak field engineers are summarized as follows:

1. The high ground water table in the area may cause mud pumping, especially during heavy rains. The presence of the water softens the subgrade and pore pressure development during passage of the trains may aid upward migration of particles.
2. The track is extremely stable in winter and deteriorates rather quickly in spring, suggesting that the frozen track stops mud pumping and the thawing of ice increases track deterioration.
3. The high speed Acela trains is believed to play a major role in track deterioration. When the Acela trains were out of commission during the summer of 2005 (other services such as Amtrak's Regional and MBTA trains were still in operation), the track experienced greatly reduced deterioration.

Geological site profile

The surficial geology of the site is mostly covered by Udorthents, which is a soil class resulting from man made activities (e.g. cut and fill operation) or erosion from in-situ ground of cliffs (USDA NRCS: Natural Resources Conversation Service; Figure 2-4). The soil directly below the track is expected to be highly compacted from the traffic. The soil profile (Figure 2-3) obtained from a boring log of the nearby Chauncy underpass highway project (300 meters away) shows that the top three meters of the soil is characterized as silty sand overlying two meters of hard silt, suggesting that the mud pumping is limited to the top three-meter layer. The groundwater level marked at 1.7 meters below the surface is confirmed through a borehole during installation of the deep piezometer. Later visual observations during installation of sensors found that the top few feet of the subgrade is heavily contaminated with oil and debris.

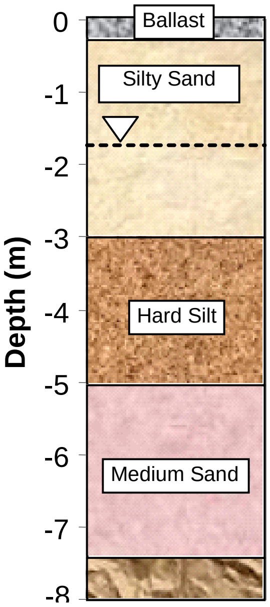

Figure 2-3: Soil profile at Mansfield site

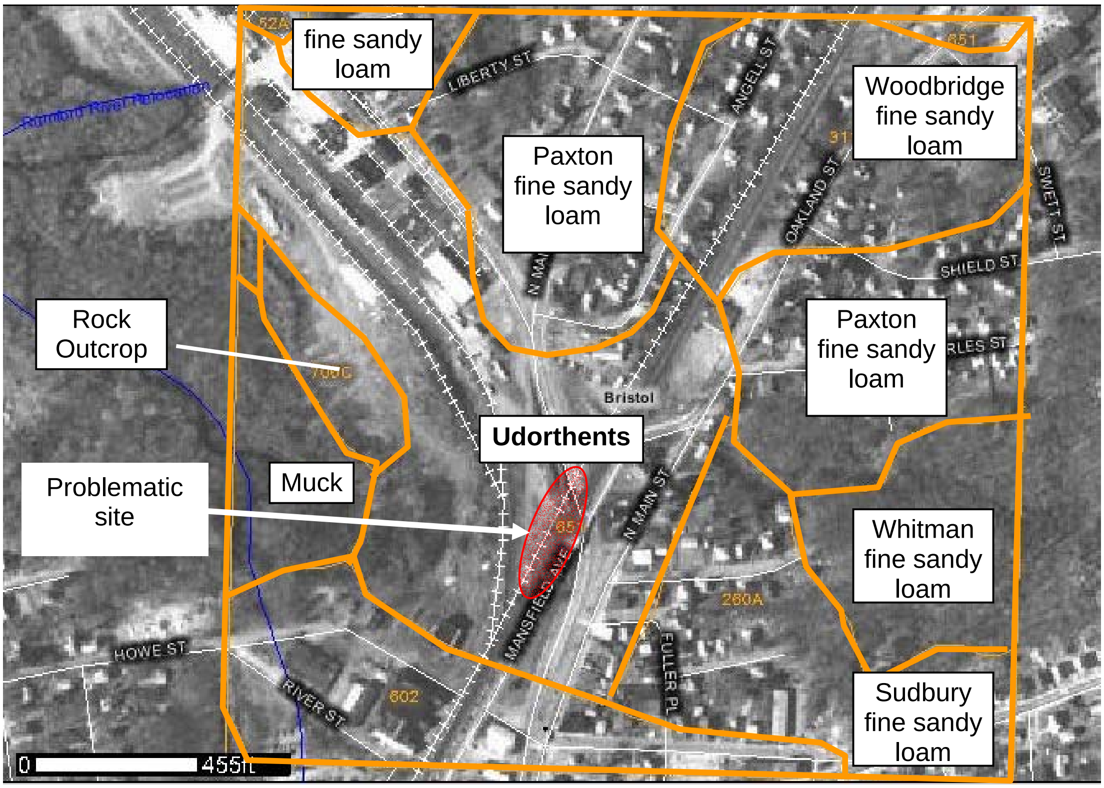

Figure 2-4: The surficial geology of the Mansfield site. Source = NRSC Mansfield Surficial Geology

In order to determine the particle size distribution (PSD), soil samples from the deep (1.5m below ground) problematic zone is collected and tested. Sieve analyses are conducted for soils with diameter above 0.1 mm and hydrometer analyses for soils below 0.1 mm diameter (Figure 2-5). The laboratory classification confirms the description of the subgrade soil as sandy silt. It has 26% fines, out of which 8% are clay. The soil's hydraulic conductivity can be estimated from Hazen's empirical formula, where

$$k = 100(D_{10})^2 \quad \text{……………………………….Equation 2-1}$$

where k = hydraulic conductivity (cm/s) and D_{10} = diameter of soil at the lower tenth percentile (cm).

Here, $D_{10} = 0.002$mm and $k = 4 \times 10^{-6}$ cm/s.

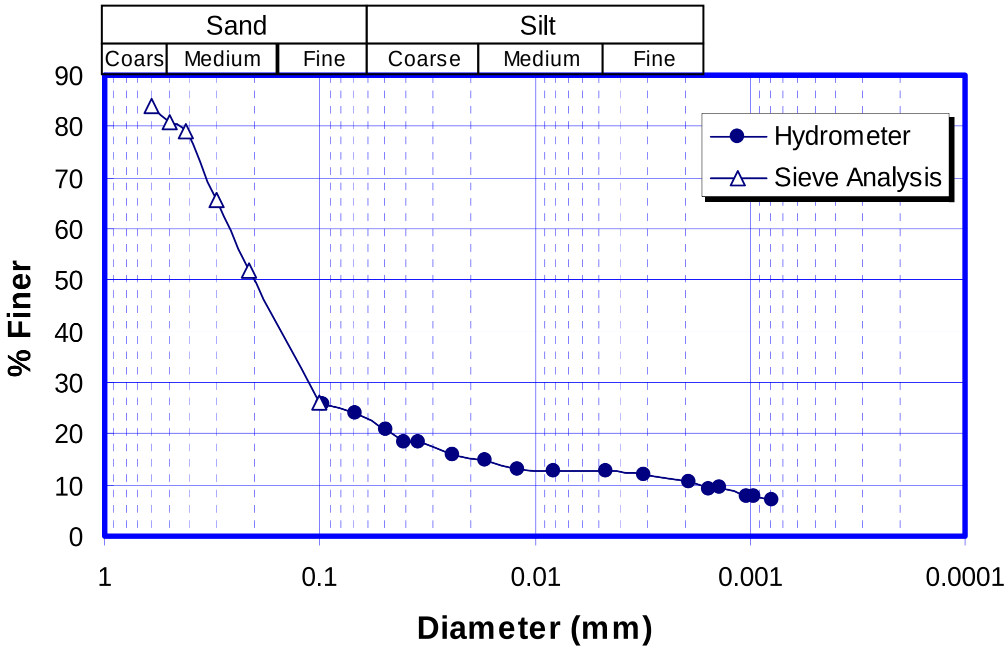

Figure 2-5: Particle size distribution for subgrade soil located at approximately 1.5m below the ground level at the problematic zone.

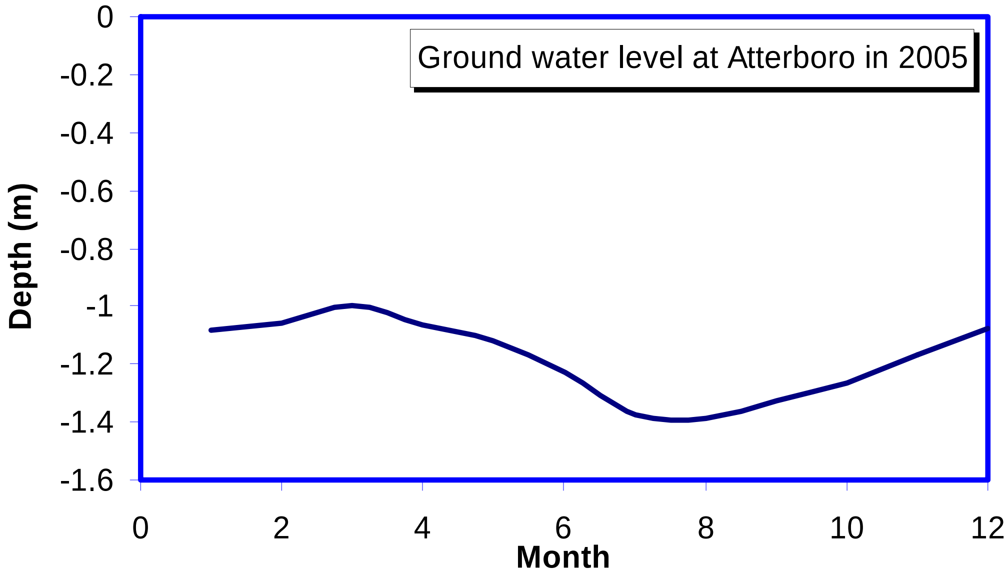

Figure 2-6: The variation of ground water level in nearby Atterboro between January (1.0) and December (12.0) in 2005 (USGS – United States Geological Survey).

The annual variation of groundwater table from nearby Atterboro district in 2005 is shown in Figure 2-6. The groundwater table is measured using open borehole well. In general, the water table does not vary much over the year, with the lowest point occurring in summer. Little information is available on the geological profile of the well and may not be representative of the hydrological condition at Mansfield.

Preliminary conclusion

The mud pumping phenomena at the Mansfield site is a recurring problem on a heavily used high-speed railway line. The site is overlain by three meters of silty sand of low permeability and the ground water elevation is about 1.7 meters below ground level. Nevertheless, the true hydrological scenario at the site such as presence of perched water table or sensitivity of the ground water table to rain infiltration is still relatively unknown. In reality, the cause of the mud pumping could be a complex interaction of man-made and environmental factors such as the in-situ soil permeability, undiscovered local faults and soft spots, presence of oil (reduces soil permeability and lowers strength), or inherent stresses in the rail (close to the welded joints).

2.3.2 Determination of useful Parameters

The scope of this research will be limited to investigating the role of water and the hydrological regime at the site. The role and contribution of different trains in the track degradation will also be monitored and studied. The summary of the factors of interest are shown in Table 2-1 and further elaborated in the following sections.

Table 2-1: The three possible factors contributing to mud pumping and corresponding four measurable parameters are shown.

Suspected Factors	**Attributes to be investigated**	**Measurable**			
		U	**A**	ρ	**T**
Water	Long term variation of groundwater table	●			
	Presence of perched water table at top subgrade	●			
	Effect of rain on track degradation	●			
	Effect of temperature and ice thaw in spring	●	●		●
Train Loading	Effect of High Speed Acela versus slower Amtrak Regionals and MBTA	●	●	●	
Track Geometry	Tracking the track degradation		●		

Note:

U = Pore pressures, A = Acceleration, ρ = Displacement and T = Temperature

2.3.2.1 Water

A systematic methodology has been developed to evaluate the hydrological regime at the both the problematic mud pumping site and a stable reference zone (between P2 and P3). The methodology can loosely be divided into studying the long term environmental effects (e.g. interaction between rainfall and rise of ground water table) and the short term dynamic effects of train imposed pore pressure accumulation.

Long term variation of water table level

The ground water level was found to be 1.7m below ground. However, the historical variation of the water level with time, season and influence of rainfall is not known. The groundwater level can be tracked by installing a deep piezometer, preferably below the ground water level. The real zone of interest, however, lies at the top subgrade closer to the ballast and subgrade interface. Since this zone is almost invariably above the water table, it is expected to be under matrix suction. There are a few interesting questions that could be explored:

a) Is the subgrade constantly saturated? Does the subgrade experience a series of wetting and drying cycle that translates to positive pore pressure and suction cycles during rain and no rain periods, such as the behavior shown in Figure 2-7?
b) Presence of a perched water table at the top layer of the subgrade (e.g. as a result of previously unidentified impermeably strata or oil accumulation or just simply clogged ballast).

The questions can be explored by placing another piezometer / tensiometer just below the ballast and subgrade interface.

Short term dynamic pore pressures

The development of mud pumping may be caused by development of dynamic pore pressures during passage of the train, especially near the ballast and subgrade interface. Acela trains impose loading frequencies of 30Hz between wheels in the bogies which may be too fast for the accumulated cyclical pore pressure to dissipate. In addition, the presence of oil may further reduce the permeability of the top subgrade.

Piezometer or tensiometer capable of measuring high response pore pressure development will be installed close to the ballast / subgrade interface. However, there are practical challenges in measuring dynamic pore pressures in the field. Firstly, there is an issue of sensor robustness; sensors in contact with ballast particles were destroyed by high traffic stresses although placing the sensors at 5cm below the interface worked (Aw 2004). Secondly, measuring pore pressure response due to impulse loading is a challenge, relying on the ability of piezometer to pick out fast transient changes in the pore pressure.

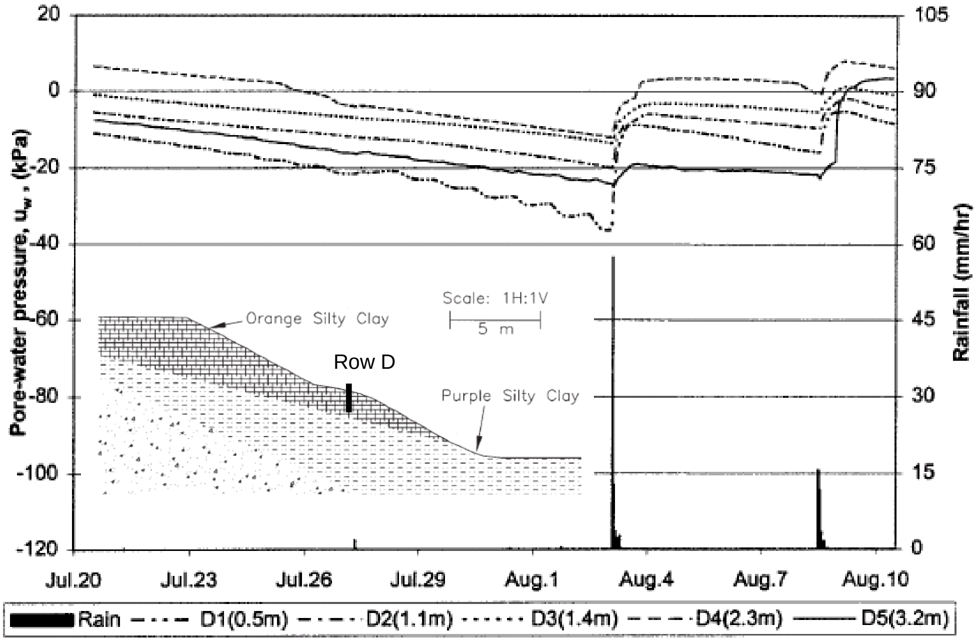

Figure 2-7: Data from five jet-filled tensiometers of different depths (D1 to D5) along row D (into the paper). Tensiometers registered increased in pore pressure after heavy rains (Gasmo *et al.,* 1999).

2.3.2.2 Train Loading

The Mansfield track is heavily used by Amtrak's Northeast Corridor Acela high speed train (240kph), Amtrak Regionals (180kph) and the MBTA commuter rail service (100kph). It serves more than 40 trains a day with 20 minute intervals during peak periods. The Amtrak Acela is generally heavier than its European counterparts (Table 2-2) due to additional carriage reinforcements in order to meet the US safety requirements. Dynamic measurements at Mansfield Wheel Impact Detector[⊺] found that full speed Acela trains imposes dynamic amplification up to twice its static load on the track.

The influence of the different trains on the track superstructure (rail, ties and subgrade) will be investigated. Preliminary conversation with Amtrak personnel found that Acela trains are a major cause in track deterioration. However, a more definitive conclusion can be found by comparing the track response to the three different trains. A useful method of measuring the track response is by analyzing the acceleration of the track (which can also be integrated to find velocity and displacements) and this can be achieved through installation of accelerometers.

[⊺] data obtained from Mike Tomas, Amtrak

The track response can be analyzed from the following perspective:

a) acceleration and displacement of top rail / tie response to the three different trains
b) acceleration and displacement subgrade response to the three different trains

Table 2-2: Comparison between Acela with high speed European and Japanese trains (after Cunningham et al). Amtrak has the highest static axle load (two axles to a bogie).

Line	Passenger Service		
	Maximum Operating Speed		Maximum Axle Load (static)
	km/h	mph	tonnes
Amtrak Acela NEC	**241**	**150**	**25.5 (engine)** **15.9 (coach)**
ICE Germany	280	174	19.4 (engine) 16.3 (coach)
AVE Spain	270	168	22.5 (engine)
TGV France	300	168	17.3 (coach)
Shinkansen Tokaido	270	168	11.0 (coach)

2.3.2.3 Track Geometry

The performance of the rail track is often controlled by the track geometry. The primary function of a track structure (i.e. rail, ties, and ballast) is to reduce the stresses of imposed wheel loads on the subgrade by distributing it over a wider area.

However, its function could be compromised if the ballast is fouled with infusion of subgrade materials such as that shown in Figure 2-8. Trial pits conducted at the site (during sensor installation) found that the fouled ballast extends down to about 40cm from the top of the tie at the edge of the track. The fouled ballast at the track center could extend deeper due to years of accumulation of material from tamping operations. Fouled ballast has poor drainage capabilities and easily trapped water which will cause further subgrade softening and mud pumping.

Figure 2-8: The ballast at the problematic mud pumping site is fouled with infusion of subgrade.

Figure 2-9 shows the laboratory-characterized particle size distribution (PSD) for the ballast – subgrade interface at the problematic zone. The presence of oil complicates the hydrometer analysis as it causes flocculation of fine-grained particles and results in overestimation of the actual grain size (i.e. flocculated particles will sink faster). The oil also cannot be adequately removed by hydrogen peroxide. As such, we assume that the PSD of the fine-grained material at the ballast/subgrade interface is similar to the underlying subgrade (due to subgrade penetration). Lifting the subgrade PSD out of Figure 2-5, the PSD of the ballast in Figure 2-9 can be plotted.

The ballast at Mansfield is highly fouled compared with the ideal clean ballast PSD (Selig & Waters, 1994) and has D_{10} of 0.002 mm and corresponding hydraulic conductivity of 4 x 10^{-6} cm/s (Hazen's formula).

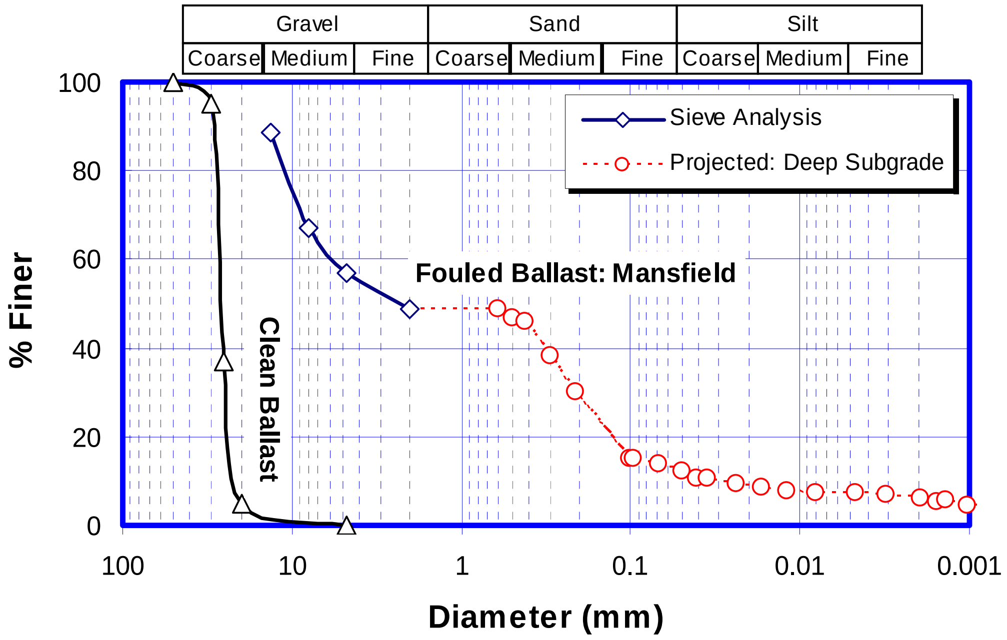

Figure 2-9: Particle size distribution at the ballast / subgrade interface. The presence of oil increases difficulty in characterizing fine-grained soil. The ideal clean ballast (Selig & Waters, 1994) is compared to the fouled Mansfield ballast. The composition of fines is obtained from the deep subgrade in Figure 2-3.

2.4 Monitoring Strategy and Sensor Placement

A monitoring strategy is devised based on the measurable criteria outlined in section 2.3.2. Table 2-3 summarizes the instrumentation adoption and measurement strategies. A total of eleven sensors comprising of four piezometers, four accelerometers and three settlement probes will be installed at the site. The sensors are installed at both the problematic and reference location to enable comparison between the two sites. Amtrak's safety regulations stipulate that the sensors will be installed between and not under the ties.

Table 2-3: Application of instrumentation and measurable parameters and scenario.

Factors	Measurable scenario	Instruments
1) Water	• Long term variation of ground water level due to rain infiltration • Development of negative pressure (matrix suction) or positive pressure during dry season and rain at top subgrade • Presence of perched water table near top subgrade	Tensiometers / piezometers at top subgrade and deeper subgrade (below the water table).
	• Dynamic pore pressure during passage of the trains	Tensiometers and piezometers at top and deep subgrade. Instruments must be capable of measuring high frequency pore pressure response.
2) Train Loading	• Track response to three different trains: Acela, Regional, and MBTA Commuter trains	Accelerometers at tie and top subgrade. Acceleration and displacement data.
3) Track Geometry	• Track degradation with time and effectiveness of tamping	Accelerometers at tie and top subgrade
	• Load transfer through the track (from tie to top subgrade)	Acceleration comparison between ties and subgrade
	• Long term track settlement	Settlement probes

Chapter 3: Mud Pumping Literature Review

3.1 Railway Track Problems

Mud pumping is one of the many railbed problems faced by the industry and is often described as the penetration of fine materials (usually from the subgrade) through the ballast resulting in differential track settlements. The fine materials penetrated from the subgrade are usually visible, appearing as dried mud (during dry days) or as pool of muddy slurry during rainy spells. A Japanese survey carried out in 1975 found that out of 17000 km of frequently used rails in Japan, more than 700km suffer from mud pumping and regular track alignment and maintenance cycle lasted only 58 days on the average (Katsumasa 1978).

3.2 Field Investigation on Mud Pumping

Before the middle of last century, track pumping was thought to be squishing of subgrade through the ballast as a result of low subgrade strength. In the early 1950s, British Railways conducted inspections by performing cross section trenching in old and new trackbeds. It was found that track movements on slurried ballasts (i.e. clogged ballast) were the worst despite having high strength subgrade (Ayres 1986). It was thus concluded that water has a role to play and since then more emphasis has been given to better understand the role of water in mud pumping.

Mud pumping frequently occurs at spots containing fine materials and access to water, either through high water table or pondage and is a recurring event if not treated properly. During the pumping process, fine materials penetrate the ballast through the voids. The ballast is now fouled (clogged with fine particles) and can no longer perform its duty as a primary drainage and stress reduction effectively. It has been found that the penetrated fine materials can originate either from the original ground, or from crushed ballast particles. There are two forms of mud pumping widely observed and reported in the literature. Ayres (1986) formally defines them as:

a) *Erosion Pumping Failure (*EPF*)* – slurry derives from the subgrade soil. The ballast particles penetrate into the subgrade forcing soil particles up into the ballast layer.

b) *Dirty Ballast Pumping Failure (DBPF*) – slurry forms in the upper ballast as a result of accumulation of attrition products. The attrition products can be made of accumulation of wind-blown deposits, brake dust, concrete sleeper erosion, and dirt dropping from the vehicles.

It is usually very hard to differentiate the two forms of ballast fouling from visual inspections (Figure 3-1).

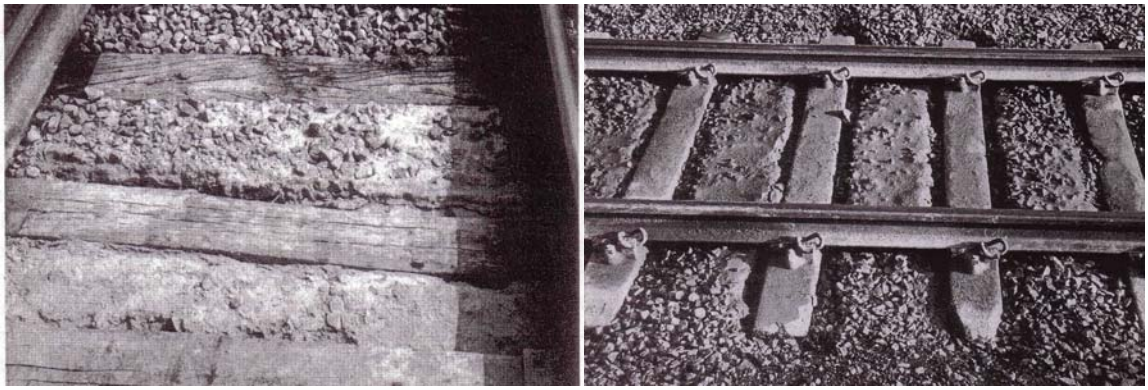

Figure 3-1: Which is which? It is hard to visually determine the DBPF (*Dirty Ballast Pumping Failure,* left picture*)* from the EPF (*Erosion Pumping Failure,* right picture). (Ayres 1986).

Tadatoshi (1977) proposed a suction driven model where the underlying subgrade particles are pull out from the suction created in the ballast during the unloading cycle (Figure 3-2). In the absence of the train, the ties are suspended from the rail due to eroded subgrade. At the onset of loading, the ties are pushed into the ground and develop high pore water pressure. During unloading, the space evacuated by the ties creates a suction that draws the fines from the subgrade and the cycle repeats for every loading.

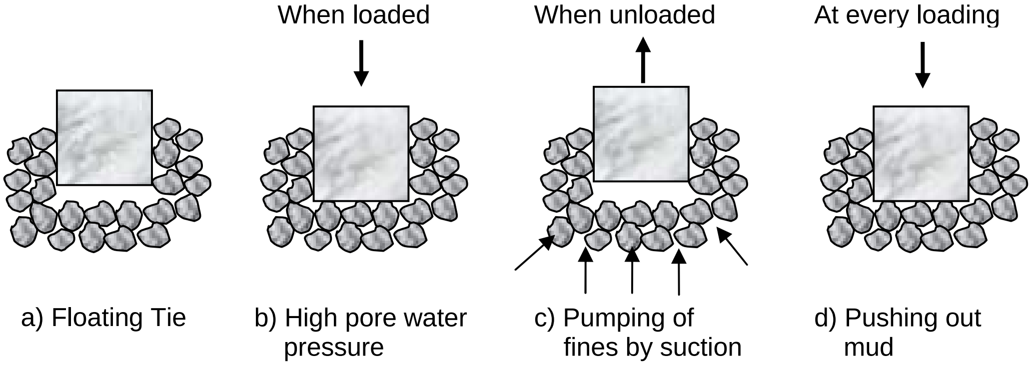

Figure 3-2: Behavior of mud pumping (after Tadatoshi 1997)

Raymond (1986), whilst investigating the performance of previously installed geotextiles in North American railways found that at some sites the ballast had been completely fouled by fine materials. Raymond suspected that the freezing and thawing cycle might have caused the subballast materials to be pumped out since the duration of fouling was over one winter (Figure 3-3). The freezing zone extends down to the sub-ballast level and during thawing, the upper subballast level is first to melt and lower level acting as a layer of impermeable frozen layer. This caused the excess pore pressure during loading to migrate upwards into the ballast.

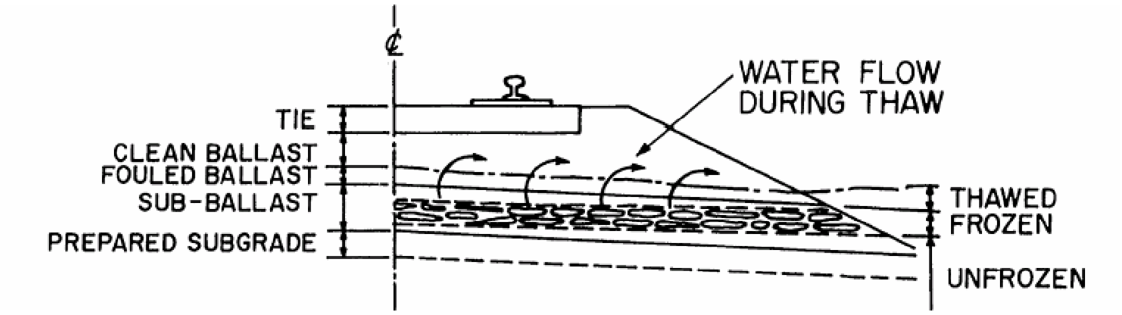

Figure 3-3: Proposed mechanism for track pumping during spring thaw on frozen track support (Raymond 1986).

Another example of slurried ballast was investigated by Blacklock (1984) at a mud pumping site on Amtrak's Bush River to Edgewood, Maryland track. The tracks exhibited soil being pumped through the ballast and experienced minor subsidence and was frequently maintained through realignment and application of fresh ballast. Night trenching investigations found that the ballast layer was filled with subgrade mud particles and oil leakage and the layer of subballast was non-existent. Repacking of the ballast in some areas caused the ballast layer to be as thick as 3ft. The typical subgrade soil found at the site is a non-plastic clayey and silty sand material. Clogging of the ballast (with subgrade and other environmental waste) reduces the function of ballast as a draining material and the trapped water will further create mud pumping problems. Recommended solutions include installing longitudinal and transverse drains for eliminating trapped water pockets in the soil squeeze areas the muddy ballast and geotextiles was suggested as a replacement for the subballast.

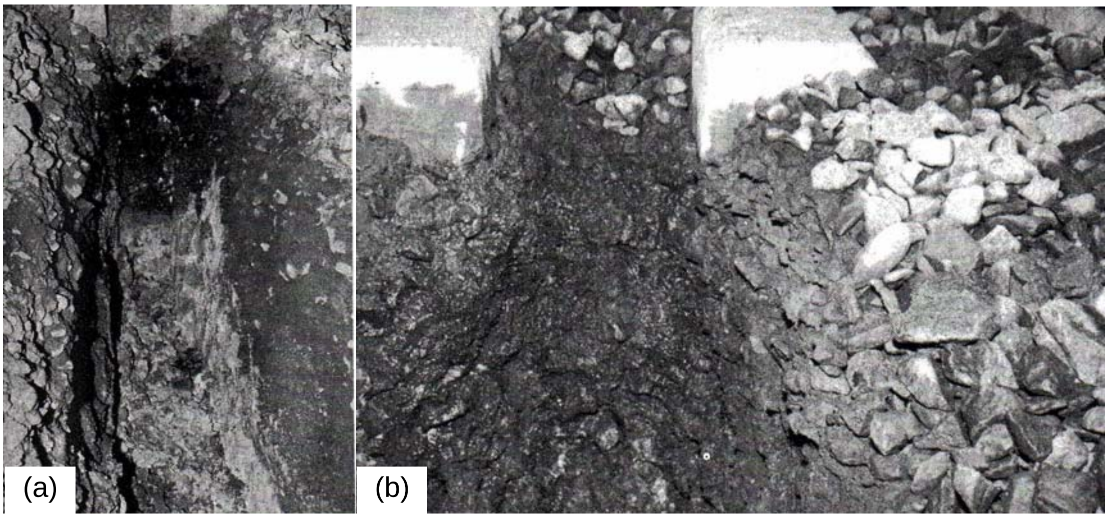

Figure 3-4: (a) Subgrade "soil squeeze" was found in the ballast layer. (b) Wet and muddy ballast after 2 hours of light rain (Blacklock, 1984).

3.3 Laboratory Mud Pumping Investigation

3.3.1 Cyclical Soil Behavior

Much of the ideas used in formulating and understanding mud pumping mechanisms are derived from cyclical soil behavior, based on observations that the track superstructure and underlying subgrade experience frequent repeated train loadings. The fundamental understanding of cyclical soil behavior was spearheaded by the Norwegian Geotechnical Institute (NGI) and MIT in the early 90's for offshore oil platform structures. The groundwork laid by earlier researchers was being incorporated into routine laboratory investigation of subgrade behavior under repeated loads. Therefore, the track behavior and response to repeated loading explicitly assumes the following:

1. **Effect of critical stress τ_c/Su**
   There exists a critical stress application ratio which, if exceeded, results in shear failure after a certain number of load cycles (under undrained conditions). The stress application ratio is defined by τ_c/Su (application of shear stress over the undrained strength of the soil). At applied stresses below the critical τ_c/Su ratio, the soil is able to accommodate large number of repeated loading without accumulating plastic deformation. With each successive cycle, the soil response "hardens" and the plastic strain generated reduces until equilibrium is achieved where the recoverable strain component greatly exceeds the irrecoverable strain component. This is also known as the shakedown condition and exhibit quasi-elastic or resilient response; the particle contacts within the soil rearrange themselves into a fabric resistant to that loading. However, at high τ_c/Su, excessive plastic strain will generate with each successive cycle of loading. Soil mechanics normally defines accumulated strain of 15% and cyclic strain of 3% or stress levels at the failure criteria as failure.

2. **One way vs two way stress cycle**
   Two way stress cycles (stress reversal) are found to be more damaging than one way stress cycles. Two way stress cycles cause accumulation of mean and cyclic strains while one way stress cycles are limited to cyclic strain accumulation. Generally, one way stress cycles are used for representing train loading (e.g. Miller 2000, Boomintahan *et al* 1998) and confirmed by Li (2000) using vertical and horizontal pressure sensors installed in the field. Nevertheless, Selig & Waters (1994) argued that railway tracks undergoing prolonged cyclical loading might, in fact, experience two way stress cycles at the subgrade level. By analyzing the stress levels in the track in the loaded and unloaded states, Selig found that the unloaded horizontal stress increases with successive loading cycles such that it ends up higher than the unloaded vertical stress. This results in two way stress cycles as the stress path progresses from the unloaded state onto the loaded state, resulting in accelerated track deterioration. Track realignment and tamping will reset the stresses

back to one way cycling. This theory has fully based on laboratory measurements of cycling soil in an instrumented box and has not been proven in the field.

3. **Development of cumulative pore pressure**

   Continuous cyclical loading have been observed to generate excessive pore pressures for low permeability soils (or even in sands if the developed pore pressure exceeds dissipation for high frequency loading) at undrained conditions. Ohara *et al* (1981) reported that excess pore pressure induced by the repeated shear stress is two to four times higher than statically generated. Generation of excess pore pressure causes two outcomes: a) reduction of effective stress causes effective stress paths to coincide with the failure state line, or b) drainage of excess pore pressure causes consolidation of the clay layer. The development of pore pressure also depends on the over-consolidation ratio (OCR)[戊]. For normally consolidated soil, the accumulation of pore pressure follows a steady increase with number of cycles. For OC soils, there will be an initial reduction in pore pressure due to dilation of fine-grained soils, followed by increase in excessive pore pressure.

A common assumption used by many laboratory tests representing track loading is the continuous cyclical loading to failure in undrained conditions. This approach is, however, strictly not representative of the actual railway condition. Firstly, the soil specimen is cyclically loaded until failure while real trains have finite number of carriages (often not more than 10 unless it is heavy axle freight train that can extend to a hundred carriages). Secondly, the subgrade is likely to exist in a partially drained state since excess pore pressures are allowed to dissipate during the time window between trains.

3.3.2 Effect of Critical Stress Application (Miller *et al.*, 2000)

Miller investigated the effect of critical stress application on partially saturated soils. By considering two soil saturation conditions (partially saturated field natural water content and fully saturated soils) and deviator stress ($\sigma_V - \sigma_H$) variation, the cyclical stable and failure regions of soil samples can be defined (Figure 3-5). The soil used for the experiments was high plasticity clay known as Mississippi Buckshot Clay obtained from man-made soft subgrade section at TTCI (Transportation Technology Center Inc). For tests conducted at the natural water content (with saturation ranging from 90 to 100%), the drainage lines were kept opened during shearing. However, Miller suggested that these tests might be partially drained due to possibility of internal pore pressure development as a result from rapid cyclical loading and highly saturated soil samples. For undrained tests, back pressure saturation was used to fully saturate the system and drainage lines were closed during shearing.

[戊] ratio of current vertical stress over the maximum historical stress experienced by the soil

The critical deviator stress (σ_1–σ_3) can be estimated by finding the dividing border between the failure region (high deviator stress causes excessive plastic deformation) and stable region (shakedown regions where the soil absorbs high cycling loads with no excessive deformation). Soils with 90% saturation have critical deviator stress which is about three times higher than that of fully saturated soils. This has significant implications for soft tracks occasionally inundated with heavy rains.

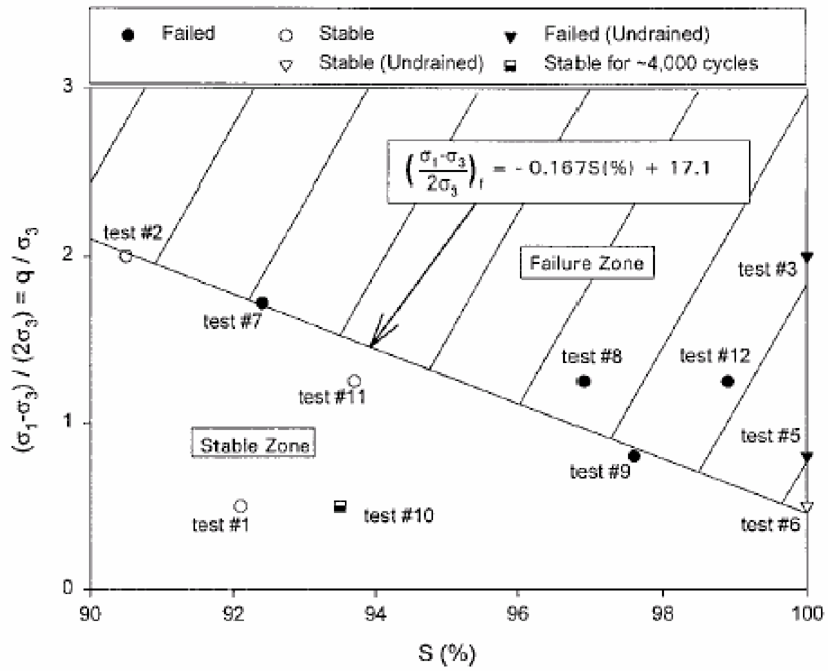

Figure 3-5: Effect of cyclic stress ratio and degree of saturation on stability of soil sample undergoing cyclical loading. Partially saturated soils were tested with open drainage in partially drained conditions. Saturated soils were backpressure saturated and tested with close drainage in an undrained manner (Miller et al 2000).

3.3.3 Pore Pressure Development at the Top of Subgrade Interface

In the 90s, there was interest in investigating the development of pore pressure at the top few inches of the subgrade. It is thought that since the fine grained subgrade soils has low permeability, the pore pressure dissipated from the subgrade within one load cycle must occur at the thin layer next to the surface (Alobaidi *et al* 1996). The dissipation of pore pressure creates a high hydraulic exit gradient which acts as a main driving force in pushing the fine subgrade soil into the ballast. This is, however, hard to prove experimentally due to difficulties in measuring pore pressure development at the ballast/subgrade interface. Researchers at the University of Birmingham, UK, attempted to investigate the correlation between pore pressure development at the interface and amount of mud pumped via cyclical triaxial tests. The cyclical tests were performed with either a layer of geotextile or geocomposite (combination of geotextile with sand layers).

The pore pressure transducer[1] was installed at 7mm below the bottom of the geotextile / geocomposite layer. In order to simulate ballast particles, balls of 15mm were epoxied on the top cap as shown in Figure 3-6. A cyclical rectangular mean stress 20 kPa was applied with cyclical stress amplitude of 10kPa (i.e. stress range between 10 to 30kPa) with frequency of 2.0Hz. At the end of the experiment, the geosynthetics and free standing water was oven dried to obtain mass of soil pumped through the experiment. The pumped soil mass can be converted into equivalent loss of thickness through the formula:

$$\Delta h \text{ (pump)} = \frac{w_f}{A_f \times \gamma_d}$$

where w_f is the mass of soil within or passing the geotextile (kg), A_f the loaded area (m^2) and γ_d (kg/m^3).

1-D Unit Cell Loading **3-D Triaxial Loading**

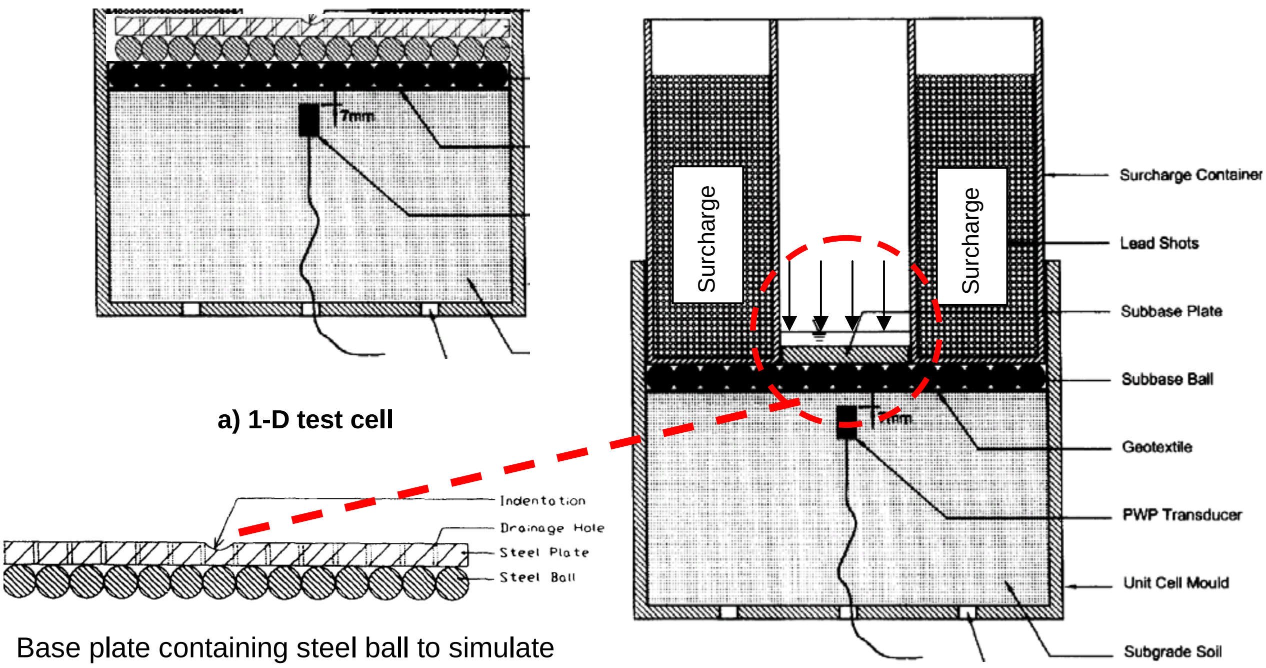

a) 1-D test cell

Base plate containing steel ball to simulate ballast particles

b) 3-D triaxial test cell. Surcharge is applied through heavy lead surrounding the specimen.

Figure 3-6: a) 1-D Test cell and b) 3D test cells (Alobaidi)

---

[1] To embed the pore pressure transducer, a 10mm diameter hole is drilled from the sample bottom. The hole is refilled after placement of the pressure transducer.

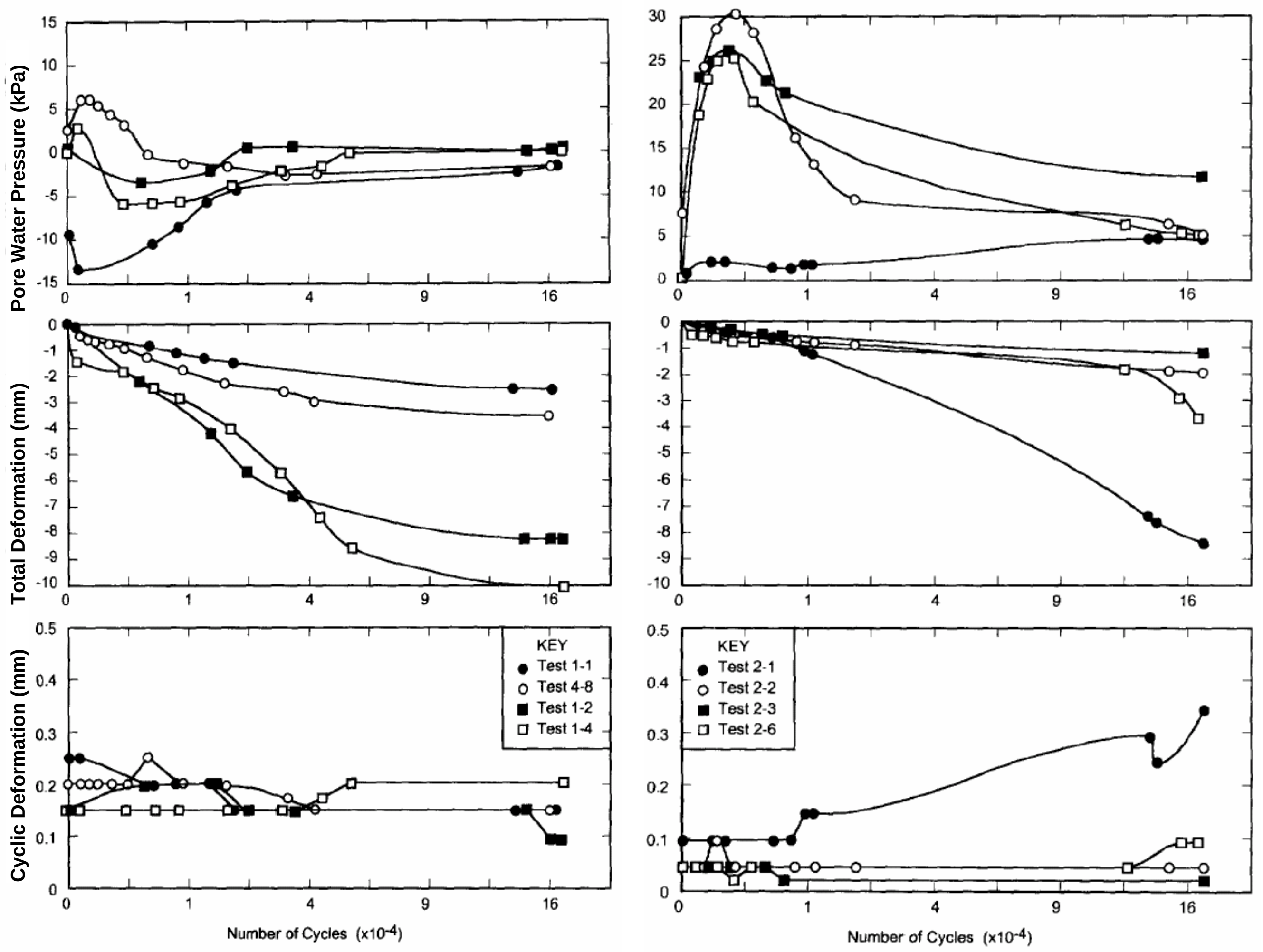

No.	Separation layer	Water Added (mL)	Mud Pump (mm)	Sub def (mm)	Total (mm)
1-1	Geotextile	500	**1.90**	0.6	2.5
4-8	Geotextile	720	**2.21**	1.29	3.5
1-2	Geotextile + 15mm sand	720	**2.74**	5.36*	8.1
1-4	Geotextile + 3D grid filled with sand	720	**4.43**	15.57*	10

* High sand layer deformation

1D laboratory measurements

No.	Separation layer	Water Added (mL)	Mud Pump (mm)	Sub def (mm)	Total (mm)
2-1	Geotextile	720	**12***	-3.6	8.4
2-2	Geotextile + 15mm sand	720	**0.6**	1.4	2.0
2-3	Geotextile + 3D grid filled with sand	720	**0.17**	0.93	1.1
2-6	Geotextile + 3D grid filled with sand	720	**2.92**	0.98	3.9

***** Pumping took place under the top cap (instrumented for total deformation) and outside the top cap area (not captured by LVDT), hence mud pump > total deformation

3D laboratory measurements

Figure 3-7: Tests results of the 1D and 3D. Total deformation (measured by LVDT at the top platen) is a combination of pumped material and subgrade deformation (Alobaidi et al 1998).

The results of the investigation for two cases[庚] (soil with geotextile layer and soil with geocomposite layer) are shown in Figure 3-7 and presented below (Alobaidi *et al* 1998). The total soil deformation, measured using LVDT at the top platen level, is a combination of soil pumped through the geosynthetics (determined at the end of the test) and soil sample deformation.

1. **Pore pressure development *near* the interface**
   Typical pore pressure development profiles near the interface are characterized by peak pore pressure around 2000 to 5000 cycles. The corresponding total deformation profiles continuously increased until 160 000 cycles and do not have the bell shape profile of pore pressures. In addition, tests 1-4 (1-D) and 2-1 (3D) have the highest mud pumping despite having the lowest pore pressure development. Since there is no discernable correlation between the pore pressure and total deformation profile, Alobaidi concluded that that high pore pressures alone do not contribute towards mud pumping.

2. **Effect of geotextile and geocomposites**
   The mud pumping is greatly affected by the type of geosynthetics used between the ballast and subgrade layers. In the 3D model, geotextile layer produces the highest mud pumping compared with the two different geocomposites which have sand layers. One possible reason suggested by Alobaidi is that the geotextile layer functions as a filter and separation layer. The excess pore pressure at the surface of the subgrade particles is able to dissipate very quickly, thus setting up high exit hydraulic gradient which pushes the soil particles upward. The geocomposite, on the other hand, functions as a barrier, prolongs the drainage path, reduces the velocity of the migrating water, and traps any subgrade particles which are pumped. In addition, the stiff layer of sand is better able to absorb and reduces the transmission of load onto the subgrade.
   The reverse is true for the I-D case. There is no difference between mud pumping produced by using geotextile and geotextile with 15mm layer of sand. The geocomposite with 3D grid filled with sand has twice the mud pumps compared with the other two layers.

3. **Standing water Effect**
   In a clogged ballast or subgrade with poor drainage, water (e.g. from rain) can accumulate above the subgrade layer and this is called the standing water effect. By adding variable amount of standing water on top of the soil specimen and soaking for 24 hours, Alobaidi *et al* (1998) studied the effect of standing water on mud pumping. The mud pumping activity increases with increasing standing water (Figure 3-8).

[庚] There are no pore pressure measurements of case of soil only (no external reinforcements)

Alobaidi also investigated the effect of frequency on mud pumping and found that frequency only had an effect at higher standing water (Figure 3-9).

The effect of standing water on the variation of water content in the soil is also investigated since the soil strength is related to the water content (Alobaidi *et al* 1999). The soil sample was consolidated to 200 kPa and unloaded to 10 kPa, soaked with 720ml of water for two weeks, and then tested for water content at various depths (Figure 3-10). The water content at depth of 2mm was 38.5%, below the liquid limit of the soil at 48.5%. However, it is possible that the water content at the top 1mm layer exceeded the liquid limit of the soil. Visual inspections found that the soil particles at the surfaced appeared loose and could easily be eroded by flowing water.

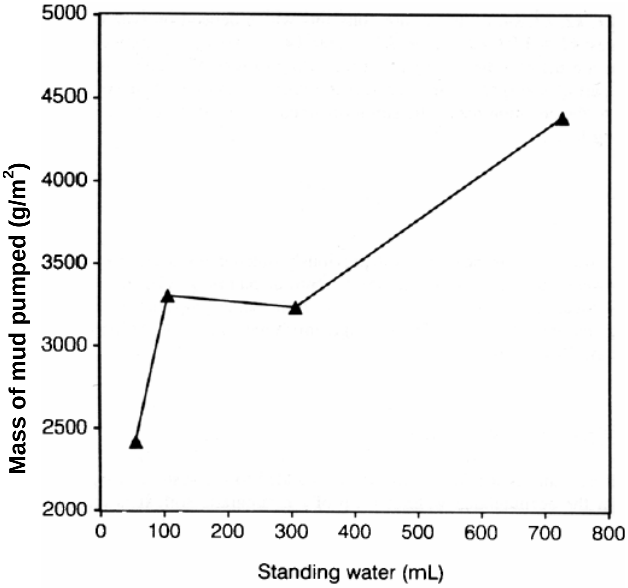

Figure 3-8: Effect of standing water on mud pumping (Alobaidi 1994).

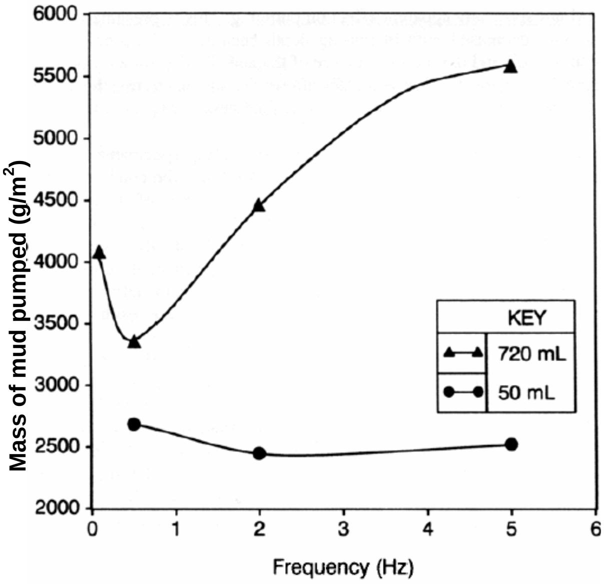

Figure 3-9: Effect of frequency on the mud pumping (Alobaidi 1994)

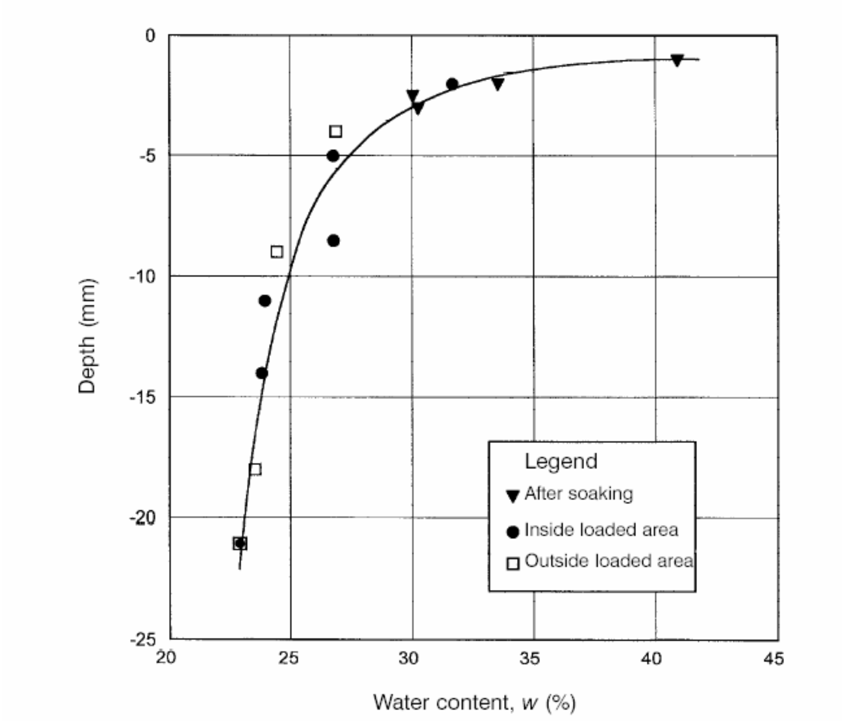

Figure 3-10: The variation of water content with sample depth as a result of two weeks soaking (Alobaidi 1994).

3.4 Theoretical Modeling and Track Degradation Models

3.4.1 Pore Pressure Development at the Interface

Alobaidi (1996) investigated the development and dissipation of pore pressure under a static load for a small domain (consisting of a few gravels and a few centimeters of subgrade) using finite element analysis. Consolidation was allowed to occur and the dissipation of pore pressure was studied. The description of the analysis is briefly described below:

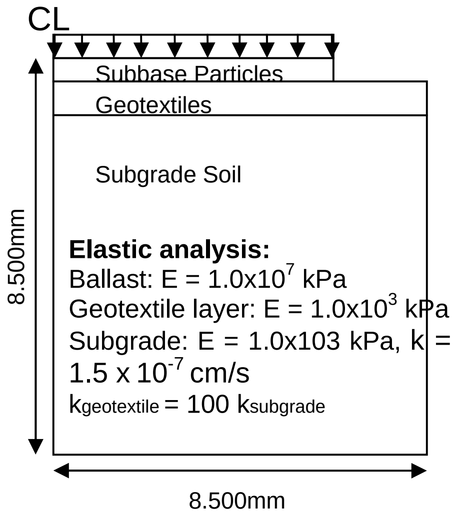

Figure 3-11: F.E. mesh to investigate development of pore pressure at small scale (Alobaidi 1996).

During the application of instantaneous loading (t = 0), pore pressure of 10 kPa and 12 kPa are generated at the center and side of the gravel particle respectively (Figure 3-12). Within 0.25s, the pore pressure at the end of the gravel dissipated quickly, reducing from 10 kPa to 0.6 kPa. This pressure difference between the center and end of the particle was equivalent to a hydraulic gradient (*i*) of 147. By 100 seconds, the pore pressure in the middle of the gravel has dissipated to 1kPa. The relatively high hydraulic gradient of 147 could be responsible for the drive in flushing the fine particles into the ballast.

Figure 3-13 illustrates the dissipation of pore pressure profile at the center and side of the gravel, replotted from Figure 3-12. The pore pressure at the end of the gravel and top two millimeters of the subgrade dissipated within 0.25 seconds[✻]. By combining the laboratory and theoretical investigations, Alobaidi suggested that mud pumping is not so much affected by the pore pressures generated during cyclical loading as by the rate pore pressure dissipation at the top subgrade layer.

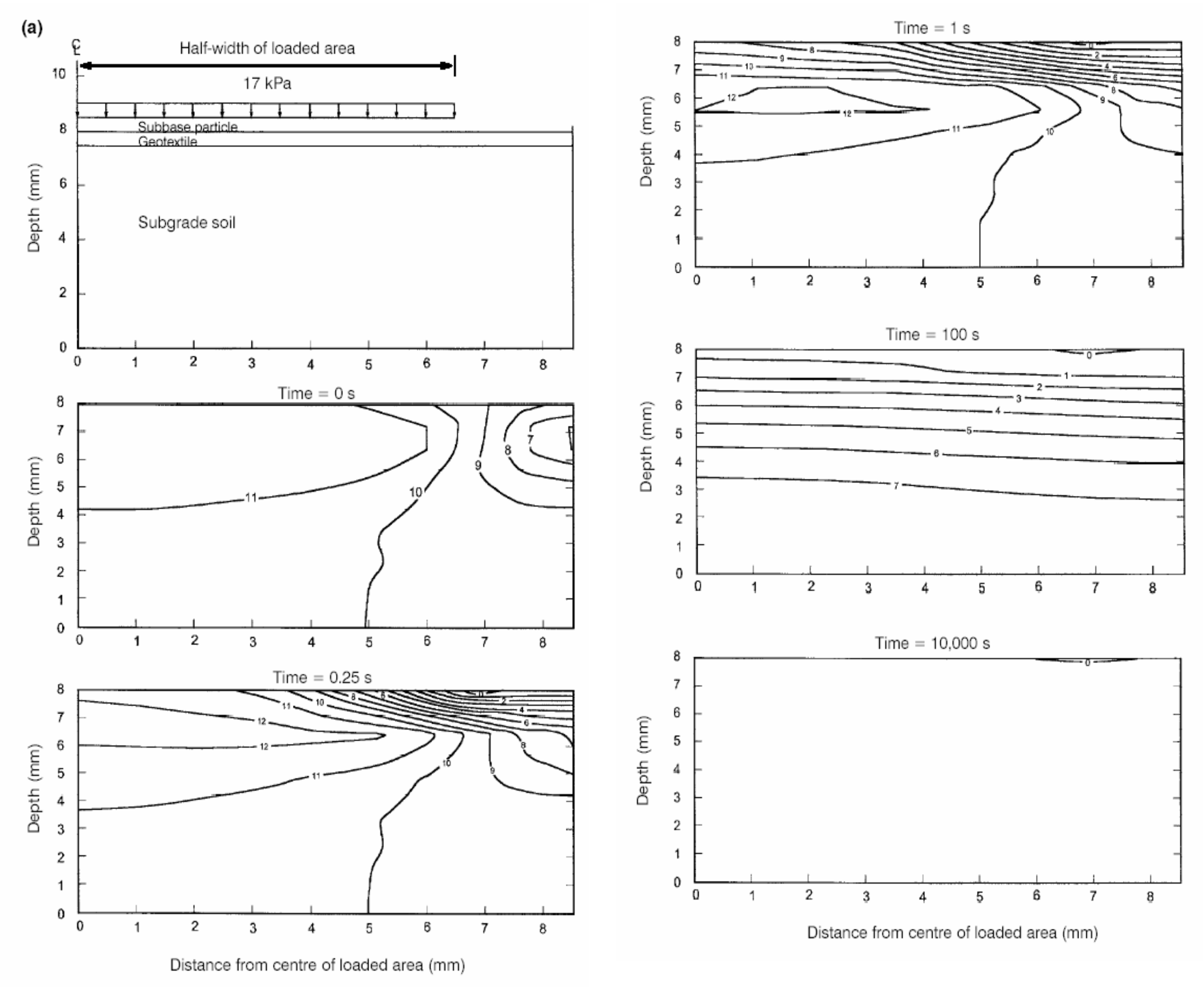

Figure 3-12: Excess Pore Pressure contours (kPa) in the subgrade between time t = 0s to 10000s (Alobaidi 1996).

[✻] Time for between wheels in the bogie is 0.04 seconds for 240kph train.

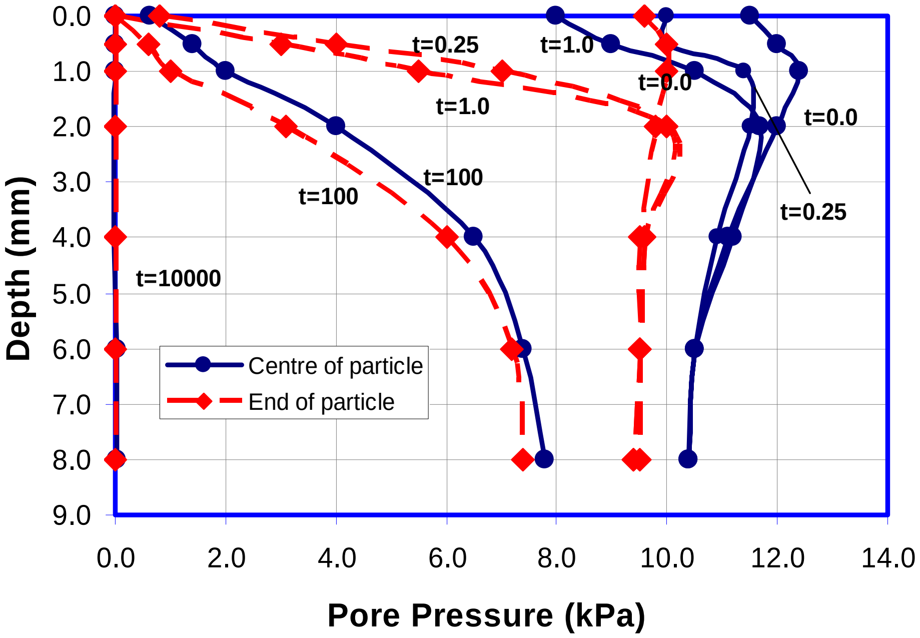

Figure 3-13: Variation of excessive pore water pressure with depth under the centre of a contact area for different time intervals (after Alobaidi 1996)

3.4.2 Track Degradation Models

The 80s and 90s saw an increased in development of analytical track models in order to capture track degradation. Early track models were primarily power curve fitting models based on temporal cumulative track displacements and were applied to a wide range of track problems with track settlement as the sole predictive parameter. The usual form of the power curve fitting model (Monismith *et al* 1975):

$$y = aN^b + c$$

where y = settlement of the track (m) or vertical strain (%), N = Temporal variable (e.g. time, number of loading cycles), and a, b, c = constants depending on the track, soil properties, and applied loading

Alva-Hurtado & Selig (1981) – ballast degradation model

Alva *et al* proposed a track model solely based on ballast degradation, without consideration of the subgrade influence. The track model came in the form of $\varepsilon = \varepsilon_1[1 + C\log(N)]$, where ε = strains in the ballast layer, ε_1 the permanent strain after the first loading cycle and *N* the series of identical loading cycles. The strains can be converted into settlement through multiplication with the thickness of the ballast layer. ε_1

captures the initial ballast densification immediately after track realignment and tamping (which loosens the ballast) and the second logarithmic term captures the long term ballast straining (due to grinding, breakage of ballast particles, etc).

Sato (1995) – ballast degradation model

Sato proposed a ballast degradation model in the form of $y = \gamma(1 - e^{aN}) + \beta N$ where y is the track settlement, *N* the number of cycles or MGT, and the terms γ,α,β represent curve fitting models. Similar to Alva-Hurtado & Selig's model, the first term represents the initial track settlement and the second term represents long term ballast degradation.

The difference between the two models lies in the shape of the model; Sato's model predicts lower initial settlement and much higher long term settlement (Figure 3-14).

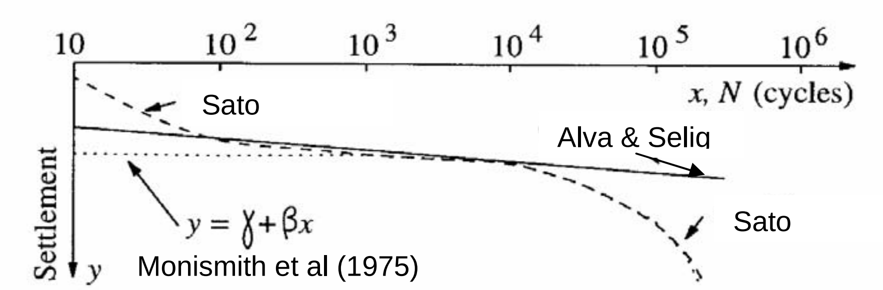

Figure 3-14: Comparison between the Monismith, Alva & Selig and Sato's track degradation model, matched at N = 100, 5000 and 100 000 cycles (Dahlberg, 2001)

Li & Selig (1998) – Subgrade degradation model

Li & Selig developed a predictive track degradation model based on degradation of problematic soft subgrade such as mud pumping and excessive vertical deformation. Borrowing ideas from cyclical soil behavior, Li & Selig suggested that most of the soft subgrade failures can be prevented if the acting wheel stresses at the top subgrade level do not exceed the critical level. In another words, it is important to keep the subgrade stresses in the shakedown region. By investigating the stress transfer[‡] through the track superstructure using multilayered three dimensional elastic finite element analysis, Li found that ballast thickness and resilient modulus of the ballast and subgrade are the most important parameters in controlling load stresses at the top subgrade level; significant subgrade stress reduction can be achieved by employer thicker and stiffer ballast. The track degradation model comes in the form of

---

[‡] The main load transfer mechanisms in the track structures are the stiff rail (transfers roughly 50% of the wheel load onto underlying tie by spreading the wheel load across several ties), sleepers, and the stiff ballast layer. In a good track, top subgrade usually receives 0.0045% of top rail stresses (Esveld 2001).

$$\varepsilon_p(\%) = a(\sigma_d / \sigma_s)^m N^b$$

where ε_p is subgrade strain, σ_d the applied deviator stress (σ_v - σ_h), σ_s the soil undrained strength (found from either triaxial compression or undrained unconsolidated compression tests), and N the number of cyclical cycles. *a*, *m* and *b* are curve fitting parameters found by matching the cyclical plastic deformation of soil samples which exist in a narrow range for a given soil type (Table 3-1).

Table 3-1: Suggested a, m, b parameters for a few soil types (Li & Selig 1998).

	Soil Classification (3-10 Samples)			
	ML	MH	CL	CH
b	0.06 -0.17	0.08 -0.19	0.08-0.34	0.12-0.27
a	---	---	0.3-3.5	0.82-1.5
m	1.4-2.0	1.3-4.2	1.0-2.6	1.3-3.9
Observations	2	2	10	7

The settlement of the subgrade layer can be found by integrating the strains over the length (T) of the subgrade layer:

$$\rho = \int_0^T \varepsilon_p dt$$

which can also be written as

$$\rho = I_p La\left(\frac{P_d}{\sigma_s A}\right)^m N^b / 100$$

where I_p is the dimensionless influence factor, L and A are arbitrary factors to make the solution dimensionless (L = 0.152m, and A = 0.645 m^2), and P_d is the dynamic wheel load (given by $P_d = P_{static}(1 + 0.33V/D)$ and V = velocity of train in mph and D = diameter of wheel in inches).

Designing the ballast thickness

Problematic soft subgrade can be, as proposed by Li & Selig, mitigated by ensuring wheel stresses at the top subgrade do not exceed the critical stress. This can be achieved by providing adequate ballast thickness. The design process of selecting adequate ballast thickness was proposed as follows:

a) Select the maximum allowable plastic strains (ρ_a) and corresponding number of wheel load cycles (N)
b) Determine the value of I_p based on the selected plastic strains and load cycles. The influence factor can be rewrite as:

$$I_p = \frac{\frac{\rho_a}{L}}{a\left(\frac{P_d}{\sigma_s A}\right)^m N^b} \times 100$$

c) The thickness of the ballast can be found from design charts such as Figure 3-15.

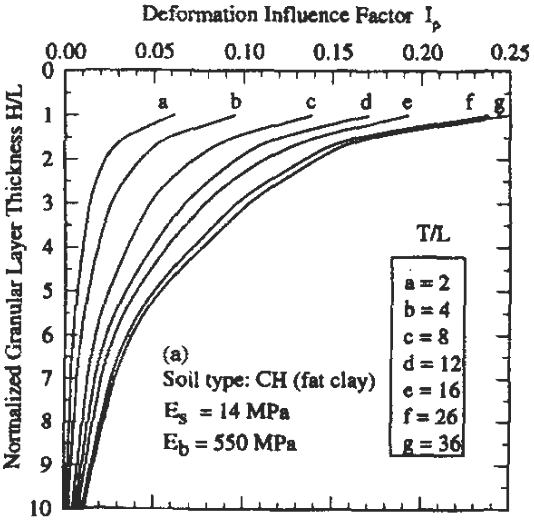

Figure 3-15: Design chart: Selecting the ballast layer thickness based on the calculated influence factor I_p and subgrade thickness (T). Design charts for various ballast and subgrade modulus are also available (Li & Selig 1998)

The effectiveness of the design method was evaluated based on two case studies. In the first case, the thickness of the ballast was prescribed for a mud pumping and progressive shear failure site in Alps, New Mexico, which required frequent track maintenance. Adoption of the program yielded favorable results; the projected track lifespan was two years based on 1.5 years of monitoring. In the second case, a problematic progressive shear failure site at Edgewood, Md and nearby problem free Aberdeen, Md was studied. The softer Edgewood has actual ballast thickness of 0.3-0.5m, which was below calculated thickness of 1m. In comparison, the problem free Aberdeen site has actual ballast thickness of 0.7-1.0m, which was greater than the calculated thickness of 0.4m.

3.4.3 Properties of Mud Pumping Subgrade Soil

A survey of 8 mud pumping soils reported in the literature lies in the region of fine, inorganic silt and clays (Table 3-2). Much of the problematic subgrade soils are classified as inorganic clays with medium to low plasticity with some silt or fine sand. Figure 3-16 shows the plasticity chart for all the problematic soil. However, the was a mud pumping at site Edgewood, MD with non plastic sandy silt subgrade material.

Table 3-2: Type of common mud pumping soil reported in the literature

Reference	Soil	Location	PI	LL	USCS Classification
Voottipruex & Roongthanee (2003)		Thailand,	21%	43%	Inorganic clay, low to medium plasticity (CL). 93.7% (#40) and 77% (#200).
Alobaidi (1999)	Keuper Marl	Birmingham, UK	23%	49%	Silty clay of medium plasticity
Hayashi (2000)	Shirasu	Japan			Gravel (8%), Sand (82%), and Silt (10%)
Boomintahan & Srinivasan (1988)	Attipattu	Attipattu, India	27%	45%	C.I. Fine silty and with uniformity coefficient of 2. Sand (80%), rest silt and clay
	Mundi-yampakkam	India	21	40	
Raymond (1986)	Copan	Kansas	30	48	soil gradation graph available
	Valley Falls	Kansas	22	45	
	El Dorado Cut	Kansas	29	48	
Ayres (1986)	Lower Lias		24	44	Over consolidated marine deposited calcareous clay
Blacklock (1984)		Edgewood, MD	N/A	N/A	Non plastic sandy silt

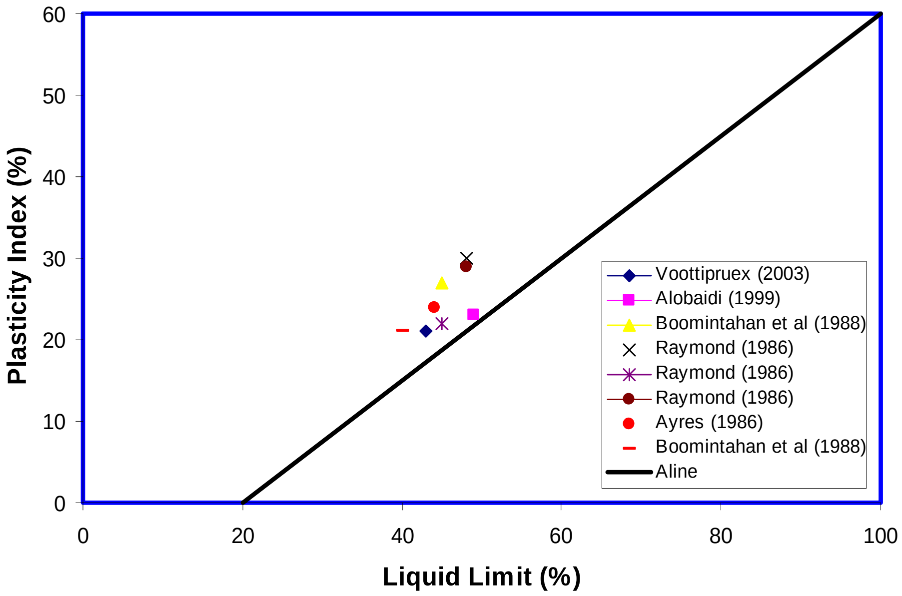

Figure 3-16: Plasticity chart of the subgrade at reported mud pumping sites in the literature.

3.5 Current Mud Pumping Remediation and Prevention Methods

There are a few methods widely used in the industry to remediate or prevent mud pumping. They are:

1. Track realignment and ballast addition

   This is the cheapest solution. Track alignment vehicles lift up the rail and new ballast materials are added to it. It is, however, a temporary solution as the mud pumping problem is not solved but alleviated.

2. Ballast replacement

   The fouled ballast is completely replaced with new ballast and granular layer of subballast. It has been reported that a layer of sand between the subballast and the subgrade works well in preventing mud pumping. The sand acts as a filter for keeping the subgrade from migrating into the ballast while providing adequate drainage from rain (Ayres 1986, Snaith and Bell 1978). It has been observed by British Railways that the subgrade typically penetrate about 2 to 4mm into the underside of the sand and then stop. Chapter 1 of the Manual for Railway Engineering (American Railway Engineering Association, AREA, 1991) recommends that placement of a well graded granular subballast having a top size of not less than 12.5mm and graded down to between 7 and 12% passing the 75 µm sieve (No 200). Case studies conducted by Li & Selig (1998) found that increasing the thickness of the ballast can improve the life span of tracks with problematic soft subgrade.

3. Subgrade improvement methods

   Remedial measures such as HMA (hot mixed asphalt) and lime stabilization can be used to strengthen subgrade material. Geotextiles are widely used as a strengthening and separation material. They are placed between the subgrade and the subballast. However, geotextiles have been found to be not very effective in stopping mud pumping (subgrade fines are too small and can still penetrate the geotextiles) and some researchers have suggested the use of sand as subballast layer instead (Ayres 1986 and Alobaidi 1998 & 1999).

Chapter 4: Instrumentation and Monitoring Platform

4.1 Overview of current railway monitoring technology

Railway operators currently maintain three types of monitoring systems depending on monitoring requirements. The first type comprises of mobile instrumentation units capable of performing track inspection over a wide area in a cost effective manner. The second type comprises of low cost monitoring platforms for temporary monitoring. The final type consists of highly sophisticated monitoring systems, normally used for applications critical to continuous operation and management of the railways.

4.1.1 Mobile Instrumentation Units (MIU)

The MIU often consist of sensors ranging from optical measurement systems (scanning rail-head profile), inertia systems (track geometry measurements), and gyroscopes (cross level measurements) attached to track vehicles and are primarily used for routine track quality inspections. They provide fast, economical and practical way of evaluating many miles of track condition and continuous operations at speeds in excess of 120km/h are common. Esveld (2001) provides comprehensive review on the measurement capabilities of various MIU. Recurring problematic sites are earmarked for frequent evaluation. However, the MIU are not suitable for in-situ long term monitoring.

4.1.2 Sophisticated and high-end monitoring platform

Railway operators maintain sophisticated and high-end monitoring systems for monitoring traffic and protect railway tracks against trains with destructive defects such as wheel geometry irregularities (e.g. wheel flats), misaligned bogies and overloaded trains. These high-end monitoring systems are developed and marketed by specialized companies such as Salient Systems Inc and Wayside Monitoring System Alliances. An example of the monitoring system developed by Wayside Monitoring System Alliances consists of sensor suites, on-site data acquisition with power backup units, and extensive data processing and backup capabilities Figure 4-2. The high speed data acquisition is triggered by the passing train and collected data are automatically stored in a database. Users are able to access the database using ftp or remote control programs for data download or visualization. For critical monitoring applications, the system can be programmed to provide warnings through short messaging system (sms) or email if sensors breached pre-determined level.

Figure 4-1: TBOGI laser sensor for misaligned bogie detection at Mansfield, MA (WID website).

The sophistication of the data acquisition platform and data manipulation is matched by the capabilities of the sensors. For example, the laser-based TBOGI sensor (Truck Bogie Optical Geometry Inspection) by WID (Wayside Inspection Devices) installed at Amtrak's weighing station near Mansfield, MA is capable of measuring the wheel-sets angles (relative to the rail) for Acela trains operating at full speed (Figure 4-1).

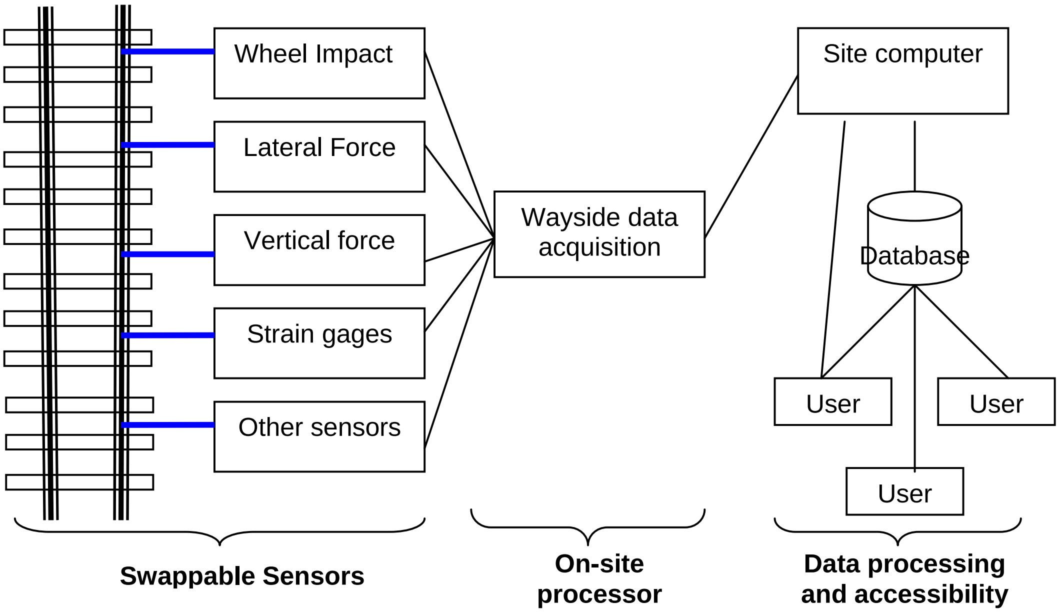

Figure 4-2: An example of custom solution data base system by Teknis, Wayside Monitoring System.

4.1.3 Low cost Generic monitoring platform

Many applications require cheaper and less sophisticated monitoring systems. Low cost remote monitoring has been gaining popularity in various railway and highway applications and many have overlapping hardware requirements. For instance, flash flood[癸] detectors consist of pressure transducers (Boselly 2001) that can be interfaced to a same data acquisition unit that can be used for measuring rail fatigue using strain gages (Lee 2005), thus reducing the need to develop separate platforms. Similarly, pressure cells and extensometers used for subgrade monitoring at several sites experiencing vertical settlement can be interfaced to this generic monitoring platform (Li 2000).

The Author developed low cost sensors and remote monitoring platform for diagnosing problematic railbed (Aw 2004, Aw *et al* 2003). The first phase prototype remote monitoring platform was assembled using Commercial-Off-the-Shelf (COTS) data acquisition products and low cost sensors developed at MIT. Aw (2004) demonstrated that laptop-based data acquisition with remote wireless Internet communication could be successfully used at a remote location provided there was sufficient on-site power supply. Further testing of the minimum power requirements at MIT found that a 30W laptop require two big solar panels of 110W (total of 2.9m^2 of area) and two backup 12V 86AH batteries to enable continuous operation through all weather conditions in the Northeast of US. While such power requirements are not impossible to provide, they are cumbersome for transportation and installation at remote sites. System portability will be enhanced if the power required by the monitoring system can be greatly reduced.

Fortunately, recent advances in low cost Wireless Sensor Network (WSN) technology with new system hardware architecture and communication can be exploited to create a low power generic remote sensing platform for monitoring applications. The WSN architecture is specifically designed to handle the rigors of outdoor, long-term remote monitoring. The network typically comprises low power, battery-operated sensor nodes that can form an ad hoc network and communicate with a primary base station which relays data to the end user via wireless Internet communication. Data processing, signal conditioning and filtering can be done at the level of the individual nodes or at the base station to reduce telemetry costs. The flexibility of the monitoring system in accommodating various monitoring applications lies in the ability to interface sensors (e.g., pressure transducers, strain gages, thermistors) with the core data acquisition. Conversations with Amtrak have indicated significant interests in a generic remote monitoring platform for other applications such as the measurement of rail neutral stress.

[癸] Flash floods killed 3000 people in the last 30 years and injured many more as cars are trapped and washed away on roadways (Slade *et al* 2002)

4.2 Wireless Sensor Network (WSN)

The selection of a remote monitoring platform used in this research is based on the following criteria:

a) Low power requirements
   - The instrumented site may be located at a remote area with no power supply. The monitoring system needs to consume little power in order to operate from batteries or small solar panels.

b) Sampling rate requirements
   - Sampling rate requirements may vary from low frequency rates (e.g. temperature or strain gage data taken once every 10 minutes) to high sampling rates (e.g. 1kHz for measurements of rail deflection under train loading). The sampling rate requirements can be easily tailored for specific applications.

c) Remote data transmission and back end processing
   - automatic periodic data transmission and data processing. The system provides near real time acquisition and viewing of collected data.

During the initial conception of this thesis, there were very few COTS with the ability of accommodating all of the three requirements. Standalone COTS with remote data transmission were expensive and had few channels for sensors (e.g. Iotech Logbook). However, the availability of COTS capable of fulfilling all three requirements have increased towards mid of year 2007, signifying that demands for low-cost and easy-to-use remote monitoring systems are increasing (e.g. Campbell Scientific CRX5000 standalone data logger, Crossbow’s wireless monitoring platforms). The selection of sampling rate capability of COTS ranges from low frequency but high resolution (22 bits) sampling to very high frequency (>1MHz) but low resolution (16-bits) sampling. Remote data transmission capabilities can be added to COTS systems through addition of wireless cellular or satellite internet modem. The most basic level requires user to log on to the remote data acquisition unit and initiate manual data transmission. However, additional software development will be needed for automatic data transmission and backend data storage and processing.

The power requirements of standard COTS and WSN networks are presented in Figure 4-3. In any given system, the power requirement is a function of the sampling rate; higher sampling requires high power consumption. Laptop based data acquisition require the highest power in the range of 30W. The power consumption can be reduced by replacing power hungry laptop computers with smaller single purpose computers. The standalone data acquisitions are made of smaller dedicated processors designed primarily for data collection, storage and remote transmission. This is reflected in smaller power consumption between 50mW to 3W which can be powered by a small solar panel.

Most WSN platforms consist of two tier power requirements. The upper tier which consists of a base station and long range communication ability consumes power similar to the standalone system. It generally draws power from an on-site power supply or solar panels. The lower tier sensor mesh requires very little power, ranging from 0.1mW to 200mW and can be distributed at tight places with no power access.

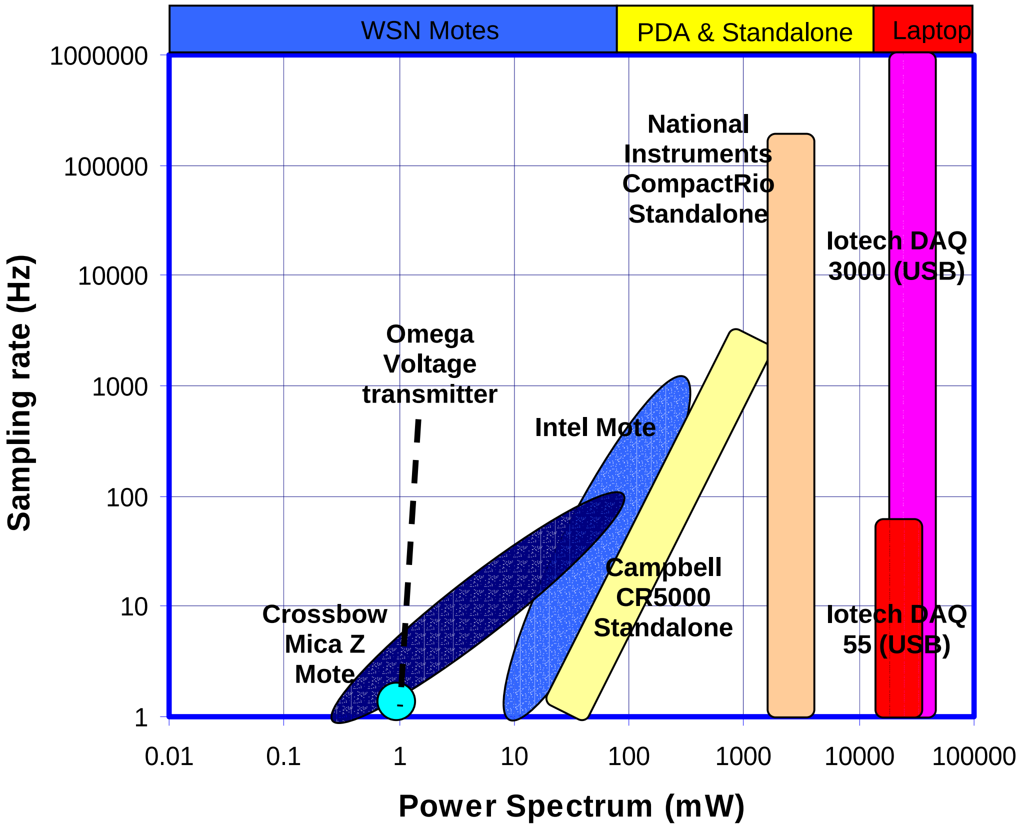

Figure 4-3: Power spectrum of available data acquisition units and the corresponding sampling rate capability. Power includes that of laptop (Iotech DAQ 3000 and 55). Power specifications are obtained from datasheets of the manufacturers.

The two tier power system of WSN is derived from its decentralized system architecture. COTS are traditionally based on multiple sensors cable connected to multiplexed data acquisitions (right of Figure 4-4). Data collected from the sensors are sequentially read (i.e. multiplexed) by the core data acquisition unit. The system can be expanded by stacking more data acquisitions together in a star network.

WSN, on the other hand, decentralized the task of the main data acquisition unit to smaller multiple data acquisitions located at the sensor nodes. Each of these nodes contains a low power CPU (Centralized Processing Unit) and data acquisition unit (left of Figure 4-4. Data collected from sensors are immediately processed before being transmitted to the base station, usually consisting of a single board computer with bigger processing capability and higher storage. The design of the sensor node data collection capabilities depends on the monitoring requirements; long term environmental with very low sampling rates requires smaller on-board CPU, memory and data transfer capability. By comparison, a vigorous sampling regime requires bigger on-board processors with high data handling bandwidth which will require bigger power.

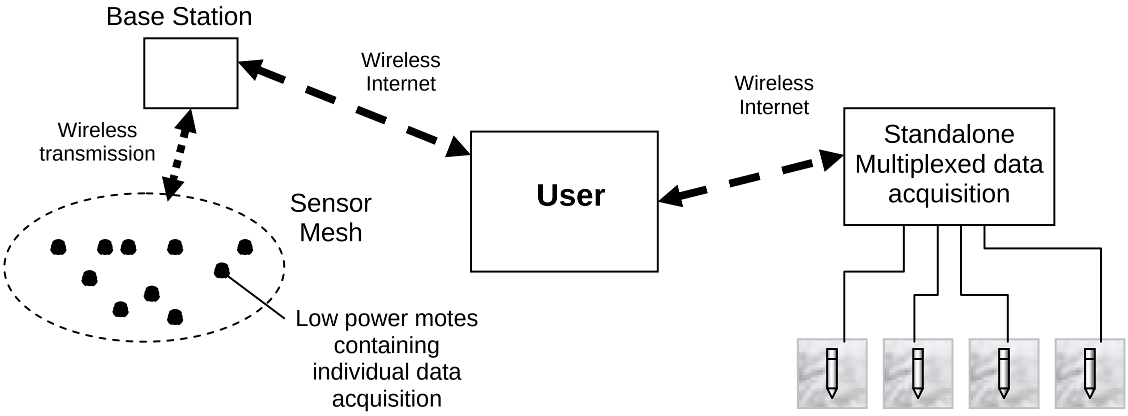

Figure 4-4: Left: General concept of Wireless Sensor Network, and right: Traditional standalone data acquisition network

In this research, a WSN system developed in a joint collaboration between MIT and Intel will be used (Stoianov *et al* 2006). This system, originally developed for heavy duty high sampling regimes, has been successfully deployed for water and wastewater in Boston. The system was installed in 2004 and was fully operational for 18 months and has a variety of sensors ranging from pH to ultrasonic sensors. As part of an on-going effort to create a generic monitoring system, this WSN platform will be adapted for railway monitoring program. Adaptation and implementation of this technology will primarily focus on the ease of hardware and software integration, as summarized below:

a) adapting and redeveloping hardware (sampling capabilities, sensor interface capabilities and etc) and backend processing (database, data processing tools, web visualizations) from a water pipe monitoring for railway monitoring applications
b) performance in a different and hostile environment
c) ease of installation and equipment maintenance

4.2.1 Wireless Data Acquisition

The proposed WSN platform consists of three major components: a) sensor nodes (transducers, A/D converters, microcontrollers and RF transceivers), b) base station, and c) data handling, storage capabilities and user interface. Figure 4-5 shows the schematic diagram of the major components of WSN. Data collected from the sensor mesh is streamed to the base station, which is then transmitted back to MIT via long range wireless Internet communication.

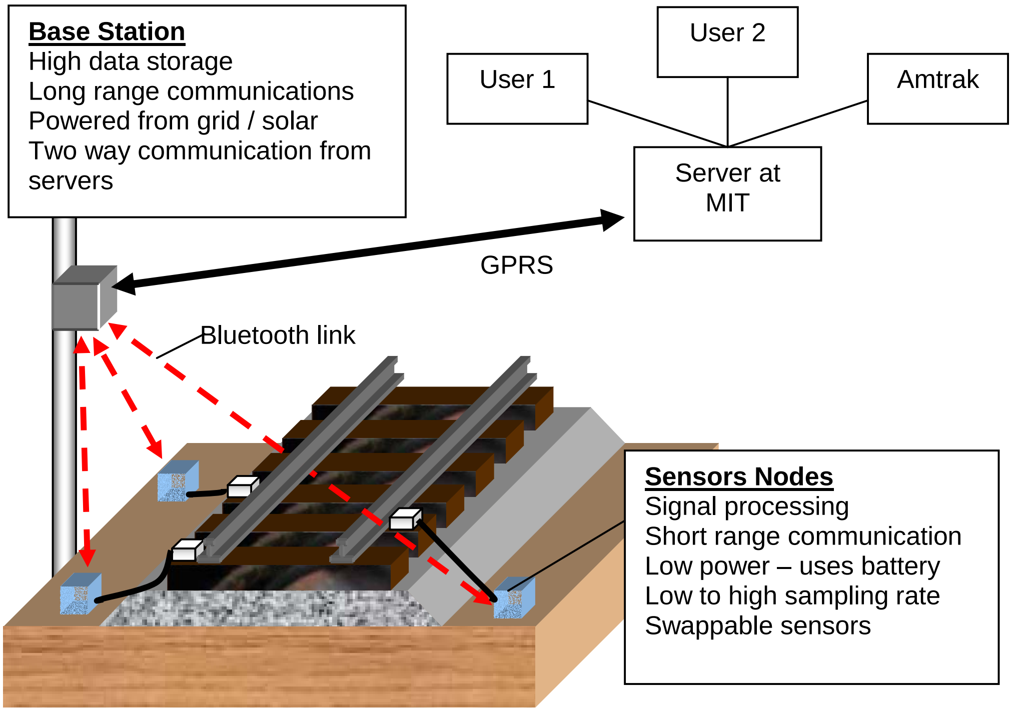

Figure 4-5: Schematic of the wireless monitoring system with applications in the railway.

4.2.2 Intel Mote Sensor Nodes

The sensor node consists of a) swappable sensors such as strain gages and temperature sensors, and b) data acquisition platform, microprocessor and wireless data transmission (mote platform). The prototype WSN was originally conceived for high speed measurements (such as hydraulic pressure transients and vibrations) that require higher bandwidths than other systems used for environmental monitoring (e.g. Mainwaring 2002). The platform is able to handle high frequency sampling rates (burst mode of 1000Hz continuously for 5 minutes), thanks to the usage of a powerful processor (Zeevo integrated 32-bit ARM7TDMI core, 64KB SRAM and 512KB Flash module), high speed data acquisition board (16 bit at 20kHz), and high transfer rate communication line (Bluetooth radio at 2.4GHz band).

The platform supports the TinyOS (http://www.tinyos.net/) open source operating program. The OS and radio stack leave about 11 KB of free SRAM to be used by the application. The motes are currently arranged in a star network, with a single hop between the sensor node and the network. The motes and batteries are placed in waterproof containers which can withstand harsh environmental conditions Figure 4-6.

Bluetooth wireless communication is used to transmit data between sensor nodes to the base station. Bluetooth, originally designed for high speed cable replacement, is used for high data transfer (1Mbps). The motes have a range of 30m with in-built antenna, but RF surveys at the highly charged site shows that this range can be extended to 80m using an external antenna. The mote is currently not set up to check for unsuccessful transmission of data to the base station. Nevertheless, checks are set up for success rate of the long range transmission to remote data center at the headquarters. If the long range transmission is unsuccessful, the base station archives the unsent data and retransmits when the long range communication is reestablished.

During system startup, the node’s initial aim is to locate the root node (located at the base station). The discovery process involves the node conducting active inquiry scan as well as listening for neighboring nodes. Once the basic network backbone is established through this distributed node discovery, routing information is exchanged between the nodes to enable continuous network connectivity. The root node (or cluster head) keeps track of each node by waiting for a *TraceRoute* packet delivered by each node. If the packets are not received within a predetermined time, the node is assumed lost (or disconnected) and the routing table within the cluster head is updated. The cluster head will then send data capture and transfer request to the nodes. Similarly, if the connection to the node is lost (e.g. cut-off by placement of physical barrier) and cannot transmit the *TraceRoute* packet to the base station, the node goes into a free state and tries to reconnect onto the network by sending inquires to nearby nodes. Two free nodes will take an average of 12 seconds for discovery, but once connected, the link can last up to 12 hours of continuous operation (Kling 2005).

Figure 4-6: Intel Mote + Data Acquisition Board and Battery packaging

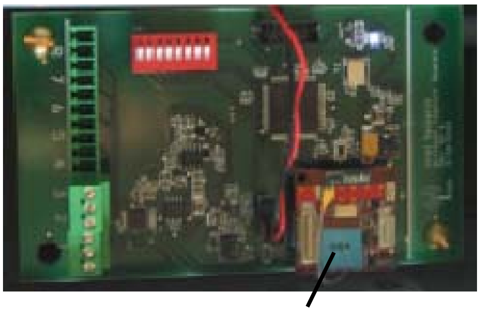

Pins:
1: Sensor output
3: Power out: 5V
4: Power out: ground

Figure 4-7: Intel Mote and Data Acquisition Board

4.2.3 Base Station (Stargate System)

The base station contains the cluster head (which controls the sensor nodes) and acts as a gateway for information transmission with the remote server (e.g. MIT server). At the heart of the system is a single board processor platform called Stargate which is developed by Intel (http://platformx.sourceforge.net/).

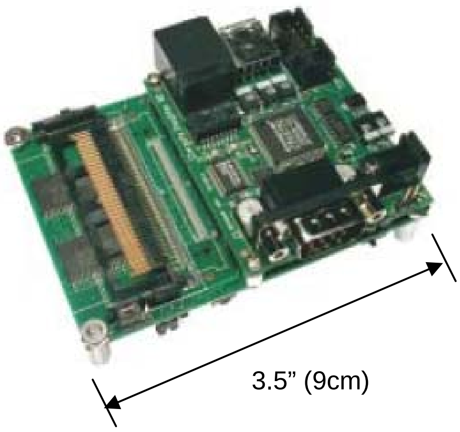

Figure 4-8: Stargate Base Station

Stargate offers a low power (≈ 500 mW) minicomputer with 400MHz, PXA55 XScale processor, 64MB SDRAM, 32 MB Flash with Ethernet, Serial, JTAG, USB, PCMCIA, Compact Flash Connectors and Bluetooth. It is running Linux OS Kernel 2.4.19. The long range communication is achieved by using General Packer Radio Service (GPRS) which offers wireless Internet connection via GSM cellular networks. Sierra Wireless A750 GPRS modem is being used.

In the previous research, the equipment has been developed to enable compact flash storage as well as 802.11b (WiFi) connectivity, enabling short range connection with the Stargate.

Various information such as the sampling rate, duration of sampling, sensor warmup time can be transmitted from the remote data center to the base station in two way directional mode. While data are being transmitted from the base station to the remote data center, updates on sampling regime will be checked. The Stargate communicates with the remote server using SSH (Secure Shell) tunnel. The use of RSA public/private key cryptography enables the base station to log on remote data center securely without the need of password authentication. Once the keys are authenticated, the Stargate has access to uploading collected data onto the server and downloading any new set of instructions.

4.2.4 Remote data center and back-end processing

The remote datacenter, located at MIT, is developed using open source Linux/PostgreSQL/Python stack. The datacenter has access to a static IP address that the base station can dial into. The base station can be programmed to dial in at fixed intervals (e.g. 15 minutes), upload collected data and obtain updated sampling rates. Once the data file is uploaded in the datacenter, it will be unzipped and stored in a database. Again, frequency of data unzipping can be specified, limited only perhaps by time it takes for data to arrive and unzipping. Users with a web browser can access the website and choose to either download the data or plot into graphs.

4.2.5 Program Architecture

The overview of system architecture for the prototype WSN is shown in Figure 4-9 and is further described in the following sections.

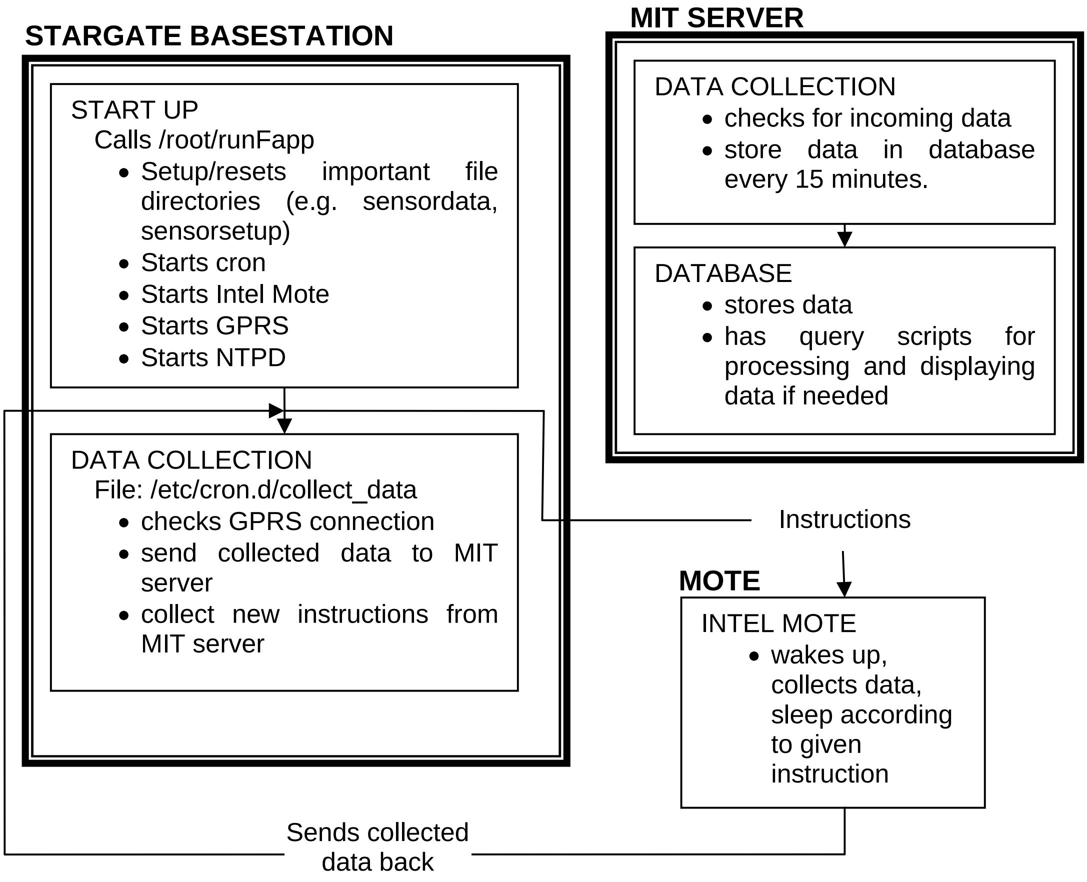

Figure 4-9: Program architecture of the data collection system

4.2.5.1 Stargate Base Station

The base station is one of the most important components of the WSN. It manages the root node (which in turn manages the entire sensor network), collects and stores data obtained from the sensor network, and transmits data onto data server at MIT. The Stargate base station uses the Linux operating system and Linux Shell Programming for the scripting. Details of the script can be found in the Appendix I.

Boot Up

When the base station is powered up for the first time, a script called /root/runFapp is executed. This script is called from S95loadFapp which is stored at the system's /etc/rc2.d.

The runFapp program will perform the following functions:

a) sets up important directories (e.g. sensordata, sensorsetup, bridge) and also starts the Intel Mote (arm-uartserver, GatewayNode and Bridge).

b) Starts the periodic cron
c) Start up the long range communication GPRS card and check validity of the connection
d) run NTPD (Network Time Protocol) that synchronise the Stargate with the Internet standard time servers.

The Stargate starts the root node through *arm-uartserver, GatewayNode* and *Bridge*. The free sensor nodes are now able to discover and form the network as described in Section 4.2.2.

Sensor nodes sampling regime management

The sampling regime of the sensor mesh network is handled through two different modes: a) single event burst mode (handled using oneshot.txt) and b) recurring sampling at predetermine period (handled using recurring.txt). The sensor nodes can be set up to collect data at the rate of *x* seconds (column 4) for a period of *y* seconds (column 2). After data collection, data will be transmitted to base station and the memory is cleared (invoked using special value of 248 in the column 5, as shown in row 4 in the example below). The sensors can be turn on for a predetermined period of time before data collection (Column 6) and this value is currently limited to 11ms.

Column 1: Mote ID
Column 2: Duration (seconds)
Column 3: Sleep Time (seconds)
Column 4: Sampling Rate (samples/sec)
Column 5: Sensor Type
Column 6: Warmup Time (ms)

```
0xf0f0f0f0 10 30 1 8   10
0xf0f0f0f0 10 60 1 5   10
0xf0f0f0f0 X  60 X 250 X
0xf0f0f0f0 X  X  X 248 X
```

where x denotes no numeric is needed, with value 1 as default.

Deciphering the column lines above gives:

First column:	`0xf0f0f0f0` means base station sending out instructions to ALL Intel Motes. This column can be replaced by unique mote IDs in order to target specific mote.
Fifth column:	If value is 8, then data streaming on the first channel is invoked. If value is 5, then data averaging on the second channel is invoked. If value is 250, then sleep command is invoked. If value is 248, then the flash is cleared.

Both oneshot.txt and recurring.txt scripts are located at /tmp/sensorsetup at the base station. The current data acquisition board is setup to collect data from 2 channels. The first channel can collect streaming data and the second channel data averaging.

Remote data transfer

The Stargate maintains periodic data transmission to the remote data center at a predetermined time. The data collection and remote transmission function is governed by the */etc/cron.d/collect_data.sh* module. Firstly, the remote transmission link to the remote data center is established. The module then automatically logs on to the remote data center server, uploads the collected data onto the remote data server, and checks for any updated *oneshot.txt* and *recurring.txt* scripts (i.e. any updates on new sampling regime). Currently, the Stargate is set to periodically send data at 15 minutes to the remote data server. This can be set by calling the *collect_data.sh* script from the Linux crontab system. In summary, invoking the *collect_data.sh* module performs the following function:

a) Calls */etc/cron.d/probe_connection.sh* to check if the GPRS connection is established. If not, reset the GRPS mode by invoking the command *pppd call ac750*.
b) Checks for data issued by sensor mesh, zips data files, and sends to data center.
c) Checks for new commands issued by the data center (e.g sampling frequency, new sleep time, etc) to be important onto *tmp/sensorsetup* in Stargate.

When the command *pppd call ac750* in (a) is invoked, the Stargate starts up Sierra Wireless Aircard 750. The GPRS connection can be tested by a simple ping command (e.g. ping www.google.com). Once the internet connection is setup, the Stargate can initiate Secure Shell (SSH) connection to the remote data center. The encrypted SSH keys enable a password-less[11] but secure connection be set up between the Stargate and the remote data center. Setting up of the SSH connection is detailed in the Appendix II.

4.2.5.2 MIT Server

The data center at MIT is built on open source Ubuntu Linux / Apache 2.2 (for web hosting) / PostgreSQL (database) / Python stack. Python programming language is used to unzip incoming data files (from Stargate) and identify good data from incomplete data (e.g. corrupted timestamps). The Python program can be periodically called from the *crontab* files (currently set at 10 minutes interval) to process incoming data and store into database system. During data processing, calibration factors are added to the data

---

[11] A password connection requires manual password entry on the Stargate side which is not possible

and stored in a field in the database, thus enabling easy access. The charting capabilities are provided by Python power graphs.

4.2.6 Power Considerations

The power usage of the WSN can be optimized through intelligent power management. The breakdown of mote's power consumption in different stages is shown in Table 4-1. During the sleep mode, the mote still draws relatively high current (when compared with other wireless communication such as Zigbee (802.15.4) due to Bluetooth's higher power consumption. Bluetooth is, however, most efficient during high rate data transmission. Prior experience at MIT shows that usage of a high sampling regime (sampling frequency of 600S/s for 30 seconds every 5 minutes interval) requires 6V 12Ah of battery for 3 months. It is possible to increase the lifespan of the battery up to a year if a lower frequency sampling regime is used.

Table 4-1: Power consumption of Imote (Nachman *et al* 2005)

Stage	*Current (mA)*	*Power required (mW)*
Sleep Mode	3	9
Imote + radio	20.7	62.1
Imote + A/D	22.3	66.9
Imote + A/D + sensor*	28.3	85

* sensor current consumption based on Freescale MPX2100 pressure transducer.

4.3 Current Sensor Technology: Application in railway

The literature review on current sensor technology will be limited to piezometer/tensiometer and settlement probe design which is relevant to this research.

4.3.1 Water Pressure Sensor (WPS)

The WPS is employed to measure fluid pressure in the ground. The chief difference between a WPS and a total stress cell lies in the water pressure sensor's ability to decouple the fluid pressure from the stresses in the soil skeleton. This is done by employing a porous element capable of absorbing the soil skeleton stress whilst allowing only pore fluid to exert pressure on the internal measuring device, as opposed to a total stress cell that measures the pressure contribution from both the soil skeleton and the pore fluid.

There are two types of dedicated WPS. The first type, known as the piezometer, is used for measuring positive water pressure and is installed below the groundwater table. The second type, called the tensiometer, measures negative water pressure and can be installed in the partially saturated zone (e.g. above the water table). Selection of these sensors is extremely important in ensuring proper water pressure measurement; the piezometer has faster measurement response but will almost inevitably desaturate in partially saturated zone; the tensiometer performs better in unsaturated conditions but has slower measurement response. Table 4-2 list the primary comparison between a piezometer and a tensiometer.

Table 4-2: Comparison between piezometer and tensiometer

	Piezometer	**Tensiometer**
Function	• Measures positive water pressure below the ground water table	• Measures water tension in a partially saturated zone
Measurement principle	• External water exerts pressure on internal pressure transducer via internal fluid. The internal fluid is separated from external water by porous filter.	• Contrary to the piezometer, water tension imposes negative pressures on the internal fluid and pressure transducers. Small size of filter pores (high air-entry) and minimal internal air bubbles keep the tensiometer saturated and operable.
Performance	• Continuous submersion in water will enable very long term performance. However, the piezometer will desaturate if the ground water is lowered. • Usage of bigger filter pores enables fast measurement response time.	• Tensiometers often desaturate in the field and require regular maintenance • Usage of smaller filter pores reduces measurement response time.

Railway subgrade monitoring is challenging because the area of interest in the subgrade may extend to both above and below the groundwater table. This calls for WPS capable assuming dual roles of the piezometer and the tensiometer.

For convenience, WPS will now be called piezometer and will be able to measure both positive and negative pore pressure.

Other important criteria of piezometer for general remote railway applications include:

a) Automated (typically incorporating an electronic pressure transducer)
b) Good long-term performance in saturated or unsaturated media or both.
c) Fast short-term performance (if used to measure pore pressure pulses from wheel loading)
d) Piezometer geometry (e.g. small measuring tip to prevent soil arching)
e) Ability to withstand high loading and frequency wheel stresses.
f) Ease of installation with minimal traffic disruption.

4.3.1.1 Dynamic Pore Pressure Measurement

The ability of piezometer to measure fast response has been a subject of interest. While traditional borehole piezometer has ground response of up to several hours (Dunnicliff 1990), recent advancement in piezometer design has pushed the response to a few seconds and below (e.g. Kutter, 1990; Cauble, 1997). The ability of piezometer to measure fast response time depends on the following factors:

a) compliance of the measuring unit
b) permeability of the soil
c) saturation of piezometer
d) frequency measurement of the transducer
e) geometry of the probe (preventing arching in the soil)

Compliance of the measuring unit

Pressure transducers generally measure pressure by tracking the deflection of the diaphragm; greater the deflection, higher the pressure. For the measuring unit to register an increase of external water pressure, a certain amount of volume of external water has to infiltrate the porous stone in order to deflect the transducer's diaphragm. This volume of water is a function of the compressibility of the measuring fluid, amount of deflection of the diaphragm, and expansion all the components (e.g. piezometer body, porous stone). For an unsaturated piezometer, the compressibility of the air inside the device will be an important parameter.

Response function (Kutter 1990)

The amount of water needed to flow through the filter to register pressure changes on the pressure transducer is given by Kutter (1990):

$$\Delta p = K \frac{\Delta V}{V}$$

where

Δp = external pressure change
K = bulk modulus of water (2.2 x 10^6 kPa)
ΔV = volume needed to go into device
V = total volume in the device.

By minimizing the total volume of measuring fluid, the volume of water needed to flow through the filter can be minimized and thus increasing response time.

Response Function in pore OIL / WATER (Henderson 1992)

Henderson (1992) developed a theoretical derivation of time response for a penetrometer in water based on a balance of fluid flow through a porous element where *at equilibrium:*

Δ Volume A (t) = Δ Volume B (t)

ΔVolume A (t) can be defined as the change of volume (i.e. in an infinitely stiff system, ΔVolume A is zero). ΔVolume B (t) governs the fluid flow through the porous stone.

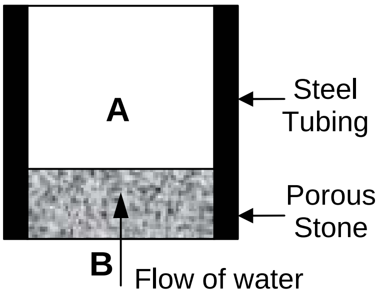

Figure 4-10: Flow balance through a piezometer

The equation of the piezometer response derived by Henderson (1992):

$$\frac{P_o}{P_a} = (1 - e^{-bt})\,;\; b = \frac{kA}{\gamma_{fluid} lM}\,;\; M = \frac{\Delta V(t)}{\Delta P(t)}$$

where:

P_o = Probe output pressure
P_a = Atmospheric pressure
t = Time
k = hydraulic conductivity of the porous stone in probe
A = cross section area of porous stone in probe
γ_{fluid} = Unit weight of silicone oil
l = length of porous stone
M = probe system compliance
ΔP(t) = change in probe system pressure
ΔV(t) = change in volume probe system

and

$$\Delta V(t) = V_{Transducer} + V_{SiliconeOil} + V_{SteelShaft} + V_{Swagelok}$$

The above equation is valid for piezometer response in pure water/oil where there are no external flow restrictions across the filter. Careful considerations will have to be given for piezometer response in soil, especially for soils with permeability lower than the filter.

The response of the piezometer is therefore proportional to the permeability of the porous stone, area of the porous stone and is inversely proportional to the system compliance, density of the measuring fluid, and length of the porous stone. Figure 4-11 shows a typical response of the piezometer with respect to the applied pressure.

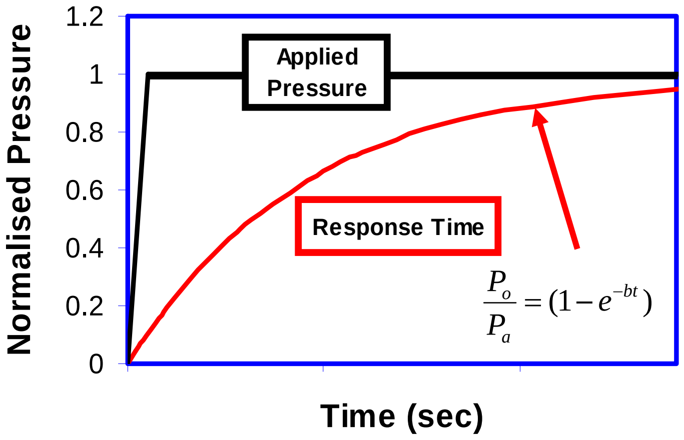

Figure 4-11: Typical response time of a piezometer with respect to the applied pressure as modeled by Henderson's equation.

Response Function in soil

If the permeability of the soil is lower than the permeability of the porous filter, the response of the piezometer will now be governed by the permeability of the soil. Water will have to flow out of the soil before entering the filter. For simplification, the value of the soil's permeability can replace the filter's permeability in the response function.

4.3.1.2 Long term water pressure measurement

The long term water pressure measurement is governed by:

a) stability of the electronic pressure transducer
b) performance in the saturated state
c) performance in the unsaturated state

Selection of pressure transducer

Where electronic pressure transducers are used as a measuring device, they are susceptible to atmospheric fluctuations, temperature cycles and long-term offset drifts. These effects have been studied and characterized in Aw *et al* (2003) and Aw (2004) and are briefly summarized here. Electronic pressure transducers made from strain gage technology (.e.g. Motorola, Omega, Data Instruments pressure transducers) or more expensive vibrating wires are subjected to hysteresis, non-linearity and offset deviation. For long term stability, the off-set deviation is the most critical characteristic. Experiences with MPX Motorola 100kPa transducer found that off-set deviation can vary as much as 5cm of pressure head over a period of one month. Off-set deviation is typically about 0.2 to 0.5% of the full scale reading: absolute pressure transducer with 100 kPa range would have off-set deviation of 5cm.

Pressure transducers come in two versions: a) absolute pressure transducers and b) gage pressure transducers. Absolute pressure transducers are referenced to vacuum (i.e. one side of the diaphragm is exposed to a vacuum sealed chamber) while gage pressure transducers are referenced to atmospheric pressure. As a result, absolute pressure transducers are sensitive to changes in atmospheric fluctuations and this effect can be removed by subtracting reading from a witness transducer. However, the noise introduced by the transducer (non-linearity, offset, and hysteresis) is now doubled due to dependence on two pressure transducers. For piezometers, the effect of atmospheric pressure can be removed simply by using differential pressure transducers, as long as reference to atmospheric pressure can be guaranteed (Aw 2004).

Variation of temperature causes changes in reading offset. Fortunately, the changes in offset can be removed by proper temperature correction procedures. Fortunately, the ground temperature does not vary much diurnally and this effect can be easily accounted for.

Performance in saturated state

If the piezometer is always below the water table, it will operate in a saturated state. This is an ideal state for piezometer as it will not be de-saturated and can perform over longer period. The real challenge for the piezometer lies in measuring pore pressure in an unsaturated state.

Performance in the unsaturated state

When the water pressure goes into tension (e.g. lowering of water table), it is possible that the piezometer will become desaturated by the following mechanims:

a) air-entry pressure is breached
b) growth of existing air bubbles or release of air bubbles in trapped crevices due to tension
c) drying or freezing of water

Positive-pressure measuring piezometers can be readily converted into tensiometers by reducing the size of the porous stone (controls condition (a)) and more rigorous saturation of the porous stone and measuring chamber (minimizing condition b and c). Condition (d) is only important at areas where prolonged dry spells or exposure to winter conditions may be encountered.

Air-entry Pressure

The air-entry pressure is defined as the suction for air to breach the water tension inside the porous stone. Considering a pore element in the porous stone (Figure 4-12 - right), the pore size is approximated by a cylinder. The water surface tension forms an elastic membrane which curves inwards from the air (i.e. water wetting against the air). The forces needed for the air to penetrate the membrane can be approximated from the formula below:

Vertical force equilibrium,

$$\sigma.2.\pi.r = (P_{air} - P_{water}).\pi.r^2 \qquad \text{.......................... Equation 4-1}$$

where P_{water} is the pressure in water, P_{air} is the pressure inside the bubble.

$$\therefore \qquad p_{air} = \frac{2\sigma}{r} + p_{water} \qquad \text{.....................................Equation 4-2}$$

and $\sigma_{\text{air-tension}}$ is the water-air surface tension (typically 72 mN/m)

From the water/air entry diagram in left of Figure 4-12, the size of the porous stone can be selected in order to prevent breach of the water membrane. Therefore, field tensiometers usually use very high air entry (> 100kPa) by selecting smaller size porous stone.

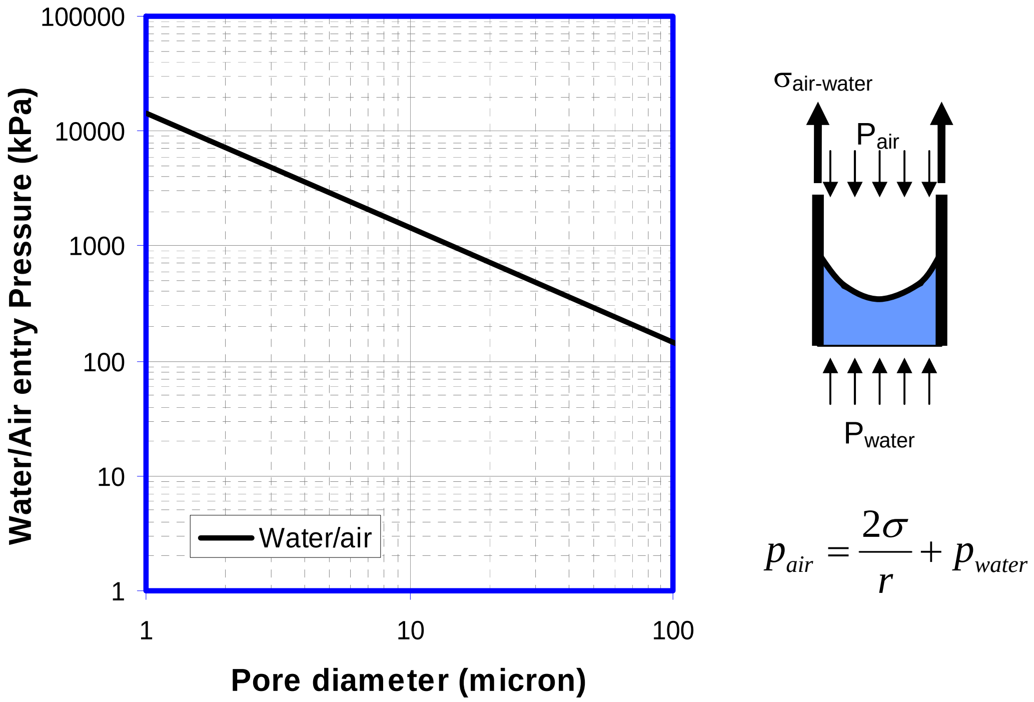

Figure 4-12: Theoretical air-entry diagram for the water in the porous stone (left) and the simplified cylindrical to model the porous stone (right).

Growth of pre-existing gas bubbles and in trapped crevices

Presence of air bubbles inside the measuring chamber influences the measuring accuracy and capacity of the tensiometer. Under positive pressure, the presence of the air bubbles is not as critical: the bubbles will still compress and transmit the required pressure, albeit at a slower response time (Rad & Tumay, 1985). However, the air bubbles will be problematic for unsaturated state measurements. The air bubbles will expand under negative pressure and the external tension pressure will not be conveyed to the pressure transducer. The expansion of air bubbles also risks inner-chamber liquid molecules from evaporating into the inner part of the bubble. This may cause premature cavitation[12] at the vapor pressure of the liquid and cause fluid in the chamber to drain into the soil. Even if the tensiometer did not cavitate, Take *et al.* (2003) observed that the tension values measured will be inaccurate and create pressure hysteresis.

4.3.2 Examples of commercial water pressure sensors

4.3.2.1 Piezometers:

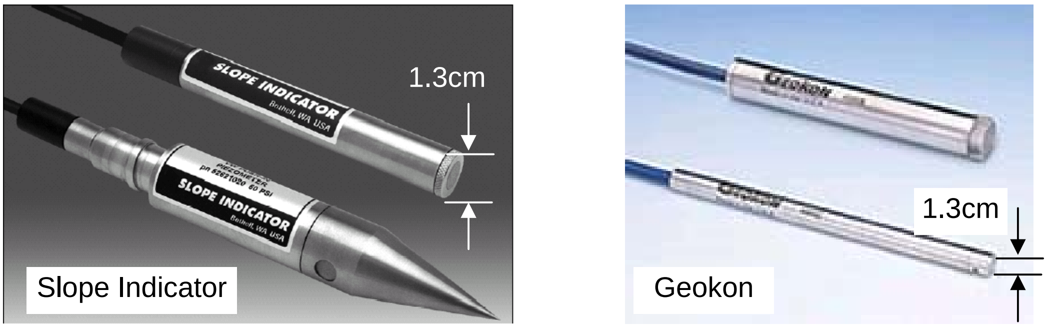

Figure 4-13: Commercial vibrating wire piezometers from Slope Indicator and Geokon

Electronic piezometers are currently widely available and are sold through companies like VW, Slope Indicators, Geokon, and etc (Figure 4-13). Most of the commercial piezometers use the vibrating wire technology. Devised in the 70s, the vibrating wire technology measures pressure changes by inferring from the frequency of a vibrating wire. Vibrating wire technology generally has good long term stability but is still susceptible to zero drifts, offsets, and long term drift (after a year or more). The drawbacks of vibrating wire technology are the slow response time (up to 10 seconds per measurement) and costly (due to relatively complicated measuring mechanism). For high speed measurements, vibrating wire technology is not an option.

---

[12] If air bubbles are not present, the piezometer will cavitate at the air entry pressure

Laboratory based piezometer

Kutter (1990)

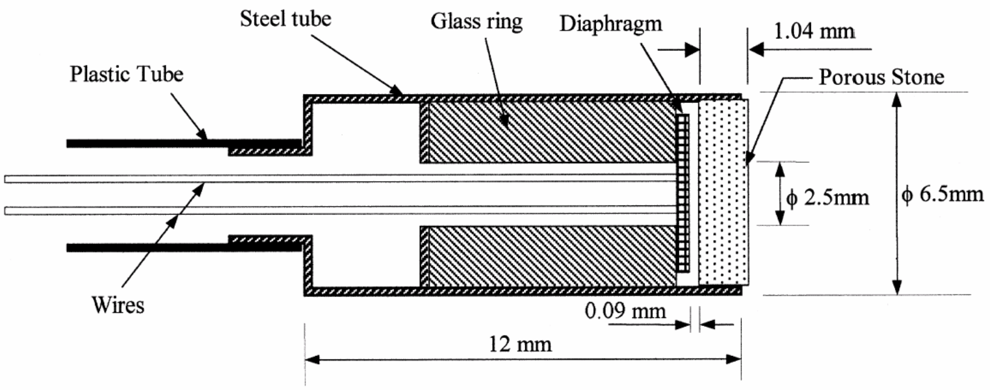

Figure 4-14: Pore water pressure transducer based on Druck PDCR81 (Kutter 1990)

The need for high response piezometer is important in applications such as measuring the pore pressure response in centrifuge. Kutter (1990) designed a miniature pore pressure transducer made of a porous stone attached to a small Druck pressure transducer. The relatively stiff system compliance led to very fast response (down to 0.001s in water) when fully saturated. However, despite being designed as a miniature pore pressure transducer, the diameter of 6.5mm is still relatively big for subgrade applications, especially if it is to be placed over the layer of ballast / subgrade interface. The relatively big diameter may cause soil arching under the application of train loading, and misleadingly measure the total stress instead of the pore water pressure. However, any modifications to this water pressure transducer will dramatically reduce the response time, as demonstrated in the next section.

Cauble (1997)

Cauble (1997) uses miniature pressure transducers from Kulite and Cooper and convert them into piezometer using a small cap and long needles. The needle probe lends its advantage in reducing arching stress in the soil while keeping the system compliance small. However, reducing the area of the tip (and hence porous stone) reduces the pore pressure response time, and it is a design trade off in determining the required porous stone size and reducing soil arching. The addition of the needle probe increases the response time of the piezometer (compared with Kutter’s which uses quite similar transducers) to 0.05s and 0.1seconds. However, Cauble’s piezometer design would be more relevant to the railway use if the development pore pressure at a very thin layer is to be measured.

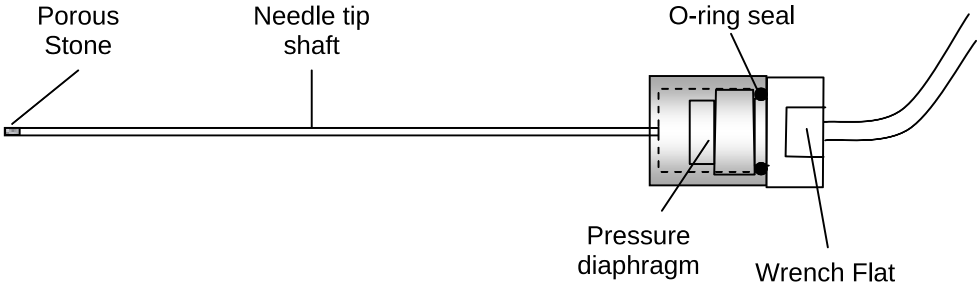

Figure 4-15: Piezometer designed by Cauble (1997).

4.3.3 Tensiometers

4.3.3.1 Types of tensiometers

The types of tensiometers which have been devised are wide and varied, ranging from sophisticated high capacity research tensiometers to simpler low capacity field tensiometers. The difference in the tensiometer capacity lies not only in the selection of high air entry filter, but also the usage of more rigorous saturation technique and better design in minimizing trapped air within the inner measuring chamber.

Research tensiometer

Research tensiometers with range of up to 20 000 kPa have been devised. The first high capacity tensiometer was devised at Imperial College (Ridley & Burland, 1993) and since then, Saskatchewan (Guan & Fredlund, 1997) and MIT (Slojborn, Toker 2002, Toker 2004) have followed suit. The high capacity tensiometers rely on using rigorous saturation technique (vacuum saturation followed by high pressure saturation), and using minimal volume of measuring chamber. The combination of rigorous saturation techniques and efficient probe design minimizes or eliminates internal bubbles so that cavitation will occur based on the air entry pressure of the porous element. An example of the high capacity tensiometer is shown in Figure 4-16.

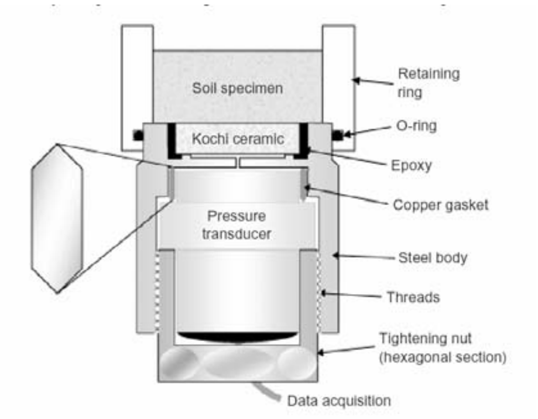

Figure 4-16: MIT Tensiometer Version 6-1 (Toker *et al* 2004)

Saturation Process (Toker *et al* 2004)

- Evacuating and applying water pressure to the device for one day
- Apply pressure of 2.5-2.8 MPa for 24 hours
- After 24 hours, release the pressure gradually

Commercial tensiometer

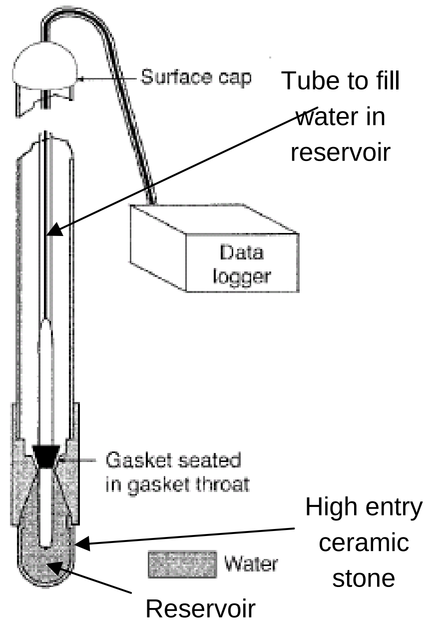

Figure 4-17: Field Tensiometer (Sission 2002)

Most commercial tensiometers rely on simpler device construction and saturation process than the research tensiometer and the measurement capacity are limited by the vapor pressure of water of 90 kPa (e.g. Fredlund and Rahardjo, 1994).

A typical commercial tensiometer is shown in Figure 4-17. Since the field tensiometer are designed to work for long periods of time, there is usually a mechanism that allows for replenishment of water as well as to flush out air bubbles that might have developed in the system. It is, however, not possible to de-air the porous stone unless the tensiometer is removed from the ground and re-saturated. Case studies have shown that continuous refilling can replenish the tensiometer back into the original suction.

Figure 4-18 shows behavior of tensiometer when ground suction exceeds the air-entry value of the porous filter. However, Sission *et al.* (2002) found that even at very low tension (≈ 30cm), the tensiometer still have to be refilled regularly (a few months). Having to refill the tensiometer regularly poses difficulties in railway monitoring and are not compatible with the low maintenance operation.

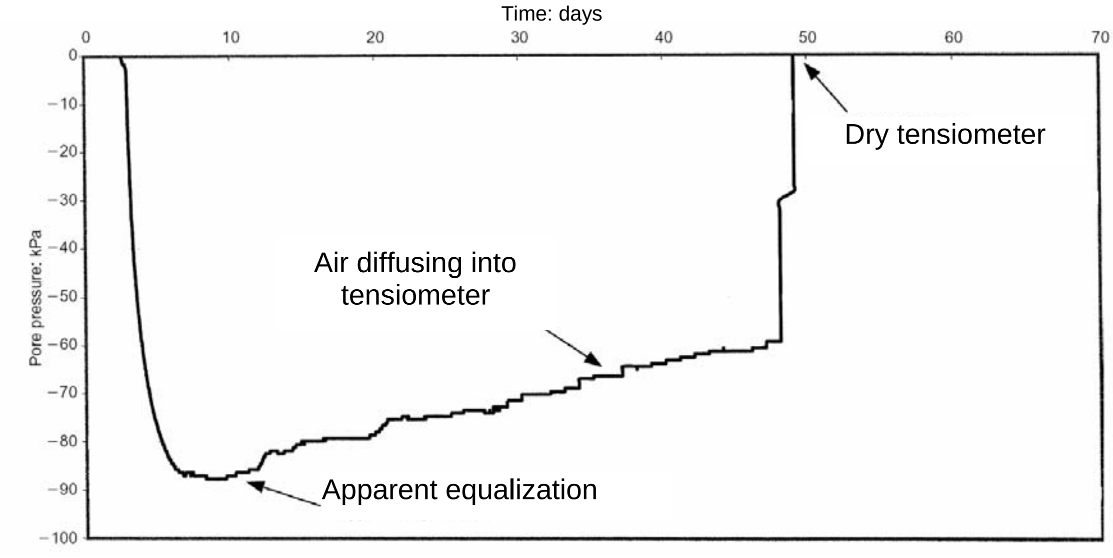

Figure 4-18: Diffusion of air into tensiometer (Ridley *et al* 2003)

4.3.4 Settlement Probes

There are many methods for measuring vertical movement in railway applications. These sensors include LVDTs (e.g. Madshus 2000), extensometers (Li 2000), and multi-depth deflectometers (MDD), (Sussmann *et. al.* 2004). Multi-depth deflectometers use multiple LVDTs at various depths in the borehole. However, extensometers and MDD are big, cumbersome, and are difficult to install under rail track.

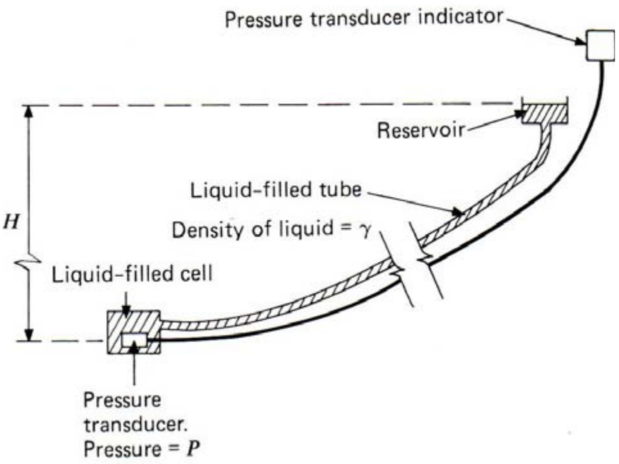

Figure 4-19: Schematic of liquid level gage with pressure transducer (DUNNICLIFF 1988).

For railway subgrade monitoring applications, liquid-based settlement probes offer a convenient method of vertical deformation measurements.

The embedded probe contains a pressure transducer which is hydraulically connected to a fixed reference reservoir located at a fixed datum point. Changes in elevation of the embedded probe cause pressure changes which are measured by the pressure transducer. The movement is back-calculated by dividing the change in pressure with unit weight of the liquid. A schematic view of the settlement probe is shown in Figure 4-19.

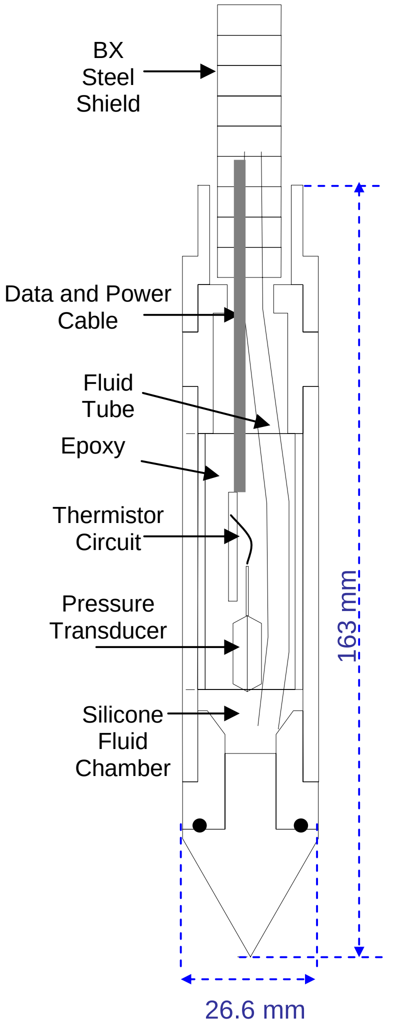

Figure 4-20: Design of a settlement probe from Aw 2004.

Extensive laboratory and field measurements of the liquid settlement probe is described in Aw (2004). Motorola absolute pressure transducers were used for the probes and corrections have to be made for temperature and atmospheric pressure. A modified version of the settlement probe has been installed and successfully tested in a London underground tunneling project (Brooks, 2004).

Figure 4-20 shows the design of phase one prototype settlement probe with temperature measurement capability installed at TTCI in Colorado (Aw, 2004). The settlement probe is made of steel components and sensitive electronic components such as the pressure transducer and thermistor circuit is encapsulated in epoxy.

Chapter 5: Equipment Development and testing

5.1 Development of Piezometer

5.1.1 Requirements and Design Challenges

Measurement of pore water pressures are generally limited to either positive water pressures or negative, and rarely are the two conditions measured simultaneously. For railway applications, the region of water pressure measurement often exists in an unsaturated state (above water table), but may be intermittently saturated during heavy rain. In addition, the piezometer will be subjected to high train induced stresses, calling for reliable and robust design. A summary of the design challenges and corresponding design solutions are detailed below:

Long term variation in ground water level

Two factors are important in measuring the long term variation in ground water level. Firstly, the piezometer must be capable of measuring both positive and negative pore pressure in the ground. In practice, the long term measurement of negative pore water pressure is never easy; field tensiometers require frequent re-saturation (every few months) due to breaching of air entry and diffusion of air, and the water-based internal fluid freezes during winter. In this research, silicone oil will be used as a water replacement medium due to its slow evaporation rate and will not freeze in winter. A high air entry porous stone is used (40 µm) to keep the piezometer saturated.

Secondly, the long term measurement accuracy of the piezometer is largely governed by the performance of the pressure transducer used. All electronic pressure transducer experiences offset drift, temperature effects and possibly atmospheric pressure (if an absolute transducer is used). These effects are well documented in Aw (2004) and therefore selection of a good transducer is critical to the performance of the piezometer.

Short term (dynamic) development of pore pressure

The ability of the piezometer to measure high frequency pore pressure response depends on the stiffness of the measuring system; system stiffness can be increased by either minimizing the volume of compressible fluids, using a stiffer transducer and with a bigger porous stone area improves the response of the piezometer to external pore pressure changes. The presence of internal bubbles adversely affects the response system and good saturation techniques will have to be carried out.

Arching of the soil

Kutter (1990) found that arching dramatically reduces the measurement capability of the piezometer, an effect that would be profound at the event of high frequency dynamic loading. A needle tip piezometer with diameter of 3.2mm is designed to reduce the arching effect and can be easily installed at a localized zone (e.g. top layer between the ballast and subgrade).

Plastic Housing

The first prototype sensors have been fabricated out of steel housing for added strength (Figure 5-1). Due to a highly energized environment, Amtrak requires that only non-metallic sensors can be installed. Consequently, the sensors were redesigned to include hard plastics as the external housing and successfully proof tested to withstand high stresses in the subgrade. The cables are protected by plastic BX cables with waterproof connections.

Figure 5-1: Steel housing from previous experiment (Aw 2004).

5.1.2 Conceptual Design and Components:

The miniature piezometer consists of the following components:

a) Measurement unit

- 40 micron porous steel element attached to a small diameter steel tubing (inner diameter of 1.76 mm)
- Omega gage pressure transducer (±200 kPa)
- Silicone Oil as internal measurement fluid.

b) Waterproof plastic enclosure which protects the piezometer.

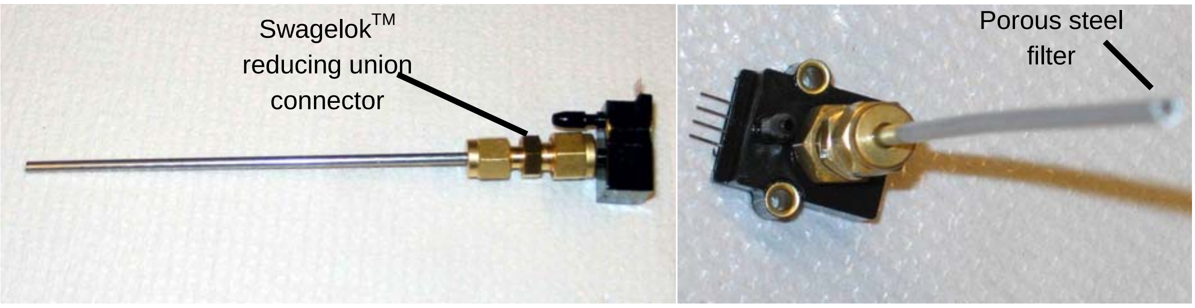

a) Side view of the piezometer **b) Isometric view of the piezometer**

Figure 5-2: Side and top view of the piezometer element showing the porous steel element in the steel tubing, pressure transducer and Swagelok™ connectors, without the plastic housing.

5.1.2.1 Measuring Unit

The measuring unit consists of a pressure transducer, miniature needle steel tip with porous stainless steel filter, and silicone oil.

Pressure transducer

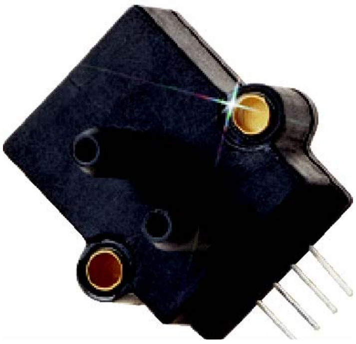

Figure 5-3: PX139 gage pressure transducer

After extensive comparison between three different pressure transducers (Omega PX139, Freescale MPX 2200A, and Data Instrument AB), the Omega PX139 differential pressure transducer with ±200 kPa capacity is selected because of its: a) good long term off-set stability, b) high voltage output (less susceptible to environmental noises), c) fast response time, and d) low cost. An amplification circuit is included within the pressure transducer, giving the output range between 0.25V to 4.25V, with zero value at 2.25V. Other transducers have low output voltage (within the millivolt region) and need external amplification before cable transmission in order to reduce the influence of environmental noises (5.2.3). Since the PX139 transducer has a port design, the steel tubing can be attached to the pressure transducer via Swagelok™ reducing union (3/16” to 1/8”). The use of differential pressure transducer eliminates the need to correct for atmospheric pressure. Full laboratory characterization of PX139 Omega pressure transducer (drift, temperature and atmospheric pressure sensitivity) will be dealt in detail at Section 5.2.2 and 5.2.3. The Omega manufacturer designed the PX139s for air pressure measurement and their compatibility with silicone oil are unknown. However, two months of laboratory tests found that silicone oil has no adverse effect on the offset stability of the transducer’s diaphragm.

Miniature Needle Steel Tip and Porous Steel Filter

The miniature steel shaft is a slender tube with an outer diameter of 3.2 mm and length of 17cm. At the end of the steel shaft resides the porous steel filter element of 1.76 mm diameter and has small pore size of 40 microns. The original porous steel filter comes in the form of a rectangular plate, which is then sheared and tapered to roughly the size of the inner steel tubing (using the grinding machine). It is then gently hammered into the steel shaft. The porous steel filter has permeability of 0.002 mm/s[13]. Connection between the miniature steel shaft and the plastic port of the transducer can be achieved using two methods of equal success. The first method involves clamping the Swagelok nut to the port using a bronze ferrule and back ferrule. Such is a standard method for metal to metal connection, but laboratory testing showed that this connection is possible

---

[13] Measured with falling head laboratory experiments

for a plastic to metal connection. The second method involved using an inverted bronze ferrule and an O-ring (similar to the concept shown in the inlet of Figure 5-4).

Silicone oil

De-aired water is frequently used in commercial piezometer and tensiometer. However, difficulties with maintaining saturation and freezing have led to favorable considerations of using silicone oil which has very low freezing point and require easier saturation procedures. A Dow Corning low kinematic viscosity silicone oil of 20 cst was selected. DeJong et al (2007) showed that low viscosity silicone oil can saturate filters under low vacuum (-68kPa) within a short period of time (15 minutes). In addition, silicone oil had been successfully used for pore pressure measurement under freezing conditions (Da Re, 2000) at MIT. However, a disadvantage of using silicone oil is the small error in measurement reading due to difference in interface between the silicone oil and the water.

5.1.2.2 Body, Cables and Sealing

Plastic Enclosure

A Nema 4X enclosure box (1.57 x 2.56 x 4.53”) is used to protect the pressure transducer from the environment. The original box is designed for usage in non-submerged areas but the waterproofing of the box can be improved by replacing the foam seal in the top cover groove with a rubber O-ring (AS568A size number of 044). The industrial grade plastic box was proof tested to pressure of 227 kg/cm^2 (22 MPa) and was sufficient to withstand subgrade stresses of 70 kPa.

Cables

The electrical cable consists of dual pair of 22 AWG Belden wires and individually shielded metal sheets and drain wire. The resistance of the cable is small (17 micro ohm/ft) and has operating temperature between -30C to 60C. The drain wire is grounded to provide a Faraday cage that will shield the cable and data transmission from environmental noises. The cables are protected by an external waterproof plastic BX enclosure. The waterproof ability of the plastic box and cables were tested by submerging the assembly into water for a week and no leakage was detected.

In-plane flexibility

The piezometer is able to provide some in-plane flexibility which decouples the measuring unit (metal shaft and pressure transducer) from the plastic box. In-plane flexibility is particularly important for vertically oriented piezometers where the plastic body is rigidly held by the soil mass. Application of train load will cause the subgrade to compress and create high compressive stresses on the joints of the plastic box and steel shaft. The in-plane flexibility can be achieved by using an O-ring (size 009) and a front ferrule in a regular Swagelok™ Male O-Seal Fitting (inlet of Figure 5-4). The O-ring will provide sealing and some lateral resistance but will not lock the steel tubing.

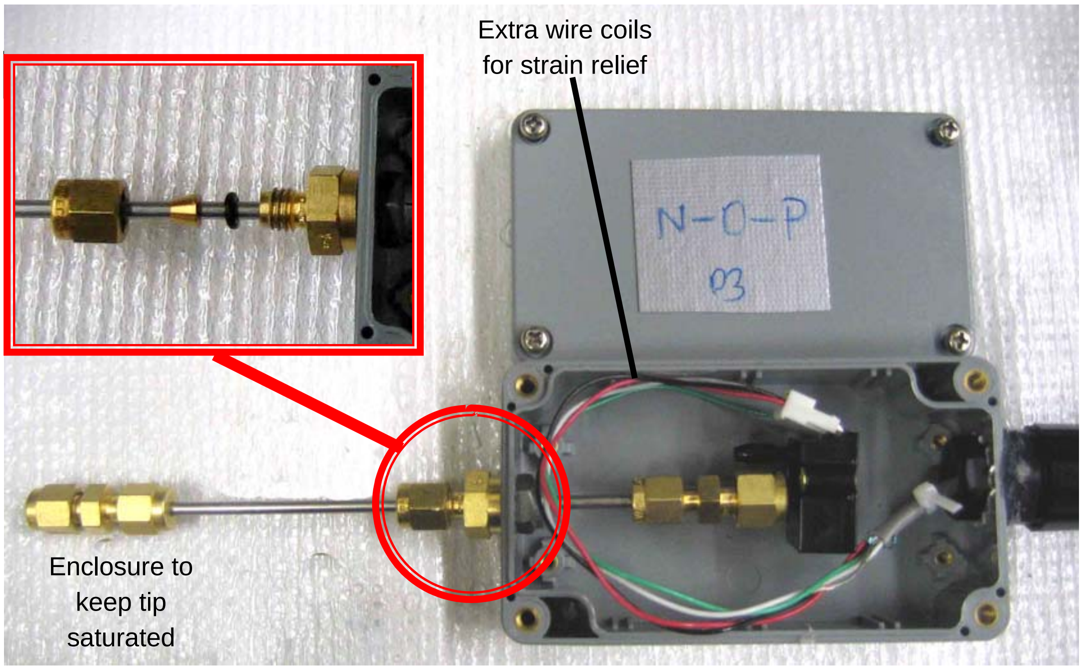

Figure 5-4: Piezometer in plastic enclosure and flexible sealing joint (inlet picture)

5.1.3 Unsaturated State: Long term performance

The long term performance of the piezometer is often governed by its ability to maintain good saturation throughout the measuring period and can be achieved by using:

a) high air entry porous stone
b) good saturation technique to ensure the piezometer will not desaturate in the field

5.1.4 Air - Entry pressure

The air entry pressure of the porous stone is defined as the pressure (or suction) needed to draw the silicone oil (or water) out of the porous stone by breaking the silicone oil - air interfacial tension. The ability of the silicone oil – air interface to maintain its integrity primarily depends on the pore size of the porous stone. A high air entry porous steel filter with pore size of 40 micron was selected to provide air entry of 100 kPa. Silicone oil has a lower surface tension compared with water and is reflected in the lower air entry;

air entry of water stands at 320 kPa for similar pore size. Therefore, care has to be exercised when measuring ground suction to ensure that the air entry of 100kPa is not breached, causing desaturation of the piezometer. The silicone oil – water interface breaks at a higher 200 kPa, as shown in Figure 5-5.

The above calculation is based on the following values for silicone oil (Svitova *et al*, 2002): Surface tension against air = 21.3 ± 0.2 mN/m; interfacial tension against water = 41.4± 0.2 mN/m. This is valid for silicone oil with kinematic viscosity between 5.0 to 200 cSt (PDMA Gelest) and the silicone oil used in the piezometer is 20 cSt. See section 4.3.1.2 for the derivation of entry pressure equation.

The presence of the interfacial membrane meant that silicone oil will always exist in a higher pressure than water (silicone oil wets against water). This introduces some minor error in the measurement.

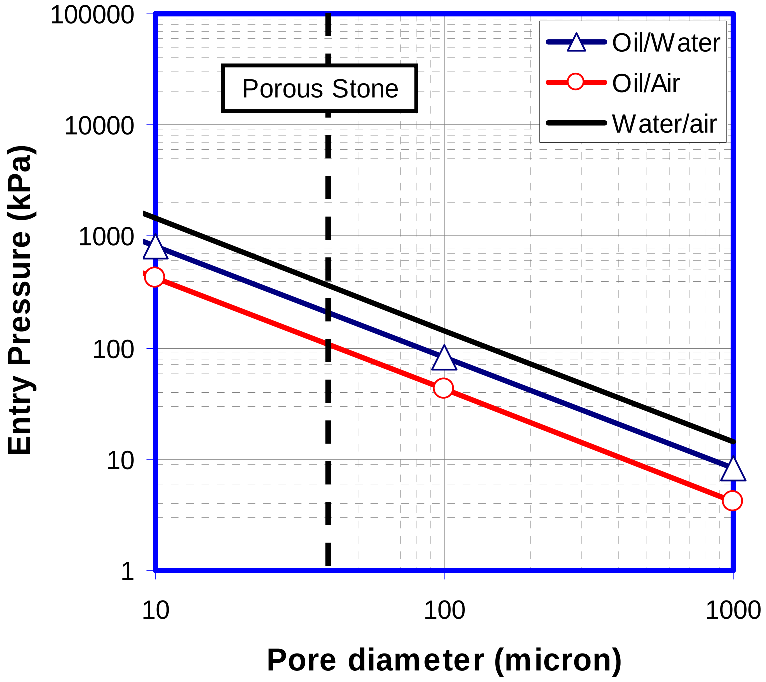

Figure 5-5: Entry pressure for three different cases a) silicone oil / water, b) silicone oil / air, and c) water / air entry with respect to pore size of the steel filter.

5.1.5 Saturation of piezometer

The sophistication of saturation procedure greatly determines the performance of piezometer in the unsaturated state. While high end saturation requires vacuum saturation followed by high pressurization, these saturation techniques are often too elaborate for practical use. The current research follows a less elaborate but still rigorous saturation procedure was proposed by Take and Bolton (2003).

1. Place the steel tubing containing the porous stone into a silicone bath and apply ultrasound for 30 minutes. Prior experience (Varney, 1998) found that the porous stone can be effectively saturated with water using this method and would be even more favorable for silicone oil which has lower surface tension.
2. Place all the components of the piezometer in a silicone oil bath and connect all components under the oil to prevent air from entering the system. The pressure transducer is saturated with very thin hypodermic needle.
3. The piezometer is then placed in a vacuum chamber and the set-up. The piezometer is currently not submerged under silicone oil. A vacuum of -100 kPa is applied to draw bubbles out of the system for 10 minutes[14].
4. The vacuum chamber is then turned 90 degrees so that the piezometer tip is submerged under the silicone oil and the oil is able to flow into the piezometer through the action of gravity. The setup is then left for another 10 minutes.
5. The vacuum pump is then released and the piezometer is allowed to further undergo saturation under atmospheric pressure for another 20 minutes.
6. While this is not being performed, an even better procedure is to put the piezometer under additional positive pressure in order to force additional microscopic air bubbles into solution. Since this procedure will only be effective when high positive pressures (way above the 200kPa limit of the pressure transducer) are applied, this step is not being taken.

The above saturation procedure was conceived from a notion that the vacuum forces most of the air bubbles out of the system and the sudden pressure increase when the system is returned back to atmospheric pressure is enough to force the remaining air bubbles into solution. The solubility theoretical frame work combining Boyle's pressure and volume law and Henry's law of solubility was used by Bishop & Eldrin (1950) and Lowe & Johnson (1960) in saturating triaxial sand samples using back pressure:

$$\Delta P = P_i \frac{(S - S_i)(1 - H)}{1 - S(1 - H)} \quad \text{……………….………… Equation 5-1}$$

---

[14] DeJong et al (2005) found that low viscosity silicone oil can saturate a filter under vacuum of -68kPa for a duration of 15 minutes

For an air bubble within the piezometer with initial absolute pressure P_i and initial saturation S_i, it will compress when ΔP of pressure is applied and will dissolve into the solution if adequately high pressure is applied. The ability of the air to go into solution is measured using Henry's constant *H*.

If the system is to be saturated starting from room pressure (atmospheric pressure), the amount of pressure (ΔP_{100}) needed to force air bubbles into solution is 456 kPa, a forbiddingly high pressure which exceeds the capacity of the pressure transducer. In contrast, if the initial pressure starts in or near vacuum, only ΔP_{100} = 4.56 kPa is needed to force the air bubbles into saturation and the act of returning the applied pressure back into atmospheric pressure is sufficient.

It is easier to saturate the piezometer using silicone oil to water since air is 9 times more soluble in oil than water. For water, Henry's constant is approximately 0.02 ml of air / ml of water at room temperature. For silicone oil, $H \approx 0.17$ ml air / ml silicone oil at room temperature (Gelest Silicone Oil).

5.1.6 Effects of unsaturated piezometer

An unsaturated piezometer operating in the unsaturated zone is unable to produce an accurate measurement of the pore pressure because changes in the negative pressure head causes the air bubbles in the piezometer to expand and will not be transmitted to the pressure transducer. The following sections quantify some of the perils of using unsaturated piezometer

Expansion of air bubbles and influence of soil matrix

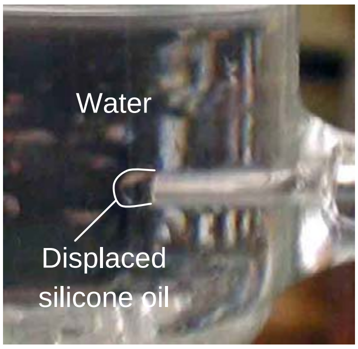

Figure 5-6: Displacement of silicone oil/water interface under application of vacuum of -60kPa.

Application of suction on the piezometer causes expansion of internal air bubbles volume which in turn causes the silicone oil to be displaced out of the piezometer tip by similar amount. Figure 5-6 shows the displaced silicone oil / water interface for an unsaturated piezometer when subjected to -60kPa of pressure. As long as the interfacial membrane remains intact, as in the case of submerged in pure water, the piezometer will not drain and cavitate. The situation becomes complicated with the presence of soil particles which may disrupt the tensile resisting capability of the interfacial membrane and cavitate.

The influence of the soil matrix on the interfacial membrane is investigated by placing the tip of the unsaturated piezometer in contact with the sand and water, and vacuum is applied in order to coax the interfacial membrane out from the piezometer tip (Case 1, Figure 5-7). A small flexible tube is used to contain the sand in order to provide a closed system such that the water in the tube is solely held back by the silicone oil / water interface; when the interfacial tension breaks, the water in tension will drain from the tube. Figure 5-8 (left) shows an initial close up view of the piezometer tip. When a negative pressure of -60 kPa is introduced, the interfacial membrane is displaced from the piezometer tip and the presence of sand caused the membrane to displace upwards (Figure 5-8 - right). Upon releasing the negative pressure, most of the silicone oil retreats back into the piezometer tip, with some residual oil trapped in the sand. This shows that the piezometer becomes slightly unsaturated though cavitation did not occur. Therefore, the conclusion that can be derived from this experiment is that an unsaturated piezometer subjected high negative pressure will only become more unsaturated due to loss of silicone oil as a result of interfacial disruption from the soil skeleton.

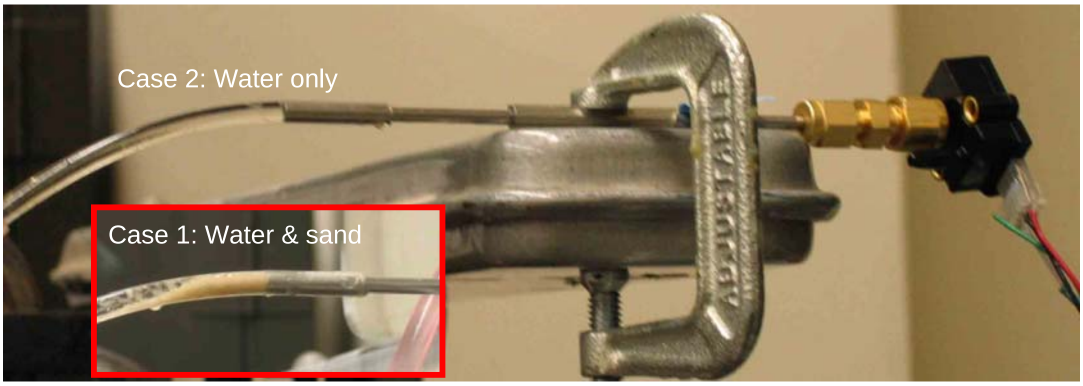

Figure 5-7: Case 1: The tip of an unsaturated piezometer is placed in contact with water and subjected to vacuum. Case 2: The tip is now placed in contact with sand and water and subjected to vacuum.

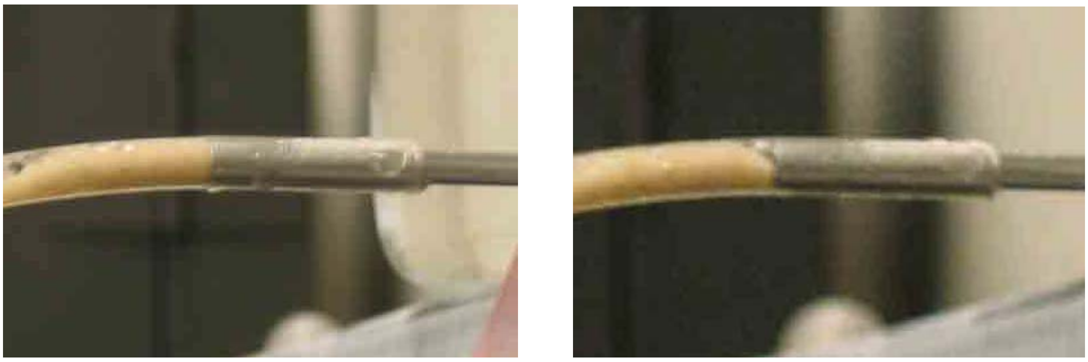

Figure 5-8: Left: Before application of vacuum. Right: During application of vacuum – the displaced silicone oil / water interface is displaced upwards.

Temperature effects

The expansion and contraction of air bubbles is sensitive to temperature changes. Figure 5-9 shows the sensitivity of an upright piezometer (with tip facing downwards) to changes in temperature. The tip of the piezometer is immersed in water (although similar response is measured when the tip is dipped in silicone oil). Increasing the temperature (just by touching the steel shaft) causes expansion of the air bubbles which increases the pressure within the system. Similarly, decreasing the temperature on the steel shaft (by placing in contact with a cold steel) causes contraction of the air bubbles that decrease the pressure within the system. By comparison, application of heat on a saturated system produced only small fluctuations.

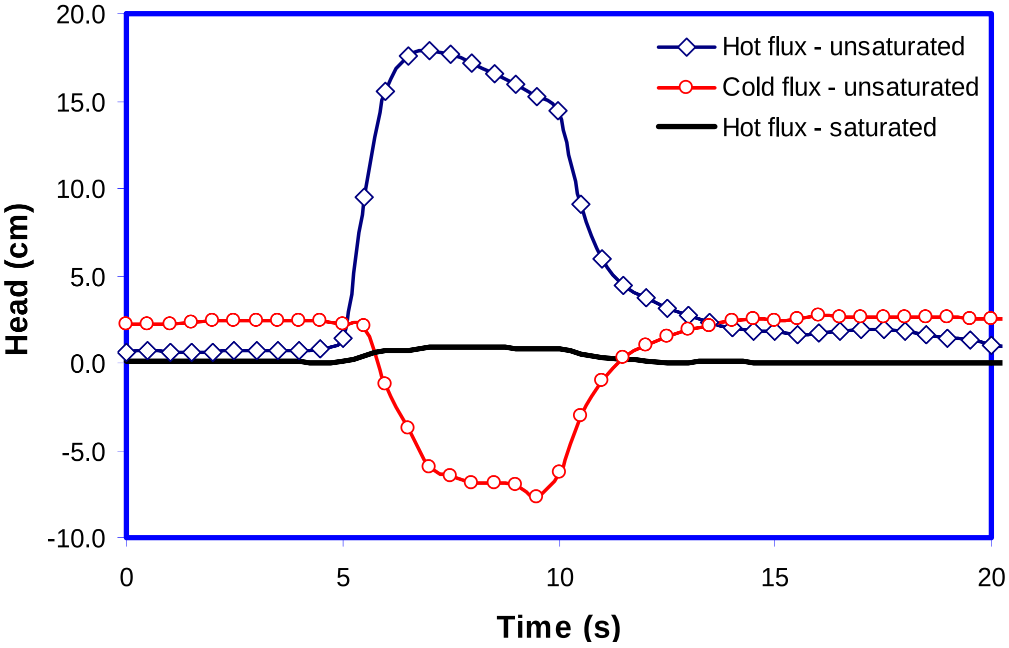

Figure 5-9: Influence of temperature on the measurement of piezometer is a function of saturation. Unsaturated piezometer is more susceptible to temperature changes than saturated piezometer.

5.1.7 Dynamics of Silicone oil / water interface

The presence of the interfacial membrane adds additional complexity to the establishment of equilibrium between the inner measuring fluid (silicone oil) and the external water. A few questions come to mind:

a) If the equilibrium between the silicone oil and water is severed, would it be re-established?

b) Would the equilibrium at the interface sustained under prolonged matrix suction?
c) Would the piezometer desaturate during drying of the soil?

Three experiments have been devised to study these factors more closely and are described below.

5.1.7.1 Severing and reestablishment of the interface

The response of the piezometer during drawdown of the water table is measured for large grain size materials (glass beads of 3.95 mm) and small grain size (fine sand of 0.4 mm). The glass beads / sand are contained in a hollow plastic tube of 1.7 m length and the water table is controlled by increasing or lowering the plastic tube (Figure 5-10). The piezometer is inserted vertically at the top of the tube and is embedded into the soil. Before the piezometer is inserted into the soil, the zero reading is first taken by ensuring the tip of the piezometer is just in contact with water.

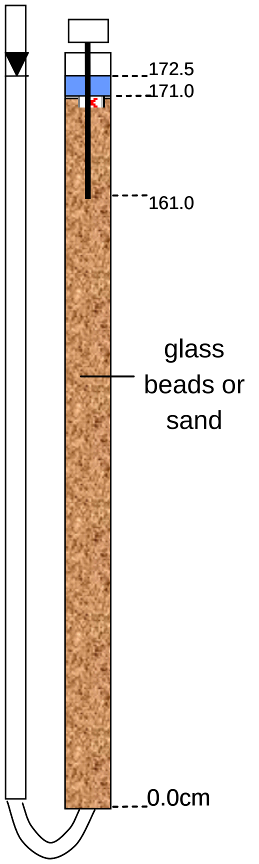

Figure 5-10: Measuring severing and reestablishment of interface

Since large grain size materials are unable to hold tension, the interfacial tension between oil and water is expected to be severed when water table is lower than the tip of the piezometer. For the smaller grain size, there will be capillary rise and the membrane will be subjected to tension over a long period of time to see if it will severe.

Glass beads 3.95 mm

With initial water elevation of +10cm above the piezometer, the water level is slowly stepped down to an elevation of -10cm below the tip of the piezometer. Since the glass beads have very low capillary rise capabilities at this diameter, the water and silicone oil interface breaks at value close to 1cm (Figure 5-11). When the water elevation is stepped up to 10cm again, the interface rejoins with the silicone oil almost immediately (Figure 5-12).

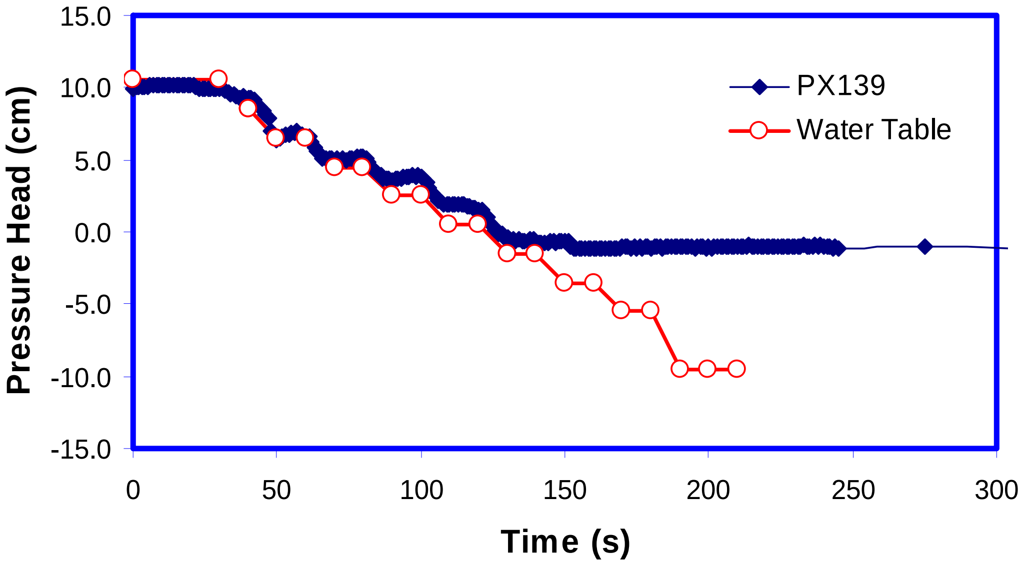

Figure 5-11: 3.95 mm diameter glass beads – water table drawdown

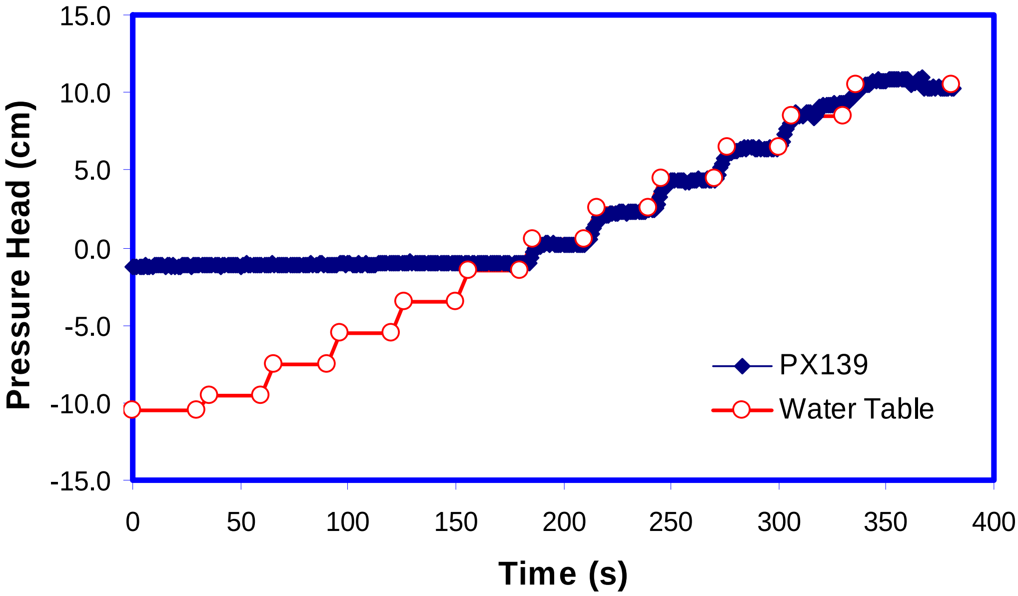

Figure 5-12: 3.95 mm diameter glass beads – rising water table

5.1.7.2 Prolonged suction effect on Piezometer

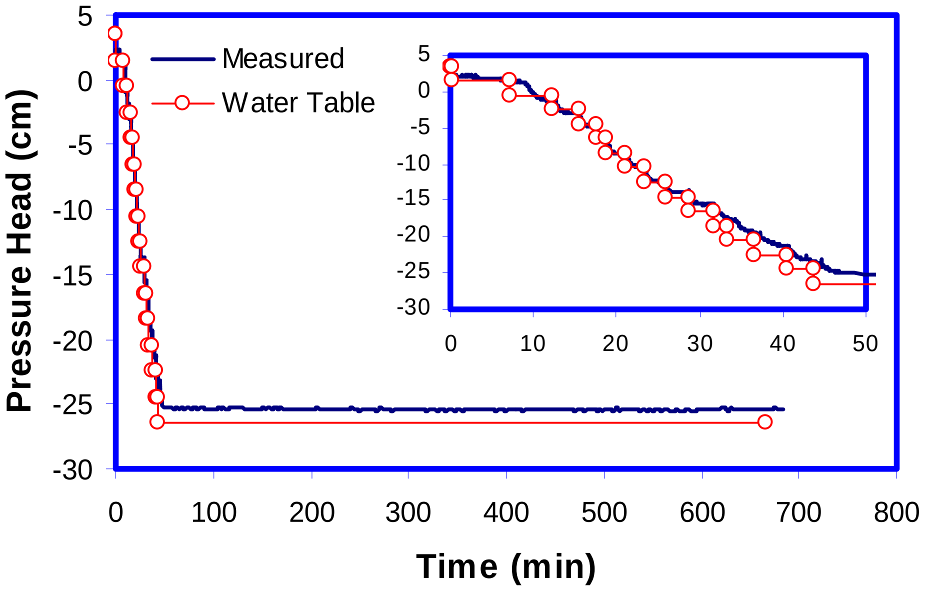

Figure 5-13: Water table drawdown to elevation of -25 cm below the tip of the piezometer and left for 11 hours.

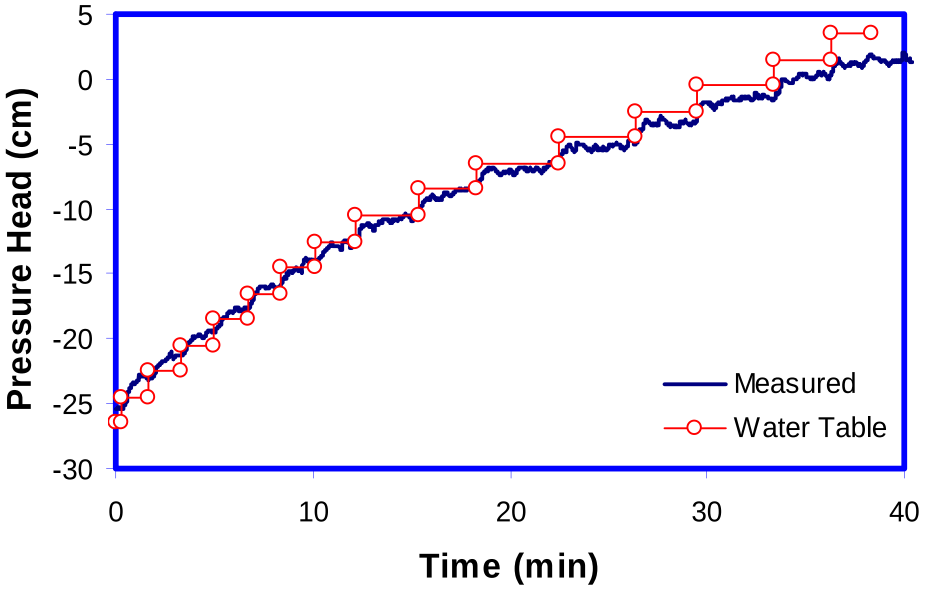

Figure 5-14: Increasing the water table after the piezometer is left in pro-longed suction of 11 hours

The fine sand has better capillary rise than gravels and is able to sustain greater tension. The water level is lowered to -25 cm below the piezometer and is left overnight. During the drawdown, the piezometer is able to track the elevation of water level (Figure 5-13). It is able to maintain measurement under suction for 11 hours. When the water level is increased, the piezometer is able to track the changes in water level well (Figure 5-14).

5.1.7.3 Drying of soil

The performance of the piezometer is investigated for the case of a drying soil. The theoretical air entry of the fine sand is between 2 to 3 kPa (20 to 30cm of head - Figure 5-15). The piezometer is placed in a beaker containing fine sand and is left for three days to dry. The measured response is shown in Figure 5-16. During drying, the drawdown of the water table corresponds to increase in soil suction. At -20 cm of head, the air entry of the fine sand is breached and cavitation occurred. Water is refilled into the beaker after three days and the piezometer measured immediate rise in water table (Figure 5-17).

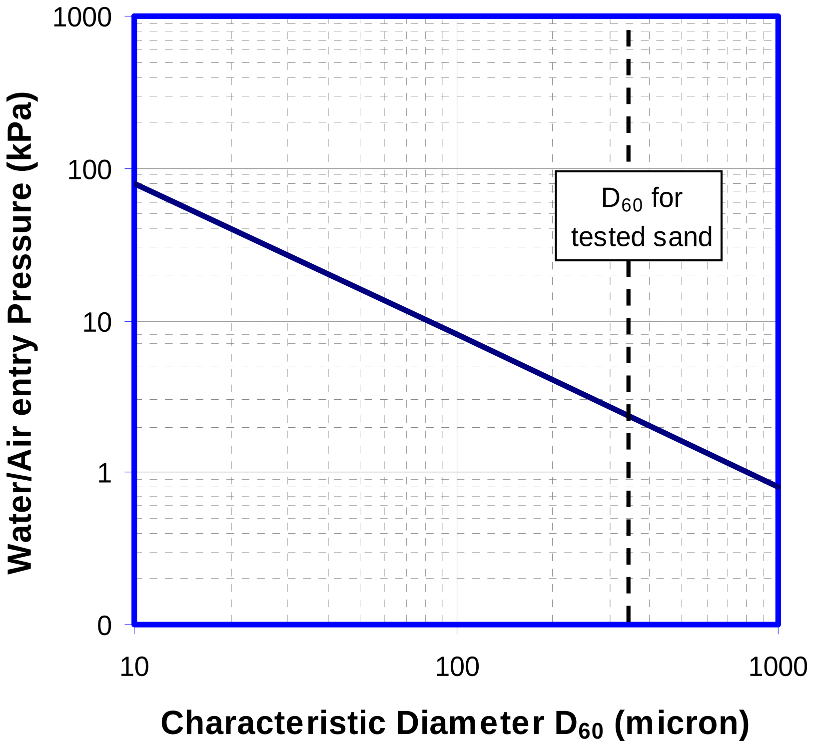

Figure 5-15: Water / air entry pressure for soil with characteristic diameter D_{60} microns. The theoretical curve is derived from a variety of particles including reconstituted Boston Blue Clay, New Jersey Fine sand, and glass beads (Sjoblom, Toker).

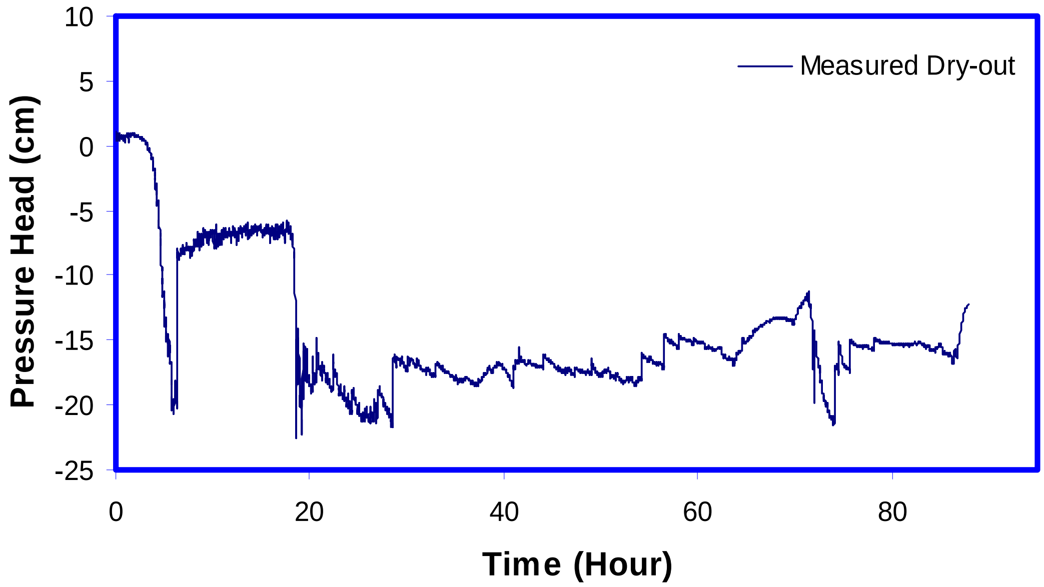

Figure 5-16: Drying of the soil. Air entry of the soil occurs at -20cm.

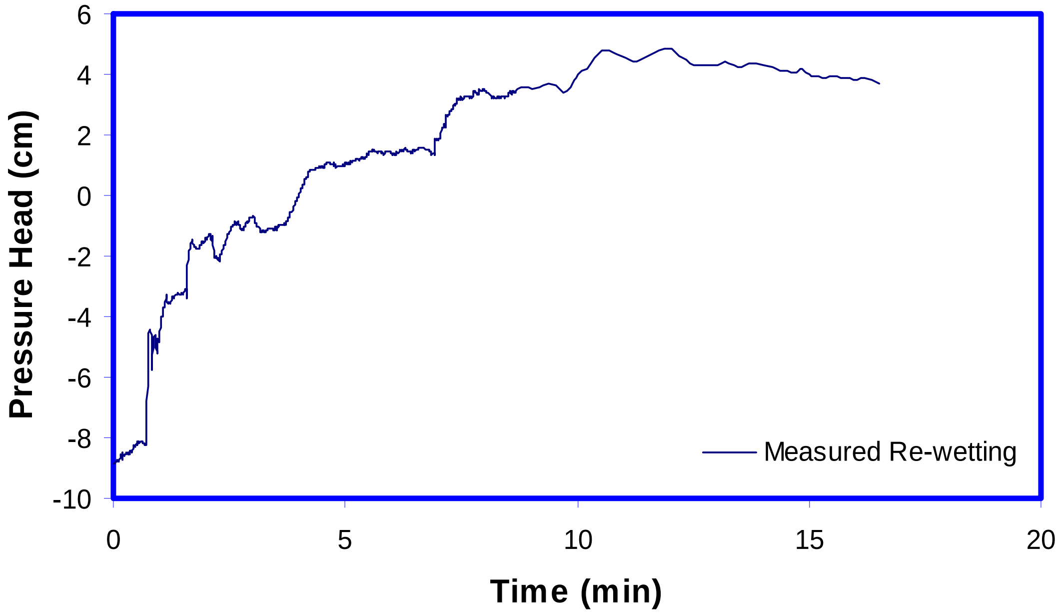

Figure 5-17: The water is reintroduced into the system after drying. The piezometer measures the increase in water level.

5.1.8 Miscellaneous – application of rain

Simulation of the rain event is performed in the lab. The water level is held at -25cm below the tip of the piezometer and water is added at the top of the tube. The piezometer is able to detect the moving water front within the time frame of seconds but immediately settled back to the original pressure (Figure 5-18).

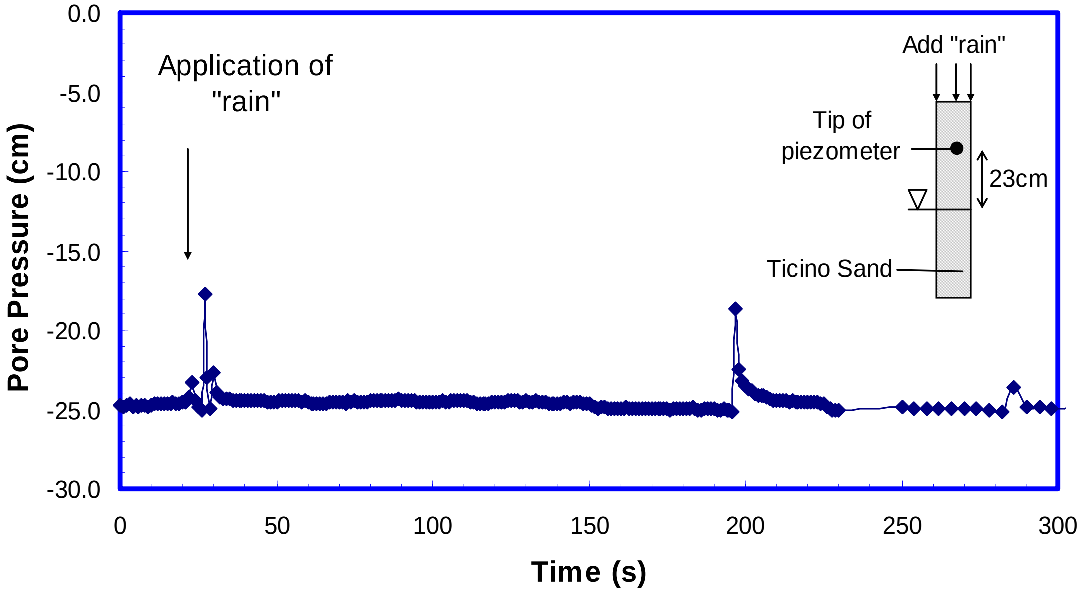

Figure 5-18: Capturing of rain event in sand

5.1.9 Saturated State: Dynamic Response

Establishing the long term performance of the piezometer in the saturated state is trivial once it has been rigorously tested in an unsaturated state; the positive ground water pressure will ensure that the piezometer remained saturated. The focus is now shifted to designing a piezometer with fast response time capable of measuring development of pore pressure within the span of train loading.

The response of the piezometer is often defined as the time for the piezometer to react and measure up to 95% of the applied stress (also known as T_{95}) and is highly dependant on the amount of water needed to cross the porous steel filter in order to displace the diaphragm of the pressure transducer (most transducers are made of small strain gage bridge). For a given piezometer configuration (with permeability of the filter higher than the soil), the fastest possible response can be derived from subjecting the piezometer to impulse load in pure liquid so that the vast reservoir liquid can freely travel through the filter to mobilize the transducer's diaphragm. However, once the piezometer is embedded in soil with permeability lower than the filter, the piezometer's response is significantly reduced since the fluid has to travel through the low permeability soil before entering the piezometer's measuring system.

The following section describe the theoretical derivation and laboratory measurements of the response of the piezometer when subjected to load under pure silicone oil (fastest scenario) and when embedded in soil (real scenario with slower response time).

5.1.9.1 Theoretical Derivation of Response in Silicone Oil

Henderson (1992) derived a theoretical response equation for a water pressure measurement device in response to an instantaneous loading in a close boundary (i.e constant applied pressure). See section 4.3.1.1 for more details.

The equation of the piezometer response is:

$$\frac{P_o}{P_a} = (1 - e^{-bt})\ ;\ b = \frac{kA}{\gamma_{oil} lM}\ ;\ M = \frac{\Delta V(t)}{\Delta P(t)}$$

where:

P_o = Probe output pressure
P_a = Atmospheric pressure
t = time
k = hydraulic conductivity of the porous stone in probe
A = cross section area of porous stone in probe
γ_{oil} = Unit weight of silicone oil
l = length of porous stone
M = probe system compliance
$\Delta P(t)$ = change in probe system pressure
$\Delta V(t)$ = change in volume probe system

The compliance of the probe is made of 3 categories: a) stiffness of the transducer diaphragm, b) compressibility of silicone oil, and c) expansion of the shaft. From the analysis, it is found that compressibility of the silicone oil and flexibility of the pressure transducer has a significant effect on the time response.

The theoretical response of the piezometer using Omega PX139 pressure transducer and a 0.002 mm/s porous stone is 0.01 second.

Calculation of pore pressure response for tip porous stone

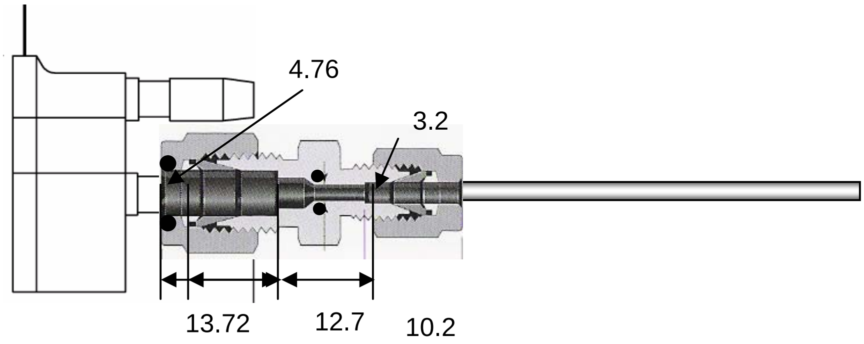

Δ Volume A:

1) Transducer characteristics (silicone diaphragm)

$\Delta V_1(t)$: = 0.4 $P_A(t)$ mm^5/N (Henderson 1992, based on Motorola MPX series)

2) Compressibility of Silicone oil

$$\Delta V_2\,(t) = V_{trans} + V_{swagelok} + V_{steel\ tube} + V_{porous\ stone}$$

$$= \frac{(2.11)^2}{4}(17)(\pi) + 380.88\text{mm}^3 + \frac{(1.4)^2}{4}(140)(\pi) = 59.44 + 380.88 + 215.51$$

$$= 665.8\text{mm}^3.$$

$$\Delta V_2\,(t) = \frac{665mm^3}{\text{bulk modulus of silicone oil}} = \frac{665mm^3}{2.19\times10^9\times10^{-6}} = \mathbf{0.299\ P_A(t)\ mm^5/N}$$

3) Expansion of steel shaft, plastic transducer, Swagelok

Expansion of steel shaft:

$$\Delta V_{steel} = \frac{a^2 D_i L\pi}{Eh}P_A(t) = \frac{(0.7)^2(1.4)(140)\pi}{(1.94\times10^5 N/mm^2)(0.9)}P_A(t) = 0.00173\ P_A\ (t)\ \text{mm}^5/\text{N}$$

where

a = inner radius = 0.7mm

E = Young’s modulus of stainless steel shaft = 194 GPa
(Roark and Young, 1975)

h = shaft thickness = 0.9mm

Expansion of swagelok

For simplicity, split the reducing union into three separate components: a) 3/16 nut, b) reducing union, and c) 1/8 nut.

ΔV$_{3/16\text{ nut}}$ = $\frac{a^2 D_i L\pi}{Eh} P_A(t)$ = $\frac{(2.38)^2(4.76)(13.72)\pi}{(0.9\times10^5 N/mm^2)(3)} P_A(t)$ = 0.0041 P_A(t) mm$^{5/}$N

ΔV$_{\text{reducing union}}$ = $\frac{a^2 D_i L\pi}{Eh} P_A(t)$ = $\frac{(3.2)^2(6.4)(10.2)\pi}{(0.9\times10^5 N/mm^2)(3)} P_A(t)$ = 0.0077 P_A (t) mm$^{5/}$N

ΔV$_{1/8\text{ nut}}$ = $\frac{a^2 D_i L\pi}{Eh} P_A(t)$ = $\frac{(3.2)^2(6.4)(12.7)\pi}{(0.9\times10^5 N/mm^2)(3)} P_A(t)$ = 0.00968 P_A (t) mm$^{5/}$N

ΔV = 0.0041 + 0.0077 + 0.00968 = **0.021 P_A (t) mm$^{5/}$N**

Therefore,
ΔVolume A(t) = 0.72 P_A (t) mm^5/N

$M = \frac{\Delta V_A(t)}{P_A(t)}$ = 0.72 mm^5/N

ΔVolume B:
k = stone permeability (measured) = 0.002 mm/s
A = inner cross sectional area (measured)= 1.54 mm^2
l = stone thickness (estimated) = 2.0mm

The theoretical response in fluid equation is

$$y = \left(1 - e^{-\frac{bt}{(\sec)}}\right)$$

where y = normalised pressure
t = time

b = $\frac{kAV(t)}{\gamma_w lM}$ = $\frac{(2\times10^{-3} mm/\sec)(1.54 mm^2)V(t)}{(9.4\times10^{-6} N/mm^3)(2mm)(7.06 mm^5/N)}$ = 227.5 sec^{-1}

This gives a response time t_{95} of $\frac{3}{b}$ = 0.013 sec.

5.1.9.2 Measured Time Response in Silicone Oil

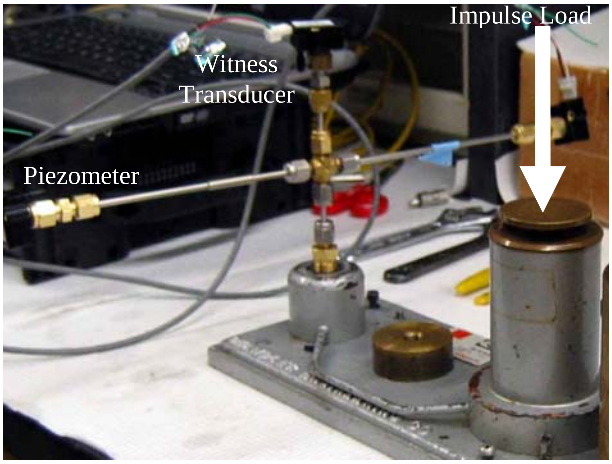

Figure 5-19: Apparatus setup for piezometer response testing in silicone oil. The apparatus is modified from Data Instrumentation pressure transducer calibrator.

The response time of the piezometer can be empirically measured using an apparatus capable of applying an instantaneous load (Figure 5-19). The piezometer and a witness pressure transducer (without filter) were attached to the apparatus and connected to a high speed data acquisition. An instantaneous load close to 40 kPa was applied at the piston and held for a few seconds.
The experiment is conducted for both a saturated and an unsaturated piezometer for comparison.

The normalized applied pressure (i.e measured pressure / applied pressure) of the saturated piezometer and the witness pressure transducer is plotted in Figure 5-20. The measured response of the saturated piezometer is 0.035 s whereas the response of the witness pressure transducer is closer to 0.014 s. The witness pressure transducer picked up the dynamic transient response of the instantaneous applied load which cannot be detected by the saturated piezometer. The unsaturated piezometer has a much poorer response time at 8 seconds as additional oil is needed to enter the system in order to compress the pockets of air bubbles although the final applied pressure will still be reached. The implication of using an unsaturated piezometer in the field is the development of pore pressure due to the passage of trains will be partially detected.

The response of the piezometer developed is compared with well known miniature piezometers (Table 5-1). In general, the response of the piezometer is similar to Cauble (1993) which utilized a miniature needle probe design. Kutter (1990) was able to achieve very quick pressure response in water due to its small liquid volume in the measuring chamber and relatively large porous stone area. However, the porous stone area (6.5mm diameter) is still relatively large compared to the layer of interest in the subgrade and may cause arching of the soil. By comparison, the proposed piezometer only has a diameter of 1.65mm. See section 4.3.2.1 for details of piezometers by Cauble and Kutter.

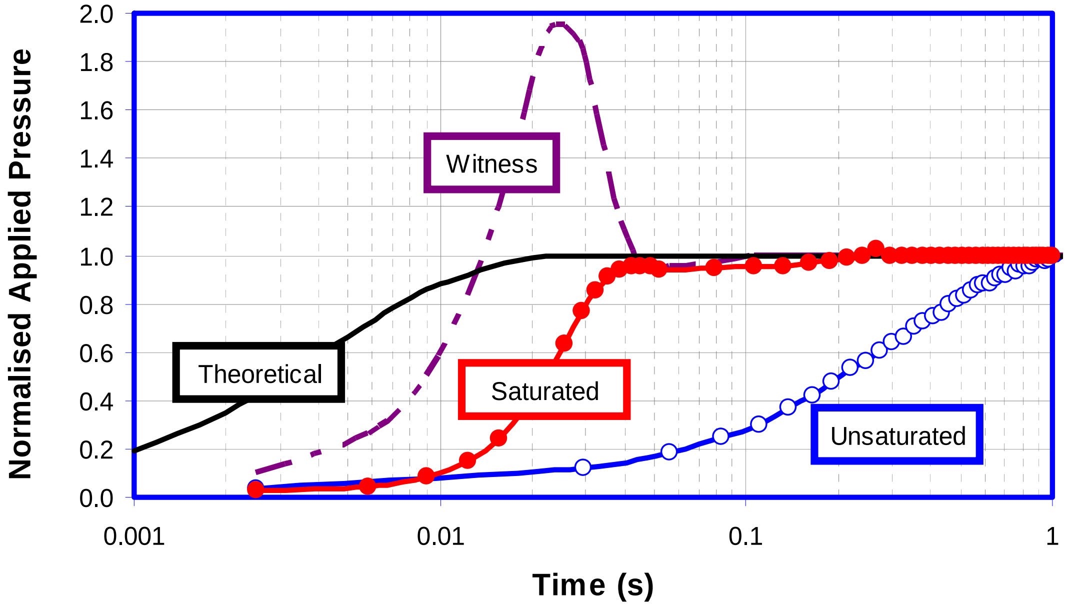

Figure 5-20: Response of the saturated piezometer, witness, unsaturated piezometer, and theoretical response.

Table 5-1: Comparison of response measurement with other piezometers

Author	*Pressure Transducer*	*Measured in water or oil*
Aw	Omega	0.04s
Cauble (1993)	Kulite	<0.05s
	Cooper	<0.1s
	Data Instrument	0.6s
Kutter (1990)	Druck PDCR81	0.001s**

** response measured by removal of pressure

5.1.9.3 Theoretical response in Soil

The response of the piezometer in soil is largely governed by the permeability of the soil. For soils with permeability higher than the porous stone (e.g. sand, gravel), the response will be governed by the permeability of the porous stone. Conversely, the response will be governed by the permeability of the soils if it is lower than the permeability of the porous stone.

Calculation of pore pressure response for tip porous stone

$$b = \frac{kAV(t)}{\gamma_w lM} = b = \frac{k_{soil}AV(t)}{\gamma_w lM}$$

but M = 0.72 mm^5/N (similar to piezometer stiffness for response in oil)
k_s = 6.95 x10^{-7} mm/s (at 450 kPa) for Maine Clay. Obtained from CRS test.

$$b = \frac{k_{soil}AV(t)}{\gamma_w lM} = \frac{(6.95\times10^{-7}\, mm/\sec)(1.54mm^2)V(t)}{(9.4\times10^{-6}\, N/mm^3)(2mm)(7.06mm^5/N)} = 0.0754 \sec^{-1}$$

This gives the response time: t_{95} = 39.7s

Two experiments are conducted to measure the dynamic response of the piezometer in soil. The first experiment is conducted in low permeability clay and the second in high permeability sand. Pore pressure development is not expected to be measured in sand (pore pressure dissipation will be fast at high soil permeability) and is expected in clay (due to its lower permeability).

5.1.9.4 Measured response in soil (clay)

The measurement of the response in soil can be conducted by inserting the piezometer into a cylindrical soil sample and apply an instantaneous load. However, there are a few differences between these tests and the response measurement in oil. The main difference lies in the open double drainage boundaries in the soil which is intended to provide control on build up of pore pressure at the boundary as well as to simulate the consolidation effect during application of a wheel load. Therefore, the measured pore pressure response should follow a Terzaghi's one dimensional consolidation curve.

Equipment set-up

The main features of the experimental setup include (Figure 5-21):

1. A cut section of the steel 3" sampling tube containing soil to be tested.
2. Porous stones placed at both ends of the soil to provide double drainage
3. Back-pressure to maintain saturation in soil is provided by introducing a bigger head at the base of the specimen which will encourage a small upward seepage.

The soil sample can be obtained directly from any 3" steel sampling tube by cutting a section of 2" (5.08cm) high. A 4mm hole is drilled at the side of the steel tube for piezometer access. Drilling of the soil can be performed by gently rotating the drill bit in the soil by hand. A thin wire is used to debond the interface between the soil and the steel tube in order to minimize side friction during loading. Filter papers and saturated porous stones (through the action of ultrasound) are placed on both ends of the soil to provide double drainage during loading. A rubber membrane held by o-rings is used to provide sealing between the bottom-half of the soil sample and the base. The sample is currently kept under constant pressure head in order to ensure that the pore pressure in the soil is always positive to ensure that saturation is not loss.

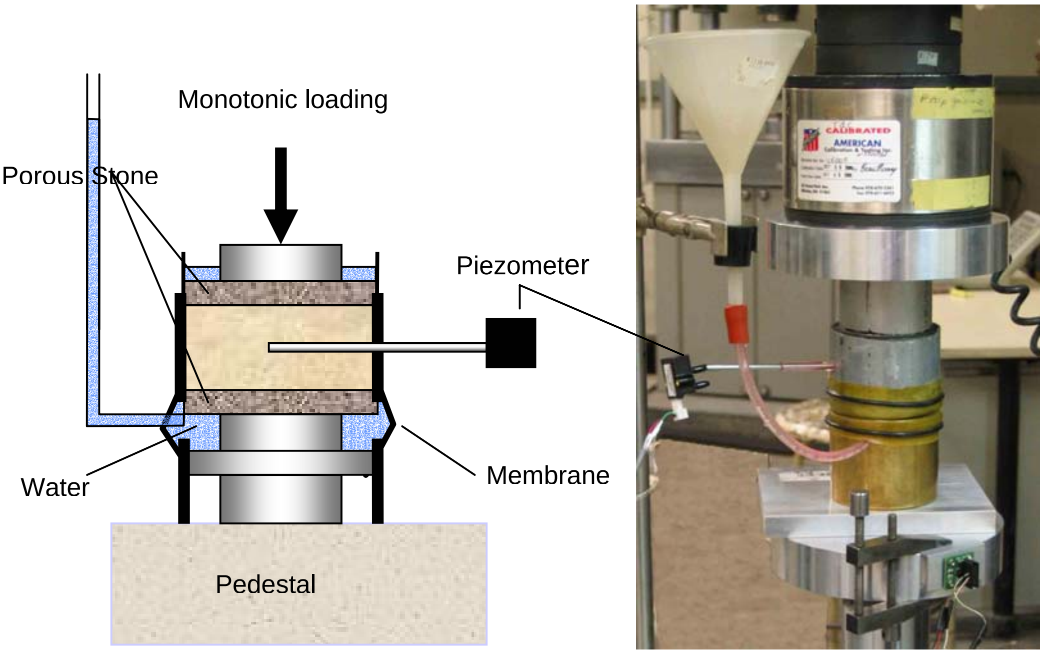

Figure 5-21: Setup for measuring response of piezometer in soil.

Properties of the soil

The soil used for this experiment is Maine clay and results of the coefficient of consolidation (cv) and coefficient of permeability were obtained from a constant rate of test (CRS).

Measured parameters from CRS test:

Coefficient of Permeability: 6.95×10^{-8} cm/s
Coefficient of Consolidation: 0.012 cm^2/s

Loading

A seating load of 450 kPa was placed at the clay for 3 hours prior to starting the test. An instantaneous loading ($\Delta\sigma_v$) of 100 kPa was applied on to the clay sample and consolidation was allowed to occur.

Result

In a one dimensional loading, the developed pore pressure is equal to the applied pressure. The theoretical development and dissipation of pore pressure at the center of the clay can be modeled by Terzaghi's one dimensional consolidation curve with double drainage (Figure 5-22). The theoretical response of the piezometer was calculated at 39.7s and therefore could not capture the initial part of the curve. The measured response is about 30s. Once the piezometer equilibrates with the external pore pressure, the second part of the consolidation curve can be captured accurately.

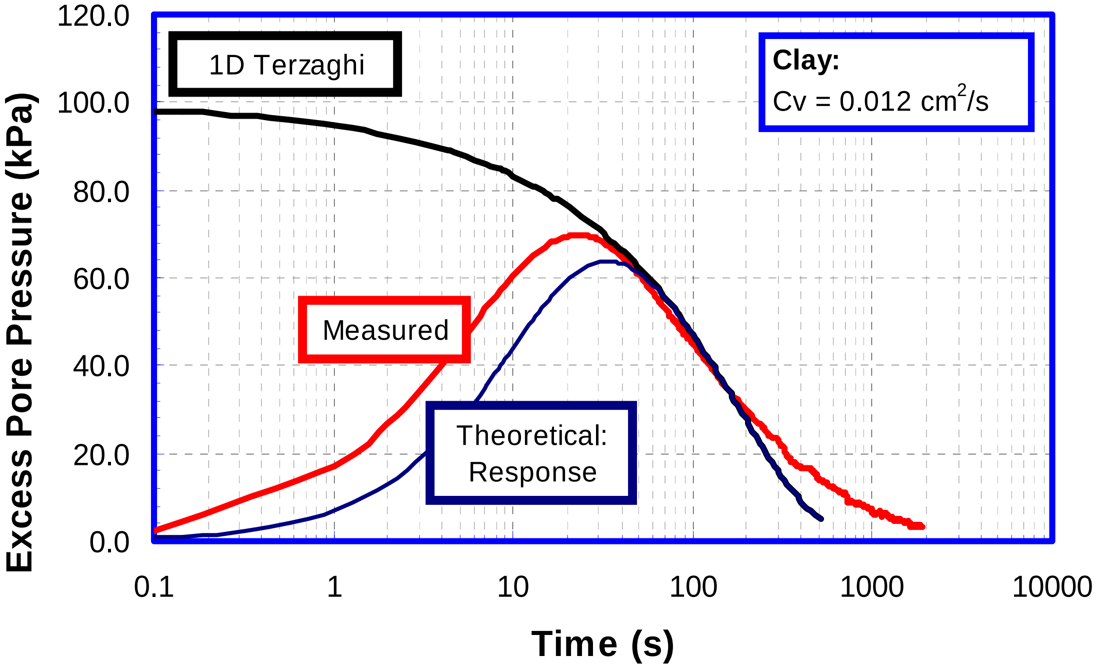

Figure 5-22: Response of the piezometer in clay with double drainage. 1D Terzaghi consolidation equation is given.

5.1.9.5 Measured response in soil (sand)

Equipment set-up

Reconstituted fine sand (diameter ≈ 0.08 to 0.11mm) is used to measure the response of the piezometer and uses equipment set-up similar to clay (Figure 5-21). The sand is laid in the tube in three layers, with tamping at each layer before the addition of another. The hole for the piezometer is created with a small drill. A saturated piezometer is inserted into the sand specimen and a seating load of 50 kPa is applied on the specimen. A bottom pressure of 10cm is applied to the specimen in order to ensure that the soil specimen is fully saturated.

Loading

An instantaneous load of 50 kPa is applied on the sand and the pore pressure response is measured and the experiment is repeated three times (Figure 5-23). The results are conditioned with a 5-window-moving average to remove the noises and retain the underlying pressure response shape.

Result

Upon application of 50 kPa of instantaneous load, the piezometer is only able to register a response of 2 to 2.4 kPa, before returning to the initial backpressure of 1.1 kPa. The full 50 kPa is not measured as the pore pressure dissipated due to the relatively high hydraulic conductivity of the fine sand and the piezometer is not able to register the full pore pressure development.

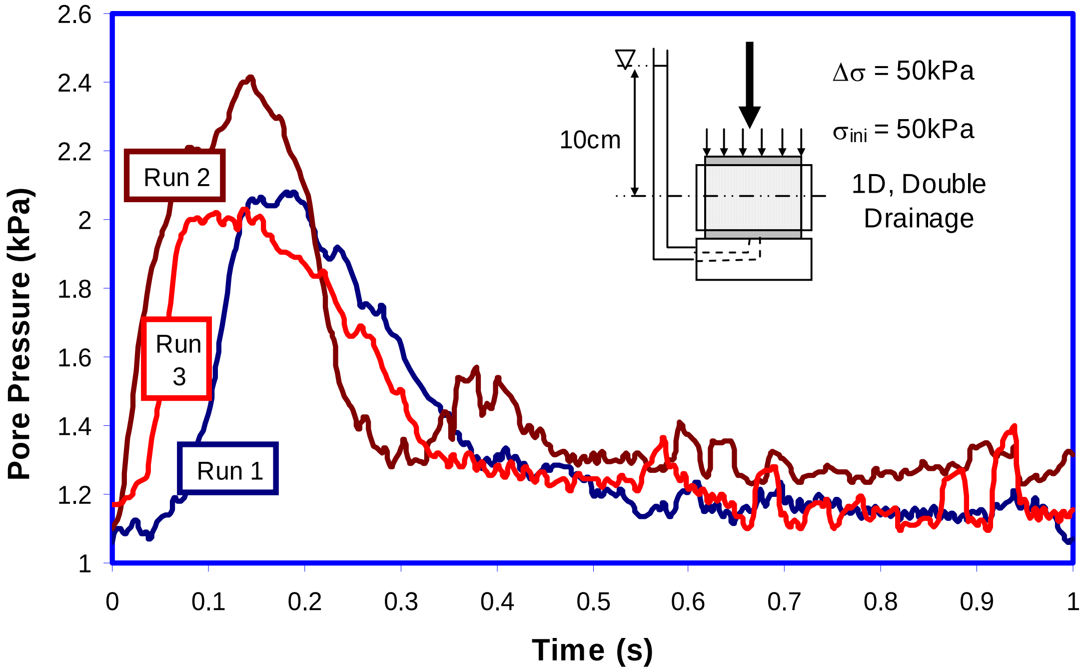

Figure 5-23: Measured response in sand with double drainage. The results are conditioned with a 5 window average.

5.2 Development of Settlement Probe

5.2.1 Principle of Measurement

The vertical settlement probe consists of a fixed reservoir head on one end and a pressure transducer (hydraulically connected to the reservoir via small tubing) embedded in the ground. Ground movement in the pressure transducer end will cause changes in pressure head relative to the fixed-end fluid head datum (reservoir). Settlement results in increased of positive pressure and vice versa. Ground movement at the pressure transducer end can be calculated by dividing the measured pressure by the liquid density. This design offers an easy and convenient way of designing small point sensors that can be easily installed under the track while maintaining a reliable point of reference on a stable ground. By contrast, and extensometer will have to be anchored deep into the ground in order to establish solid reference point. Silicone oil is used due to its low freezing temperature and will not freeze in winter.

5.2.2 Key design issues:

Prior experience (Aw 2004) found that the performance of the settlement probe is almost solely dependent on the performance of the pressure transducer. Selection of a pressure transducer with good long term offset stability and temperature sensitivity is of paramount importance.

The key issue with the design of the settlement probe is in the stability of the long term drift offset. Settlement measurements of the railway track are often not more than an inch (25.4mm), and hence it is important that the long term stability does not exceed a few millimeters. Since the lesson learned from the previous research is central to the development of the new settlement probe, it will be dealt in detail in the following section.

Long term offset stability

Long term reliability of the transducer depends on the long term drift of the pressure transducer, which is typically 0.5% of the full scale for most strain-gage based pressure transducer; up to 5cm pressure head drift for a 100 kPa pressure transducer and twice that if an absolute pressure transducer is used to account for subtraction of atmospheric pressure effect from a witness pressure transducer. The Motorola MPX 2100 absolute pressure transducers (Aw 2004) has long term drifts of up to 5 to 7cm over 2 months of testing (Figure 5-25) even when installed under controlled conditions in the laboratory. These absolute pressures are sensitive to the atmospheric pressure (Figure 5-24) which is removed by subtracting readings of the settlement probe from a witness pressure transducer. Hence, the accuracy of the measured displacement is also dependant on the performance of the witness pressure transducer which may experience different temperature conditions than the probe.

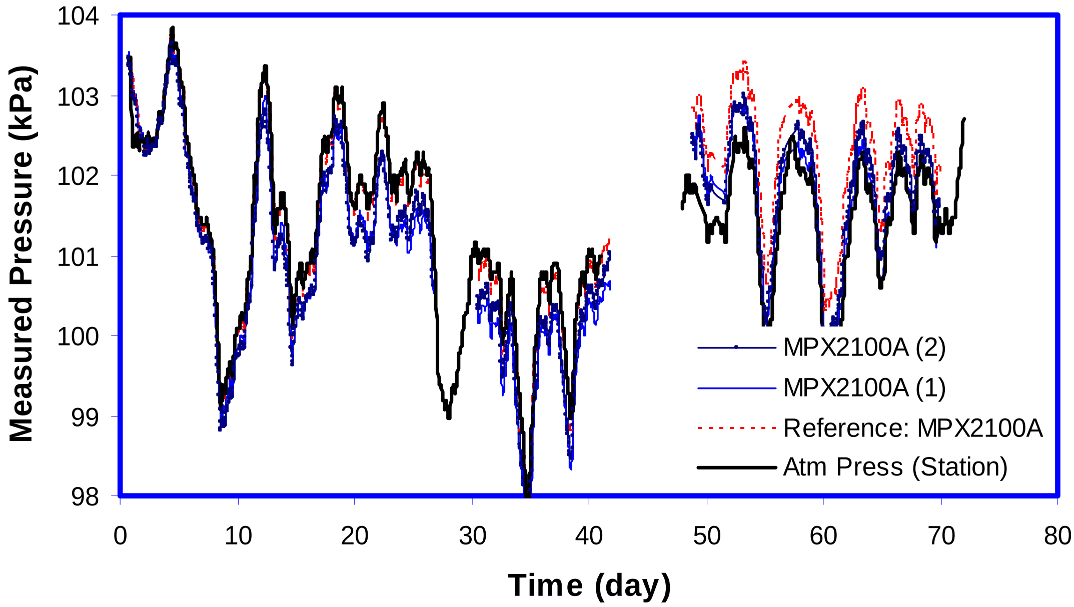

Figure 5-24: Uncorrected measurement from two settlement probes (MPX2100A 1 & 2), reference MPX2100A absolute pressure transducer for zero settlement. The measured trend corresponds to the atmospheric pressure (Atm Press – Station) obtained from a nearby weather station.

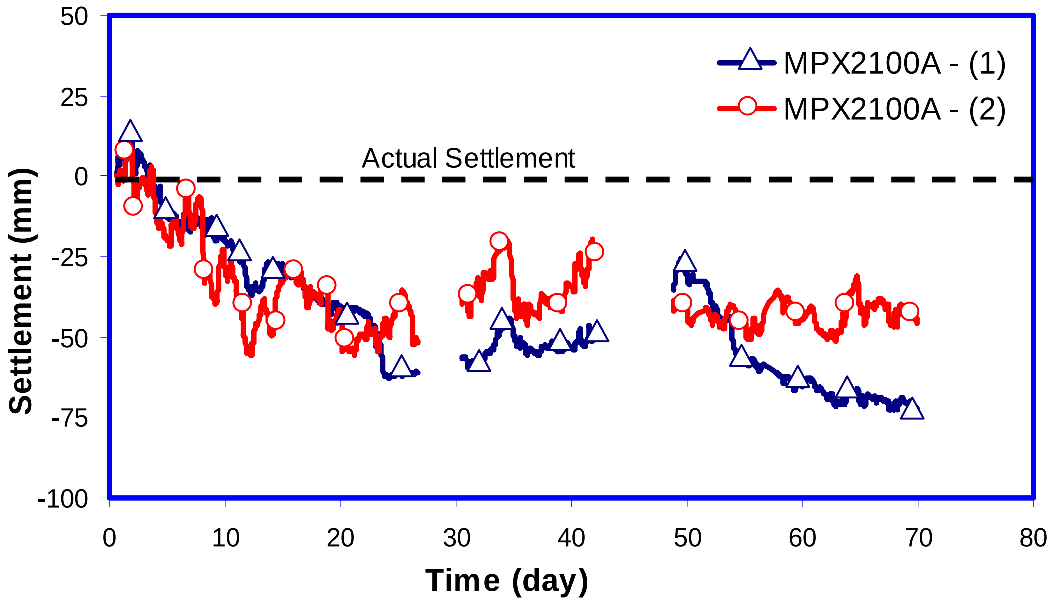

Figure 5-25: Corrected measurement from the two settlement probes (subtracted from the reference MPX2100A). Offset drift of up to 50 and 75mm occurred within the 70 days of testing, compared with zero actual settlement.

Temperature effects

MPX2100A absolute pressure transducers are sensitive to temperature changes; 10°C of temperature change can result in over 2 cm of reading error (Figure 5-26). Since only the offset and not the calibration curve changes with temperature, these inaccuracies can be easily removed through using linear temperature correction curve. In addition, another source of error lies in the temperature gradient between reservoir (above ground subjected to daily temperature fluctuations) and the probe (below ground with constant temperature) which causes changes in fluid density. Again, this temperature-density correction can be easily applied.

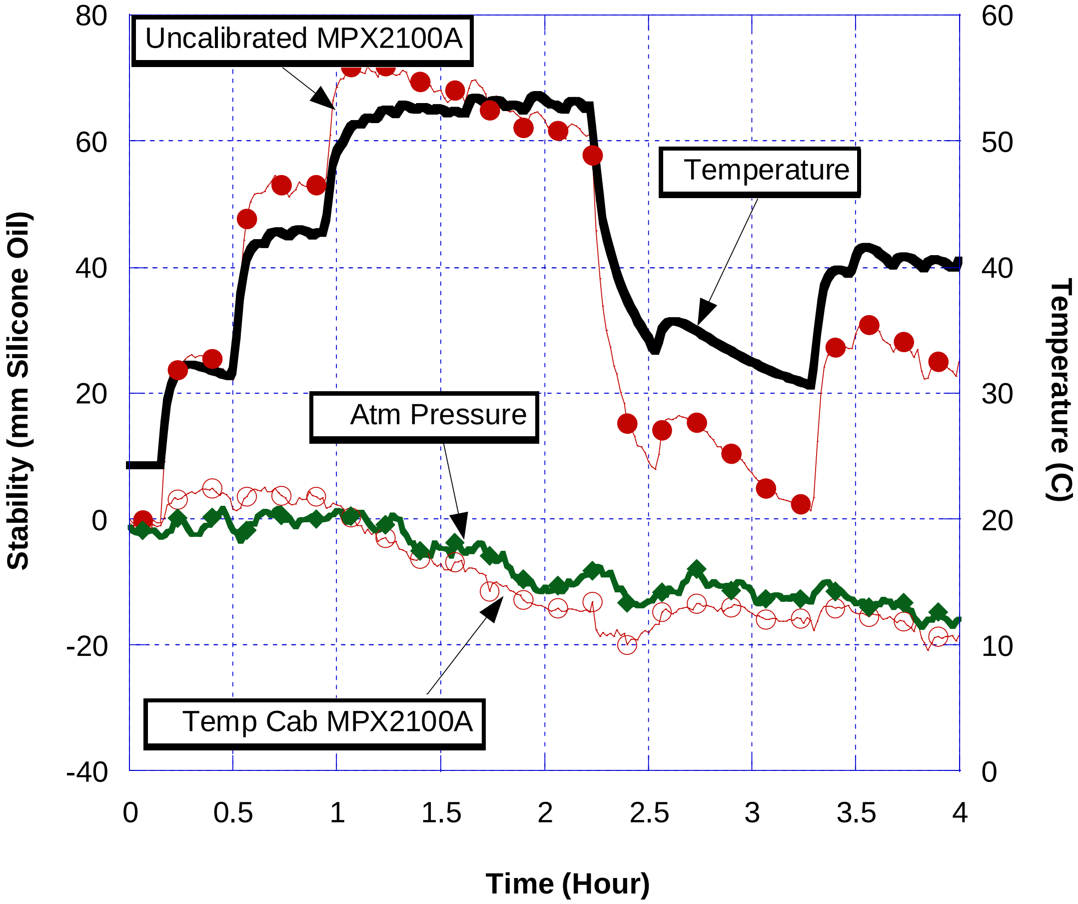

Figure 5-26: Effect of temperature on the MPX2100A absolute pressure transducer (temperature uncalibrated MPX2100A). Application of temperature calibration brings the measured data closer to the real atmospheric pressure (obtained from weather station). Aw (2004).

5.2.3 Settlement Probe components and fabrication

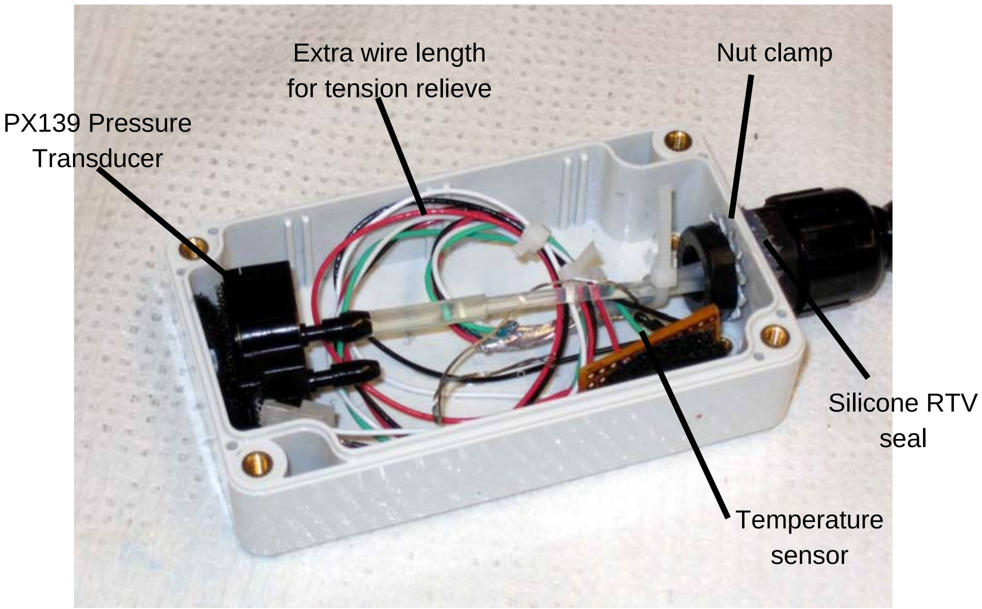

Figure 5-27: Settlement Probe

The new settlement probe is completely redesigned from the previous research project. A differential Omega PX139 pressure transducer with better long term offset stability and temperature sensitivity was selected. PX139 has in inbuilt pre-amplification circuit and produces high output voltage – 4V over ± 35 kPa range, resulting in 1mV = 1.8mm of sensitivity. By comparison, the 100kPa MPX2100A pressure transducer has output of 40mV and sensitivity of 1mV = 266mm. Therefore, the PX139 is less susceptible to environmental noises than the MPX139 pressure transducers. Table 5-2 shows the manufacturer's summary of the pressure transducer's performance and the measured laboratory performance. More details on the tests are given in the section below.

The fabrication of the settlement probe is similar to the piezometer (uses Nema 4X box and waterproof BX cable connectors). Two out of the three settlement probes contains a thermistor for temperature measurement. A 4mm diameter Nylon 11 tubing (with internal diameter of 2.7mm) is used to connect the reservoir to the pressure transducer. Nylon 11 material is chosen because it remains impermeable to air and prevents air diffusion through the tubing (Dunnicliff, 1988). The nylon tube is fastened to the port of the transducer using a wire tie.

Table 5-2: Summary of the transducer reliability (transducer in fully assembled settlement probe)

	Repeatability		**Non Linearity + Hysteresis**		**Temp Err**		**Drift**	**Accuracy**
	mV	**mm**	**mV**	**mm**	**mV**	**mm**	**mm**	**mV**
Manufacturer	6.11	11	2	3.6	0.2mV/C	0.4mm/C	NA	
Lab Cab				3.84	0.172mV/C	0.2mm/C	±2mm/ 60 days	0.156mV

Effect of hysteresis, non-linearity and long term offset stability

The performance of the PX139 can be characterized by three criteria: a) hysteresis (the loading and unloading paths are different), non-linearity (deviation of the measured data from an assumed linear calibration curve), and long term offset stability. Hysteresis and non-linearity can be established by performing a pressure stepping calibration procedure by changing the elevation of the settlement probe[15] and comparing the measured movement against predetermine known movements. In order to obtain statistically significant data, the stepping up and down calibration is performed 14 times and yielded a linear regression curve with root mean square of 0.99991 (Figure 5-28).

The non-linearity (difference between the measured data and corresponding linear regression curve) and hysteresis (difference between loading and unloading curve at a particular applied pressure) history for the fourteen curves has standard deviation of 1.027 mV(1.88 mm) and 0.947 mV (1.76 mm) respectively (Figure 5-29).

The long-term offset stability is investigated by monitoring the settlement reading of the settlement probe (ideally zero) and two witness pressure transducers (connected to a breadboard in a grounded steel box and will not be affected by environmental noises picked up by cabling and etc) over a period of sixty days. The two pressure transducers in the breadboard showed good long term stability (≈±0.4mm) while the settlement probe has range of -1 to +3 mm (Figure 5-30). The performance of the latter can be attributed to effect of noise collected in the 10 meters of cable which is still within tolerable region and may improve with installation since the probe is grounded.

---

[15] The fully fabricated settlement probe has 10 meters of cabling and silicone oil tubing. The data acquisition is enclosed in a steel box which is grounded to offer protection against environmental noises.

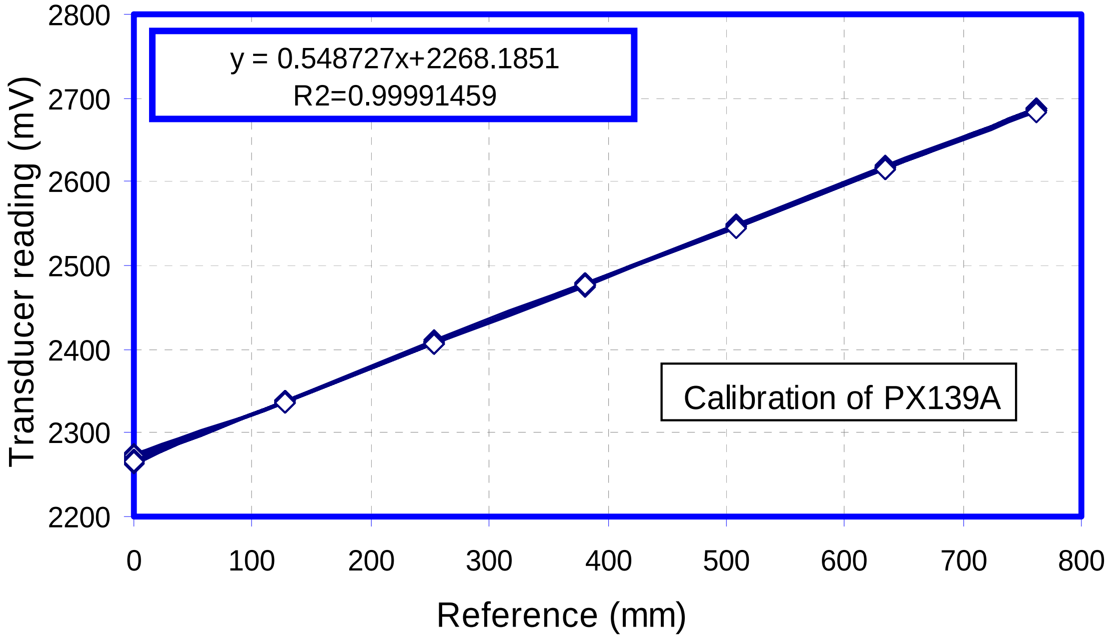

Figure 5-28: Calibration of the settlement probe, repeated 14 times and fits into linear regression curve with root mean square of 0.99991.

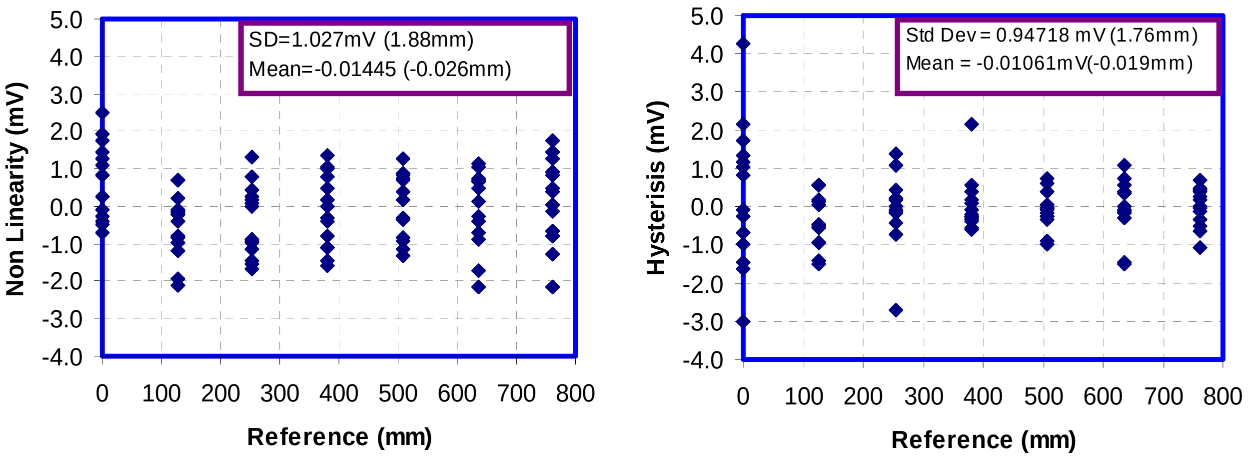

Figure 5-29: Hysteresis and non linearity of PX139A.

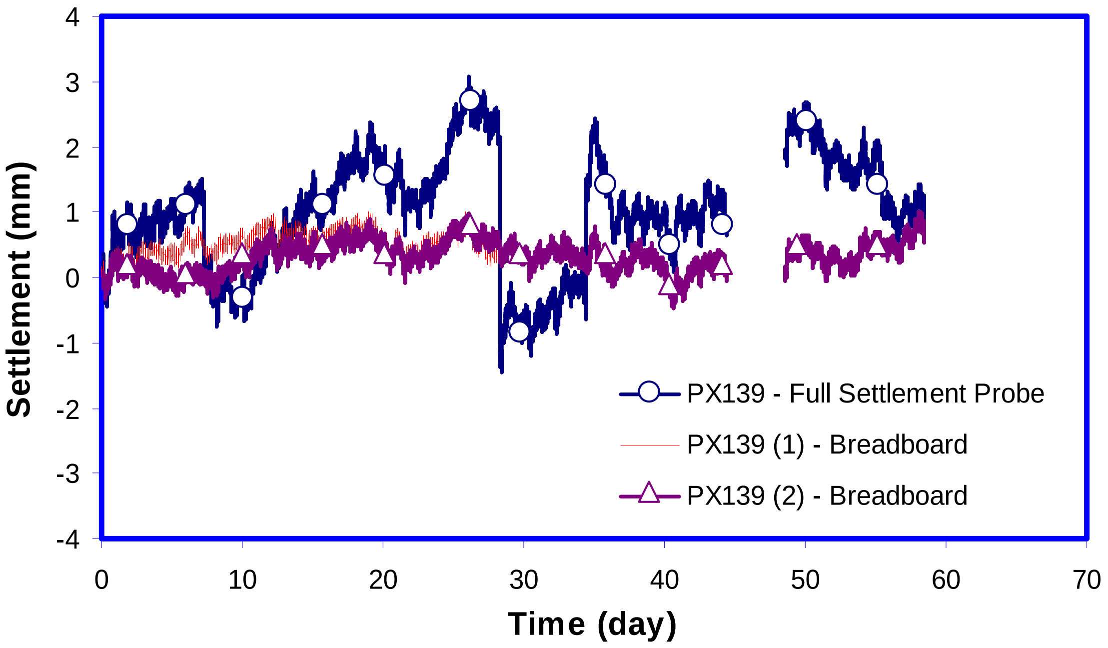

Figure 5-30: Offset stability for PX139 settlement probe compared with 2 PX139 pressure transducers attached in breadboard (to remove influence of external electrical noise caught in cabling).

Effects of temperature

While the effects of the temperature on the pressure transducer can be measured, determining the effects of temperature on the settlement probe is more complicated since the effect of differential temperature gradient on the density of the silicone oil is now important. An easier and efficient way of calibrating the settlement probe is to perform the temperature calibration on a field installed settlement probe over a period of 3 days which will implicitly account for changes in temperature related density changes (Figure 5-31). 25^{o}C of temperature changes can cause up to 5mm of apparent settlement, resulting in average change of 0.2mm/^{o}C (Figure 5-32). The temperature hysteresis is rather large, with the biggest deviation occurring at average ±1.5mm from the linear regression. Overall, the effect of temperature is small and can be significantly removed by using the temperature calibration curve.

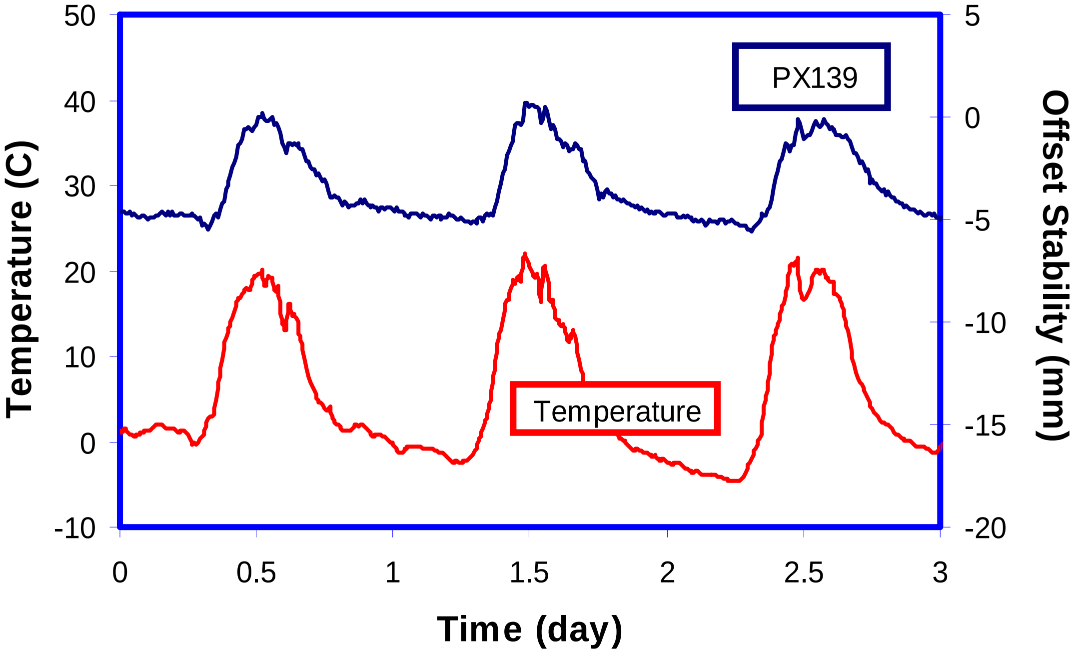

Figure 5-31: Three temperature cycles effect on the PX139 pressure transducer.

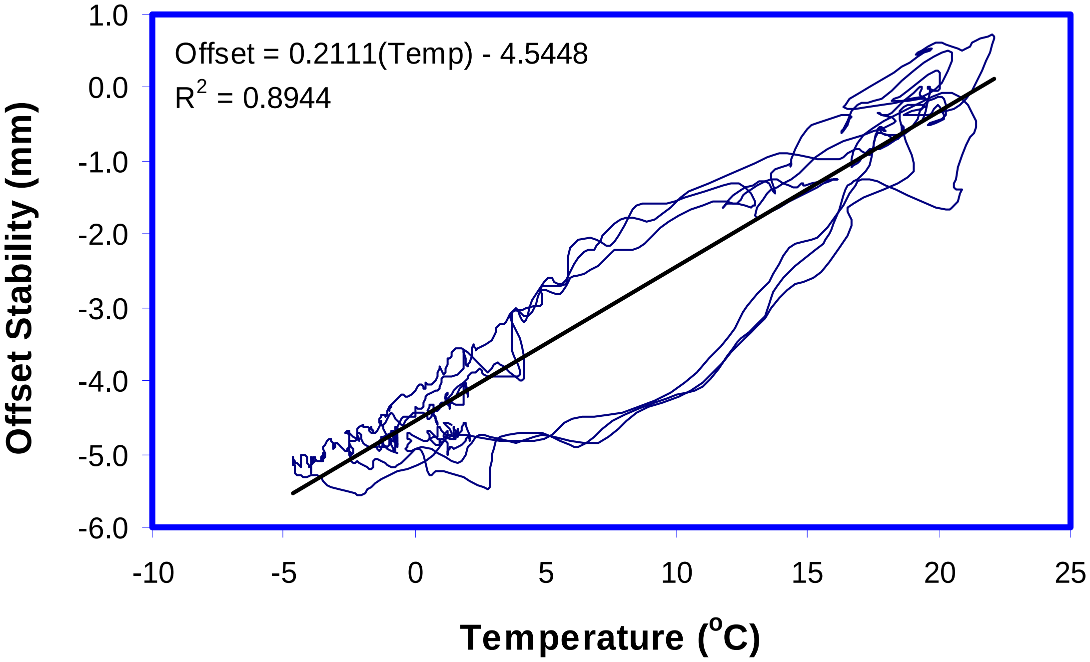

Figure 5-32: Effects of temperature on fully fabricated PX139 (connected to cables but not to the reservoir) installed in the field. With the offset stability pegged at zero at 20°C, the offset will vary as much as 5mm with changes of 25°C.

Pre-Field calibration

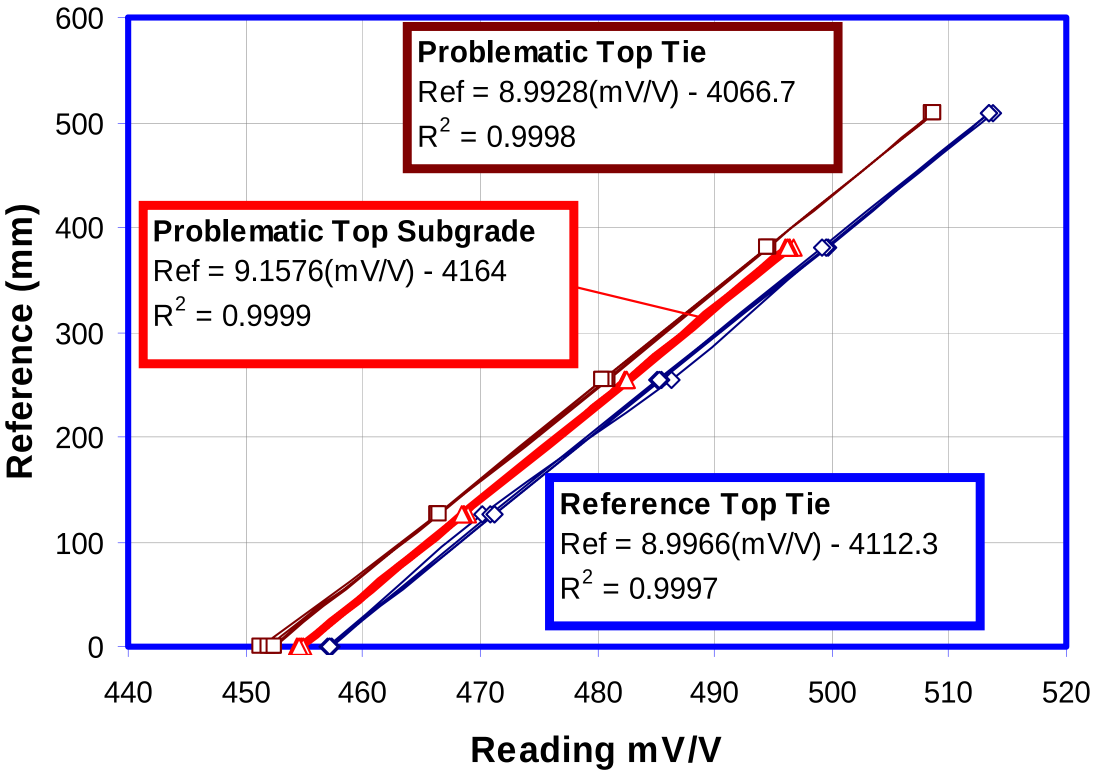

Figure 5-33: Pre-field installation calibration of the three settlement probes

Three settlement probes will be installed in the field and are calibrated two days prior to field installation (Figure 5-33). The probes are stepped up and down 3 times.

5.3 Accelerometer

5.3.1 Selection of Accelerometer

The selection of the accelerometer depends primarily on the a) range of acceleration, b) number of axis, c) ease of fabrication, and d) costs. Typical peak accelerations of 3g have been measured at high speed trains in Europe (Thalys, velocity of 300 kph, Degrande *et al* 2001). Since there is currently no acceleration measurements on problematic track, accelerometers with higher range of ±75g, ±18g and ±5g are selected for top problematic tie, top reference tie, and top subgrade respectively.

Analog Devices produces a number of low costs dual axis accelerometers (less than $10) with amplified voltage output and ranges of ±75g, ±18g and ±5g are selected (Table 5-3). The accelerometer uses a polysilicone surface-micromachined structure built on top of a silicon wafer. Acceleration deflects the polysilicone structure and the deflection is measured by a differential capacitor and produces voltage which is proportional to acceleration.

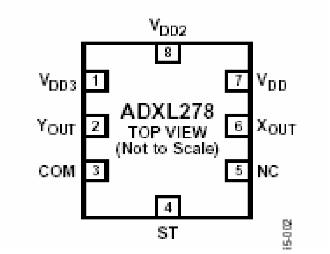

Figure 5-34: ADXL with 16 lead LFCSP

Table 5-3: Accelerometers selection and description (Omega manufacture sheet)

Parameter	***ADXL 278***	***ADXL 321***	***ADXL 320***
Location	Top Tie (Problematic)	Top Tie (Reference area)	Top subgrade (Prob. & Ref.)
Range (g)	±35g (x axis) ± 70g (y axis)	±18g	±5g
Non linearity	± 0.2%	± 0.2%	± 0.2%
Resonant Frequency (kHz)	24	5.5	5.5
Sensitivity (mV/g)	27 mV/g (x-axis) 55 mV/g (y-axis)	63mV/g	174mV/g
Offset (V)	2.5V	2.5V	2.5V
Frequency Response (3dB)	400Hz	50Hz**	50Hz**

For Vin = 5V

**Filter was removed in order to capture high frequency imposed by the trains

The accelerometers come with 8-lead LFCSP and can be attached to wires using small tip soldering iron (Figure 5-34). In order to remove the complexity soldering at such small scale, pre-packaged accelerometers which has easy pin-type connectors are tested. These pre-packaged accelerometers are only available for the ±18g and ±5g accelerometers and are equipped with 50Hz low pass filters. The 50 Hz low pass filters are removed in order to enable capture of higher train load frequencies.

The ±75g accelerometer comes with 8-lead LFCSP and is not factory pre-packaged. The accelerometer are expoxied on a hard plastic board and the construction is as follows: a hard plastic board of size 2.5cm x 6cm is cut and 8 small holes corresponding to the location of the pin output in the accelerometer. Small wires are inserted through the plastic board and are soldered on to the accelerometer chip using small tip soldering iron. The accelerometer is held by a heat sink clipped to prevent overheating from the soldering process. After soldering, the accelerometer is then pushed to be close to the hard plastic board and a layer of epoxy is applied to hold the accelerometer in place and to protect the fragile solders. Table 5-3 summarizes the properties of the accelerometers.

5.3.2 Accelerometer components and fabrication

The body components, cable wires, plastic BX cable enclosures and sealing are similar to both piezometers and settlement probes (see 5.1.2 for more information). Figure 5-35 shows the set-up of the accelerometer in the plastic housing.

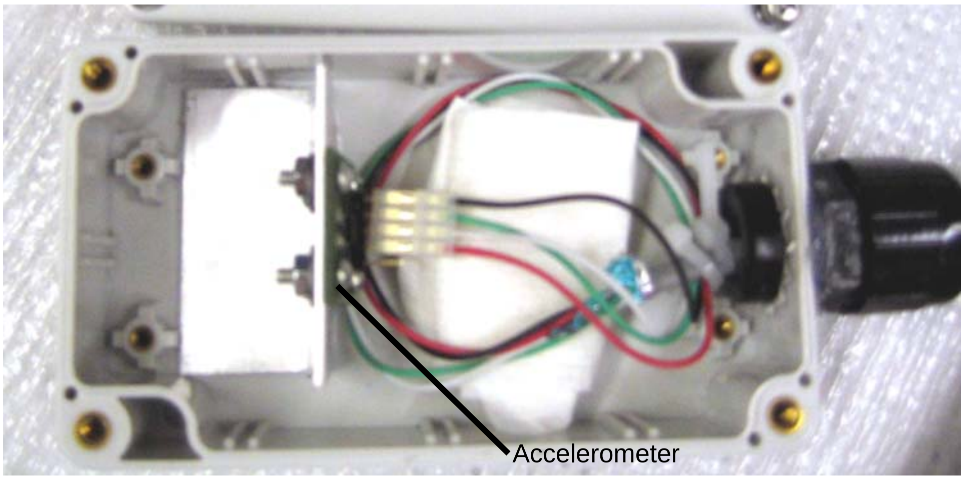

Figure 5-35: Set-up of the accelerometer in the plastic housing.

5.3.3 Calibration and characterization

Two types of calibration tests will be performed: a) determination of minimum measurable frequency and amplitude, and b) measurement of high frequencies.

1) Magnitude calibration of ±5g, ±18g, and the ±70/35g accelerometer

The magnitude of the accelerometer is calibrated by rotating the accelerometer 360 degrees around the axis, therefore changing from 0g to 1g to -1g. The full scale magnitude will be extrapolated from this calibration factor. The calibration for various accelerometers: ±5g (Figure 5-36), ±18g (Figure 5-37) and ±70/35g (Figure 5-38) are shown below.

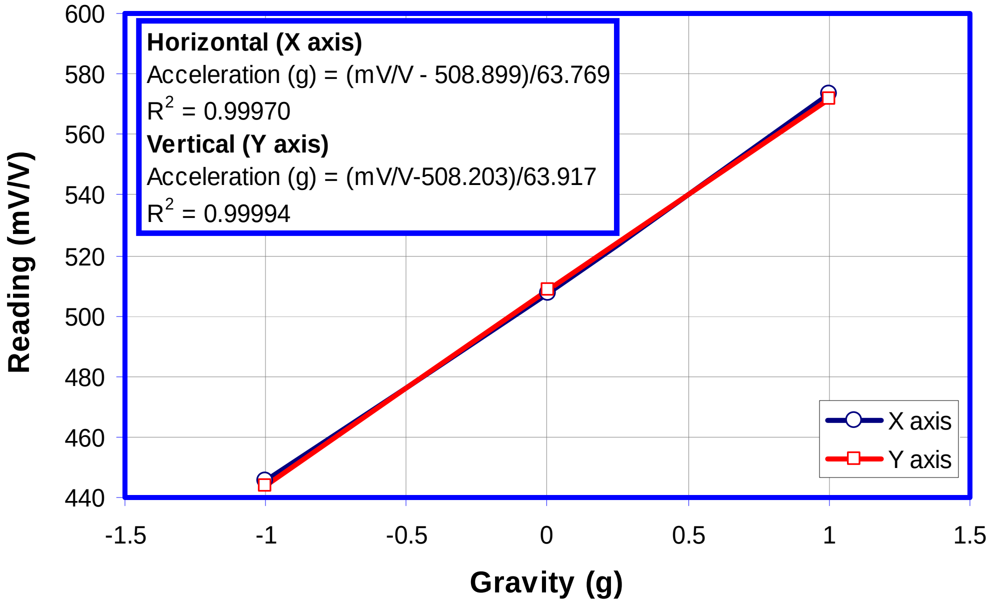

Figure 5-36: Calibration of the ADXL320 (±5g) accelerometer

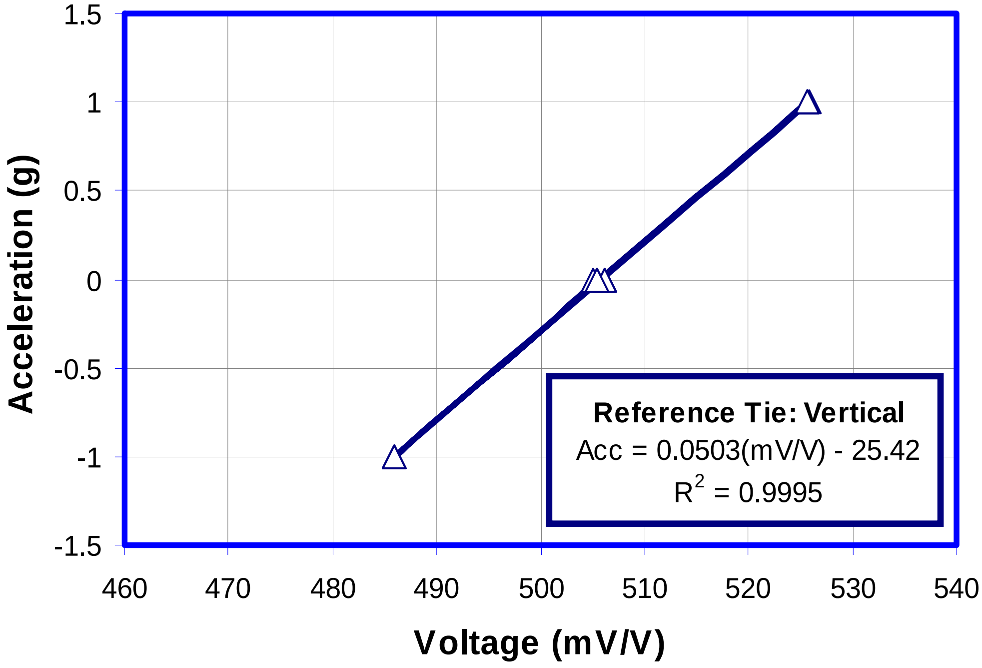

Figure 5-37: Calibration of the ADXL 31 (±18g) accelerometer

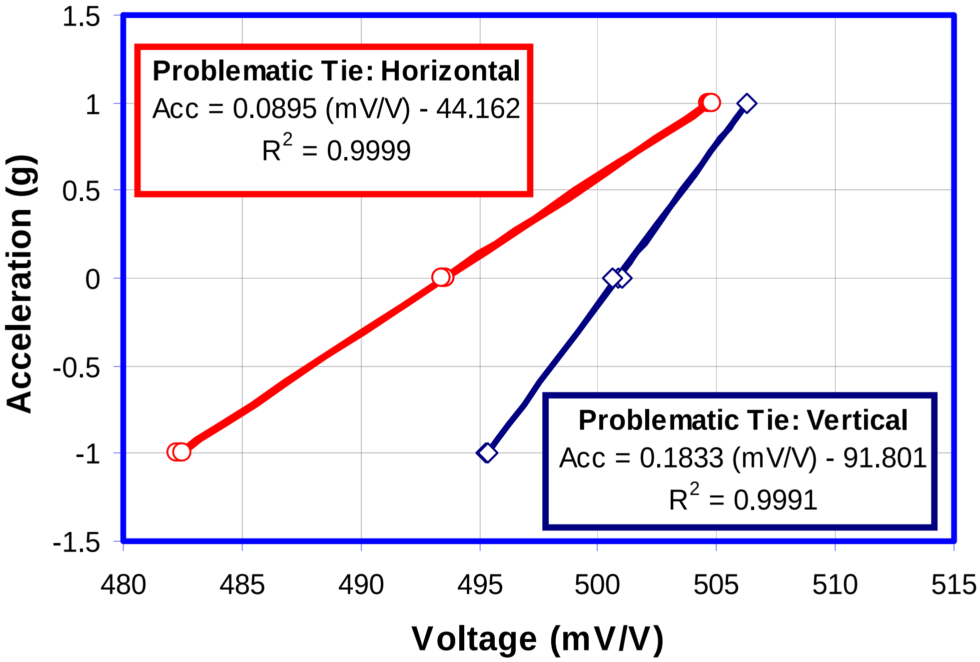

Figure 5-38: Calibration of the ADXL 278 (70g/35g) accelerometer

2) Sensitivity of frequency and amplitude measurements

Aim of this exercise is to determine the sensitivity of the accelerometers in measuring frequency and amplitude measurements, in particular low levels of frequency and amplitudes. Two types of tests are performed at two different acceleration levels, one at a comfortable measuring range of 1g, and another at very small levels of 0.03g, which can be achieved by adjusting the amplitude and frequency of the imposed load according to the theoretical formula:

$$a = A\omega^2 (\sin \omega t)$$

where a = acceleration (m/s^2)

ω = radian frequency (rad/s

A = amplitude (m)

Two ±5g accelerometers are placed on a horizontal shake device and are firmly held in place with a G-clamp (Figure 5-39). The accelerometers are linked with a high speed (100kHz) data acquisition unit (Iotech Wavebook).

Figure 5-39: Horizontal shake device with two accelerometers attached.

a) Case 1: Zero acceleration

Firstly, the noise band of the accelerometer is obtained by taking measurements of a stationary accelerometer (Figure 5-40) which gives small noise band (<0.0025g). Since both axes of the accelerometers lie perpendicular to gravity, the ideal reading should be zero.

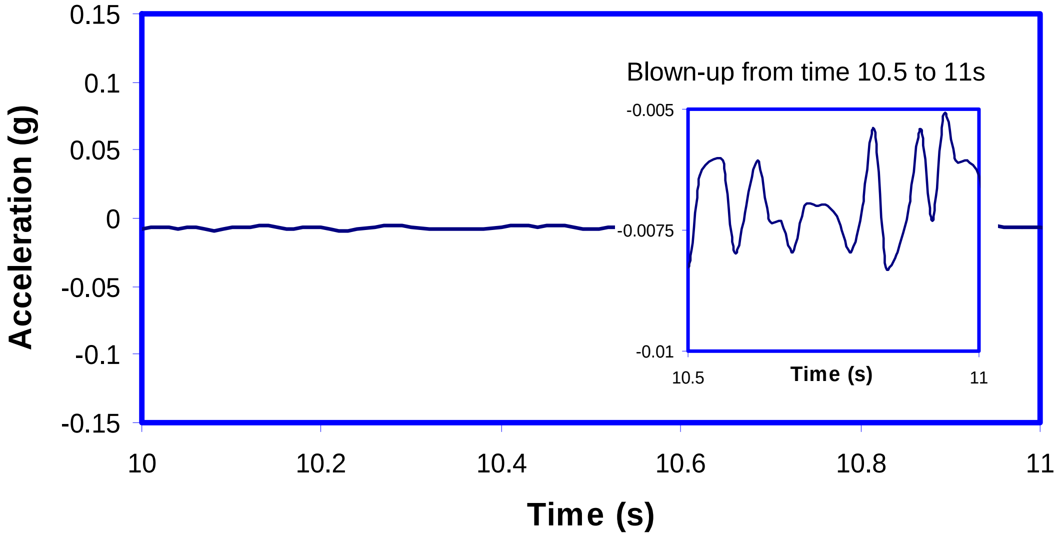

Figure 5-40: Noise band when the accelerometer is at rest.

Case 2: 0.03g imposed acceleration (2mm amplitude, 2Hz)

The accelerometers are subjected to small accelerations of 0.03g by imposing displacements of 2mm amplitude and 2Hz frequency. At such low acceleration, the noise to signal ratio of the measured acceleration is poor, with the “true” acceleration marred by higher frequency noises (Figure 5-41). This signal is mathematically composed by superposition signals of various frequencies and amplitudes which can be decomposed using fourier transform and plot of a frequency spectra curve (Figure 5-42). The signal is currently a mixture of the true frequency of 2Hz and higher frequency noises of 10Hz which can be easily removed using low pass filter. A low-pass 5th order Butterworth filter with cut-off frequency of 5Hz is found to be sufficient in removing the high order noises and its magnitude-frequency response is plotted in Figure 5-43. The disadvantage of using filters is the phase change that is applied to the signal (ie minor shift in the time domain) but this can be easily corrected and is not critical in this application. The filtered and time corrected curve approximates the imposed acceleration curve quite well (Figure 5-41).

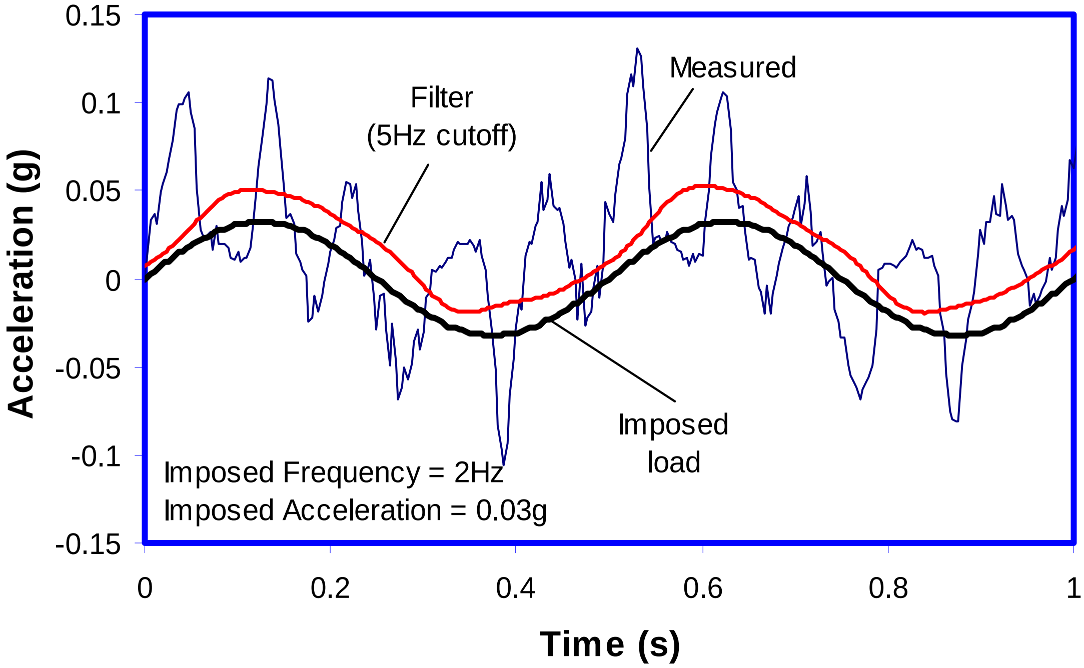

Figure 5-41: Measurement of small acceleration – imposed cyclical acceleration with amplitude of 2mm and frequency of 2Hz. The 10Hz noise frequency can be removed using a 5th order Butterworth filter with 5Hz cutoff frequency.

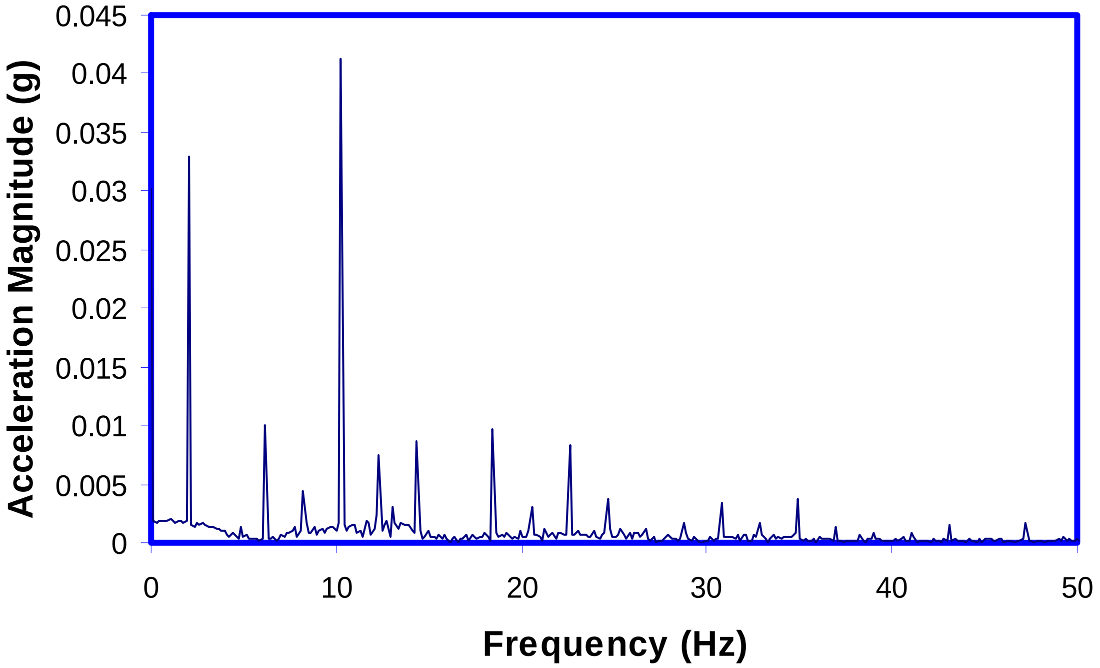

Figure 5-42: Frequency spectra of the measured imposed acceleration of 0.03g. The "true" acceleration of 2Hz is polluted by higher frequency noises (6Hz, 10Hz and higher).

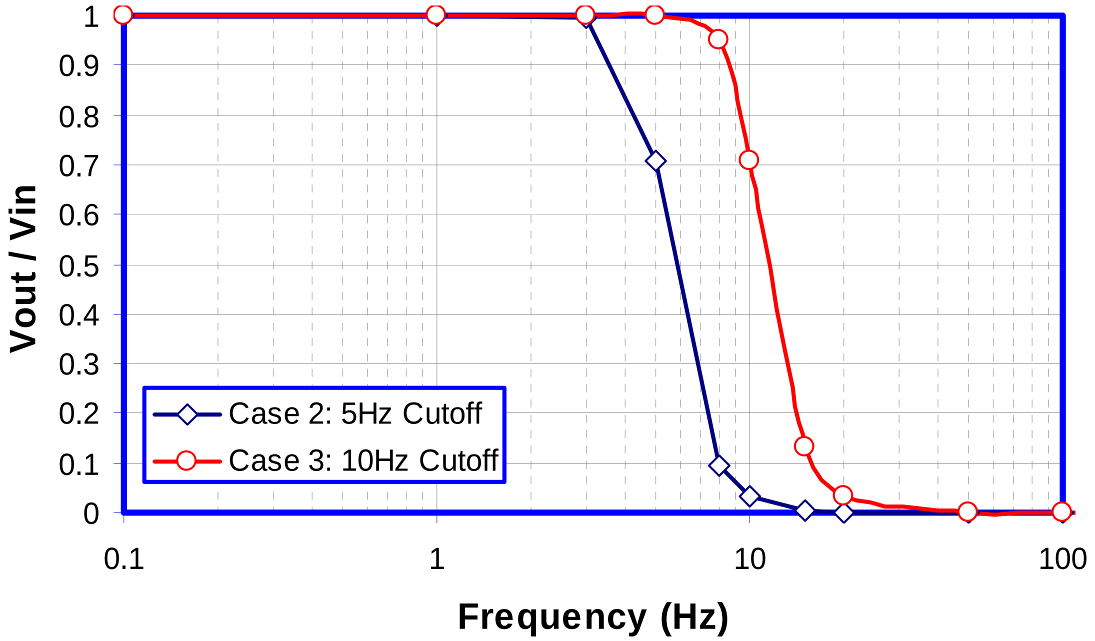

Figure 5-43: Response of a 5th order Butterworth filter at two different cutoff frequencies: a) Case 2 – 5Hz cutoff, and b) 10Hz cutoff.

Case 3: 1g imposed acceleration (10 mm amplitude, 5Hz)

The imposed acceleration is increased to 1g, which is within the comfortable measuring range of the accelerometer. The accelerometer captures the imposed acceleration well, although the infusion of higher frequency noises in the signal is still clearly visible, particularly at locations where the shake device changes direction. Here, the accelerometers are not at fault; the inertia and lashback effect of the system which occur during the change of direction causes the dynamic spikes and is a result of the shake device not rigidly secured to the floor. A fourier transformation of the acceleration into the frequency domain confirms the existence of the high frequency noises (Figure 5-45) which can be removed using a 5th order Butterworth filter with 10Hz frequency cut-off (Figure 5-43). The filtered signal fits the theoretical acceleration curve very well (Figure 5-44). More details on the use of Butterworth filter is presented in section 5.3.4.

Case 4: Imposed high frequency (120Hz)

Two accelerometers with range of ±18g and ±70g are placed in a high frequency shake device capable of producing frequency up to 120Hz (different shake device from case 2 and 3). ADXL 278 (70g) has an internal filter of 400Hz and gives quite good acceleration reading. ADXL 321 (18g), on the other hand, had the physical filter of 50Hz removed and produced lots of high frequency noise which had to be removed using filters with 400Hz (to match the performance of ±70g accelerometer). Once the 400Hz filter is applied, both accelerometers give almost similar acceleration measurements (Figure 5-46), therefore capable of measuring high frequencies which is within the range of train loading.

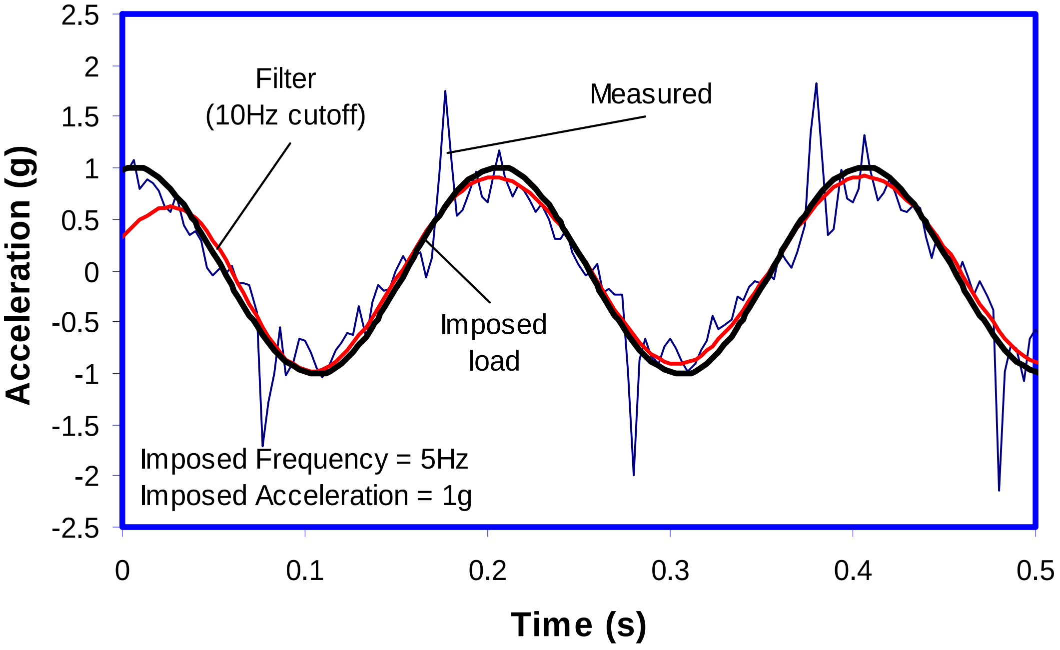

Figure 5-44: Horizontal shaking of accelerometer on a shake table at 5Hz frequency and 10mm amplitude.

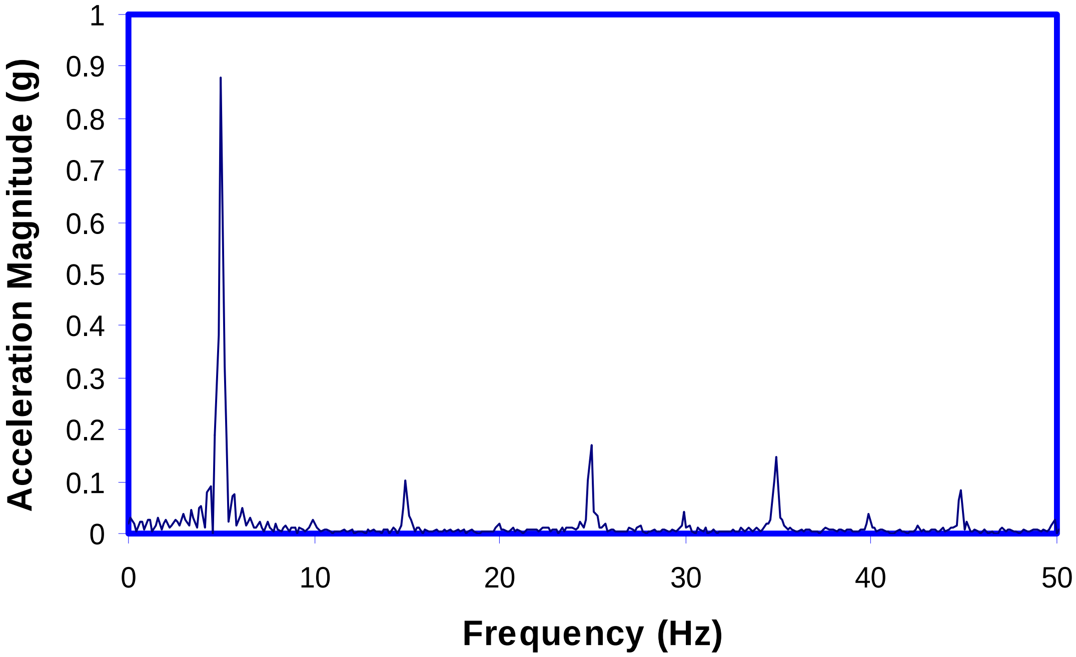

Figure 5-45: Frequency spectra of the measured imposed acceleration of 1g. The "true" acceleration of 5Hz is infused by higher frequency noises which can be removed by filter with 10Hz cut-off frequency.

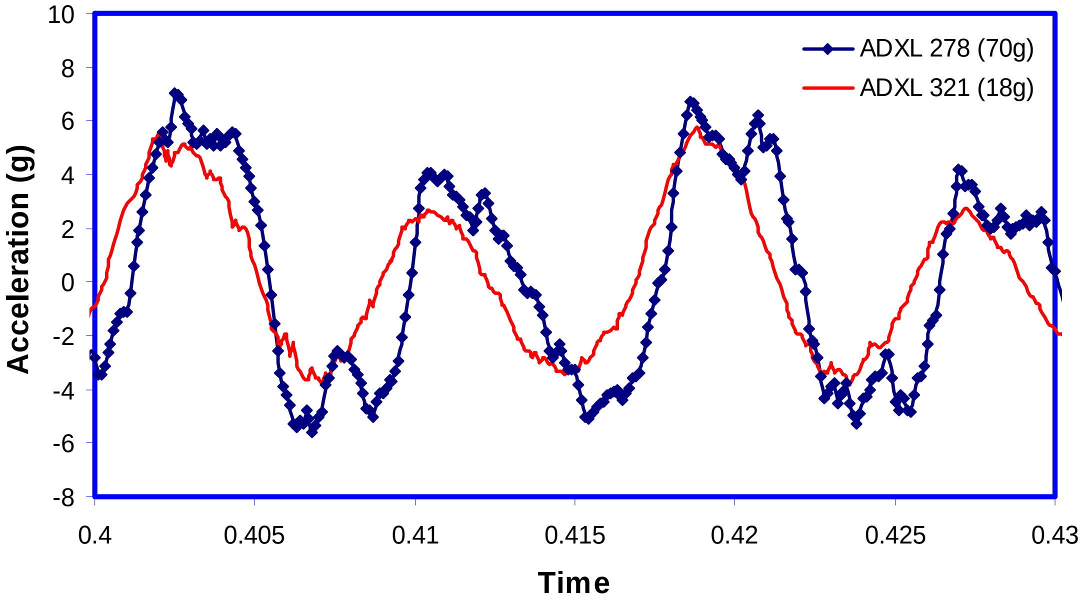

Figure 5-46: Horizontal shaking of ADXL 278 (70g) and ADXL 321 (18g) using a high frequency shaker of 120Hz. Filter cutoff of 400Hz is applied to ADXL321 (18g) whereas ADXL 278 (70g) has an internal filter of 400Hz.

5.3.3.1 Effect of temperature

The accelerometers have very good temperature compensation and are insensitive to variations in temperature. 13 accelerometers shows an average of 0.02V (20mV) of offset change over a range of 100C temperature change and this corresponds to a total 0.057g (Figure 5-47). The temperature offset can be classified as 0.00012mV/V/C change. Hence, in a daily temperature cycle of 10C, the temperature offset is 0.0012mV/V or 0.0057g, which is very small. For this application, temperature effect is also not important because train measurements are only conducted over a period of few seconds and temperature is relatively constant within that time frame.

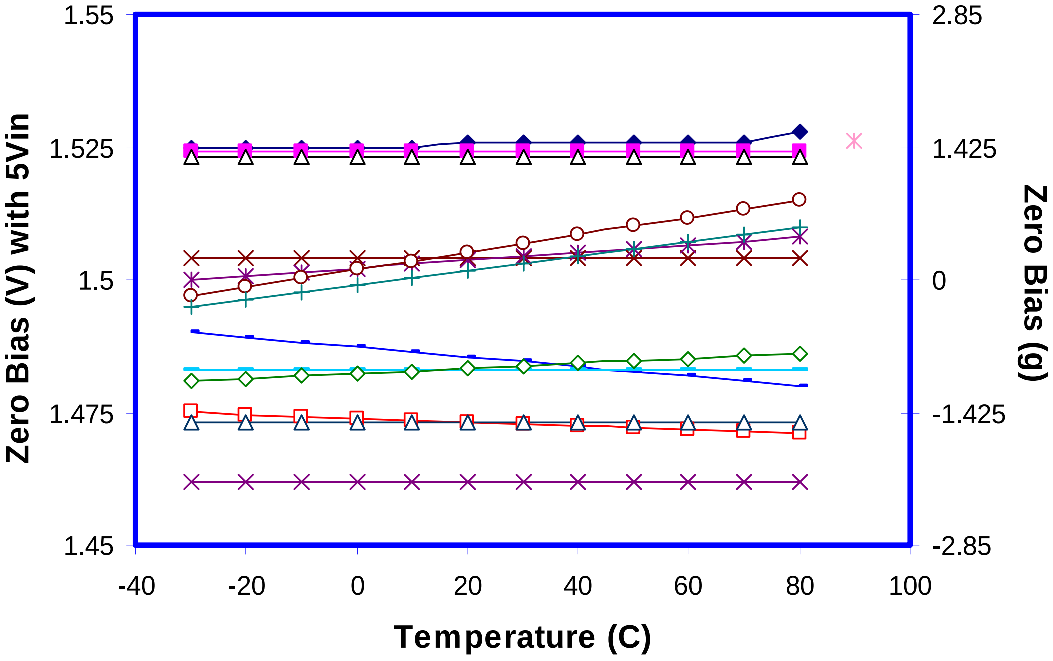

Figure 5-47: Zero Offset vs temperature for 13 accelerometers (Manufacturer's specifications).

5.3.4 Butterworth Filter applications

For signals which are contaminated with high frequency noises, low pass digital filters such as Butterworth filters can be used to remove the noises. A plot of Butterworth filters with different orders are shown in Figure 5-48 and 5th order filters are found to offer sufficient resolution. The Matlab code for creating a 5th order Butterworth filter and applying to the signals are shown in Appendix 5.

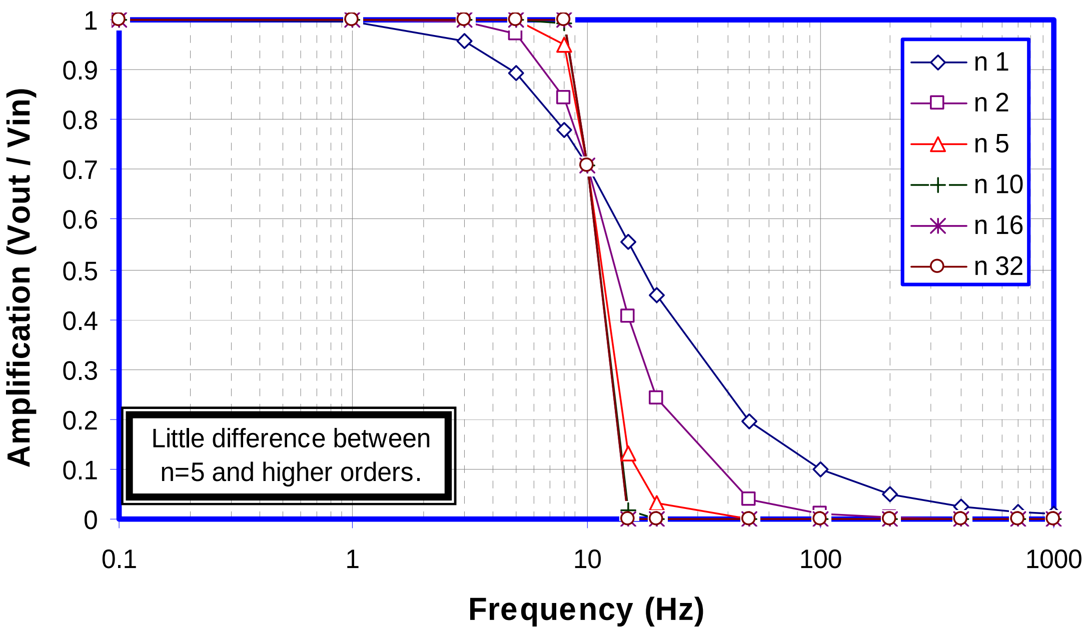

Figure 5-48: Comparison between different orders of low pass Butterworth filters with 10Hz cut-off frequencies. There are little differences between 5th order filters and high order filters.

5.4 Temperature Sensor

The atmospheric and ground temperature can be measured using Omega 44005 thermistors. The thermistor is made of #32 tinned copper wires, and has a working temperature range of –60 to 150C (Figure 5-50). The thermistor can be arranged in a differential circuit (Figure 5-49) and produces single-ended voltage output. The thermistor changes resistance with temperature. Since the resistance changes are uniquely correlated with absolute temperature, a unique calibration curve can be obtained from the output voltage (Figure 5-49).

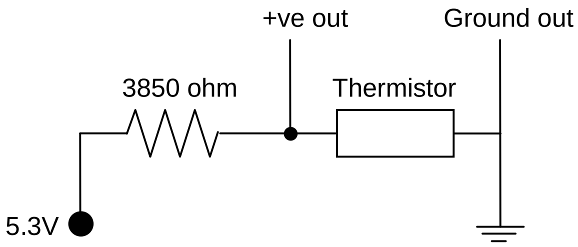

Figure 5-49: Circuit for single-ended thermistor output

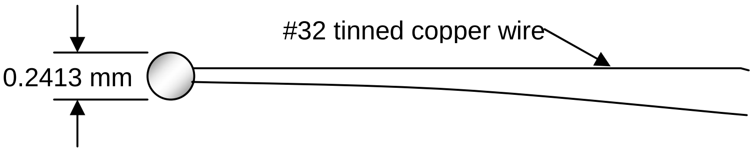

Figure 5-50: Omega 44005 thermistors (3000 ohm at 24C).

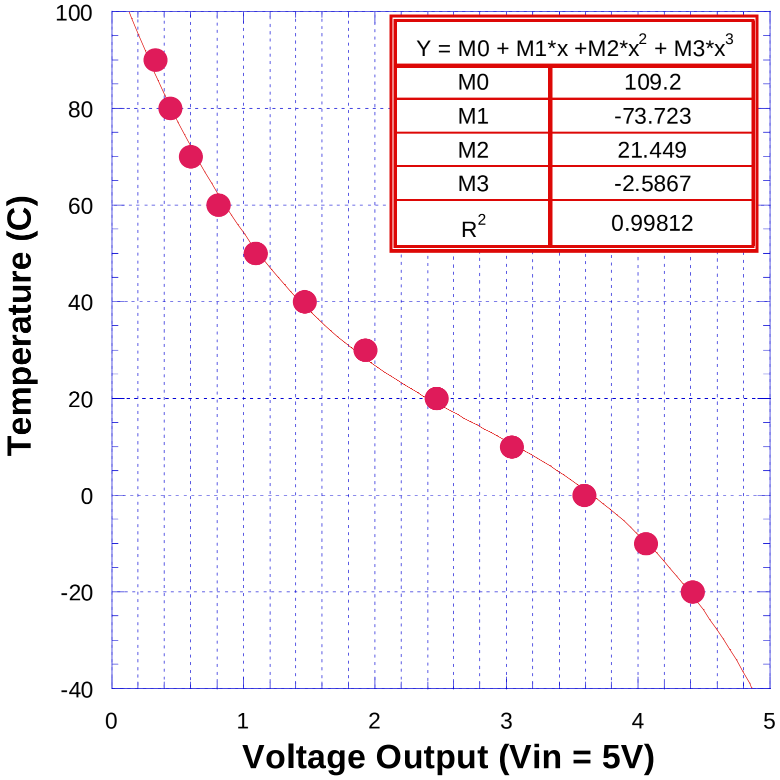

$Y = M0 + M1*x + M2*x^2 + M3*x^3$

M0	109.2
M1	-73.723
M2	21.449
M3	-2.5867
R^2	0.99812

Figure 5-51: Calibration of the Thermistor

Chapter 6: Field Installation

6.1 Introduction

This chapter describes field installation of the wireless monitoring platform and the sensors at the high speed railway line with recurring mud pumping problems. The selected site is located near the Mansfield (MA) train station which is heavily used by Amtrak's high speed Acela, Regional, and MBTA commuter trains. The field installation schedule window is set at spring / early summer of 2006 to avoid the frozen ground of winter and yet early enough to capture active track degradation during spring and summer. The field installation is carried out in three different phases. The first two phases involved field installation of sensors using commercial data acquisition (high speed data acquisition Iotech Wavebook and high resolution Iotech Personal DAQ). The wireless monitoring platform is introduced in the third phase as a proof-of-concept platform for Amtrak's monitoring program. The platform obtains data from welded strain gages and temperature sensors which has no bearing to the mud pumping problem but is of vital interest to Amtrak, thus demonstrating the versatility of the generic monitoring platform.

6.2 Installation of sensors (Phase 1 and 2)

A total of 11 sensor boxes (accelerometers, settlement probes, piezometers and temperature) were installed at Mansfield site (Figure 6-1) and described in Table 6-1. The sensors were installed at two locations (problematic and reference) and three depths (tie, ballast/subgrade interface, and deep subgrade). The problematic location is marked by high vertical tie displacements (due to formation of gap below the ties) and the stable reference by rocking motions (to accommodate the nearby high-displacement problematic site). The embedded sensors were connected to wayside instrumentation box via buried plastic BX cables (Figure 6-2).

The field installation at a busy high speed line required greater logistical and safety planning than low traffic TTCI heavy axle load test track (Aw 2004), including personnel safety training prior to field installation. The field installation was divided into two phases in order to simplify logistical process. The first phase (trial run) involved installation of wayside instrumentation box and track surface sensors (accelerometers and settlement probes on top tie). The performance of the sensors were evaluated for three weeks before commencement of more demanding phase two that would involve installing sensors in deep subgrade. The field installations are planned such that they are:

1. easy, quick (installation in 3 hours) and require minimum crew.
2. does not disrupt busy train traffic at approximately a train every half an hour.
3. does not require heavy machinery and dismantling of the track.

Table 6-1: Locations and labels for the sensors.

Location	Elevation	Sensor	Name
Problematic	Top of tie	Settlement	PT-S
		Accelerometer	PT-A70g
			NT-A18g
	Ballast/sub	Accelerometer	PBA-5V
		Piezometer	PBP
		Settlement	PBS
			PBS-Temp
	Deep	Piezometer	PDP
			PDP-Temp
Reference	Top of Tie	Settlement	NT-S
			NTS-Temp
		Accelerometer	NTA-18g
		Piezometer	NBP
	Ballast/sub	Accelerometer	NBA-5V
			NBA-5H
		Piezometer	NBP
		Settlement	NBS
	Deep	Piezometer	NBP

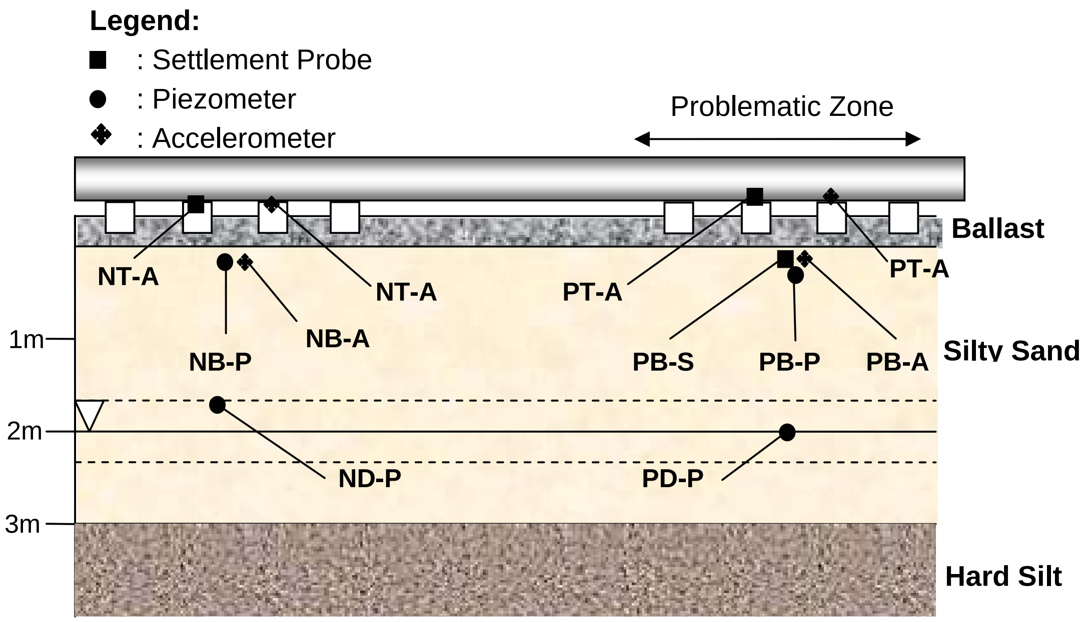

Figure 6-1: Schematic location of the sensors and the corresponding sensors notation. The reference zone and the problematic zone are located at about 5 ties away (3m)

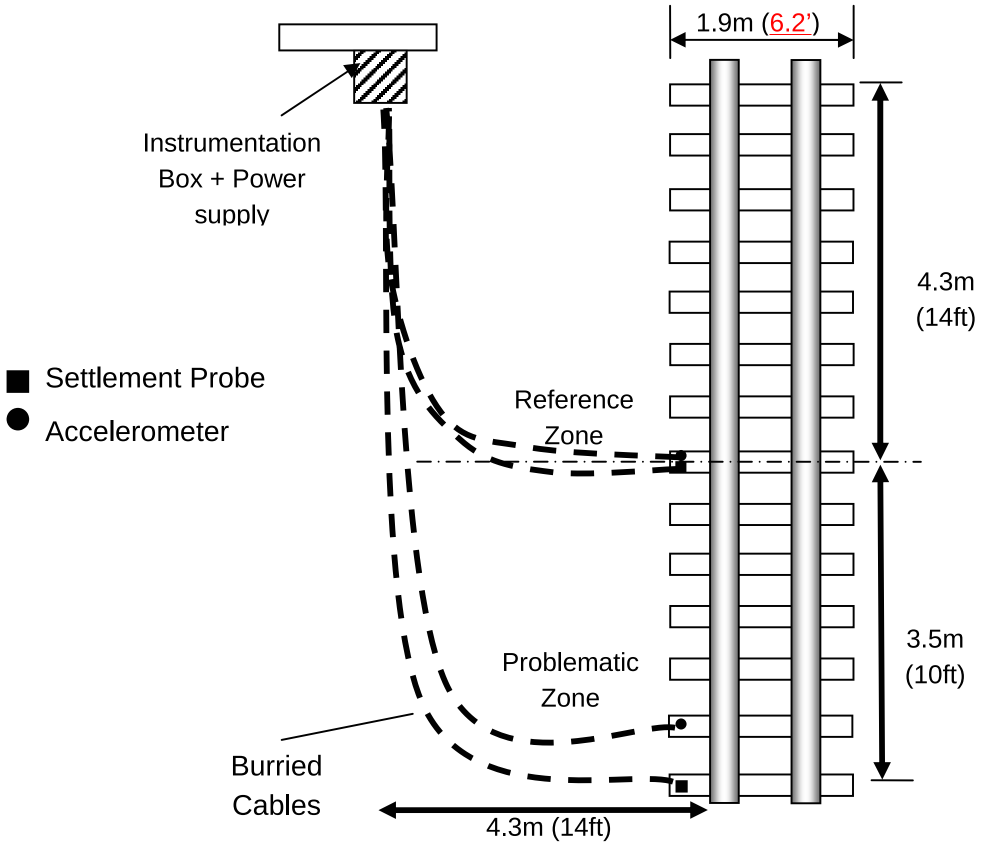

Figure 6-2: Plan view of the instrumentation layout.

6.2.1 Top of tie (Phase 1 Installation)

The first phase field installation was conducted on 10th May 2006 and took 3.5 hours (8am to 11.30am), encompassing installation of surface sensors (2 accelerometers and 2 settlement probes) and data acquisition. The working conditions were wet; it had been raining all week and had light rain during installation. The data acquisition and laptop units were housed in an instrumentation box and power supply (120Vac) were tapped from existing power source at the site.

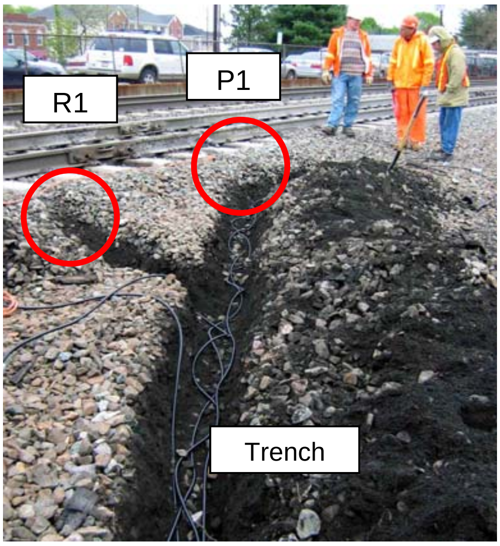

Figure 6-3: Trenches for installing sensor cables

Trenches up to one-foot deep were dug to bury the BX cables connecting the sensors and the data acquisition. The cables were buried for safety protection and to provide more constant temperature for temperature sensitive settlement probes. P1 and R1 referred to the problematic and reference zone (Figure 6-3). The trench was backfilled with existing materials after cables were installed. During trenching, the subgrade was found to be moist but not ponded. The problematic spot, was, however, noticeably wetter. During passage of trains, fine materials were splashed out of the ballast and ponding were seen temporary when the suspended tie settled under wheel loading.

The four sensor boxes would be attached to the top tie using epoxy. Since it had been a rainy week, there were concerns epoxy would not be able to bond well with the concrete ties. In order to simulate wet concrete, a gypsum block was presoaked in water for ten minutes and a sample sensor box was epoxy on it. Preliminary test showed that epoxy was able to form strong bonds with the wet porous gypsum block. Therefore, the epoxy should work with concrete ties too.

Prior to installation of the sensors, the surface of the wet concrete tie was dried using hot air blower. The epoxy (available at most hardware stores) was applied to the boxes and concrete tie (Figure 6-4a). It was allowed to set for 10 minutes. A layer of silicone protection was applied on the sensor to protect the epoxy from weathering (Figure 6-4b) and the sensor is now ready for usage (Figure 6-4c).

Figure 6-4: a) the epoxy was allowed to harden during the 10 minutes setting time, b) application of silicone spray to protect weathering of epoxy, c) final working stage of the sensor.

6.2.2 Installation under ballast and subgrade (Phase 2 Installation)

The second phase installation took place on the 16th June 2006 and took four hours of trenching, sensor installation, backfill and wiring to the data acquisition. Trenches were dug on the same location as first phase installation (Figure 6-5).

Figure 6-5: Trench digging

Installation of deep piezometer

The piezometer was installed at a depth of 1.92m (problematic area) and 1.44m (neutral area) from the top tie. A one man auger was used to create the hole in the ground (Figure 6-6). The zero reading for the piezometer (in vertical orientation) was taken before placing the piezometer into the hole. The hole was backfilled with a few inch of original subgrade material and compacted to ensure piezometer was in full contact with soil for optimum water pressure measurement. The hold was then fully backfilled with original ground materials (Figure 6-7).

Figure 6-6: Augering until 1.8m depth for deep piezometer installation.

Figure 6-7: Backfilling the piezometer with Insitu soil filling.

Ballast/subballast interface sensor installation

The ballast between the ties was excavated by shovel. Amtrak safety regulations prevented sensor boxes from being installed directly under the tie. The piezometer was installed in a horizontal manner. The piezometer tip was backfilled and compacted. The accelerometer (and settlement probe for the problematic area) was placed on top of the piezometer (Figure 6-8). Train operation was allowed to continue despite partial removal of the ballast.

Figure 6-8: Placement of sensors between the ties at the ballast-subgrade interface.

The sensors were backfilled with subgrade material up to 1.5cm on top of the sensors. Ballast gravels were then backfilled. Since no major excavation was done, no rail compaction was required.

6.3 Visual condition of the track

During the excavations, the ballast was found to be extremely fouled (Figure 6-9). Subgrade materials had fully penetrated the ballast and subballast layer was not found. In addition, gaps between the base of the tie and ballast were found at the problematic area (Figure 6-9a). The problematic tie was suspended through rail actions. During wheel loading, the suspended tie was hammered on to the ballast, creating high dynamic forces. These actions were witness during the excavations. The ballast extends about 18cm from the bottom of the concrete ties.

Figure 6-9: a) Fouled ballast between the concrete ties at the problematic area, b) Installation of sensors just below the fouled ballast.

6.4 Installation of the wireless monitoring platform (Phase 3)

The WSN platform is currently used as a proof-of-concept, taking measurements from rail strains and temperature which are of great interest to Amtrak, but are not related to the mud pumping problem. The WSN platform installed on 9 April 2007 consists of one sensor node that has two active channels (accommodating strain gages and a thermocouple at channels 0 and 1 respectively) and a base station. In this first attempt at field operation, the base station and the sensor node are both placed within instrumentation box (protection from weather) and powered using on-site power supply. The data is collected at rate of once every 10 minutes for 10 seconds. The collected data is sent to server at MIT via long range communication GPRS. The GPRS card was powerful enough to send signals through the metal instrumentation box.

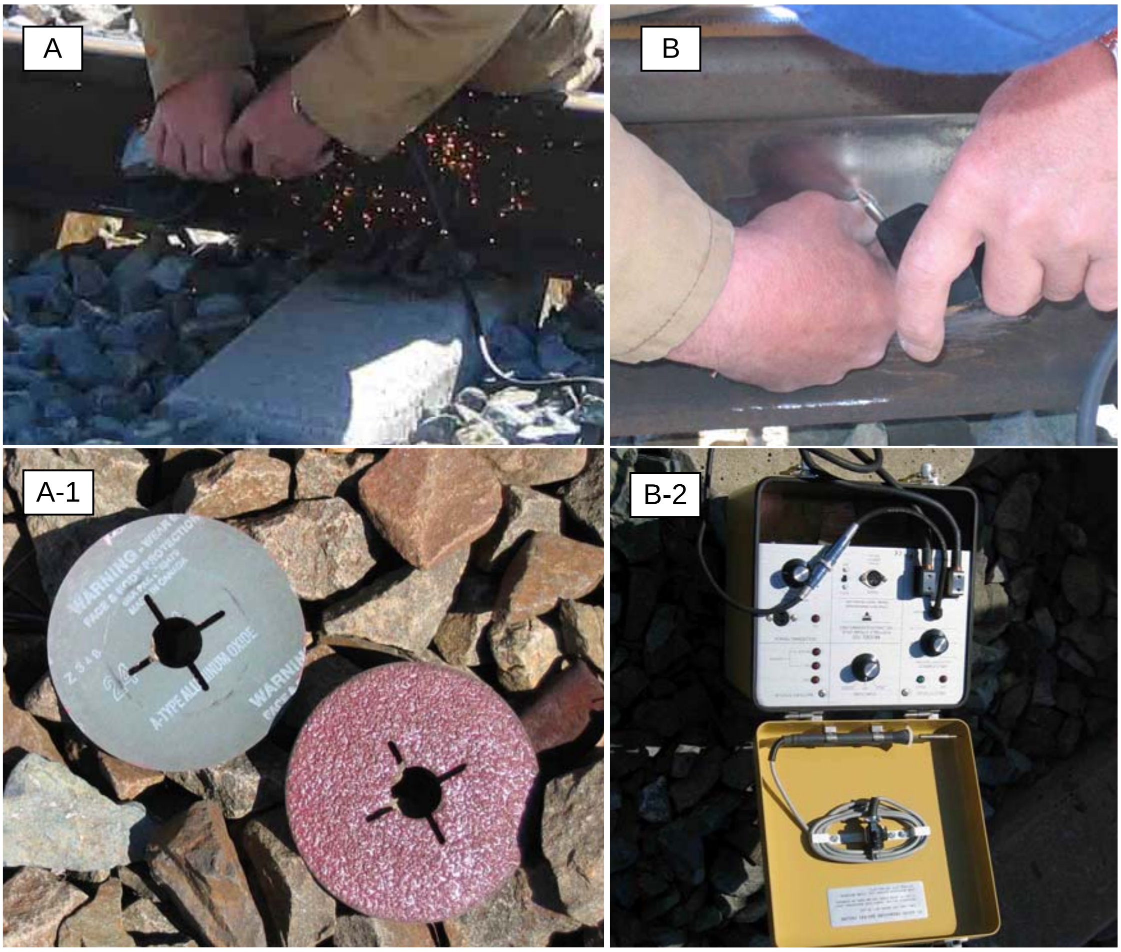

Figure 6-10: Installation of strain gage and thermocouple on the rail. Firstly, the rail surface is grinded (A) using aluminum oxide sand paper (A-1). Strain gage on metal plates were spot welded (B) onto the rail using portable battery operated spot welder (B-2).

6.4.1 Installation of strain gages and thermocouples

A total of two set of strain gages were installed on both sides of the rail. The thermocouple was installed on the outside of the rail. The second thermocouple was installed at the instrumentation box for measuring ambient temperature. Prior to installation of the sensors, the surface of the rail was polished using coarse grained aluminum oxide[16]. The strain gages and thermocouples were welded onto the rail using battery operated spot welder (Vishay Measurements Model 700). The spot welder applied high current and energy of 3 to 50 joules which is sufficient to melt and fuse the strain gage and rail. The surface preparation and installation is shown in Figure 6-10.

The strain gages were arranged in half Wheatstone bridge arrangement. Two of the strain gages were aligned in direction parallel and perpendicular to the rail which made up first half of the Wheatstone bridge. The second half of Wheatstone bridge consisted of two 350ohm resistors. The signal from the Wheatstone bridge was amplified using 1000 gain amplifier before feeding into the wireless sensor node. The active amplifiers were installed at the instrumentation box. The welded configuration and final protection form of the strain gages and thermocouple is shown in Figure 6-11.

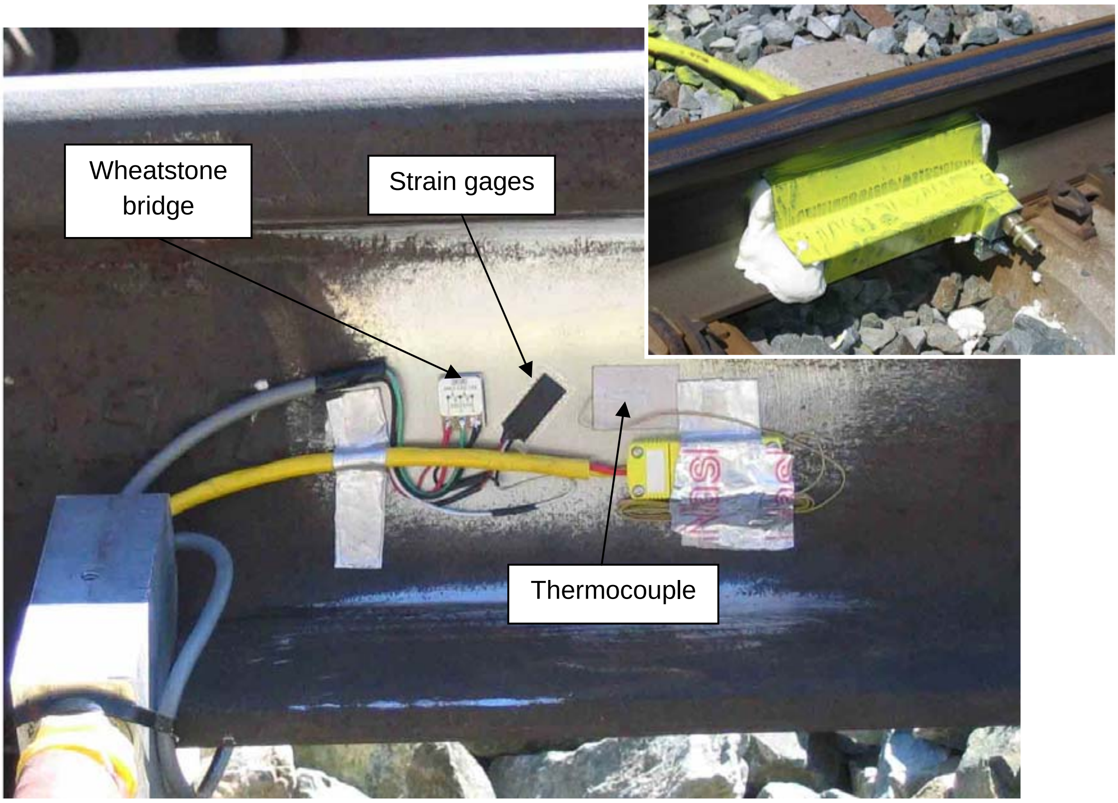

Figure 6-11: Arrangement of the welded strain gages and thermocouple on the rail. The sensors were protected by clamps and waterproof foam in the final form (inlet).

---

[16] The aluminum oxide disintegrate at high heat (during polishing) to create new surface for further polishing.

Chapter 7: Results of Field Measurements

This chapter presents field results from the track sensors (mud pumping) and wireless monitoring platform (rail strain and temperature). The track sensors were installed over two phases (surface sensors on May 2006 and embedded sensors on June 2006). Field data were collected for a year (until May 2007) which spanned all four weather seasons and three track maintenance cycles. The high frequency data collection was collected once a week until an upgrade of data acquisition[17] on 22 February 2007 enabled automatic data collection for every train (Table 7-1). The long-term data collection system (piezometer, temperature sensors) was continuously in operation until end of February 2007, except for two periods due to laptop failures between 10 Aug to 12 Oct 2006 (days 50 to 114) and 9 Nov to 22 Dec 2006 (days 140 to 183).

The performance of low cost prototype sensors is evaluated in terms of robustness and long term performance in harsh railway environment. The low-cost accelerometer chips are extremely robust and survived one year of field monitoring. Halfway through the data collection period (i.e. October 2006), two of the accelerometers were brought back to MIT for calibration. There was very little deviation offset and calibration factors from the pre-field installation values. However, the fabrication process can be improved: three out of the four accelerometers were detached from the sensor box due to failure at the epoxy/box interface and is addressed by the application of more epoxy. As for the piezometers, three out of four sensors performed well (maintained saturation) for six months after installation. The piezometer installed at the deep problematic location failed two weeks after installation (output voltage registered full range of 5 V). All of the three settlement probes did not meet design expectations and failed at the pressure transducer and liquid-filled tubing connection. High dynamic vibration from the trains caused slippage of the plastic tube from the transducer port and future design should include more robust tubing connections. This is, however, a simple design flaw that can be fixed.

7.1 Track acceleration measurements

Track acceleration response for all three types of trains (Acela, Regional, and MBTA Commuter Rail) at two different locations (problematic and reference zone) and depths (tie and just below the ballast/subgrade interface) are captured using high speed data acquisition. Parametric studies found that sampling frequency of 10 kHz is ideal in capturing individual wheel acceleration profile of the high speed trains and over a thousand track acceleration data have been obtained. The following sections (7.1.1 and 7.2.1) show typical track acceleration profile for all three trains.

---

[17] Iotech Personal DAQ/3000 allows automatic triggering and data saving after each sampling event.

Table 7-1: High speed data collection of the instrumentation program

Date	File Reference	Problematic Area						Reference Area					Comments
		Tie		Subgrade				Tie		Subgrade			
				Top			D*			Top		D*	
		A	S	A	S	P	P	A	S	A	P	P	
10 May	F1a Regional F1b Acela F1c Acela F1d CRX	●	●					●	●				**Phase 1** – tie accelerometer and settlement probe added
17 May	F2a Regional F2b-MBTA F2c-Acela F2d-Acela F2e Regional	●	●					●	●				
14 June	F3c-Acela F3d Regional F3e-Acela	●						●					SP fluid tubing connections failed
26 June	F4b-Acela F4c-Regional F4d-Acela			●		●	●	●		●	●	●	**Phase 2** – accelerometer and piezometer added in top and deep subgrade
7 July	F5b-Acela F5c-Regional			●		●		●		●	●	●	Deep piezometer failed
17 July	F6b-Acela			●		●		●		●	●	●	
Track Realignment and Tamping													
27 July	F7d Regional			●		●		●		●	●	●	
2 Aug	F8c-Acela			●		●		●		●	●	●	
10 Aug	F9c-Local F9d-Acela	●	●	●		●				●	●	●	Repair PTA, PTS
6 Sep	F10b-Acela	●		●		●		●		●	●	●	Tube leakage of settlement probe
15 Sep	F11b-Acela	●		●		●		●		●	●	●	
12 Oct	F12b-acela	●		●		●		●			●	●	RBA de-bonded
18 Oct	F13b-CRX F13c-Acela			●		●		●			●	●	PTA de-bonded
27 Oct	F14b-Acela			●		●		●			●	●	
Track Realignment and Tamping													
2 Nov	F15b-Acela			●		●		●				●	RBP desaturated
9 Nov	F16b-Acela F16c-regional F16e-regional F16f-mbta			●				●				●	F16e regional coming from reverse direction. PBP shows fluctuated readings
29 Dec	F17-Acela			●				●				●	

Date	File Reference	Problematic Area						Reference Area					Comments
		Tie		Subgrade				Tie		Subgrade			
				Top			D*			Top		D*	
		A	S	A	S	P	P	A	S	A	P	P	
4 Jan	F18-Acela	●		●				●				●	Re-bond PTA
Track Realignment and Tamping													
18 Jan	F19b Acela	●		●				●				●	
31 Jan	F20b Acela	●		●				●				●	
16 Feb	F21b Acela	●		●				●				●	
22 Feb - 18 Mar	F22-New	●		●				●					New high speed data acq. capture all trains
5 to 9 Apr	F23-New	●		●				●					

Note: A = Accelerometer, S = Settlement Probe, P = Piezometer, D* = Deep

7.1.1 Acela: Full train acceleration measurements

Starting with the high-speed Acela trains, the typical track acceleration responses for the four instrumentation locations are shown in Figure 7-1 and Figure 7-2 for a ***deteriorated track***. The track acceleration responses are accented by impulse-type peak accelerations at the onset of wheel impacts (all 32 wheel-sets of the train) and relatively low accelerations between wheels. The magnitudes of wheel-induced peak accelerations vary with locations (problematic vs reference zone) and depths (top tie vs top subgrade) and will form the basis for discussions in the section below:

Reference Tie (bottom of Figure 7-1)

The track superstructure is designed such that the wheel-induced stresses are adequately dissipated through the ranks of structural components - starting with the rail, ties, and ballast – down onto the subgrade. The rail and ties, according to load transfer model of Esveld (2001), are primary stress dissipation components, shouldering up to 99.97% of the wheel-induced stresses. This is evident in the acceleration response of the tie at the reference spot, chalking up to high wheel-induced peak accelerations of ±10g. In general, the response of the track can be grouped into three phases: a) track response due to group effect of four closely-spaced wheels (i.e. bogies at end of two adjacent carriages), b) impulse-like peak accelerations due to wheel impact, and c) little or no accelerations at the middle of the carriages.

Problematic Tie (top of Figure 7-1)

The track acceleration response for the problematic tie is very much similar in nature to the reference zone: the collective four-wheel group effect, the impulse-like wheel impact, and the small accelerations at the middle of the carriage. However, the wheel-induced peak accelerations at the problematic tie are much greater than the reference tie, reaching up to ±15g and ±20g. This high wheel-induced acceleration magnitude can be attributed to the large tie displacements resulting from the cavity[18] between the ballast and the tie. The acceleration profile is measured using an accelerometer with ± 70g resolution.

Reference Top Subgrade (bottom of Figure 7-2)

The reduction of wheel stresses from the ties to the top subgrade level (below the ballast/subgrade interface) is manifested by the decrease in the magnitude of accelerations. The track response at the reference area is marked by contributions from the four-wheel group effects and impulse-like wheel impact accelerations. The magnitude of the peak wheel-induced accelerations, averaging at ±2g, is much smaller than the ±10g accelerations experienced at the reference tie.

Problematic Top Subgrade (top of Figure 7-2)

The wheel-induced acceleration magnitude for the top subgrade at ±4g is higher than that of the reference top subgrade (±2g) but lower than the corresponding problematic tie (±20g). The high acceleration response of the problematic tie is triggered by the action of ties slamming onto the ballast and the underlying subgrade.

The four track acceleration response presented above provides a general idea on how the wheel-induced accelerations at the ties (bigger in magnitude for the problematic area than the reference) are transmitted down onto the subgrade level (also bigger in magnitude at the problematic area) when the track is at a deteriorated stage. The next section will compare the difference in track response between the newly maintained stage and the deteriorated stage.

---

[18] The cavity between ballast and the tie was visually confirmed during the second phase installation of the sensors.

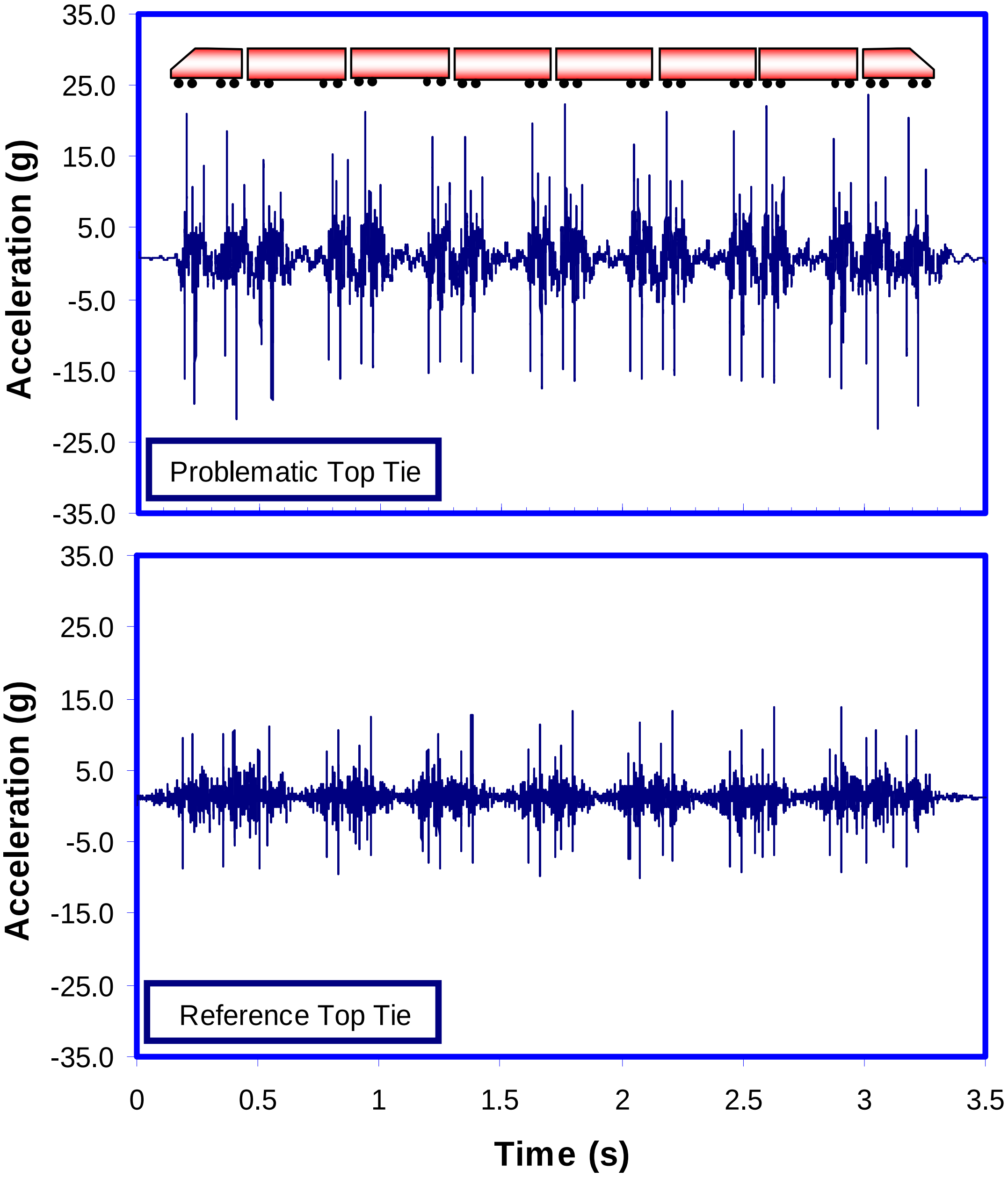

Figure 7-1: Tie acceleration in problematic area (top) and neutral area (bottom). File: F18d Acela

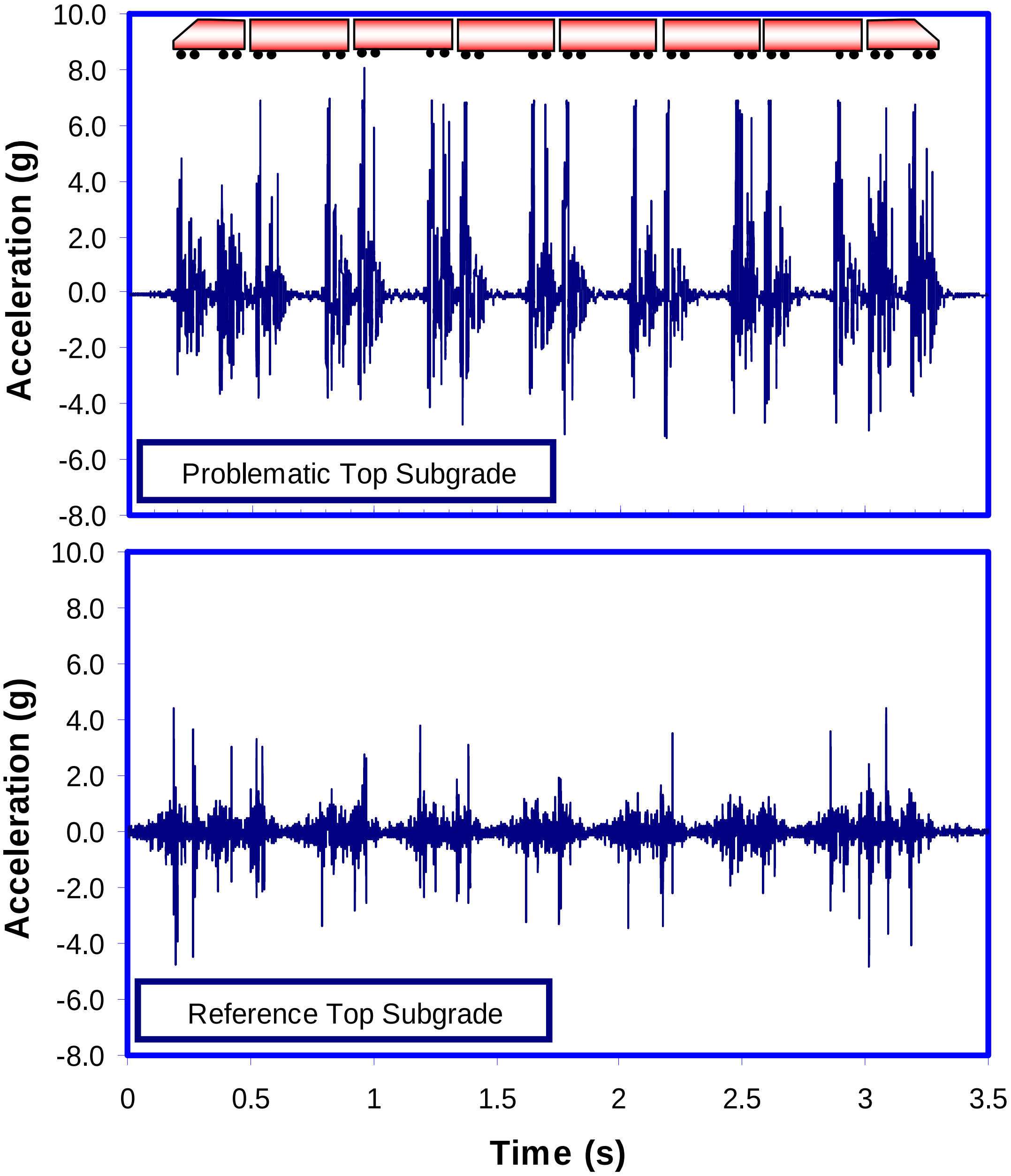

Figure 7-2: Subgrade-ballast interface acceleration in the problematic zone (top) and neutral zone (bottom). File: F18d Acela

7.1.2 Acela: Newly Maintained Stage vs. Deteriorated Stage

This section compares the acceleration response of the track after maintenance (ideal case) with the deteriorated stage for the problematic tie and the subgrade using wheel acceleration data from end bogies of two adjacent carriages to enable more detailed comparisons.

Newly Maintained Track (1 week after maintenance)

1. Problematic tie response (top of Figure 7-3)

   The track was realigned one week prior to the response measurements and this represents the best-case scenario of track stability. The acceleration time-series response is marked by four strong wheel-induced peak accelerations with magnitudes at +7 to -10 g and indirect wheel responses at times 1.80 and 1.96 s (i.e. vibration of the instrumented tie due to wheels at distance roughly five ties after passing the instrumented tie). The group effect of four-closely-spaced wheels is not noticeable here; the foundation and track superstructure is stiff enough to support wheel loads and prevent excessive track vibrations.

2. Problematic top subgrade response (bottom of Figure 7-3)

   In contrast with the tie response, the top subgrade response has no obvious peak accelerations (i.e. impulse-like wheel induced accelerations) but has the influence of four-wheel-group effect. This group effect appears as uniform sinusoidal accelerations with magnitude of ±1.6 g and duration of 0.3 seconds. The uniform sinusoidal shape of the acceleration profile is a result a phenomenon known as tie action; the location of the wheel on or between the ties has different stress effect on the subgrade. In addition, the accelerometer is installed between two ties and is probably being influenced by both ties. The long duration is caused by overlapping of wheel-induced stress zones: the track superstructure spreads the wheel loads over a greater area in the subgrade and overlapping of these stress areas leads to prolonged group effect.

Deteriorated Track

1. Problematic tie response (top of Figure 7-4)

   The track response at the deteriorated state is illustrated by the partial time record of the train passage described in section 7.1.1 and is a snapshot of measurements from a largely unrestrained tie due to gaps between the ties and the ballast. Wheel passages induce impulse-like peak accelerations with greater magnitudes (-15 g to 12 g) and visibly noisier accelerations between the four wheels: the unsupported tie is now displacing even when the wheels are several ties away.

2. Problematic top subgrade response (bottom of Figure 7-4)
   The effect of the suspended ties slamming onto the subgrade is more pronounced at the top subgrade level. The dynamic wheel impacts translate to four distinctive peak accelerations (-6 to +5 g) in addition to the uniform tie actions seen during the newly tamped state (seven tie-action pulses in both states). Immediately after the passage of the fourth wheel, the seven tie-action pulses in the subgrade decayed (poorly damped) much slower in the deteriorated stage (time 2.07 to 2.12 s).

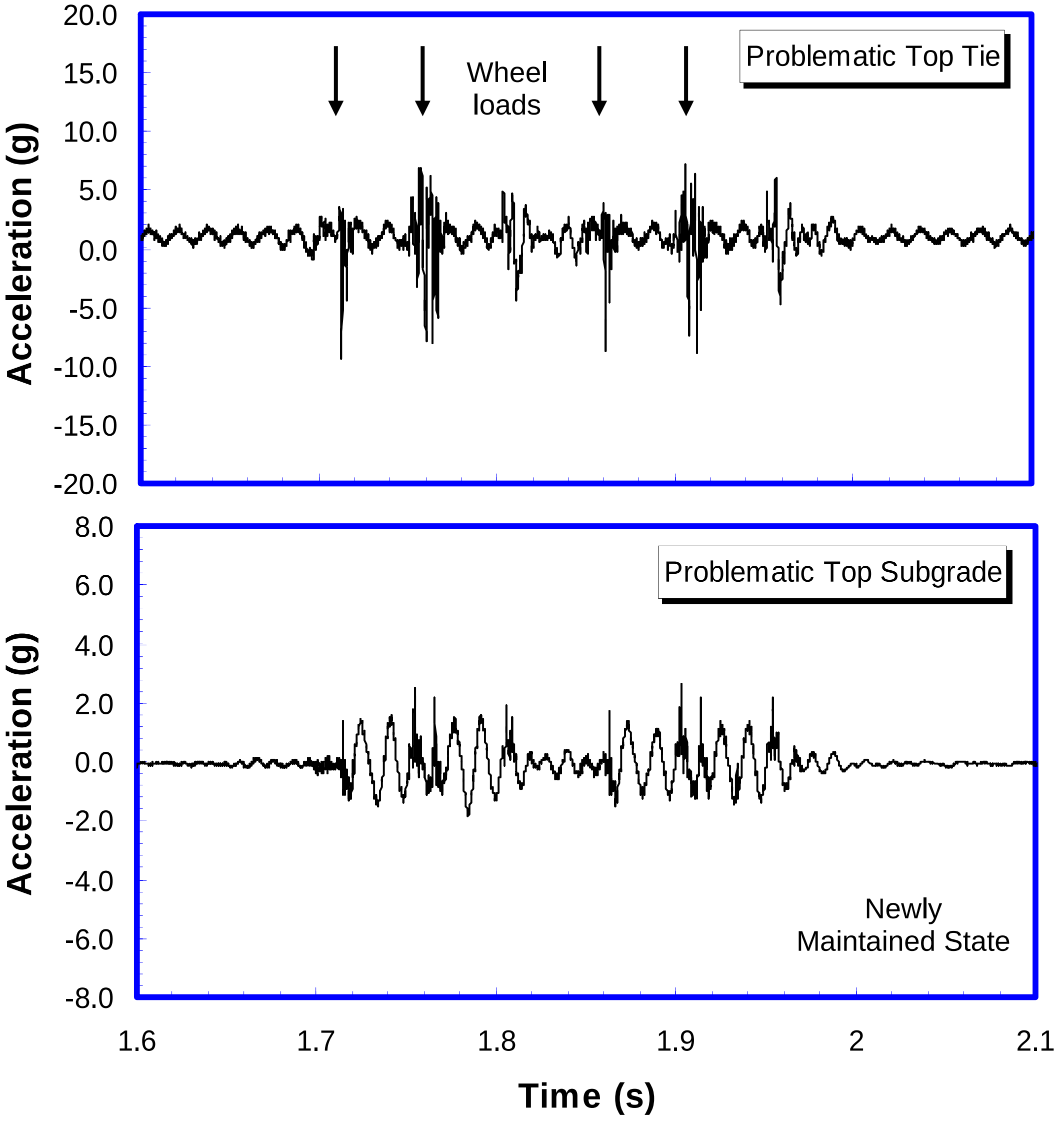

Figure 7-3: Bogies in adjacent carriages (total of four axle loads) in problematic tie (top) and subgrade/ballast interface (bottom) for Acela train. Data is obtained one week after a newly maintained track. (File: F20b-acela)

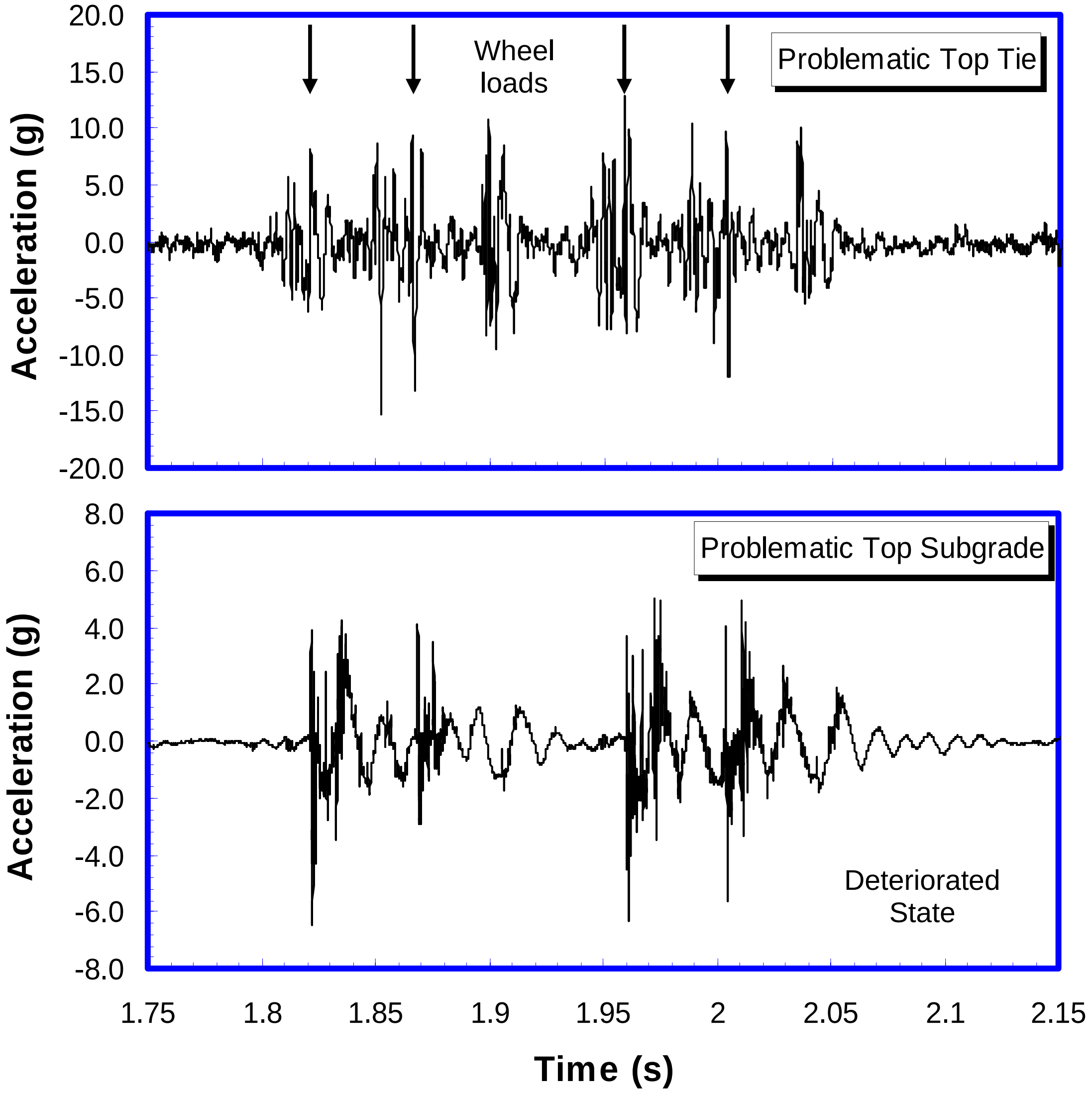

Figure 7-4: Bogies in adjacent carriages (total of four axle loads) in problematic tie (top) and subgrade/ballast interface (bottom) for Acela train. Data taken when track is at a greatly deteriorated stage (File: F12b-acela).

7.2 Frequency Response Spectrum

The track acceleration response can also be decomposed and plotted in the frequency domain using Fast Fourier Transformation techniques. The frequency response spectrum offers a convenient method of identifying components contributing towards track acceleration response. Figure 7-5 shows the frequency decomposition for problematic tie and top subgrade before and after track realignment. The y-axis represents the magnitude of the Fourier acceleration co-efficient[19]. As roughly determined from the acceleration time series, the track response at the top subgrade consisted of two loading sources; dynamic high frequency vibrations (> 70 Hz) and lower frequency tie actions. The tie actions are a result of the wheel imposing unequal loads on the subgrade depending whether it is on or between the ties.

The effect of having a suspended tie in the deteriorated stage was manifested in high frequency vibration and high very low frequency components. The high frequency components found at the tie (>88 Hz where 88 Hz was the fundamental tie frequency) represented high frequency track vibrations as a result of the unrestrained tie vibrating in space and slamming onto the ballast. These high frequency components are significantly reduced after track realignments as the ties are restrained. The low frequency components control the displacements. The addition of low frequency components at the tie and subgrade level during the deteriorated stage means that the instrumented tie and top subgrade are displacing and feeling the effects the wheel a few ties in advance prior to loading directly above the instrumented area. It is possible to determine the length of rail displacement profile on the rail caused by wheel loading through the measured low frequency components. At the instrumented tie, the full displacement rail length is between 3 ties and 5 ties and this corresponds to low frequency range from 15 Hz to 44 Hz[20] (Figure 7-6). This means the instrumented tie is feeling the effects of the wheel up to two ties in advance. In another words, the low frequency components determine the length of the displacement profiles. After track realignment, lower frequency spikes (below 50 Hz) were significantly reduced for both tie and top subgrade since the tie was now supported by underlying ballast and was not free to displace as easily.

---

[19] e.g. an acceleration sine wave with amplitude of 5 g and frequency of 10 Hz will appear as Fourier acceleration of 5 g spike at 10 Hz frequency

[20] The fundamental one tie length is measured from the center between to two ties to the adjacent center between two ties (Figure 7-6). The corresponding frequency is found by dividing the train velocity with effective length. Higher-order tie lengths are possible in the form of 3, 5, 7, and etc. ties.

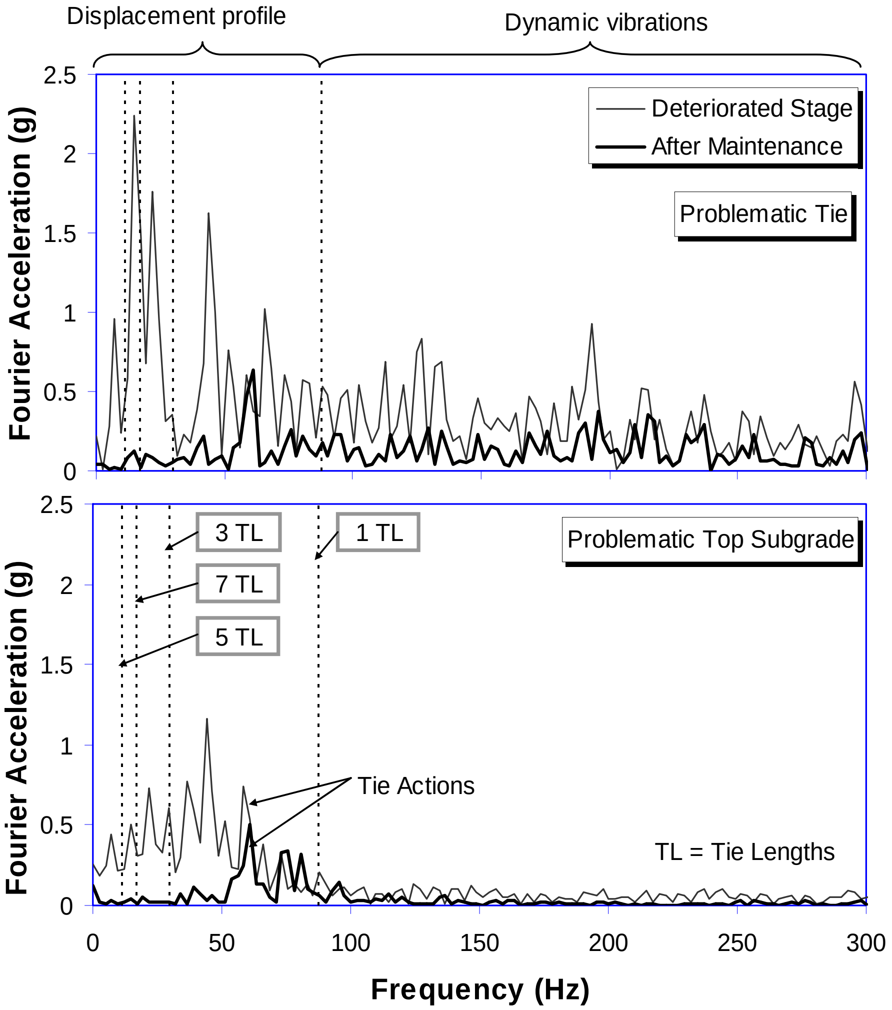

Figure 7-5: The frequency response of the track before and after tamping for bogies at carriages end of an Acela train (File: Train of F18 and F19)

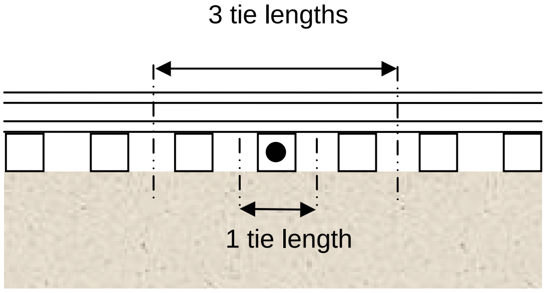

No. Ties	Tie Length (m)	Freq (Hz)
1	0.6	88
3	1.8	30
5	3	17.6
7	4.57	11.6

Figure 7-6: Schematic of the tie lengths and frequency. The measured tie width and spacing at the problematic area is 0.23 m and 0.37 m respectively.

7.2.1 Comparison between Acela, Regional and MBTA commuter

The track responses for the three different trains at the problematic top subgrade level within the same hour are shown in Figure 7-7. At this location, both Acela and Regional were operating close to their maximum speed (220 kph and 180 kph respective) while the MBTA commuter train was slowing down (<60 kph) in anticipation of the commuter rail station next to the instrumented site. The Regional train depicted in Figure 7-7b had a total of one engine and 8 carriages, although the passenger carriages have been found to vary from 6 to 8 carriages in general. The Acela train produced rather uniform wheel-induced peak accelerations of ±4 g. The Regional train produced more variable peak accelerations ranging from ±3 g to ±5 g, perhaps implicitly indicating the variable state of the wheel qualities. The MBTA commuter rail had the lowest peak accelerations averaging at less than ±1 g.

From these comparisons, it is clear that visual observations of the peak accelerations are difficult in providing an objective comparison between the three trains. As such, better tools for capturing the essence of train loadings are developed and described in Chapter 8.

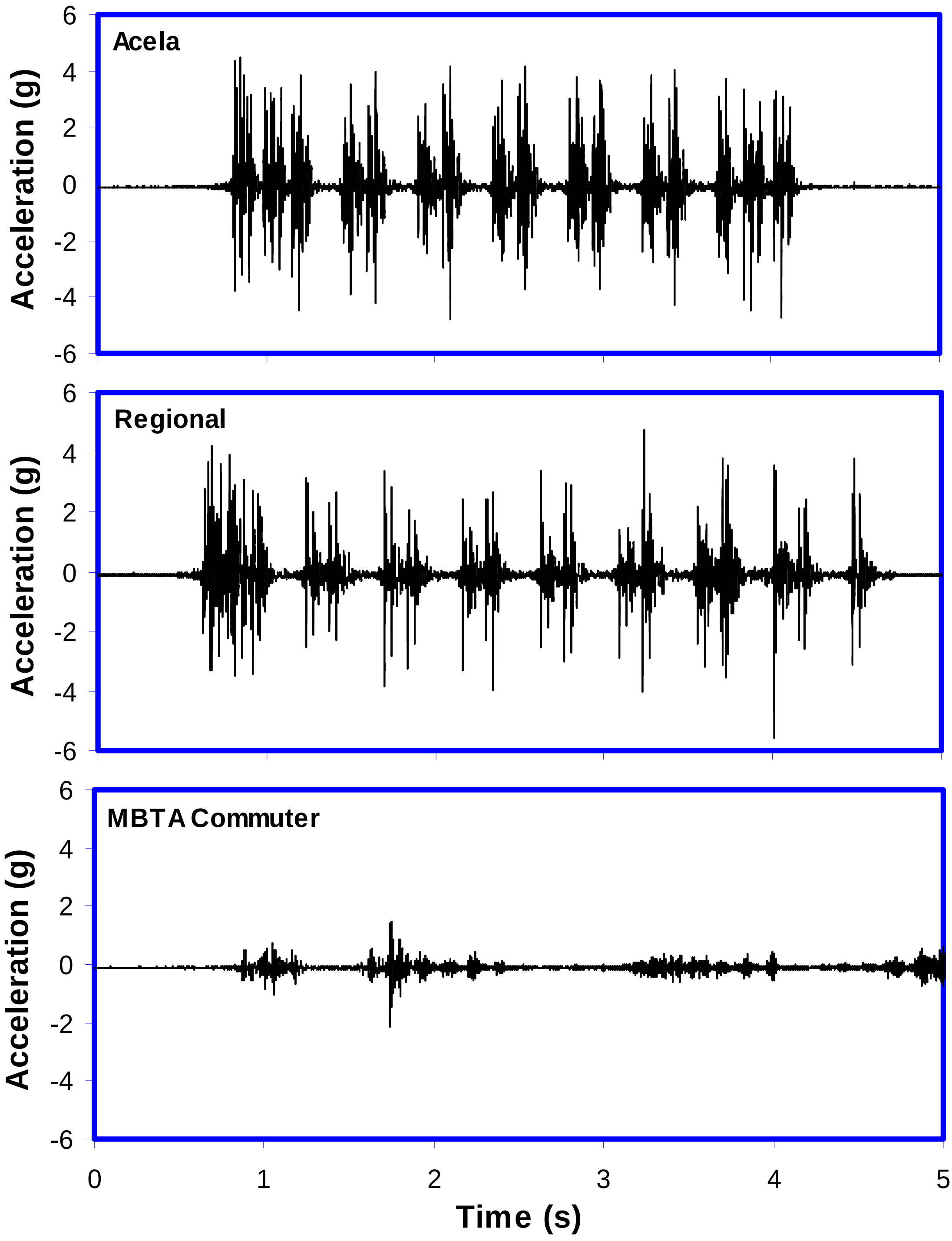

Figure 7-7: Measured accelerations in the problematic top subgrade for three different trains taken within the same hour (File: F16 Acela, Regional and MBTA). The MBTA shown is not the full train profile.

7.2.2 Measurements of Poor Wheel Geometry (Miscellaneous)

Poor wheel geometry refers to conditions including wheel flats (non spherical wheels as a result of wear and tear or abrasion[21]) and non-aligned wheel axles. One example of wheel flats captured by the accelerometers is shown in Figure 7-8. For average wheel-induced peak amplitudes of roughly ±0.5g, the single wheel flat registered ±4g which is eight times higher than the good wheels and has detrimental effect on track serviceability. Over the course of data collection, many trains showed uncharacteristically high track amplification on a single wheel on all four instrumented locations. Detection of wheel flats is extremely important in the railway industry and this instrumentation has the potential of offering low cost alternative: a single accelerometer installed at the top subgrade and data processing capable of picking out uncharacteristically high acceleration (either through threshold values or a few standard deviations from the average wheel loadings).

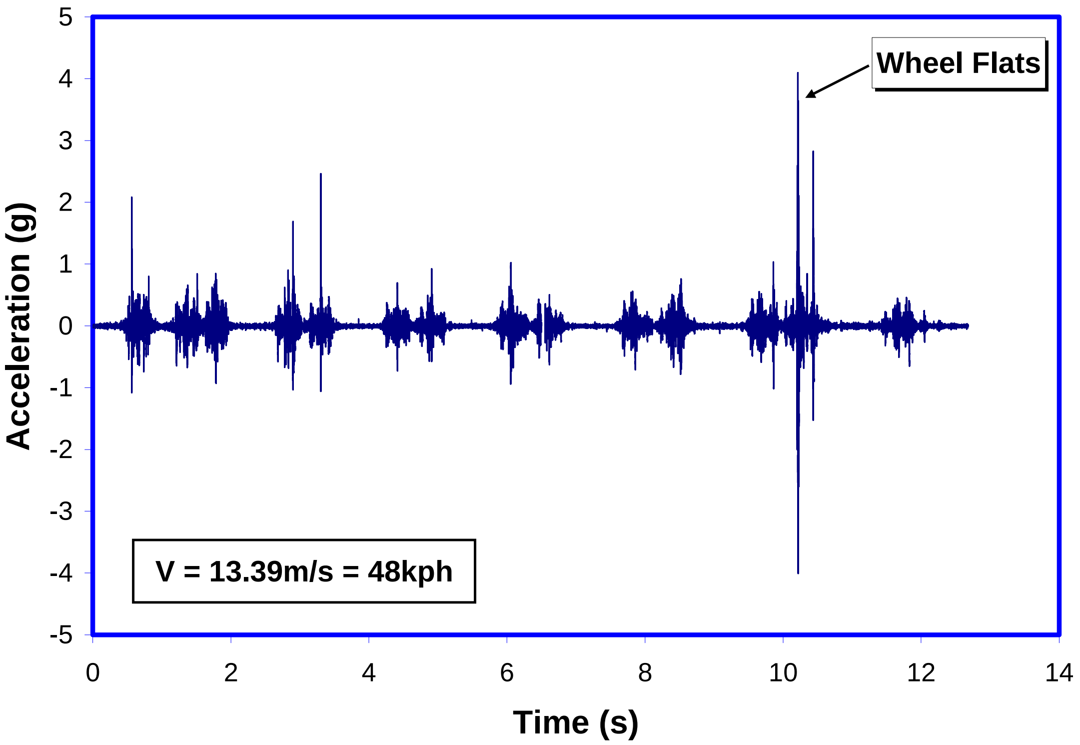

Figure 7-8: Measurement of Wheel Flats on a MBTA Commuter train at the problematic top subgrade (File F9c-Local). This is not a complete train profile.

---

[21] One of the common occurrence of wheel flats is caused by dragging of wheel-clamped carriages over long distance due to localized failure in brakes.

7.3 Track displacements

The acceleration data can be processed (i.e. doubly integrated) to reveal dynamic track displacements. Numerical integrations are employed, using the sampling rate as the governing time-steps. The first integration of acceleration to obtain velocity (with initial velocity as 0 m/s):

Velocity: $v_n = v_{n-1} + \frac{1}{2}(a_n + a_{n-1}) \cdot \Delta t$ ……………………(Equation 7-1)

Integration of velocity to find displacement (with first displacement as 0 m):

Displacement: $s = \frac{(v_n - v_{n-1})}{2} \cdot \Delta t + s_{n-1}$ …..(Equation 7-2)

where

a = acceleration (m/s^2); s = displacement (m); ν = velocity (m/s);
Δt = sampling time (s)

In reality, acceleration data obtained by accelerometers are subjected to various noises such as accelerometer's non-linearity, drift, baseline shifts, angular rotations (Boore 2001 & 2005) and low resolutions (e.g. data acquisition sampling resolution) such that direct integration often leads to erroneous and artificially high displacements. However, there are several widely used techniques available in obtaining reasonable displacements trends. Firstly, a low pass filter can be employed in removing high frequency noises. Secondly, baseline corrections can be applied at the velocity and displacement level to remove accumulated velocity and displacement error. Baseline corrections should be kept linear and are guided by known boundary conditions in that the velocity and displacements are zero at the middle of the carriages.

The integrated displacement profiles at the newly maintained problematic top subgrade for the three different trains are shown in Figure 7-9. Only the two end bogies of adjacent vehicles are shown and plotted on a normalized x-axis time scale (i.e. normalizing differences in velocity between the three different trains). The displacement profiles, given the generous leeway in baseline correction applications, should be taken as a guideline rather than absolute values. The MBTA commuter rail has the smallest displacement magnitude and downward subgrade displacements resulting from the two bogies were clearly seen. And in between bogies (i.e. center of the carriages), subgrade displacement returned to zero. The high speed Acela trains and Regional trains produce displacements that are four times greater than the MBTA trains. At less than half a millimeter of peak displacements, the subgrade undergoes very small displacements even for the high-speed Acela. For a deteriorated stage, peak displacements for Acela are 0.6 mm, which is in general still relatively small. The processing uncertainties arising from the back-calculated displacements present difficulties in pursuing further more detailed analysis of the dynamic displacement data. However, the back-calculated displacements can be improved by using smaller acceleration range (hence higher resolution) and higher resolution data acquisition system (smaller voltage input range[22]).

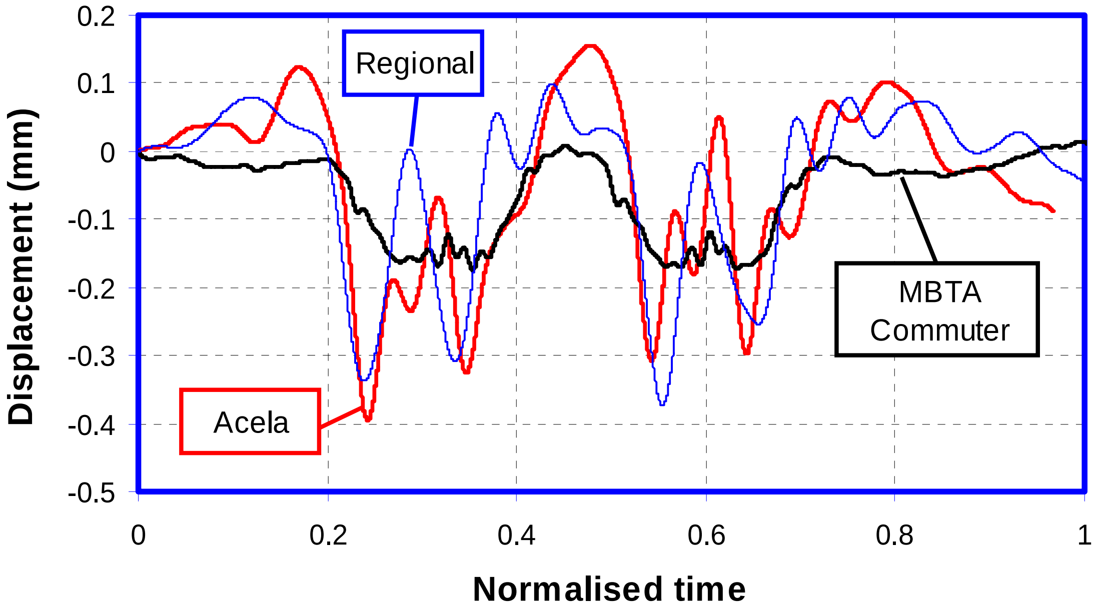

Figure 7-9: Comparison of the displacement profile at the problematic top subgrade for the three different trains (File F9 and F16). The accelerations are filtered using 40Hz filter before integrating for displacements.

7.4 Pore Water Pressure Measurements

The water pressures of three different scenarios are measured: a) long-term variations of the groundwater level, b) single shorter-term rain event, and c) dynamic train-induced pore pressures. The long-term water pressures and rain events are measured using the high resolution Iotech DAQ 55 at 10 minutes sampling intervals. The rainfall intensity is obtained from nearby Plainville weather station (www.wunderground.com). The dynamic train-induced pore pressures are measured using high speed Iotech Wavebook at 10kHz sampling rate. The piezometer installed at the problematic deep subgrade failed after a heavy rain. Therefore, only results from three other piezometers are presented in the

---

[22] The Iotech high-speed data acquisitions only allowed a fixed input range of ±10V.

following sections. The zero readings of the piezometers were based on the readings above ground and the tips were submerged beneath the water surface.

7.4.1.1 Long-term variation in groundwater level

The long-term variations of the pore pressures measured at three locations are shown in Figure 7-10. The piezometer installed at the reference deep zone (1.4m below tie) measured a negative head of -25cm[23] at the start of the summer (day 20.0 in mid of Figure 7-10). At the top subgrade, piezometers installed at the problematic and reference zone measured negative head ranging from -150cm to -134cm (top of Figure 7-10). Over the course of summer and fall, the deep piezometer measured an increase of pressure head to positive 7.5cm even though there was little change of pore pressure measured at the top subgrade level. The positive change in pore pressure measured at the deep subgrade suggests that the in-situ water table rose over the summer, most likely due to frequent rains over summer (bottom of Figure 7-10). The period of no-data between days 50 to 110 was due to a combination of frequent laptop failure from overheating (extreme high temperatures during summer) and track safety license renewal.

The in-situ groundwater level can be estimated by plotting a linear hydrostatic line through the pore pressure readings obtained from the deep piezometer and the intersection between the hydrostatic line and the zero pore pressure line is the groundwater level (Figure 7-11). The groundwater table is estimated at -1.7m in summer and -1.36m in fall. If the linear hydrostatic line is extended from the pore pressure measured by the deep piezometer in summer to the top subgrade elevation, it intersects with the pore pressures measured by the two top subgrade piezometers. This suggests that the top subgrade has a healthy matrix suction driven by full capillary rise from the ground water level and there is no evidence of a perched water table within the subgrade. The perched water table[24] (ponding) would have shown up as positive pore pressures at the top subgrade.

The small increase of in-situ water level in the deep subgrade is not felt at the top subgrade; the partly saturated nature of the top subgrade meant that it is insensitive to the small variations in the groundwater table. The small variation of groundwater level throughout summer and fall was consistent with nearby groundwater well documented at Atterboro (Figure 2.6).

---

[23] Pore pressure head is obtained by dividing the pressure (kPa) measured by the piezometer by unit weight of water (9.81 kN/m^3).

[24] Perched water tables are usually caused by layers of impermeable soil

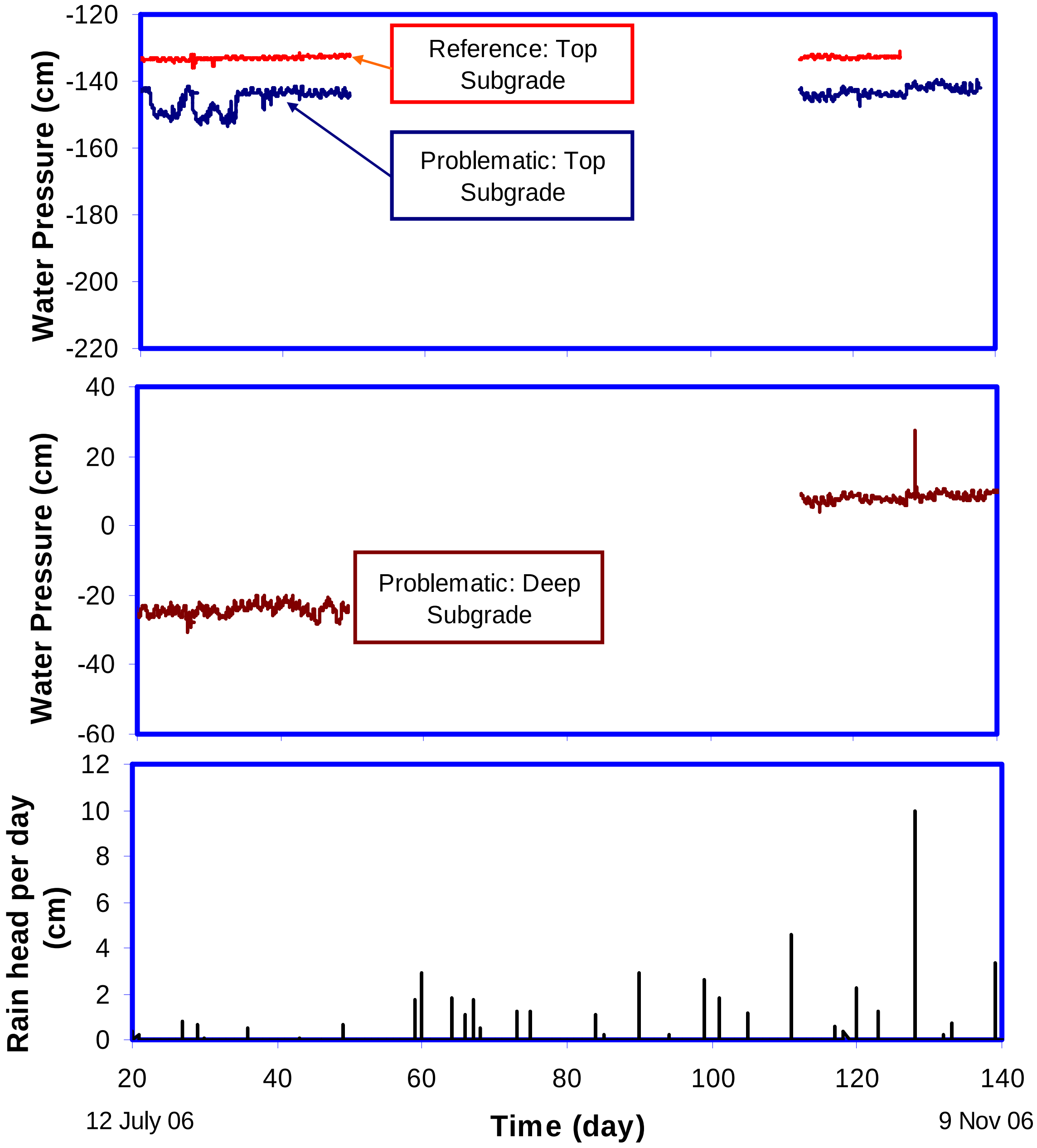

Figure 7-10: Problematic and reference top subgrade (top). Reference deep ground water level (mid). The rain data is obtained from a nearby station at Plainville (www.wunderground.com)

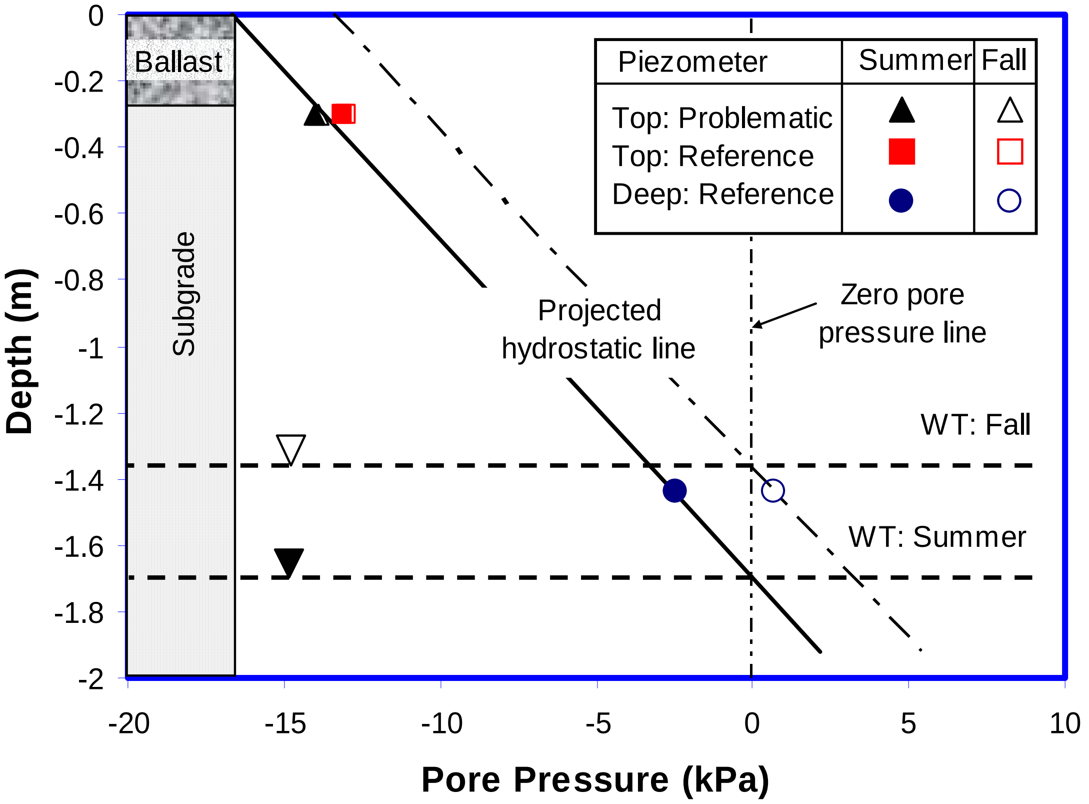

Figure 7-11: Changes in the estimated groundwater table (WT) and matrix suction at the top subgrade from summer to fall.

7.4.1.2 The effect of rain on matrix suction

The long-term pore pressure data described in the previous section shows that the top subgrade is always under matrix suction and there is no evidence of positive pore water pressure build-up. This section explores a shorter period of the subgrade response to one rainfall event. The rain event with duration close to a day was recorded[25] on the 128th day (28 August 2006). The piezometer at the top subgrade measured a small rise in pore pressure (change of 2 cm) while the deep piezometer measured a sharp but temporary rise of 20 cm. This observation further suggests that the rain merely replenishes the matrix suction upon infiltration into the subgrade.

---

[25] Weather station for city of Plainville (www.wunderground.com)

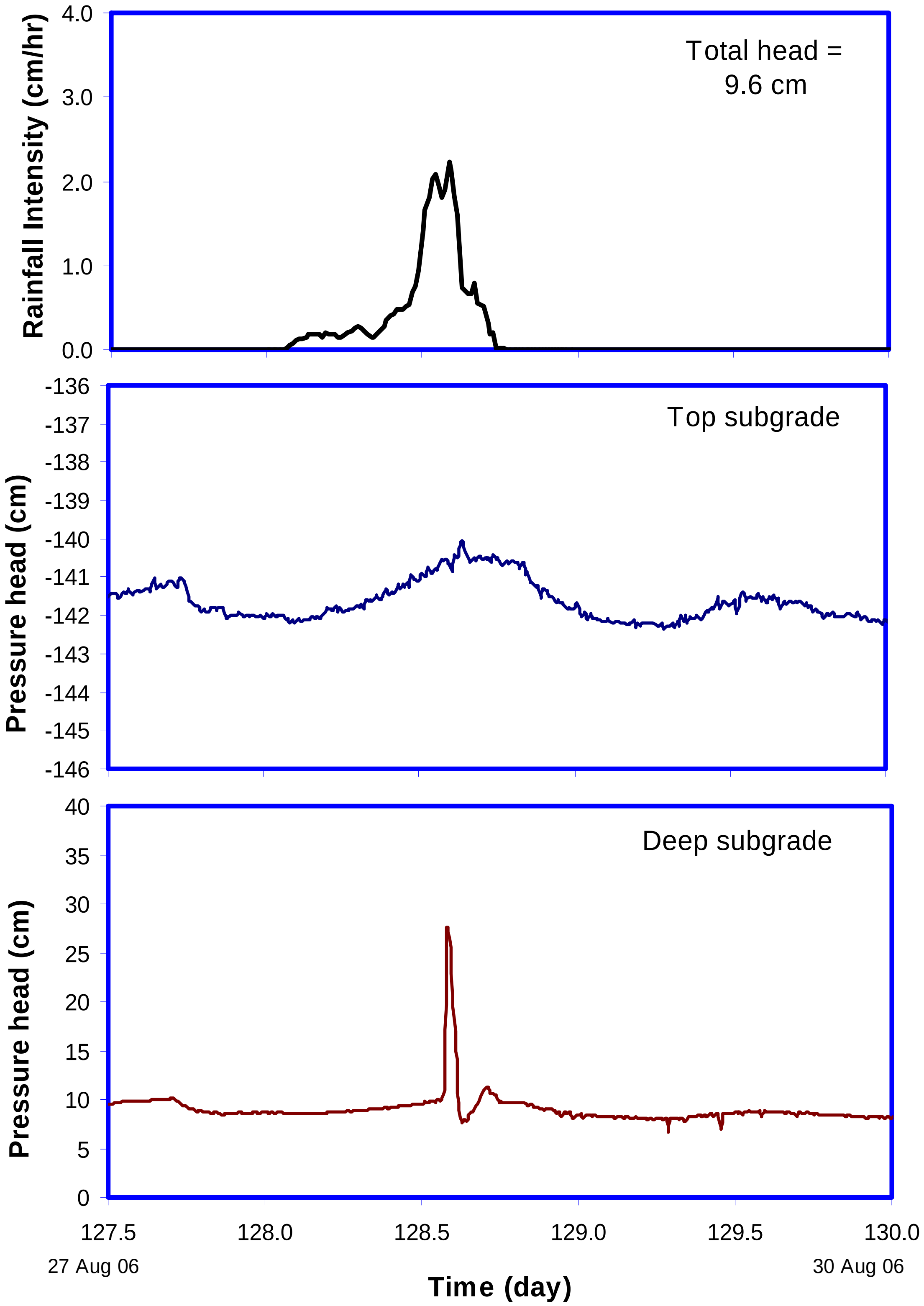

Figure 7-12: Capturing rise of groundwater table during rain event: 28 Aug 2006 (day 128)

7.4.2 Dynamic Pore Pressure Generation

The short-term train-induced pore pressures are measured at the three piezometer locations using sampling frequency of 10 kHz. The train passage is cyclic in nature; the cyclical pore pressure development framework predicts that successive wheel loadings cause a cyclic wheel-induced pore pressure component (change in average total stress) and an accumulation of shear induced pore pressures under undrained conditions (i.e. fully saturated case). It is the accumulation of the shear induced pore pressures

The cyclic wheel-induced pore pressure component has an elastic response: removal of wheel load causes instantaneous reduction of pore pressure. It is the accumulation of average pore pressures that is problematic: it reduces effective stress and prolonged high cyclical loads can cause failure.

The form of the original unprocessed data is shown in middle graph of Figure 7-14 and the acceleration data is provided for reference on the wheel positions (top graph of Figure 7-14). Unfortunately, the noises derived from the low-resolution data acquisition masked useful data. The high frequency noise band (below) is removed using a 300Hz low pass filter (Figure 7-13) to reveal the underlying pore pressure trend (bottom of Figure 7-14).

Problematic Top Subgrade:

The full problematic top subgrade acceleration response and the low-pass-filtered excess pore pressures are shown at the top and bottom of Figure 7-14 respectively. At the onset of train loading, the piezometer registered a positive “pulse” in the pore pressure (≈2 cm), suggesting that the average pore pressure that developed was immediately dissipated. Subsequent wheel loadings caused development of elastic cyclic pore pressures but with no increase in cumulative average pore pressures. A negative water pressure “pulse” was measured when the train left the instrumented area. This trend is typical for all the dynamic pore pressure data. The close up of the positive “pulse” and development of water pressure due to wheel loading is shown in Figure 7-16: the rapid build-up in the pore pressures due to incoming train are immediately dissipated even as the individual wheel-induced cyclic pore pressures are being generated.

Reference Top and Deep Subgrade

The track response acceleration data and the filtered (300Hz filter) dynamic water pressure for the reference top subgrade are shown in top and mid Figure 7-15. The train-induced pore pressure regime displayed similar characteristics as the data measured at the problematic top subgrade: fast build-up and dissipation of the average pore pressure at the on-set of the train, no build-up in the average pore pressures throughout the train loading, short-lived individual wheel-induced cyclic pore pressures, and a negative “pulse” after the train passage. The deep subgrade piezometer shows similar response, although the initial positive “pulse” is only a third of the value at the top subgrade.

Comparison with Finite Element Analysis

A 3D elastic finite element analysis (FEA) is performed to estimate the magnitude of pore pressure pulses under single wheel loading. An undrained condition is (i.e. response under fully saturated conditions with no drainage) and the pore pressure pulse is controlled by the increments in octahedral stresses ($(\Delta\sigma_1+\Delta\sigma_2+\Delta\sigma_3)/3$). The FEA estimates pore pressure pulses of 20kPa (200 cm head) and 4.5kPa (45 cm) for the top subgrade and deep subgrade respectively (Appendix IV).

The piezometers at the top subgrade and deep subgrade captured cyclic pore pressures that are smaller than the FEA-predicted pore pressures. Even for the pre-processed data, pore pressure spikes[26] of 5 kPa (50 cm) are still smaller than the FEA estimated 20 kPa (200 cm) spikes. There are two reasons for this. Firstly, the FEA analysis assumes a fully saturated condition while the real subgrade is mostly unsaturated and under matrix suction. Under these conditions, the real generated pore pressures will be much lower than the predicted ones. Secondly, the theoretical response of the piezometer in Mansfield silt is one second. The piezometer is able to measure the three-second train-induced average pore pressures but not the dynamic wheel-induced cyclic pore pressures.

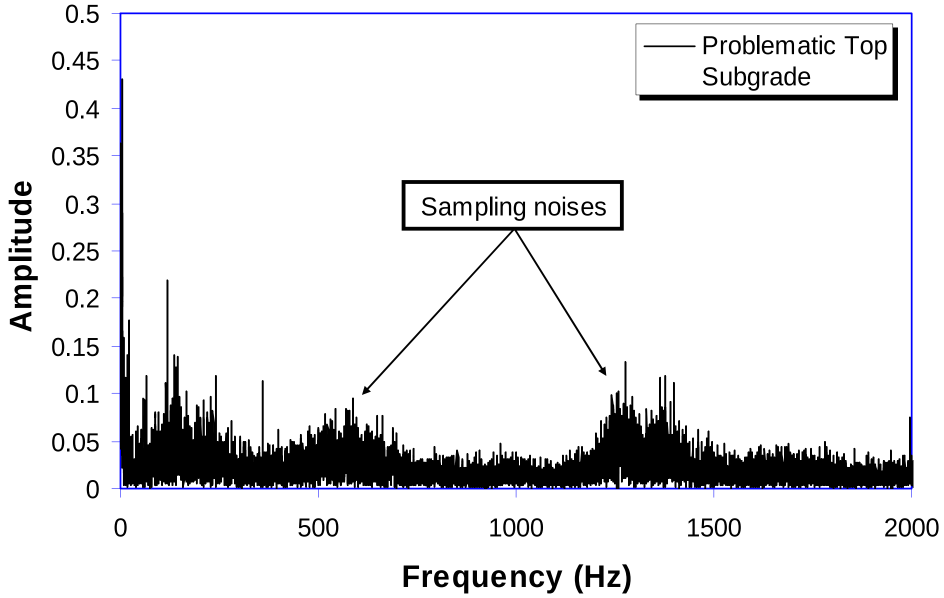

Figure 7-13: Frequency spectrum of the PBP piezometer (F13b-Acela). Most of the high frequency noise lies in the 500Hz range.

---

[26] These high frequency spikes are removed by the low pass 300 Hz filter.

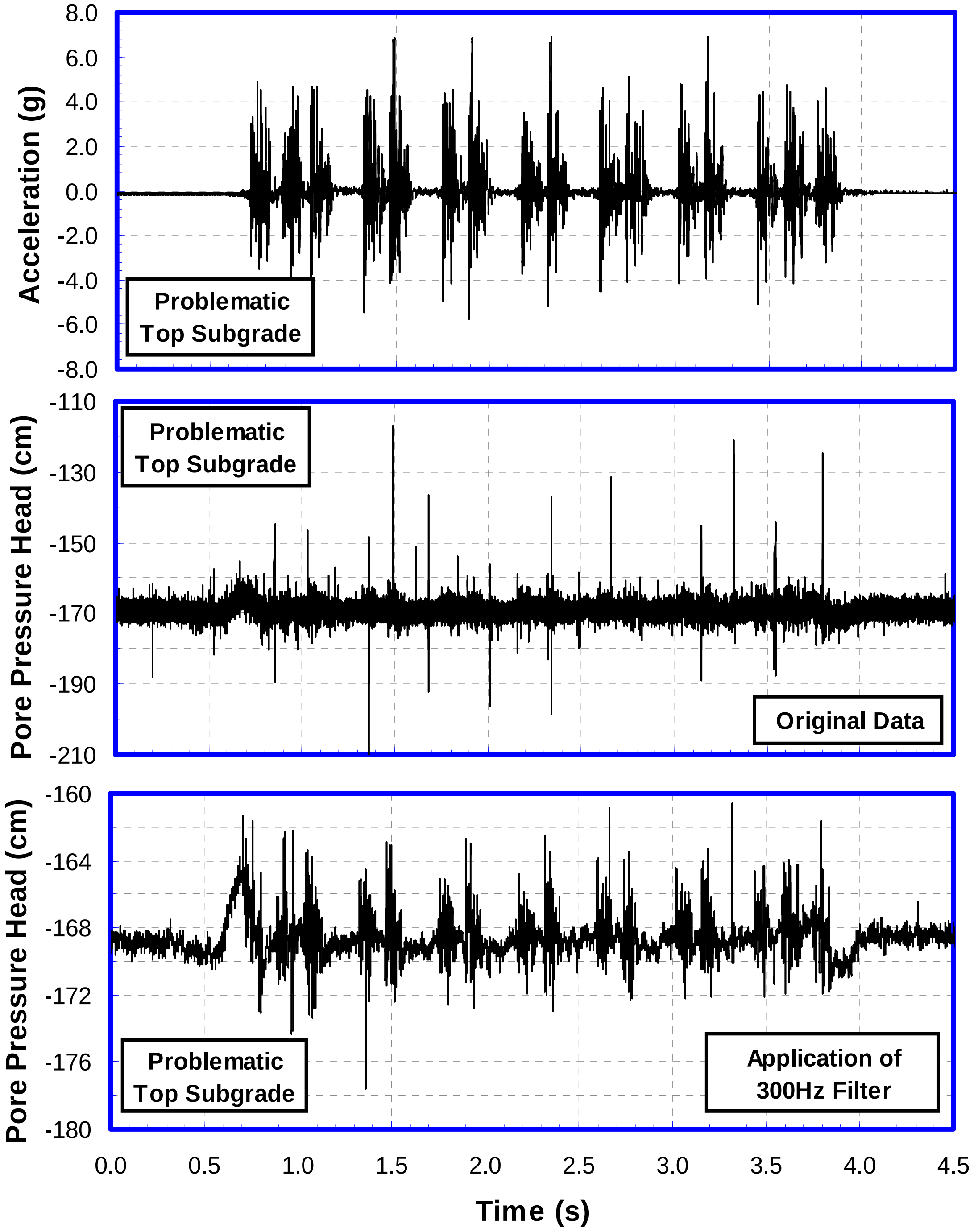

Figure 7-14: Measurement of the pore pressure at the problematic top subgrade and the corresponding acceleration after rain (File F13b-Acela).

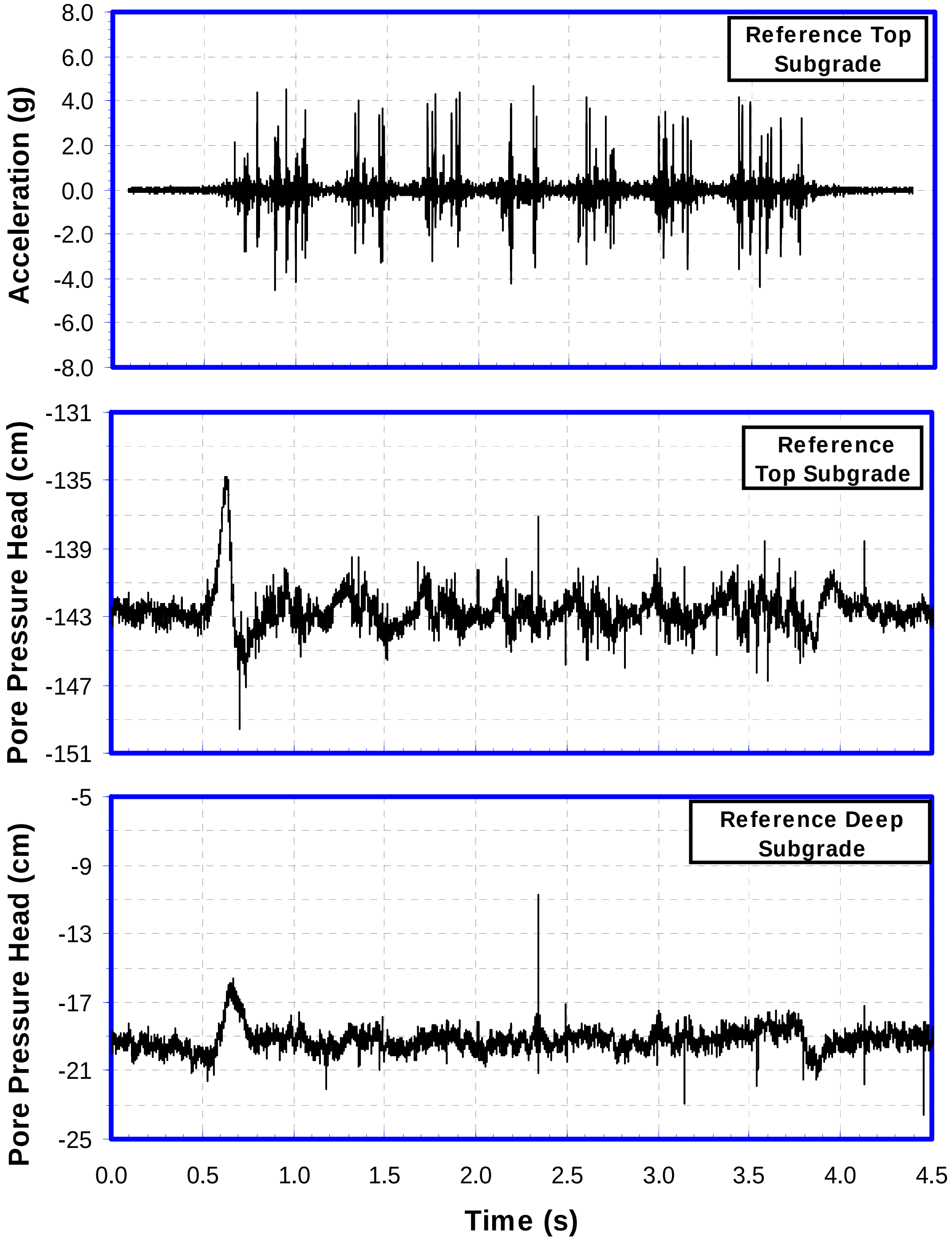

Figure 7-15: Dynamic water pressure measurement in the reference top subgrade (mid graph) and deep subgrade (bottom graph). (File F13-Acela for water pressures and F11-Acela for acceleration)

Close up of the pore pressure

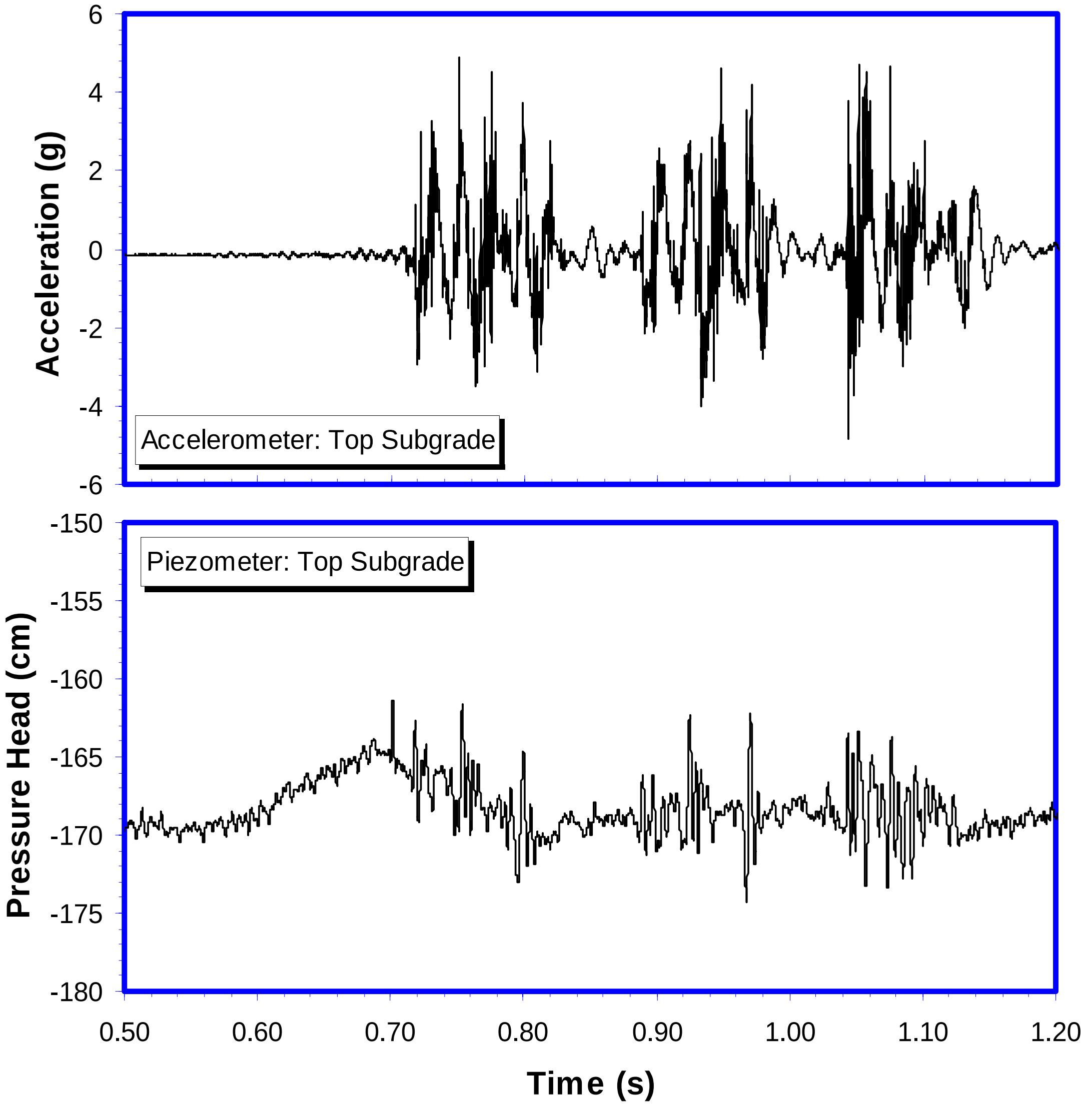

Figure 7-16: Close up of the pore pressure response measured at the problematic top subgrade. This represents the on-set of the train, and the piezometer is only quick enough to capture small pressure response.

7.5 Temperature sensors

The temperature variation at the Mansfield site was captured using thermistors. Prior experience found that thermistors are robust and reliable sensors for harsh field usage (Aw 2004). The temperature sensors were installed at top tie, just below the ballast / subgrade interface and in the deep subgrade. Data were acquired once every ten minutes using 16-bit resolution Iotech data acquisition.

Field thermistors measured summer temperature that reached 50^0C during the day and dropped to 18^0C during the night. The sensor box containing thermistor on the top tie was completely exposed to sunlight. In comparison, sheltered temperature sensor obtained from nearby Plainville weather station showed lower temperature during the day (25 to 30^0C) but similar temperature during the night (Figure 7-17). The temperature at the top subgrade was inert to diurnal temperature fluctuations and assumed value of daily temperature averages.

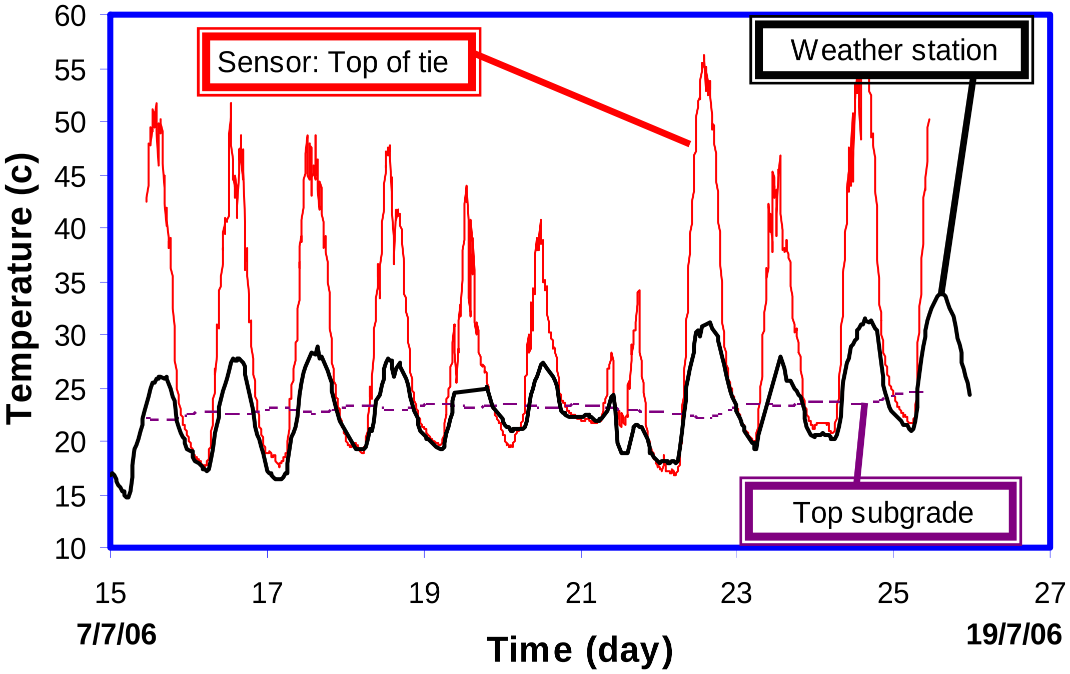

Figure 7-17: Graph showing temperature in the tie (unsheltered), top subgrade, and sheltered temperature obtained from weather station

7.6 Wireless Monitoring System: Rail measurements

This section presents the performance and data collected from the proof-of-concept WSN. The long-term data collected by the strain gages and temperature sensors installed on the rail are completely unrelated to the mud pumping characterization presented thus far but are of interest to Amtrak, thus demonstrating the versatility of the WSN in accommodating various different monitoring applications. The sensor node is programmed to wake up once every ten minutes for data collection. During each data collection, each channel takes 10 seconds of readings at frequency of 1 sample/sec. However, only the last reading of the 10 seconds is taken into account since the first 9 seconds is to allow full activations of for the sensors.

The primary usage of the collected data is to determine the changes in the internal rail forces due to the changes in temperature relative to the neutral rail temperature. The rail neutral temperature is the temperature that the rail is experiencing no internal stress and is widely taken as the installation temperature of 32.2 ^{0}C (90 ^{0}F). The changes in internal forces are indirectly measured by the strain gages according to the equations[27]:

$$P_{rail} = P_{rail}^{\varepsilon} + P_{rail}^{t} \quad \text{……………………………………Equation 7-3}$$

where P_{rail} (internal rail force resulting from thermal stresses, kN) has a longitudinal strain-related component P_{rail}^{ε} and a temperature-induced component P_{rail}^{t}.

$$P_{rail}^{\varepsilon} = (\varepsilon_{rail} \cdot E) \cdot A \text{……………………………………..Equation 7-4}$$

and

$$P_{rail}^{t} = (t_{neutral} - t_{rail}) \cdot A \cdot E \cdot \alpha \quad \text{…………………………..Equation 7-5}$$

The ε_{rail} (strain in the rail) measured by the strain gage is given by:

$$\varepsilon = \frac{2(V_{rail} - V_{neutral})}{(1+\mu) \cdot V_{exite} \cdot K \cdot Gain} \quad \text{………………………….Equation 7-6}$$

where V_{rail} = current strain gage voltage $V_{neutral}$ = strain gage voltage at rail neutral temperature, V_{exite} = strain gage excitation voltage = 10V, $t_{neutral}$ = rail neutral temperature = 32.2 ^{0}C, t_{rail} = current temperature measured at the rail, E = Young's Modulus of the rail = 200 x 10^6 kN/m^2, α = thermal co-efficient expansion of steel = 11.5x10^{-6} m/m.^{0}K, A = rail cross-sectional area = 0.0088 m^2, μ = Poisson's Ratio = 0.285, K = strain gage constant = 2.1, Gain = signal amplification = 500

---

[27] Equations obtained from personal communications with Michael Tomas, Amtrak

During the installation of the strain gages, the actual strains in the rail and temperature are unknown. By assuming the neutral temperature is at 32.2 ^{0}C, the strain gage voltage at this “no internal stress state” is empirically obtained from field measurements at this temperature: this sets the reference voltages for the strain gage and temperature. Figure 7-18 shows the rail strains (top), temperature (middle) and estimated rail forces[28] (bottom) for one month of data from 6/6/07 to 7/7/07. Positive values refer to compression state. Figure 7-19 provides the temperature comparison between the rail thermocouple and nearby weather station (www.wunderground.com). The temperature measured by the exposed thermocouple shows more diurnal variation than the sheltered weather station temperature sensor.

Performance of the WSN

The performance of the WSN can be measured in terms of the success rate of the collected data on the sensor node reaching the MIT server. This WSN experiences data losses due to connection problems at both the cluster network (sensor node to base station) and long range communication (base station to MIT server). However, it is the connection failure at the cluster network which is most problematic: if the communication between the sensor node and base station fails, the data will be completely lost; but if the long range communication fails, the data will be archived and sent on the next successful connection.

The data transfer success rate can be calculated by considering the percentage of actual received data package over theoretical expected amount of data package. The overall one-month average of successful data transmission for the cluster network and the long-range GPRS communication are 83.34% and 49.2% (compare with Stoianov et al., 2006 of 65-85% and 78-90% respectively). The comparatively higher cluster reception in this research is a result of placing sensor node and base station within the same instrumentation box compared with 80m range used by Stoianov. However, the long range GPRS data transfer has lower yield in this research and is most likely caused by interference from the highly electrified area.

The effect of rain on the long range GPRS data transfer rate is investigated (rain does not affect the cluster head since they are protected by the instrumentation box). By considering 6-hour periods of wet and dry conditions (Figure 7-20), both the conditions are found to produce similar data transfer success rate, suggesting that rain has a minor role to play.

---

[28] The CWR rail goes into compression when the ambient temperature is above the atmospheric temperature. At high temperatures, the risks of lateral track buckling increases (see Kish *et al.* 2003).

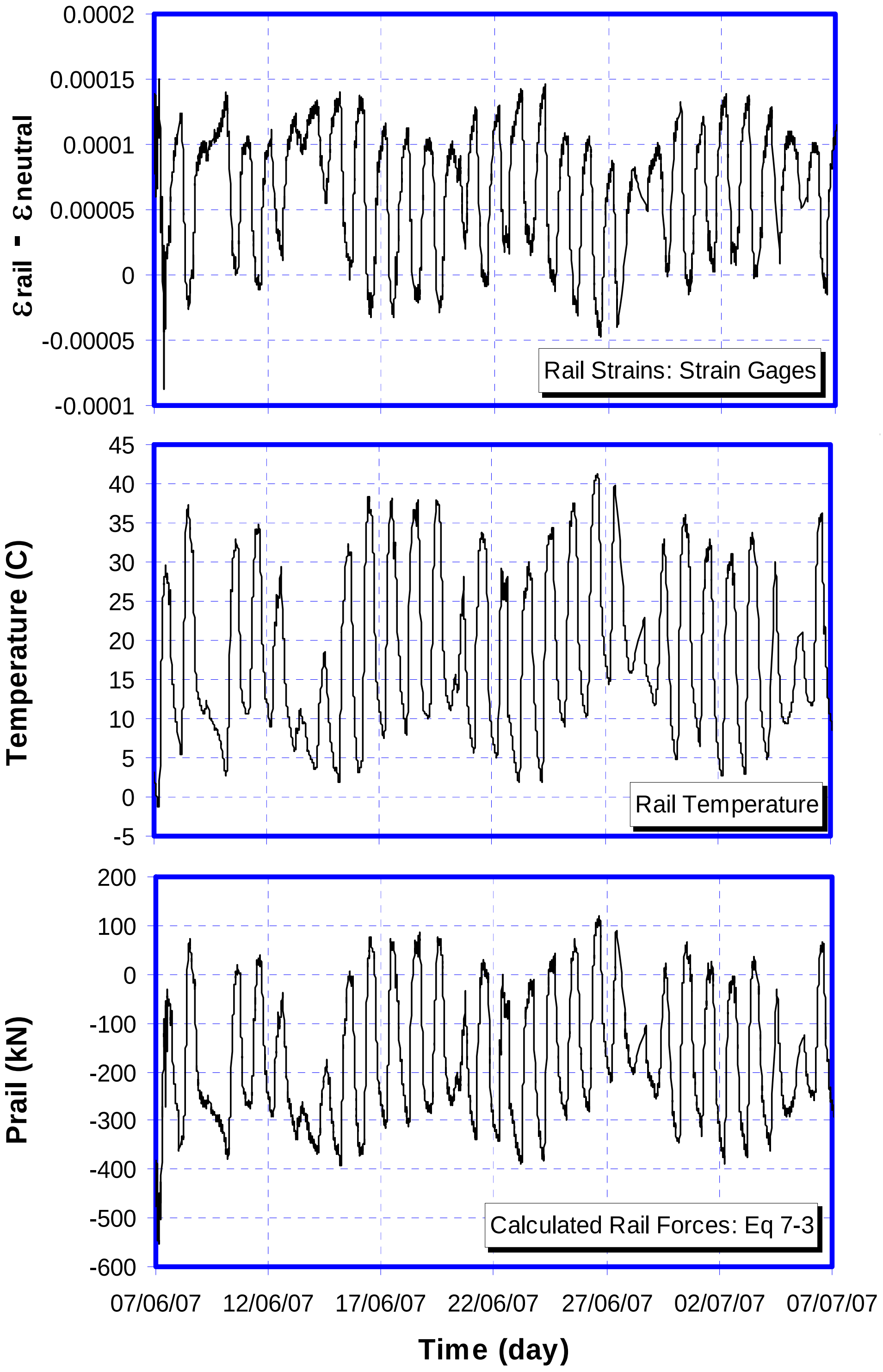

Figure 7-18: The internal rail force and temperature data on the *rail* collected by the WSN network.

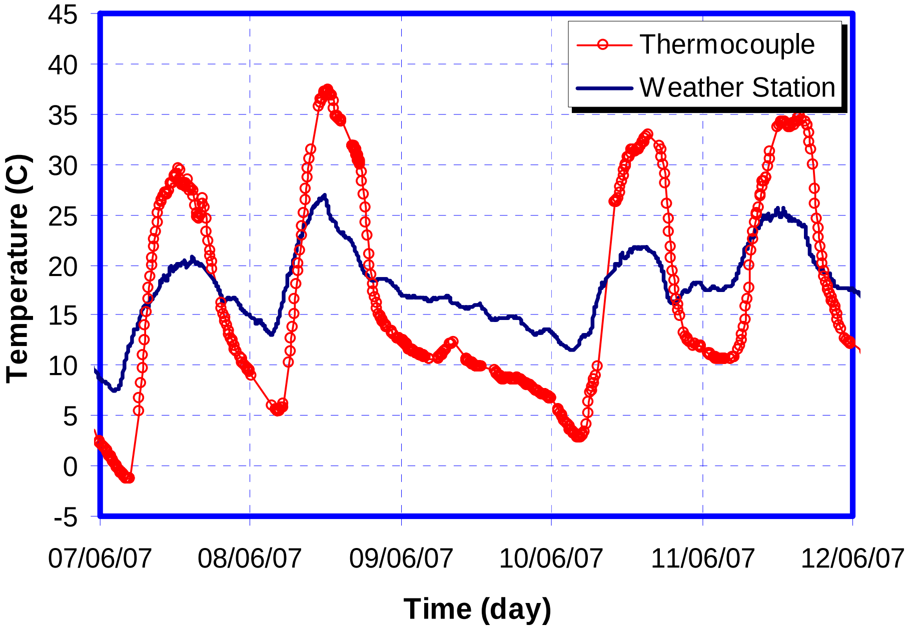

Figure 7-19: Temperature comparison between the thermocouple installed on the rail and the weather station (www.wunderground.com).

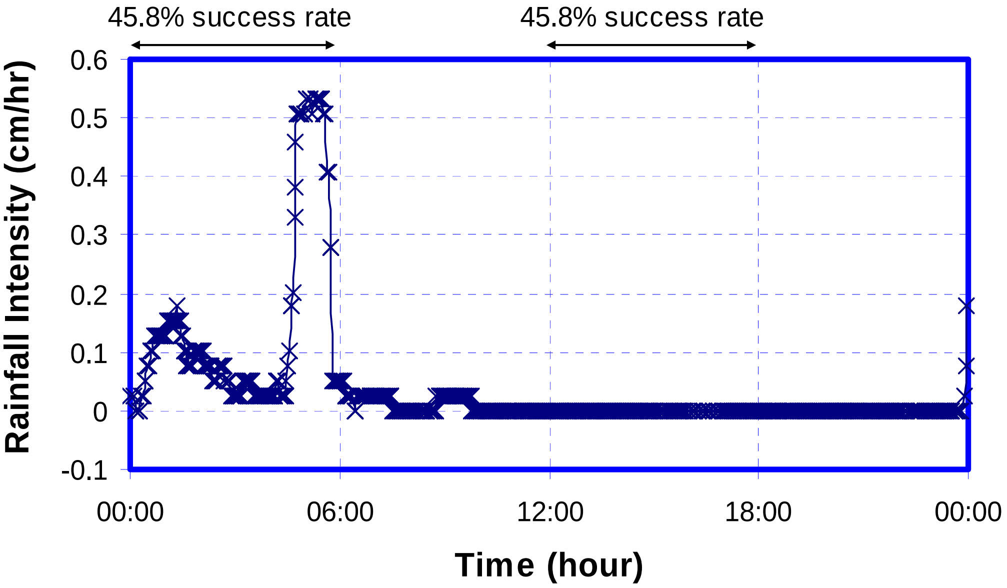

Figure 7-20: The measurement of LONG-RANGE GPRS data transmission success rate over six-hour period in both wet (12am to 6am) and dry (12pm to 6pm) conditions on July 5th 2007.

Chapter 8: Analysis of Field Data

This chapter presents the summary of the field results (Chapter 7), development of tools capable of aiding the analysis of field results, and a hypothesis of the Mansfield mud pumping mechanism.

8.1 Methods for quantifying track degradations

The track acceleration response time-series presented in Chapter 7 provides qualitative insights on track behavior during the newly maintained stage and the deteriorated stage, although they do not provide objective measure of the changes in track behavior between the two serviceability stages and effect of different train loadings. This section presents the development of semi-empirical acceleration-based methods for quantifying the observed track degradation. Currently available track degradation models that are based on permanent track settlement and strains[29] are not suitable for application to the Mansfield site as the mode of degradation is characteristically observed through greater vibration rather than settlement accumulation.

The track degradation model is derived from measurements of the acceleration response of the subgrade during train loading and exploits predictable track behavior characteristics. The track deterioration is marked by a clear increase in the acceleration measured in the subgrade for a given train loading while newly realigned track has lower acceleration. The track acceleration response profile due to a train event will be represented by a single scalar quantity and a collection of multiple single numeric values over time provides a visual track degradation trend. The acceleration-based models can also be used to analyze the following:

- Tracking track degradation with time
    - Evaluating changes in the track response due to train traffic with time.
- Evaluating relative contributions of different trains to track degradation
    - Role of Acela, Regional and MBTA trains in causing track degradation
- Role of rain and temperature changes in track degradation

Two methods of quantifying track degradations are proposed: a) peak acceleration method and b) energy method.

---

[29] e.g. Li 1998, European, German and British models as detailed in Chapter 3

8.1.1 Peak Acceleration

The peak acceleration method selects the highest absolute vertical peak wheel acceleration for a single train event. The tracking of peak wheel acceleration indirectly represent maximum force experienced by the track. As such, tracks at deteriorated state produced greater track response acceleration than newly aligned ones. Figure 8-1 (bottom) shows the track degradation history of Acela trains over a period of nine months, measured at the problematic top subgrade level. Each of the data point represents a train event.

The lowest peak acceleration, immediately after track realignment, stood at 4.5g. The peak acceleration gradually rose with traffic until reaching critical values of 7 to 8g. Since 8g was the maximum possible capacity of the accelerometer, the actual peak acceleration during the deteriorated stages might actually be higher. Immediately after track realignment, the peak acceleration values again dropped to approximately 4.5g.

There is a limitation of this simple procedure. The peak acceleration method only worked for trains with excellent wheel geometry and similar wheel load distributions. Presence of wheel geometrical irregularities (e.g. wheel flats) will alter peak acceleration response, often increasing it by a factor of two to four. Examples of artificially high track acceleration due to wheel flats are shown Figure 8-1 (represented by data points on days 210, 223, 245.6) in comparison with a train without wheel flats (day 239.0). The inherent dependency of wheel geometry rendered this method unreliable for representing track degradation. Nevertheless, the peak acceleration method, if used with a method that can represent average wheel contributions, could be exploited to identify trains with wheel flats. This will be further discussed in the next section.

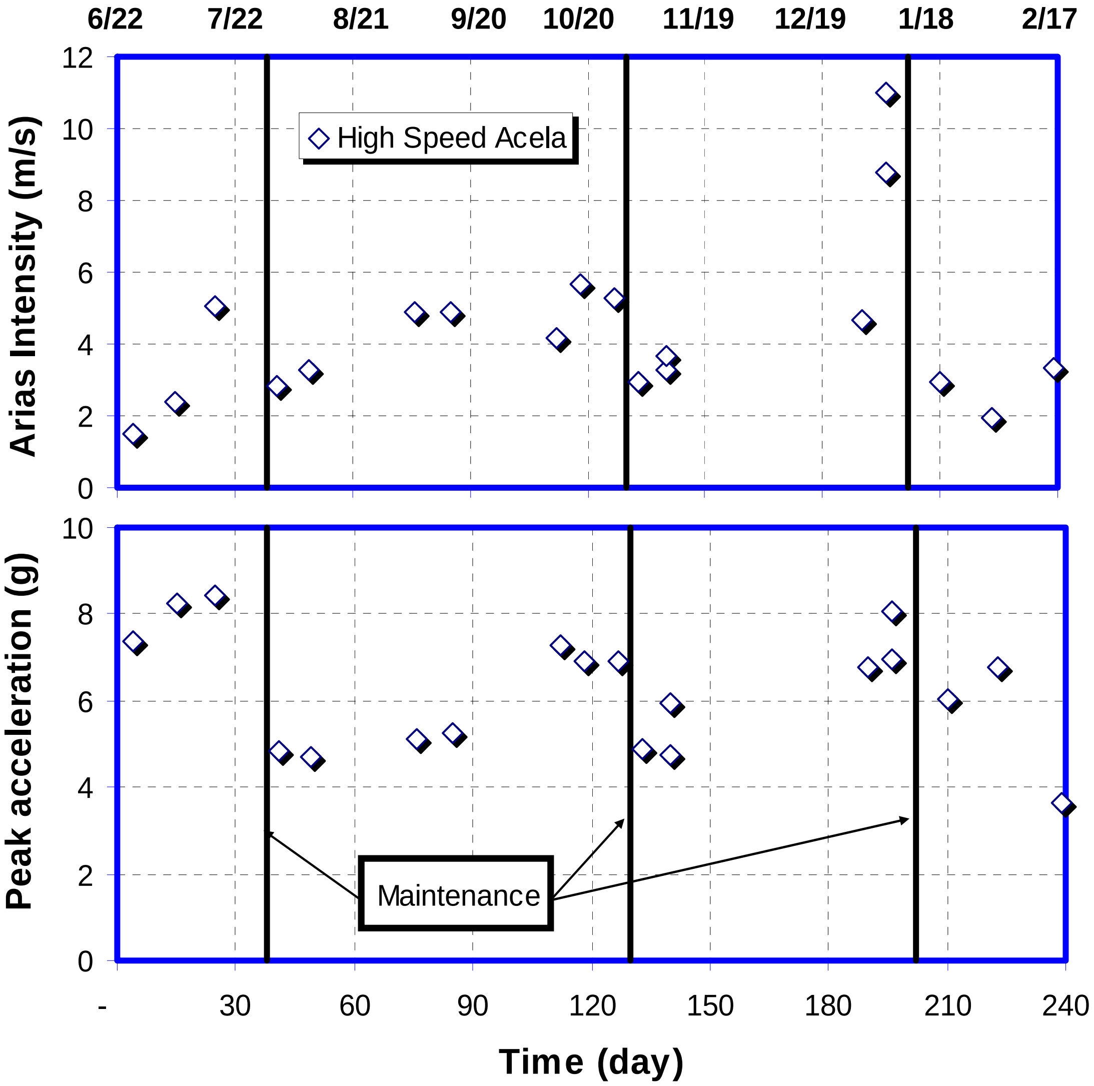

Figure 8-1: Detection of wheel flats using combination of Arias Intensity (top) and peak acceleration (bottom) for Acela trains. Wheel flats caused high peak acceleration (i.e. single very high peak acceleration event) but low Arias intensity (averaged over multiple wheels).

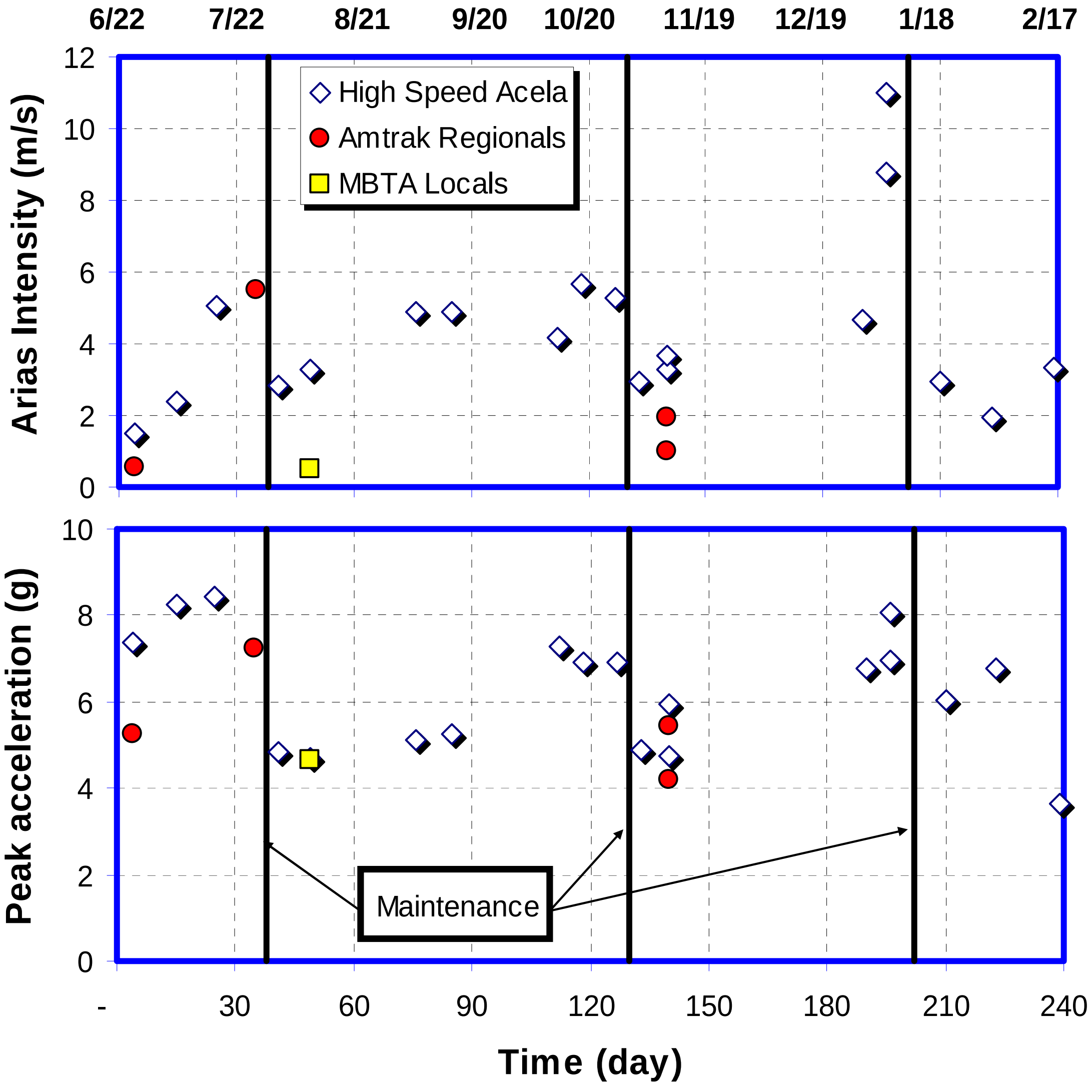

Figure 8-2: Comparison between Acela trains with Regional and MBTA trains using Arias Intensity and peak acceleration methods.

8.1.2 Energy Method (Arias 1970)

The limitation of the peak acceleration method that is greatly affected by single high wheel induced acceleration can be addressed by using an energy method. An example of the energy method was developed by Arias in the 70s and is referred to as Arias Intensity. Arias Intensity measures the intensity of the track response system and is defined as the energy dissipated per unit mass, effectively removing the effects of the mass in the system. Arias Intensity, originally developed for as an empirical tool for measuring the strength of earthquake, is becoming increasingly popular as an earthquake intensity measurement tool. Researchers have utilized the Arias Intensity in measuring the attenuation of earthquake with distance (e.g. Hwang *et al.,* 2004; Travasarou *et al*, 2003), evaluating earthquake-induced landslides (Harp & Wilson 1995), and investigating liquefaction potential of soils deposit during earthquake (Kayen & Mitchell, 1997). The attraction of the Arias Intensity stems from its ability in capturing both the magnitude and duration of the earthquake, making it easy to compare between different earthquakes. Arias Intensity has not been used for track degradation analysis. This thesis proposes a novel application of Arias Intensity for railway track degradation analysis.

The Arias Intensity is directly proportional to the summation of the amplitude square of the Fourier acceleration in Fourier transform spectrum. Mathematically this can be expressed as:

$$I = \frac{\pi}{2g}\int_0^\infty |X(\omega)|^2 \, d\omega \text{ where } X(\omega) = \int_{-\infty}^\infty x(t)e^{-j\omega t}dt \text{ ....(Equation 8-1)}$$

where g = gravitational acceleration in m/s^2

Readers are referred to the original paper by Arias (1970) for complete derivation of this equation. It is generally computationally expensive to transform the acceleration profile into frequency spectrum and summing the amplitude square. Fortunately, it is possible to compute Arias Intensity based on the acceleration profile in the time domain. By considering the Parseval's transform, the Arias Intensity can be rewritten as:

$$I = \frac{\pi}{2g}\int_0^\infty |X(\omega)|^2 \, d\omega = \frac{\pi}{2g}\int_0^\infty |a(t)|^2 \, dt \text{ ....(Equation 8-2)}$$

where the right hand side of the equation expresses accelerations in the time domain.

Parseval's theorem showed that Arias Intensity can be computed solely by summing the squared acceleration amplitude. The summation to infinity parameter can be replaced by the total duration of the train passage, T, since the acceleration profile is zero after the train event and has no further contribution to Arias Intensity. Rewriting the Arias Intensity equation:

Arias Intensity $I = \frac{\pi}{2g}\int_0^T |a(t)|^2 \, dt$ …………………………………..(Equation 8-3)

In this form, the acceleration time-series, $a(t)$, measured from the accelerometer is directly placed in the equation. Arias Intensity is therefore greatly affected by the magnitude of the acceleration and duration of the trains.

The track degradation response due to high-speed Acela trains is shown in Figure 8-1 (top) and each data point represent single train event. The Arias Intensity is not normalized by the number of train carriages[30] in order to measure the full energy imparted by the trains on the track. In another words, trains with 10 carriages should rightly produce greater wear and tear on the tracks (hence high Arias Intensity) than trains with 3 carriages (lower Arias Intensity). In addition, this simplifies data processing that will be critical for autonomous data collection. Arias Intensity for Acela trains ranged from 2.5 (after track alignment) to above 8.0 (greatly deteriorated). The progression of track degradation over time could be tracked. The effects of track realignment could be seen, appearing as immediate drop in Arias Intensity after the operation. The observed critical stage which will trigger track realignment process was 6.0, although the track degradation had been allowed to occur above that (11.0 at one point).

Figure 8-2a compares the Arias Intensity for the three types of trains at the Mansfield site. These results show that the Acela trains were undisputedly the leading contributor, followed by Regional trains (roughly half of Acela's contribution) and MBTA commuter trains.

Since this method considers the overall energy dissipated by the track, it is not greatly affected by single wheel flat events. A combination of the Arias Intensity and peak acceleration method could be used for detecting trains with wheel flats. By studying the track degradation history, profiles with unexpectedly high peak acceleration but low Arias Intensity would likely point towards wheel flats.

---

[30] The Acela trains have fixed number of carriages (2 engine & 6 passenger carriages) although Regional trains vary from 4 to 6 passenger carriages (and 1 engine).

8.2 Role of temperature and rainfall

Role of Rainfall

The historical rainfall data for the Mansfield site (www.wunderground.com) was punctuated by mostly dry Summers and wet Falls conditions (Figure 8-3). The rate of track degradation did not seem to be reflective of the rainfall pattern: the high rate of track degradation from days 0 to 30 occurred during dry spell and wet days of 30 to 120 produced lower rate of track degradation. There is certainly very little correlation between the track degradation and rainfall.

Role of Temperature

Amtrak observed that the track was particularly stable during the winter (no track realignment was required during winter), suggesting frozen ground played a role in stiffening of the ground. Temperature sensors installed at the top subgrade found that ground temperature only reached freezing point of 0^0C at around day 230 (early February). The subgrade temperature was directly correlated to roughly the average diurnal atmospheric temperature due to high latent heat of the earth.

Figure 8-4 showed a particularly interesting interaction between ice and thawing of ice with track degradation. There was a heavy snow fall on 14 February (day 237) and followed by two weeks of cold spells (top subgrade temperature at zero degrees). The icy condition on the track is shown in Figure 8-5. The frozen ground is a boon for track stability. Visual inspection found the problematic tie extremely stable under train loading and was easily passable as a non problematic site (low Arias Intensity values between days 245 to 255).

From day 251 onwards, atmospheric temperature increased and encouraged ground thawing. The subgrade temperature was expected[31] to be zero throughout the time of thawing which occurred over span of a few days due to big amount of ice and snow. The thawing process clearly had a devastating effect on the track. Arias Intensity shot up from stable track to greatly deteriorated stage within a few hours[32]. It took one Acela train to lift the Arias Intensity from 1 to 4.5 and from another from 4.5 to 8.0. Regional trains did not appear to cause high Arias Intensity even when track was deteriorated. When the average atmospheric temperature dropped below freezing point, the track becomes frozen and Arias Intensity for both type of trains dropped to below 3.0 (stable value). This warm and thaw cycle was repeated again on day 264 and 267 with corresponding expected track degradation behavior.

---

[31] Temperature data from sensors were terminated in order to allocate computing resources for the new Iotech data acquisition capable of continuous data capture.

[32] Figure 8-5 showed Arias Intensity for *every* Acela and Regional trains between days 250 to 270.

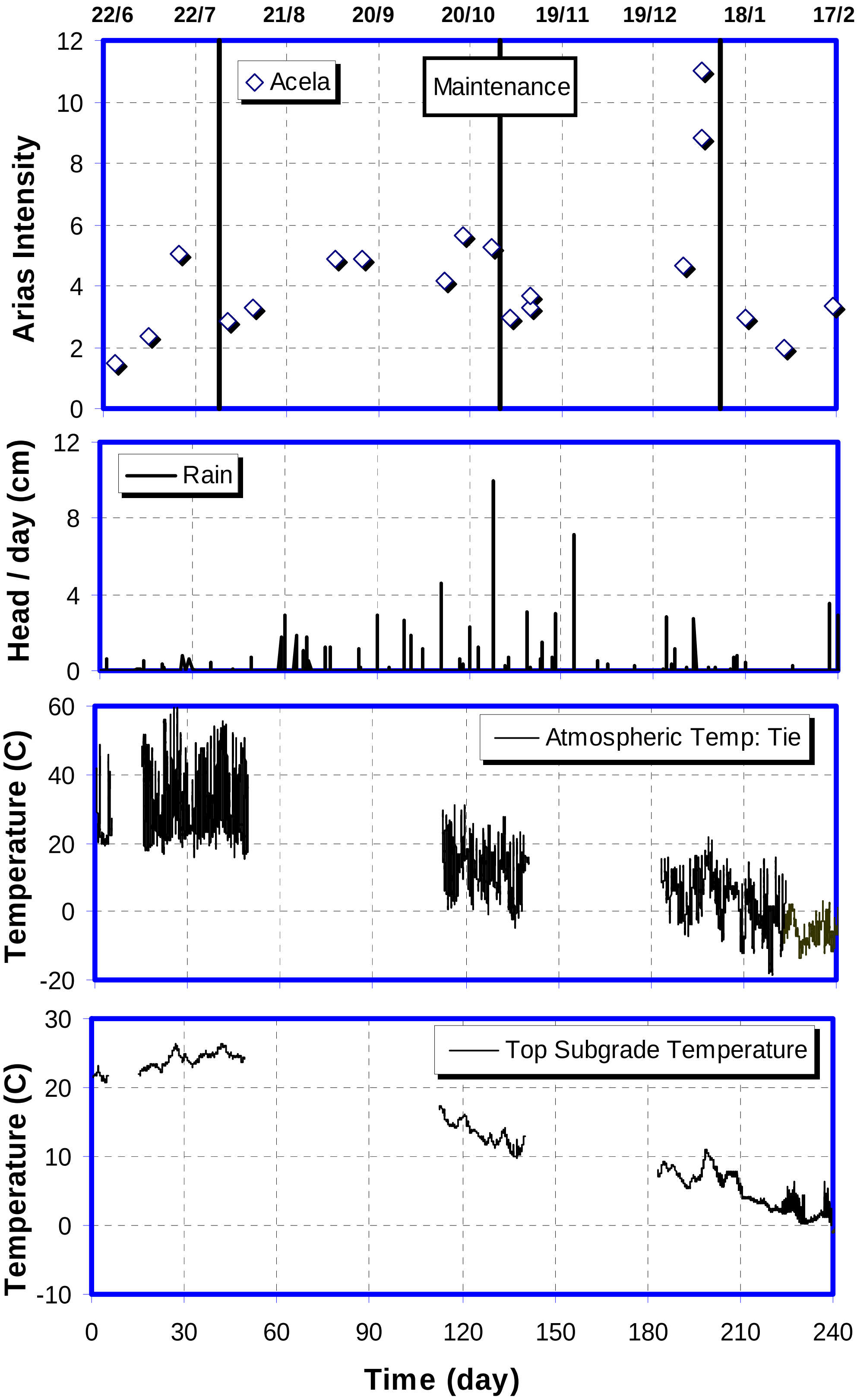

Figure 8-3: Track degradation for 9 months from summer until end of winter.

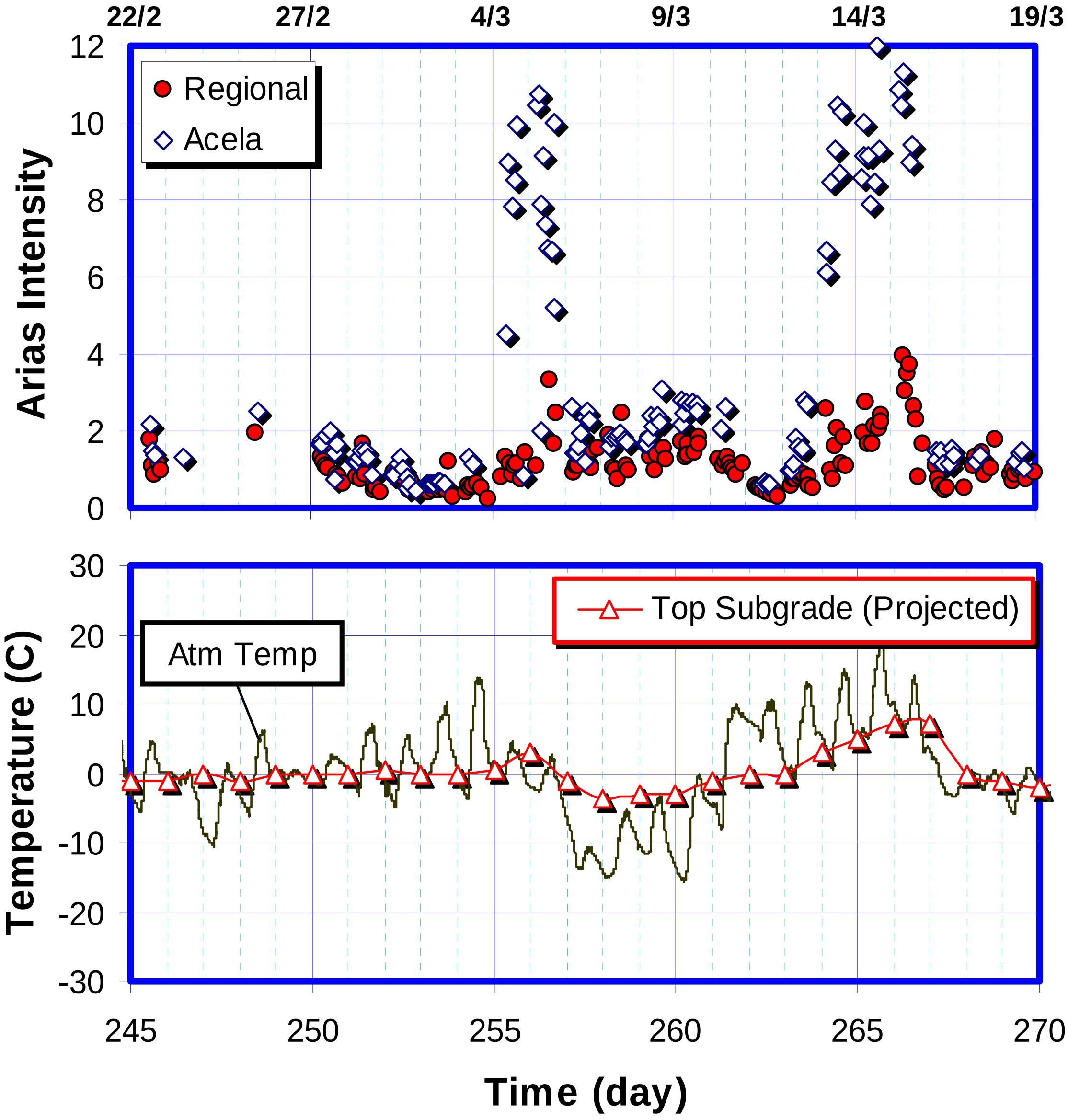

Figure 8-4: Close up of the track degradation during winter, subjected to fluctuation temperature. All Acela and Regional trains are shown between day 250 to 270.

Figure 8-5: Frozen ground, picture dated 16 Feb 07 (day 239).

8.3 Field Data Summary

This section summarizes the results and analyses of the field data. The results are divided into four categories: a) water, b) train loading, c) track geometry, and d) soil classification.

Water

1. Minimal influence from the ground water table
   The small variation in the deep groundwater table (1.7m below ground) and matrix suction at the top subgrade (capillary rise from the groundwater table) suggest that the groundwater table has no effect on the mud pumping problem.

2. No perched water table (ponding)
   There is no evidence of ponding at the top 1.7m layer of the subgrade. Ponding shows up as positive pore pressure at the top subgrade piezometer and is usually caused by an impermeable layer trapping water within the subgrade.

3. Rain effects
   The rain merely replenishes the matrix suction at the top subgrade with little increase in pore pressure. This confirms the absence of perched water table within the subgrade layer.

4. Dynamic pore pressure

   Within the small time frame of one train event, the dynamic pore pressure profile consists of no accumulations of train-induced average pore pressures and some wheel-induced cyclic pore pressures. Since it is the accumulated average pore pressure component that causes more permanent reduction in effective stresses and the wheel-induced cyclic pore pressure component is elastic in response (i.e. the developed pore pressure disappears immediately after removal of wheel loading), the passage of a single train does not cause mud pumping within the subgrade layer.

5. Ice thaw

   The thawing of ice in spring and passage of Acela trains accelerates the track deterioration; the track changes from stable into completely deteriorated stage with just two passages of Acela trains in what would have taken trains two months to achieve the same track deterioration. This is because the ice melts from top down and cannot drain due to the still-frozen subgrade.

Train loading

1. Out of the three passenger trains at the Mansfield site, high speed Acela trains are responsible for accelerating the track degradation.

Track Geometry

1. The track geometry at the Mansfield site is not at an optimal state: the fouled ballast contains 50% subgrade fines by mass that lowers its hydraulic conductivity; the ballast layer is thin; and the subballast layer is absent.
2. The tie is suspended at the problematic area at the deteriorated stage.
3. The track undergoes continuous gradual degradation throughout train operations.

Soil Characterization

1. The top three meters of the subgrade soil consists of low permeability silty-sand. The silty-sand material, classified as SM by the Unified Soil Classification, is a material that is susceptible to erosion and frost heave.

8.4 Hypothesis: Mud pumping mechanism

The field investigation and monitoring provides some useful insights into the mud pumping mechanism at this site. It eliminates many of the factors which were thought to be important in causing the mud pumping mechanism. This section focuses on some of the possible mechanisms that might cause mud pumping at this site:

1. Perched water at the ballast / subgrade interface due to rain
   The permeability of the subgrade is lower than the fouled ballast. The rate of infiltration into the subgrade is slower than the rain supply and the temporary retention of water at the ballast / subgrade interface causes the following: a) loosening of the surface fines at the subgrade, and b) flushing of the loosen particles during the passage of the trains. This is consistent with the visual observations where muddy spots were seen after rain and muddy water (most likely mixture of subgrade soils, ballast powder, and dust) were thrown up during passage of the trains.

2. Lateral ballast movement
   There are currently no data to differentiate the accumulation of ballast thickness at the problematic and reference site; visual inspections found no difference of ballast thickness between the two, suggesting that there is no accumulation of long-term track settlement. An implication of this is the creation of the gap beneath the tie is due to local compression of the ballast and possible lateral spreading of ballast particles.

3. Localized soil characteristics
   The presence of localized soil deficiencies might account for the recurring problematic zone versus the nearby reference zone. These localized soil deficiencies might occur in the form of lower elevation of subgrade profile at the problematic zone (thus encouraging the collection of water). Once the gap beneath the ties is formed, the stresses at the subgrade are further exacerbated by the additional high dynamic stresses imposed by pounding of the ties.

8.5 Cost of the Monitoring System

The attractiveness of the sensors and monitoring platform lie in their low cost form factor and relative easy fabrication and installation. All the sensors share many components – enclosures, cabling, sealing – and these simplify manufacturing logistics. The cost associated with deploying the sensors and monitoring system is influenced by the size of the project and economy-of-scale: bigger projects lower the cost per unit sensor. The monitoring project development cycle and cost structure consists of the following: a) sensor fabrications and calibrations (Table 8-1), b) field monitoring hardware (Table 8-1),

c) field installation (Table 8-2), d) user-end servers and web capabilities (Table 8-3), and d) long-term system maintenance. The cost structure of the monitoring system is divided into material and labor cost. The material cost represents the total hardware cost required to bring the sensor or base station to field-ready conditions and includes external boxes and 6 m (20 ft) of cables. The man-hours quoted assumed familiarity with the system: experienced personnel need less than the recommended hours. In addition, developing numerous similar sensors at once increases productivity: complete development of piezometers into their final field-installation form takes three hours for one piezometer but takes only seven hours for four piezometers.

An example of the monitoring application with three separate instrumented sites (ranging from bridge approach differential settlements to excessive track vertical settlement) is shown in Table 8-4. Each of the instrumented sites has sensors and monitoring hardware costing not more than $5000 in materials and 30 man-hours and each of the sites is connected with only one server located at the user-end. The cost of the user-end processing system depends on the level of sophistication needed: a basic stripped-down version of the server is long range communication capability but real-time data output requires only 8 hours of set-up; a full system with near real-time data displaying capabilities require three weeks or more of development time.

Table 8-1: Estimated cost of sensors and monitoring platform.

Sensors / WSN	*Process*	*Material Costs*	*Man Hours*
Piezometer	• Fabrication* • Saturation • Calibration	$120	3 hours
Settlement Probe	• Fabrication* • Saturation • Calibration	$120	2 hours
Accelerometer	• Soldering & fabrication* • Calibration	$60	3 hours
Temperature	• Soldering & fabrication*	$50	2 hours
Base Station** + GPRS card	• Programming • Fabrication	$1350	4 hours
Sensor Node***	• Programming • Fabrication	$600	2 hours
Wireless Internet providers	• Monthly wireless internet subscription from providers such as T-mobile or Verizon	$720 per year	

* Fabrications include sensor boxes and 6 m (20 ft) of wires and plastic sheath

** One base station supports multiple sensor node.

*** One sensor node supports four data acquisition channels (i.e. four sensors). The first generation iMote is no longer in production. However, the new generation iMote 2 and four-channel data acquisition board can be obtained from xBow (www.xbow.com) for $550.

Table 8-2: Field operational support equipments *per site*.

Equipment	*Process*	*Material*	*Man Hours*
Solar Power System (Base Station)	- Solar panels - Power inverter, batteries	$650	1.5 hours
Instrumentation Box	- Installing Instrumentation box on-site	$100	0.5 hour
Sensors	- Installing sensor under track	$0	1 hour per trenching*

* Total time per location. This is true for installation of one sensor or multiple sensors per location

Table 8-3: Server and back-end processing.

Equipment	*Process*	*Material*	*Man Hours*
Server (basic long range communication)	- Configure Linux - Configure Apache web server - Configure SSH for long range communication	$1000 (for computer)	8 hours
Back-end processing	- Data archiving, database, web viewing capabilities	$0	3 weeks**

** 3 weeks or more depending on the system sophistication required

Table 8-4: Cost estimation example for a monitoring program consisting of three instrumented sites.

Site	*Application*	*Hardware*	*Material Costs*	*Man Hours*
User-end		- Server - Near real-time data display	- $1000 - $0	- 8 - 3 wks
		User Total	***$1000***	***3 weeks***
Site 1	Rail Neutral Stress Measurements	- 2 strain gages and 2 thermocouples - Base Station and 1 sensor node - 1 year Internet subscription - Field operational support	- $400 - $1950 - $650 - $750	- 7 hrs - 6 hrs - 0 hrs - 4 hrs
		Site total	***$3750***	***17 hrs***
Site 2	Bridge Approach differential Settlement	- 3 settlement probes and 1 temperature sensor - Base Station and 1 sensor node - 1 year Internet subscription - Field operational support	- $410 - $1950 - $650 - $750	- 9 hrs - 2 hrs - 0 hrs - 5 hrs
		Site total	***$3760***	***16 hrs***
Site 3	Long term settlement (e.g. track overlying peat)	- 3 settlement probes, 3 piezometers, 2 temperature sensors - Base Station and 2 sensor node - 1 year Internet subscription - Field operational support	- $820 - $2550 - $650 - $750	- 17 hrs - 7 hrs - 0 hrs - 5 hrs
		Site total	***$4770***	***29 hrs***

Chapter 9: Summary, Conclusion & Recommendations

This chapter presents the work and achievements of the instrumentation development, installation program, field data summary, and a hypothesis of the mud pumping mechanism at Mansfield (under summary); lessons and experience drawn from the instrumentation and field analysis (under conclusions); and recommendations for future improvement (under recommendations).

9.1 Summary

9.1.1 Development of a Remote Monitoring Platform

Wireless Monitoring Platform

A wireless monitoring system capable of performing automatic data collection, remote data transfer, and providing near-real time data processing and viewing is developed (Chapter 4). This system uses relatively low power (5W at the base station and 40mW at the sensor node) and therefore requires relatively small continuous power support systems. This system is adapted from a high-frequency water and sewer pipes monitoring (Stoianov et. al. 2006) for railway monitoring application. In this proof-of-concept demonstration, the sensor node collects low frequency data (once every 10 minutes) from the strain gages and temperature installed on the rail. The voltage output from the sensors are digitized at the sensor node and sent to the base station. The base station (Stargate) functions as a data gatherer (with no data processing) and sends data back to MIT via secure long-range wireless Internet connection. Intelligent power management at the sensor node level enables the sensor node to sleep between readings and reduces power consumption. If needed, the hardware architecture of the system is capable of handling up to 1000Hz of burst sampling rate. The back-end processing (database and server) is built using open source Linux/Apache/PostgreSQL/Python stack. The development of the back-end processing includes a program tailored to manage incoming data files, data archive, and provide near real-time data visualization.

Sensors

The low-cost prototype sensors consisting of piezometers, accelerometers, settlement probes and temperature sensors aimed at characterizing subgrade problems are developed (Chapter 5). The hazardous nature of rail bed monitoring, intensive safety demands of Amtrak, and low-cost objective of this research meant that the sensors have been designed with the following features: usage of new low-cost transducer technologies; usage of hard non-conducting plastic enclosures for operation in highly electrified areas; and small form factor for easy field installations.

The piezometers are designed to measure both long-term groundwater table variation and short-term train-induced pore pressures. The small needle-probe design minimizes the compressibility of the measuring device in an effort to increase the piezometer response time. Laboratory tests in Chapter 5 find that the piezometer's response is most efficient for load applications in pure water or silicone oil with no drainage. For soils, the piezometer's response is largely governed by the soils' hydraulic conductivity: high hydraulic conductivity results in dissipation of pore pressure before the piezometer has a chance to react, and low hydraulic conductivity results in slower piezometer response. The low viscosity silicone oil, a novel application for piezometers, is used as the internal measuring fluid and it has several advantages. Firstly, the silicone oil will not freeze during winter or evaporate during dry conditions. Secondly, the silicone oil-water interface breaks during drawdown of the water table and reattaches during uprising of the water table, thus preserving saturation of the piezometer. This is, however, not to be confused with drying of the clay that causes decrease in soil saturation and tremendous increase in soil suction.

Recent advances and commercial availability of very low costs accelerometers provides this research an opportunity to evaluate their performance in the field. For less than $10 each, Analog Devices iMEMS (integrated Micro-Eletro-Mechanical) accelerometers are excellent alternatives to higher end accelerometers costing a sixty times more. The accelerometers, with capacities ranging from ±5 g to ±75 g, are calibrated for their magnitude and tested for response in a high frequency shaking device. Accelerometers with ±75 g and ±18 g ranges are installed at the tie and ±5 g are installed at the top subgrade. The accelerometers are used to measure high frequency wheel-induced acceleration response at the tie and top subgrade using high frequency data acquisition system (10 kHz sampling rate). They are particularly successful at measuring wheel flats events that leads to faster track deterioration. The acceleration data can be doubly integrated to find dynamic displacements.

The liquid-based settlement probe is based on capturing the pressure changes in the liquid (reference to a fix datum) due to elevation changes in the embedded probe. The long-term performance of the settlement probe is greatly determined by the offset stability and temperature variation of the pressure transducer. Usage of a gage Omega pressure transducer minimizes the offset stability error to ±2 mm and the effect temperature variation can be removed through temperature calibrations.

The temperature sensor embraces thermistors (temperature sensitive resistors) that are low cost and extremely reliable. The thermistors have been used to successfully measure seasonally temperature at the tie (atmospheric temperature), top subgrade and deep subgrade.

9.1.2 Diagnosis of mud pumping at Mansfield

It had been recognized very early on the highly localized mud pumping spots were complex problems. There are four localized mud pumping sites in the area, each site spanning ten to eleven ties and contained within one of the double track lines. In addition, the evolution of mud pumping mechanism is still relatively unknown in literatures (Chapter 3). Consequently, the field instrumentation was designed as “a first cut” attempt at gaining insight how the recurring mud pumping might be occurring. The scope of the instrumentation was narrowed to investigate the role of water and train loading on track degradation. Chapter 7 provided in-depth investigation in the field results.

Role of water

Water is expected to play an important role in mud pumping simply because absence of water may prevent mud pumping. According to Amtrak[33], the high water table and fouled ballast are major contributors to the mud pumping problem. Some of the remedial proposal had included installation of surface and deep drainage system.

In this research, water is divided into three categories: a) the long term variation of in-situ ground water table; b) the effect rainfall on the subgrade pore pressure regime; and c) the dynamic train-induced pore pressure development. Observations from the deep piezometer reveal small seasonal changes in the deep ground water level. The ground water level is estimated at 1.6 m and 1.4 m deep in summer and fall respectively. The small seasonal variation of groundwater level is consistent with measurements from a nearby well in Atterboro where the groundwater table experienced a small seasonal increase from summer to fall (Figure 2.6). A hydrostatic matrix suction line projected from the deep piezometer pore pressure in summer coincides with the pore pressure at the top subgrade level, suggesting that the top subgrade is under full matrix suction as a result of capillary rise effect. The matrix suction (negative pore pressures) at the top subgrade effectively rule out the presence of perched water tables (ponding) which would otherwise appear as positive pore pressures. In addition, rain fall events at the site causes very little increase in pore pressure at the top subgrade, suggesting that rain merely serve to replenish the matrix suction and point towards the absence of perched water table in the subgrade. In summary, the in-situ groundwater level, perched water table and rain do not cause mud pumping within the subgrade.

The dynamic water pressure developed during passage of train was measured with high frequency 10 kHz sampling rate (similar to train acceleration). Typical dynamic pore pressure profile consisted of high frequency wheel-induced cyclic pore pressures and longer train-induced average pore pressures. For low permeability Mansfield silty sand, the theoretical response of the piezometer is one second, rendering it sufficient for the

---

[33] Personal communication with Brian Moroney

three-second Acela passage pore pressure measurements but unable to capture the individual wheel loads. However, within the framework of cyclical effective stress analysis, it is the accumulation of average pore pressures that reduces effective stress and cyclic wheel-induced pore pressures play a minor role. The average pore pressure have a brief positive pulse prior to arrival of the first wheel, have no cumulative pore pressures during wheel loadings, and have a negative pulse as the train left the instrumented area. The pore pressures measured during passage of the train are much smaller (less than 20 kPa at the top subgrade) than those expected from static finite element analyses of stresses induced by train loads (38 kPa assuming undrained conditions within the subgrade soils). This behavior is explained in part by the incomplete saturation of the upper layers of subgrade, but also reflects limitations in the physical response rate of the piezometer (slower response due to low permeability silty sand material).

Historical rainfall data showed relatively dry summer and wetter falls. The track (based on Arias Intensity) continued to degrade throughout the two seasons. And since the track continued to degrade even during the relatively dry summer, if rain had any role to play, very little rain (<0.5 cm per unit area) was needed to cause incremental track degradation. It was possible that rain was trapped in the fouled ballast, increased water content at the top subgrade, and thus increased susceptibility of ballast particles penetrating into subgrade during train loading.

Winter conditions in Massachusetts are generally very cold. However, year 2006 was unseasonably warm and mid February arrived before the average diurnal atmospheric temperature and top subgrade temperature plunged below freezing point. Mid February also saw heavy snow fall which covered the track for a few days. The track degradation parameter (Arias Intensity) was noticeably lower during freezing track and icy conditions. The thawing of the ice and snow, starting from the top ballast and progress downwards onto subgrade, generating ponding at the track, causing immediate track deterioration. Subsequent freezing and warming cycle caused the track oscillating between stiff (low Arias Intensity) and greatly deteriorated stage (very high Arias Intensity). The thawing of the track was disastrous; the track was completely deteriorated due to the passing of just three Acela trains which would otherwise have taken two to three months of traffic during summer.

Track Geometry

The track response due to train loading at two levels (tie and top subgrade) was primarily measured using acceleration. And the acceleration response of the tie and top subgrade is directly correlated to the state of track degradation; highly deteriorated track resulted in high track acceleration response and vice versa. The Arias Intensity provides a simple practical indication of the degradation of subgrade support. The Arias Intensity measures intensity of the track response system (defined as energy dissipated per unit mass) during passage of the train. Empirical data found that the upper bound of good track operation was 5.5 Arias Intensity, although the track reached 11.0 on occasions before track maintenance. The lower bound of track operation immediately after track realignment was 2.5.

A combination of Arias Intensity method and peak acceleration method can be used to identify trains with wheel flats. Validation checks can be performed by referring to the acceleration profile and wheel flats will show up as uncharacteristically high wheel peak acceleration.

Train Loading

The Mansfield track site is used Amtrak's high speed Acela, Regional and MBTA commuter trains with combined total of forty trains a day. Of the three trains, Acela is the fastest (at 240 kph maximum speed) and is clearly the major contributor to track degradation. Its Arias Intensity is, on the average, about twice that of Regional and much higher than MBTA trains. This research finding complemented initial observation that the track required much less maintenance when Acela was out of commission in most of year 2005 due to brake problems.

9.1.3 Suggested Mud Pumping Mechanisms

The extensive field instrumentation and data analyses suggest that water plays a relative minor role within the subgrade. This leads to suggestions that the mud pumping mechanism may be triggered at the ballast layer and at the ballast/subgrade interface. This thesis proposes three different mechanisms that might have cause mud pumping while acknowledging that it could be cause by other top subgrade surface mechanisms (Chapter 8, section 8.4). The three mechanisms are: a) perched water at the fouled ballast and ballast / subgrade interface, b) lateral ballast movement, and c) localized soil characteristics such as lower elevation of the subgrade profile at the problematic zone that encourages accumulation of water.

9.2 Conclusions

9.2.1 Performance of the Monitoring system

Sensors

The performance of the sensors over the one-year monitoring period in the general exceeds expectations. The embedded sensors are easily installed using shovels and augers with no disruption to the traffic. This is an attractive proposition at remote sites with limited machinery and personnel.

The piezometers are able to measure the long-term variation of pore pressures in the top and deep subgrade and train-induce pore pressures. The relatively simple construction of the piezometer meant that it can be quickly assembled and saturated within a few hours.

The low costs MEM accelerometer chips had proven to be robust and reliable throughout the monitoring period, surviving high accelerations at the tie and top subgrade. The acceleration profile of the track measured at the tie level is inundated with high frequency tie vibrations, making it a less suitable input parameter for the Arias Intensity track degradation than the accelerations measured at the top subgrade. The accelerations response of the top subgrade is recommended for all Arias Intensity calculations. Attempts to back-calculate the dynamic track displacement from acceleration data have so far been difficult due to low resolution data resulting from data acquisition noises (16-bit resolution over ±10 V signal input range) and high accelerometer range. Therefore, the back-calculation experience of the accelerometer can be improved by using data acquisition capable of handling smaller signal input range (e.g. 0 to 5 V) and high resolution.

The settlement probes have great potential for usage in long-term railway vertical displacement monitoring. The current settlement probe design requires better connection design between the pressure transducer port and liquid-filled tube: severe track vibrations cause the tube to slip from the transducer’s port and drains the inner fluid. This is a purely mechanical design inadequacy and can be solved with better connection design. The settlement probes were more sensitive to changes in ambient temperatures than piezometer (since higher reading resolution was needed for displacement) and temperature-related offset changes will need to be corrected.

The temperature sensors are able to capture diurnal and seasonal changes in the temperature at the tie, top subgrade and deep subgrade level. The temperatures are useful for investigating the influence of freezing and thawing on the track deterioration as well as provide temperature corrections for the settlement probes.

Wireless Monitoring Platform
The WSN platform has been in operation for 3 months with good hardware reliability; the sensor node has been continuously collecting data without the need to reset the equipment; the base station has a watchdog circuit that restarts the base station every 24 hours to prevent hardware freezing. Hardware reliability and continuous unmanned operation are important attributes for remote monitoring.

The adaptation process of the WSN for railway monitoring is easy for the hardware (sensor node, base station, and long-range communication) and more complicated for the back-end processing. For applications with similar sampling regime (1000 Hz or below), hardware adaptation merely requires changing the sampling rate, duration of sampling, and sleep time of the sensor node on a configuration file. Setting up of the long range communication requires some knowledge in SSH (Secure Shell) to enable secure communication. For more advanced applications at the user-end such as automatic data processing, archiving and web-capabilities, detailed knowledge on database programs and Linux programming is needed.

9.2.2 Mansfield Mud Pumping Site

The field data and analyses on the aggravating factors of mud pumping raised some important questions on the evolution of mud pumping mechanisms. The lack of positive pore pressures in the subgrade (even at levels 1.5 cm below the ballast / subgrade interface) during rain and train loadings suggest that the mud pumping problem could be limited to ballast / subgrade interface. This finding impacts the selection of remedial measures for mud pumping: remedial measures that prevent the collection of perched water table may be more effective than one improving the strength of the subgrade. The top-down ice thaw track degradation at this site conforms to the mechanism suggested by Raymond (1986). The still-frozen bottom subgrade layer causes ponding of free water at the ballast/subgrade interface.

9.3 Recommendations for Future Research

9.3.1 Arias Intensity

The Arias Intensity method is useful as an acceleration-based track degradation tool and can certainly be used at other problematic sites. There is, however, a caveat: increasing track deterioration must result in increasing track vibrations. Other possible fields of applications include attenuation of track vibrations due to high speed trains and the effect of building damages. Currently, track vibrations and attenuation with distance are measured in terms of Peak-Particle-Velocity (e.g. Degrande & Schillemans, 2001). Similarly, Dowding (2000) studied the effects of ground motions from high speed trains on structures and humans using PPV. The Arias Intensity method, with its ability to quantify both magnitude and duration of the ground accelerations, can be an attractive method for these applications.

9.3.2 Sensors and wireless monitoring platform

The prototype sensors and the remote, wireless monitoring platform have tremendous potential in rail bed monitoring applications. The usage of the sensor suite (piezometers, accelerometers, settlement probes, and temperature sensors) can be extended to other problematic rail bed site such as extensive vertical settlements (e.g. track overlying peat and organics), progressive shear failures, bridge approach differential settlements, and etc. At places ear-marked for expensive remedial measures, the sensors can be used to characterize the effectiveness of the remedial measures.

The wireless monitoring platform is currently powered by the on-site power supply. Future iterations of the power supply source can incorporate solar panels or power harvesting devices (e.g. wind turbines) to power the 5W base station. The sensor nodes with power consumption of less than 100mW can be powered from batteries or power harvesting devices. The sensor nodes can also be packaged with waterproof containers so that they can be buried in the ground. The transformation of the WSN from long-term data collection into high frequency data collection will require significant development in system-wide triggering (e.g. a sensor node is triggered by the incoming train and alerts the rest of the sensor nodes to wake up and collect data) and sophisticated power management.

This research represents one of the early attempts at converting a primarily research prototype based wireless monitoring platform into practical monitoring hardware and it required significant time investment. The first generation of Intel Mote used in this research is no longer in production and has been replaced by next generation Intel Mote 2. The next generation of Intel Mote is capable of handling higher bandwidth sensors (suitable for high speed acceleration data) and real time monitoring. However, incorporation of the new Intel Mote into existing monitoring platform will require additional modification to ensure platform compatibility. Fortunately, the commercial wireless monitoring realm has been rapidly progressing. Commercial companies such as Crossbow (www.xbow.com) provides remote wireless monitoring hardware and software at various entry levels ranging from fully pre-programmed modules to professional development kits for expert users.

9.3.3 Mud Pumping

9.3.3.1 Laboratory Characterization

The initial conception of the instrumentation program was developed to study an unknown problematic track mechanism. The resulting monitoring program crafted to investigate obvious possible catalyst eliminated the influence of water in the top and deep subgrade level. And through process of elimination, the track deterioration mechanism could, in fact, occurred at the very top layer of the subgrade and fouled ballast. However, the underlying failure mechanism is still unknown and next research stage should aim to better understand the driving mechanism behind this problematic site.

Starting with a simplistic model consisting of ballast and subgrade materials, cyclical confined loading tests can be performed in controlled laboratory setting[34]. Using materials from the Mansfield site (ballast and subgrade material), the cyclical loading test replicating field stresses and loading may shed light to some of the following critical questions:

a) Depth of ballast particle penetration into subgrade before achieving equilibrium
b) Effect of using fouled ballast
c) Effects of water impoundment and changes in subgrade water content.
d) Effects of introducing a layer of subballast (e.g. clean sand)

---

[34] Other cyclical tests using ballast and subgrade material had been performed by Alobaidi *et al.* (1998) and Boomintahan & Srivinasan (1988)

REFERENCES

Alobaidi, I. M, Hoare D.J (1994). "*Factors Affecting the Pumping of Fines at the Subgrade Subbase Interface of Highway Pavements: A Laboratory Study*", Geosynthetics International, Vol 1., No.2, pp 221-259

Alobaidi I, Hoare D.J (1996), "*Development of Pore Water Pressure at the Subgrade-Subbbase interface of a Highway Pavement and its Effect on Pumping of Fines*", Geotextiles and Geomembranes 14, pp 111-135

Alobaidi I, Hoare D.J (1998),"*Qualitative Criteria for Anti-Pumping Geocomposites*", Geotextiles and Geomembranes 16, pp221-245

Alobaidi I, Hoare D.J (1999), "*Mechanisms of Pumping at the Subgrade-subbase Interface of Highway Pavements*", Geosynthetics International, Vol 6, No 4, pp241 – 259

Alva-Hurtado, J. E. and Selig, E. T. (1981) "*Permanent strain behavior of railway ballast*". In Proceedings of the 10th International Conference on *Soil Mechanics and Foundation Engineering*, Stockholm, Sweden, 1981, Vol. 1, pp. 543–546 (A. A. Balkema, Rotterdam, The Netherlands).

Arias A, (1970), "*A Measure of Earthquake Intensity*", R.J. Hansen, ed. *Seismic Design for Nuclear Power Plants*, MIT Press, Cambridge, Massachusetts, pp. 438-483.

Ayres D.J (1986), '*Geotextiles or Geomembranes in Track? British Railways' Experience*,' Geotextiles and Geomembranes **3,** p129 – 142

American Railway Engineering Association (AREA) (1991), "*Manual For Railway Engineering*," Vol.I and II

Aw E.S, Germaine J.T, Whittle A.J (2003), "*Monitoring System to Diagnose Rail Track Settlement due to Subgrade Problems*", Soil and Rock America 2003, 12th Panamerican Conference on Soil Mechanics and Geotechnical Engineering, Vol 2, pp 2715-2720

Aw E. S. (2004), "*Novel monitoring system to diagnose Rail Track Foundation Problem*", S.M Thesis, Massachusetts Institute of Technology

Blacklock J.R. (1984), "*Night 'n' Day Track Study to Cure Subgrade Woes",* Railway Track and Structures, June, pp25-30

Boomintahan S, Srinivasan G.R (1988), "*Laboratory Studies on Mud Pumping into Ballast under Repetitive Rail Loading",* Indian Geotechnical Journal, v 18, n 1, Jan, 1988, p 31-47

Boore D.M (2001), "*Effect of Baseline Corrections on Displacements and Response Spectra for Several Recordings of the 1999 Chi-Chi, Taiwan, Earthquake*", Bulletin of the Seismological Society of America, 91, 5, Oct, pp 1199-1211

Boore D.M, Bommer J.J (2005), "*Processing of Strong-Motion Accelerograms: Needs, Options, and Consquences*", Soil Dyamics and Earthquake Engineering 25, p95-115.

Boselly S.E (2001), "Roadway Flash Flooding Warning Devices Feasibility Study", Innovation Deserving Exploratory Analysis Programs, Final Report for ITS-IDEA Project 79

Brooks J.R (2004), "*Rapid Development of a Wireless Infrastructure Monitoring System*", S.B, Civil Engineering, Massachusetts Institute of Technology, June 2004.

Cauble D.F (1997), "*An Experimental Investigation of the Behavior of a Model Suction Caisson in a Cohesive Soil"*, PhD Thesis, Massachusetts Institute of Technology

Cunningham J, Ebersohn W, Marcolongo V, Tomas M, Trosino M, "*Amtrak's Vehicle/Track Interaction Measuring System: Integrating the Control Strategies of Engineering, Mechanical and Operations"* Presentation Slides.

Culler D, Estrin D, Srivastava M (2004), "*Overview of Sensor Networks",* IEEE Computer Society, August, pp 41-49

Da Re G., (2000), "*Physical mechanisms controlling the pre-failure stress-strain behavior of frozen sand*", PhD Thesis, MIT

Dahlberg T (2001), "*Some Railway Settlement Models – A Critical Review"*, Proceedings for Institutions of Mechanical Engineering, Vol 215, Part F, pp 289 - 300

Degrande G, Schillemans L (2001), "Free Field Vibrations During the Passage of a Thalys High-Speed Train at Variable Speed", Journal of Sound and Vibration, 247, p131-144

DeJong, J.T., Yafrate, N.J., and Don. J. DeGroot. "*Development of a Miniature Piezoprobe for High Resolution Detection of Stratigraphic Interfaces*", *ASTM Geotechnical Testing Journal*, Vol. 30, No. 4.

Dowding C.H (2000), "*Effects of Ground Motion from High Speed Trains on Structures, Instruments and Humans*", Proc. of Wave2000, Balkema, Rotterdam, pp29-42.

Dunnicliff J (1988), *Geotechnical Instrumentation for Monitoring Field Performance*', Wiley, p199 - 295

Esveld C (2001),"*Modern Railway Track*", 2nd edition, Delft University of Technology, MRT-Productions

Federal Railroad Administration (2005), "*Railroad Safety Statistics 2004 Annual report*", Office of Safety Analysis, U.S DOT, Nov 2005.

Federal Railway Administration (2002), *"Track Safety Standards Compliance Manual"*, United States Department of Transportation, Office of Safety Assurance and Compliance

Fredlund, D. G. and Rahardjo, H., (1994), "*Hillside Slope Stability Assessment in Unsaturated Residual Soils*," *IKRAM Seminar on the Geotechnical Aspects of Hillside Development,* Kuala Lumpur, Malaysia, pp. 1–41.

Gasmo J, Hritzuk K.J, Rahardjo H, Leong E.C (1999), "*Instrumentation of an Unsaturated Residual Soil Slope*", American Society for Testing and Materials, pp134-143

Kayen R.E, Mitchell J.K, (1997), "*Assessment of Liquefaction Potential during Earthquakes by Arias Intensity",* Journal of Geotechnical and Geoenvironment Engineering, Dec 1997, pp1162-1174.

Katsumasa (1978), "*Mud Pumping on Tracks—Present state and countermeasures*", Japanese Railway Engineering, Vol.17 No.4,

Kish A, Sussman T, Trosino M, "*Effects of Maintenance Operations on Track Buckling Potential*", Proceedings of International Heavy Haul Association, May 2003, Konrad J.M, Grenier S, Garnier (2007), "*Influence of Repeated Heavy Axle Loading on Peat Bearing Capacity*", Ottawa 2007

Kutter B L, Sathialingam N, Herrmann L.R (1990), "*Effects of Arching on Response Time of Minature Pore Pressure Transducer in Clay*", American Society for Testing and Materials, pp164-178

Lee H, (2005), "*Hybrid Uni-Axial Strain Transducer*", IDEAS Annual Progress Report, Jan 2005, TRB, HRS-15/28

Li D & Selig E, (1998), "*Method for Railway Track Foundation Design",* Journal of Geotechnical and Geoenvironmental Engineering, April, pp316-329

Li D (2000), '*Deformations and Remedies for Soft Railway Subgrades Subjected to Heavy Axle Loads'*, Geotechnical-Special-Publication, n103, ASCE, Reston, VA, USA p307 – 321

Lowe J & Johnson T.C (1960), "*Use of Back-Pressure to Increase Degree of Saturation of Triaxial Test Specimens"*, *Proceedings of ASCE research conference on sehar strength of cohesive soils,* Boulder, pp 819-836

Harp E, Wilson R. (1995), "*Shaking Intensity Thresholds for Rock Falls and Slides: Evidence from 1987 Whittier Narrows and Superstition Hills Earthquake Strong-Motion Records*", Bulletin of the Siesmological Society of America, Vol 85, No 6, Dec 1995, pp 1739-1757

Hayashi, S. & Shahu, J. T. (2000),"*Mud Pumping Problem in Tunnels on Erosive Soil Deposit*". Geotechnique 50, No. 4, p393 – 408

Henderson, E (1994), "*Evaluation of the Time Response of Pore Pressure Measurements*", S.M Thesis, Department of Civil Engineering, Massachusetts Institute of Technology

Hwang H, Lin C.K, Yeh Y.T, Cheng S.N, Chen K.C (2004), "*Attenuation Relations of Arias Intensity Based on the Chi-Chi Taiwan Earthquake Data"*, Soil Dynamics and Earthquake Engineering, 24, pp509-517

Madshus C & Kaynia M (2000), "*High Speed Railway Lines on Soft Ground: Dynamic Behaviour at Critical Train Speed*", Journal of Sound and Vibration (2000) 231(3), pp 689-701

Mainwaring A, Polastre J, Szewczyk R, Culler D, (2006), "*Wireless Sensor Networks for Habitat Monitoring*", IRB-TR-02-006, June, Intel Berkeley Research

Miller G.A., The S.Y, Li D, Zaman M.M., (Feb 2000), '*Cyclic Shear Strength of Soft Railway Subgrade'*, ASCE, Journal of Geotechnical and Geoenvironmental Engineering, p139 – 147

Monismith , C.L, Ogawa N, and Freene C.R (1975), "*Permanent Deformation Characteristics of Subsoil Due to Repeated Loading*.", *Trans Res. Rec*. 537, pp1-17

National Transportation Safety Board (1999), "*Derailment of CSX Freight Train Q316 and Subsequent Hazardous Material Release at Cox Landing, West Virginia*". Accident Report NTSB/RAR-00/01

Rad N.S & Tumay M.T (1985), "*Pore-Pressure Response of the Piezocone Penetrometer"*, Geotechnical Testing Journal, , Vol 8, Sept, No 3, p125 – 131

Raymond G.P (1986), "*Geotextiles Application for a Branch Line Upgrading*", Geotextiles and Geomembranes **3** pp 91-104

Ridley A.M, Burland J.B, (1993), "*A New Instrument for the Measurement of Soil Moisture Suction*", Geotechnique **43**, No. 2. pp 321-324

Ridley A.M, Dineen K, Burland J.B, Vaughan P.R (2003), *"Soil Matrix Suction: Some Examples of its Measurements and Application in Geotechnical Engineering"*, Geotechnique 53, No 2, pp 241-253

Sato, Y (1995). "*Japanese studies on deterioration of ballasted track*", *Veh. System Dynamics*, 24, pp197–208.

Selig E.T & Water JM (1994), '*Track Geotechnology and Substructure Management'*, Thomas Telford

Sisson J.B, Gee G. W, Hubbell J. M., Bratton W. L., Ritter J. C., Ward A. L, Caldwell T. G. (2002), "*Advances in Tensiometry for Long Term Monitoring of Soil Water Pressures*", Vadose Zone Journal, 1, pp310-315

Slade R.M, Patton J (2002), "Major *and Catastrophic Storms and Floods in Texas*", U.S Geological Survey Open-File Report 02-193, (*http://pubs.usgs.gov/of/2003/ofr03-193/cd_files/USGS_Storms/floodsafety.htm#overview*)

Sritova T, Theodoly O, Christiano S, Hil R.M, Radke C.J (2002), "*Wetting Behavior of Silicone Oils on Solid Subtrates Immersed in Aqueous Electrolyte Solutions*", American Chemical Society, June, 18, pp6821-6829

Stoianov I, Nachman L, Whittle A, Madden S, Kling R. (2006), "*Sensor Networks for Monitoring Water Supply and Sewer Systems: Lessons from Boston*", WDSA.

Sussmann T., Ebersohn W., Tomas M, Selig E.T, (2004), "*Trackbed Deflection Under Combined Freight and High Speed Passenger Service*", GeoTrans 2004, ASCE, pp 1602 - 1609

Tadatoshi I (1977), "*Measures for Stabilization of Railway Earth Structure."*, Japan Railway Technical Service, 290

Take W.A, & Bolton, M.D (2003), "*Tensiometer saturation and the Reliable Measurement of Soil Suction", Geotechnique* 3, No 2, pp159-172

Travasarou T, Bray J, Abrahamson N (2003), "*Empirical Attenuation Relationship for Arias Intensity*", Earthquake Engineering and Structural Dynamics, 32, pp1133-1155

Toker N.K, Germaine J.T, Sjoblom K J, Culligan P.J, (2004), "*A New Technique for Rapid Measurement of Continuous Soil Moisture Characteristic Curves*" Geotechnique 54, No 3, pp176-186

Varney A. (1998), "*A Performance Comparison between a Novel Tapered Piezoprobe and the Piezocone in Boston Blue Clay*", M.S Thesis, MIT

Voottipruex P & Roongthanee J, (2003), "*Prevention of Mud Pumping in Railway Embankment. A Case Study from Baeng Pra-Pitsanuloke, Thailand*", The Journal of KMITB, Vol 13, No 1, Jan-Mar 2003, pp 20-25

Wong R.C.K, Thomson P.R, Choi E.S.C (2006), "*In-Situ Pore Pressure Responses of Native Peat and Soil and Train Load: A Case Study"*, Journal of Geotechnical and Geoenvironmental Engineering, ASCE, Oct 2006, pp 1360-1369

.

Appendix I

The scripts for Stargate base station are presented below. The scripts are written by Ivan Stoianov and modified by Aw, Eng Sew.

/etc/rc2.d/S95loadFapp (link to loadFapp)

```
#!/bin/sh

#This software program is available at
#http://www.opensource.org/licenses/bsd-license.html
modprobe gpiomon
/bin/runwdog &
mknod /dev/watchdog c 10 130
insmod -f /root/sa1100_wdt.o timer_margin=120
/bin/wdog &
chmod +x /root/GatewayNode
ln -s /dev/tts/2  /dev/ttyS2
/root/runFapp &
S95loadFapp
```

Called from /etc/rc2.d/S95loadFapp

/root/runFapp

```
#!/bin/sh

mkdir /mnt/cf1/sensordata
mkdir /mnt/cf1/sensorsetup
mkdir /mnt/cf1/bridge
mkdir /tmp/sensorsetupnew

rm /tmp/sensorsetup/recurring.lock
rm /mnt/cf1/sensorsetup/recurring.lock
rm /mnt/cf1/sensordata/*.p
rm /tmp/sensordata/*.p

cp /root/recurring.txt /mnt/cf1/sensorsetup/

ln -s /mnt/cf1/sensordata /tmp/sensordata
ln -s /mnt/cf1/sensorsetup /tmp/sensorsetup
ln -s /mnt/cf1/bridge /tmp/bridge

echo "sleep for 5 seconds before starting cron"
sleep 5
/etc/init.d/cron start # start cron

# NOTE: NEED TO CHANGE location1 to RIGHT HOSTNAME
hostname -v location2
route del default
route add default ppp0

# Start GPRS
echo "Start GPRS in 10 seconds"
sleep 10

pppd call ac750
```

```
echo "sleep for 10 seconds before proceeding"
sleep 10
echo "Start NTPD"
date -s "Thu Jun 9 9:00:00 EDT 2005"
ntpdate -t 10 clock.nyc.he.net bitsy.mit.edu
ntpd -g -q             # update time once and exit
sleep 30
ntpd                   # start ntp that'll update time

rm /root/gatewaysave.*

echo "sleep for 30 seconds before starting Mote App"
sleep 30

/root/arm-uartserver -3 COM3 9000 > /root/dump_uart.txt &
/root/bridge -s -serial SOCK > /dev/null &
/root/GatewayNode 100 41 60 > /dev/null &

echo "sleep for 15 seconds before ejects wlan0"
sleep 15
cardctl eject 1
sleep 5
echo "initialization completed"
```

/etc/crontab

```
#
SHELL=/bin/sh
PATH=/usr/local/sbin:/usr/local/bin:/sbin:/bin:/usr/sbin:/usr/bin
#
# m h dom mon dow user  command
* * * * * root test -e /usr/sbin/anacron || run-parts --report
/etc/cron.minute
17 * * * * root test -e /usr/sbin/anacron || run-parts --report
/etc/cron.hourly
25 6 * * * root test -e /usr/sbin/anacron || run-parts --report
/etc/cron.daily
47 6 * * 7 root test -e /usr/sbin/anacron || run-parts --report
/etc/cron.weekly
52 6 1 * * root test -e /usr/sbin/anacron || run-parts --report
/etc/cron.monthly

// this command changes the frequency which Stargate sends data to
// the MIT server
0 *     * * *   root    /etc/cron.d/collect_data.sh
15 *    * * *   root    /etc/cron.d/collect_data.sh
30 *    * * *   root    /etc/cron.d/collect_data.sh
45 *    * * *   root    /etc/cron.d/collect_data.sh

10  *      *  *  *    root     ps  -ef  |  grep  bridge  |  grep  -v  grep  >>
/dev/null || /etc/cron.d/runShut.sh
20  *      *  *  *    root     ps  -ef  |  grep  bridge  |  grep  -v  grep  >>
/dev/null || /etc/cron.d/runShut.sh
40  *      *  *  *    root     ps  -ef  |  grep  bridge  |  grep  -v  grep  >>
/dev/null || /etc/cron.d/runShut.sh
```

```
50 *       * * *    root     ps -ef | grep bridge | grep -v grep >>
/dev/null || /etc/cron.d/runShut.sh

12 8     * * *   root    cardctl insert 1
12 10     * * *   root    cardctl eject 1
7 0     * * *   root    /etc/cron.d/runShut.sh
12 11   1,8,15,22 * *   root    /etc/cron.d/clearLog.sh
```

/etc/cron.d/collect_data.sh

```
#!/bin/sh

export PATH=$PATH:/etc/cron.d/
data_dir=/tmp/bridge    # dir containing sensor data
archive_dir=/tmp/archivestosend # dir containing archives
logfile="/etc/cron.d/thelogfile.txt" # path to log file

# logging routine, writes to $logfile
log() {
  echo $1                              # to screen
  echo `date` $1 >> $logfile  # to log
}

# check that the iMote app has noted previously issued cmds
acquire(){
  while test -f $1
    do
      log 'noticed a lock '$1', waiting to acquire the lock'
      sleep 10
    done
}

# log the initialization message
log "-----------------------------------------------"
log "Stargate: preparing to send data to data center..."

# check that gprs connection is active by probe_connection.sh
if probe_connection.sh|grep "pppd is up"
then

  mkdir $archive_dir

  # compute the name of archive
  archive_name=data`date '+%m.%d.%y.%H.%M.%S'`.tar.gz
  log 'creating an archive '$archive_name

  # --remove-files takes out the links
  current_dir=${PWD};
  cd $data_dir
  tar cvzfh $archive_dir/$archive_name . --remove-files
  cd $current_dir

  if scp $archive_dir/$archive_name mansfield@ceelaptop-341-1.mit.edu:~
   then
      # file successfully sent to the server
      log "Successfully sent data to the server"
```

```
    else
      #file not sent successfully - move archive into
/tmp/sensordatadone
      #the archive will be gzipped on the next iteration
      cp $archive_dir/$archive_name $data_dir

      log "unable to send data to the server successfully"
      log "archive moved to /tmp/bridge"
  fi

  # remove all the original files
  for datafile in `tar tzf $archive_dir/$archive_name`
      do
        rm /tmp/bridge/$datafile
        rm /tmp/sensordata/$datafile
      done

  # remove the original archive
  rm $archive_dir/$archive_name
# get commands from server
 scp -oProtocol=2 mansfield@ceelaptop-341-
1.mit.edu:~/`hostname`/sensorsetup/oneshot.txt /tmp/sensorsetupnew/

  scp mansfield@ceelaptop-341-1.mit.edu:~/sensorsetup/recurring.txt
/tmp/sensorsetupnew/

  log "Successfully checked server for commands"

  if test -f /tmp/sensorsetupnew/oneshot.txt
     then

        log "received burst observation cmds"
        log "renewing cmds in /tmp/sensorsetup"

        # wait until mote app notes prev. cmds
        acquire /tmp/sensorsetup/oneshot.unlock

        # take out old one - insert new one
        rm /tmp/sensorsetup/oneshot.txt
        cp /tmp/sensorsetupnew/oneshot.txt /tmp/sensorsetup

        # tell app that new cmds are ready
       touch /tmp/sensorsetup/oneshot.unlock
     else
        log "no burst observation cmds rcvd"
  fi
  if test -f /tmp/sensorsetupnew/recurring.txt
     then
        log "received periodic observation cmds"
        log "renewing cmds in /tmp/sensorsetup"

        # acquire the lock
        acquire /tmp/sensorsetup/recurring.lock
        touch /tmp/sensorsetup/recurring.lock

        # update the periodic cmds
```

```
        rm /tmp/sensorsetup/recurring.txt
        cp /tmp/sensorsetupnew/recurring.txt /tmp/sensorsetup

        # remove the lock
        rm /tmp/sensorsetup/recurring.lock
     else
        log "no periodic observation cmds rcvd"
  fi
# take the temp files out, since new ones
  # have been stored in /tmp/sensorsetup
  rm -rf /tmp/sensorsetupnew/oneshot.txt
  rm -rf /tmp/sensorsetupnew/recurring.txt
  log "completed receiving commands from the server"

  # check in with the data center
  # recording own ip in data center ip file
  ip=`/sbin/ifconfig|grep P-t-P`
  command='echo '$ip' >> ~/'`hostname`'/ipaddr'

else
   log "no connection to data center"
   log "will attempt to connect later"
fi

(END)
```

Calls from /etc/cron.d/collect_data.sh.
Aim: To check if the GPRS is working

/etc/cron.d/probe_connection.sh

```
#!/bin/sh

export PATH=$PATH:/etc/cron.d/:/sbin/:/usr/sbin/:/bin/
logfile="/etc/cron.d/thelogfile.txt" # path to log file

# logging routine, writes to $logfile
log() {
  echo $1                               # to screen
  echo `date` $1 >> $logfile  # to log
}

# kills pppd
kill_pppd(){
  log "stopping pppd ..."
  kill -9 `cat /var/run/ppp0.pid`
  log "stopped pppd"
}

# make sure gprs card is activated
probe_gprs(){
  log "checking gprs card..."
}
# restarts the gprs card
restart_gprs() {
  kill_pppd
```

```
  log "Restarting pcmcia gprs ..."
  /sbin/cardctl suspend 0
  log "waiting 5s before starting gprs"
  sleep 5
  /sbin/cardctl resume 0
  log "waiting for gprs card to come back up (20 s)"
  sleep 15
  log "Restarted gprs"
}

# result of ping test
ping_test_result=0      # no network connection assumed
                        # initially - need to check this

# tries an end to end test by pinging the data center
# returns 1 on success and 0 otherwise
pingtest(){
ulimit -t 40           # 40 seconds should be plenty
if (ping -c 4 db.lcs.mit.edu)| grep "PING db.csail.mit.edu"
   then
       log "detected ping results"
       ping_test_result=1
   else
       log "ping was unsuccessful"
       ping_test_result=0
   fi
ulimit -t unlimited
}

# try to make sure gprs card is turned on
probe_gprs

# check to make sure that pppd is up
if ps -A | grep pppd;
   then
        pingtest
        if [ "$ping_test_result" -eq "1" ]
           then
               log "pppd is up"
           else
              #pppd running, but ping failed, kill pppd, restart gprs
               card (in restart_gprs), wait for 15 minutes
               log "pppd up, but ping failed"
               restart_gprs
               log "will try to restart pppd later"
           fi
  else
     # get the connection up and running
     log "The pppd daemon was not running"
     log "Restarting pppd ..."

     # check that the daemon was restarted
     if (pppd call ac750)| grep "Serial connection established"
        then
            # assume a fresh connection - no need to ping
            log "Successfully restarted"
            log "pppd is up"
```

```
        else
            # pppd wasn't running and wasn't able to
            # restart pppd
            # thus, restart gprs and try again in 15 mins
            log "Unable to restart pppd"
           restart_gprs
            log "Will try to restart pppd later"
        fi
  fi

(END)
```

Called from /etc/crontab

/etc/cron.d/runShut.sh

```
#!/bin/sh
export PATH=$PATH:/etc/cron.d/
GP=/proc/platx/gpio/GPCTL
echo c59 > $GP
echo s60 > $GP
echo "Watchdog On"
echo c58 > $GP
echo s58 > $GP
shutdown now
runShut.sh (END)
```

Called from etc/crontab

/etc/cron.d/clearLog.sh

```
#!/bin/sh
> /etc/cron.d/thelogfile.txt
clearLog.sh (END)
```

Appendix II

Instructions for setting up the GPRS long range communication and secure shell transfer (SSH) are presented below. Script written by Ivan Stoianov, modified by Eng Sew

Setting up the GPRS:

Sierra Wireless A750 on Stargate
----
1. Follow the directions given by sierra wireless for setting up A750 on Linux: http://www.sierrawireless.com/SupportDownload/ac7x0_linux.asp

2. Clear /etc/ppp/options
3. Edit ac750 and ac750chat files in /etc/ppp/peers as following:

ac750:
```
-detach
/dev/modem
115200
defaultroute
crtscts
persist
lock
connect '/usr/sbin/chat -v -t3 -f /etc/ppp/peers/ac750chat'
```

ac750chat:
```
'' AT
OK AT+cgdcont=1,"IP","internet3.voicestream.com"
OK ATD*99#
CONNECT ''
```

4. Setting Up DNS (provided by T-mobile or MIT)
use/edit the following /etc/resolv.conf:
```
nameserver XX.XX.X.XX
nameserver XX.XX.X.XXX
search mit.edu
```

5. Reboot the stargate (reset button)

6. Start GPRS - type the following at the console: pppd *call ac750*

7. Test: ping google.com

Setting up Linux server and SSH file transfer protocol
Equipments needed:

1. A Linux server with static IP address
2. Stargate base station with working GPRS (see setting up GPRS above)

1. Setting up Linux server

Any personal computer can be set up as a Linux server. Download the Ubuntu operating system from www.ubuntu.com into a CD (compact disk). The Ubuntu should be burned as an image file and this can easily be done on commercial CD writer softwares or through the free ImgBurn software (http://Imgburn.com). Place the CD into the computer and restart the computer – the Ubuntu installation guide will appear. Follow in the instructions in the guide.

After Linux installation, you will have to setup up an OpenSSH server. This can be done by the following steps:

Log in as root in Ubuntu:

```
su
```

You will need to enter a password for the root.

Install the SSH Server

At the root prompt, type:

```
apt-get install ssh openssh-server
```

You may be prompted to insert the installation CD again.

Configure the Network

The server needs a static IP address (DHCP: Dynamic Host Configuration Protocol will not work). Most computer administrators will be able to provide that easily. In addition to a static IP address, you also need a domain name. MIT generally provides a domain name with the static IP address. If you have access to the MIT Athena cluster, you can check the domain name by typing `hostinfo XX.XX.X.XXX` where xxx is the IP address..

Type: `vi /etc/network/interfaces`

And change the information to reflect your system:

```
# The primary network interface
auto eth0
iface eth0 inet static
        address XX.XX.X.XXX
        netmask 255.255.0.0
        gateway XX.XX.X.X
```

Restart your network

```
/etc/init.d/networking restart
```

To check if it is working, run

```
hostname
hostname -f
```

and that should give you the same hostname.

2. Setting up SSH

Check your connection by typing the following:

```
ssh account@hostname
```

In my case, it is

```
ssh account@hostname
```

You will be prompted a password for the account upon connection. However, we need to bypass the password prompt as it will halt the Stargate operation (while waiting for your password). This can be achieved by using a

However, password will not work in the field because it stops the Stargate operation. Therefore, we need to use a passwordless method. This can be done by generating a DSA key.

At the stargate:

`ssh-keygen –d` (or `ssh-keygen –d –f filename` if you store it to a file)

Enter a blank passphrase (i.e. just press “enter” and no password is entered)

This will generate a private and public key called id_dsa and id_dsa.pub in the Stargate root area (or root/.ssh). The private key id_dsa contains information of the username and password.

Now, append the id_dsa to id_dsa.pub using the following command

```
cat id_dsa >> id_dsa.pub
```

Send the public key to your server by:

```
scp id_dsa.pub account@hostname:~/.ssh/
```

At the server side:

change the name of id_dsa.pub to authorized_keys

```
cat id_dsa.pub >> authorized_keys
```

This should give you a passwordless connection.

Test your connection using the following command from the Stargate

```
ssh account@hostname
```

Appendix III

The results for constant rate of strain test on the Maine clay are presented below.

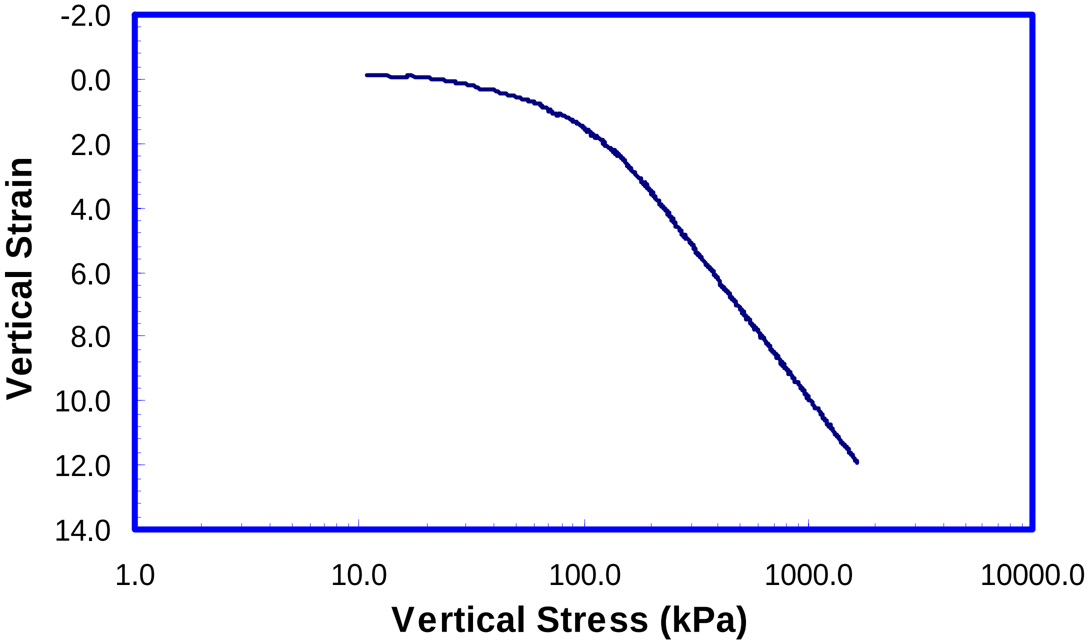

Figure 11-1: Vertical stress strain profile for the Constant Rate of Consolidation

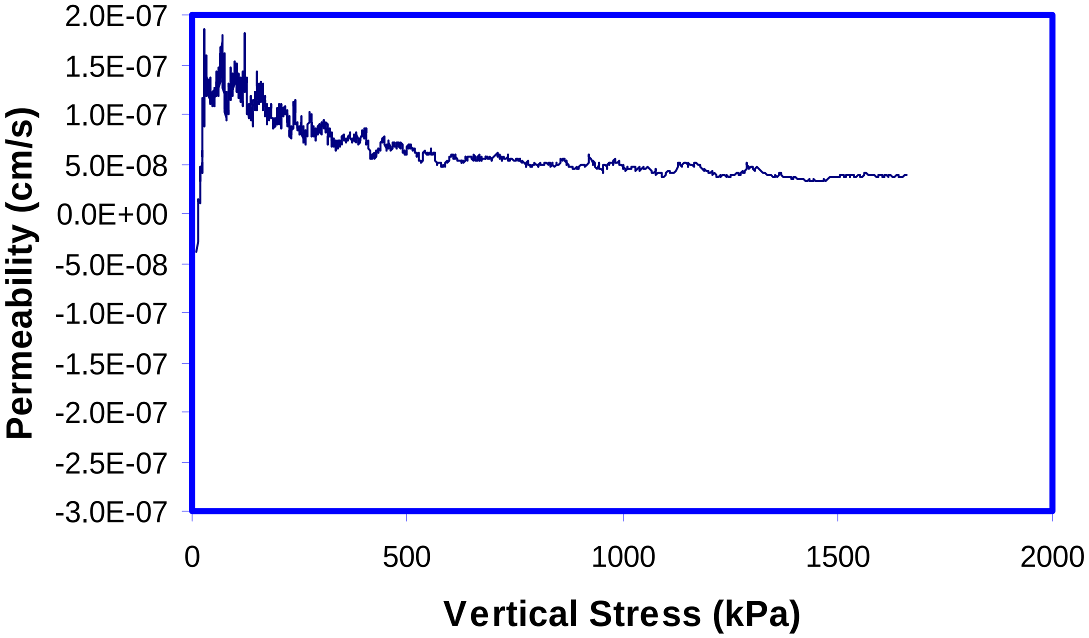

Figure 11-2: Permeability of the soil for the CRS test

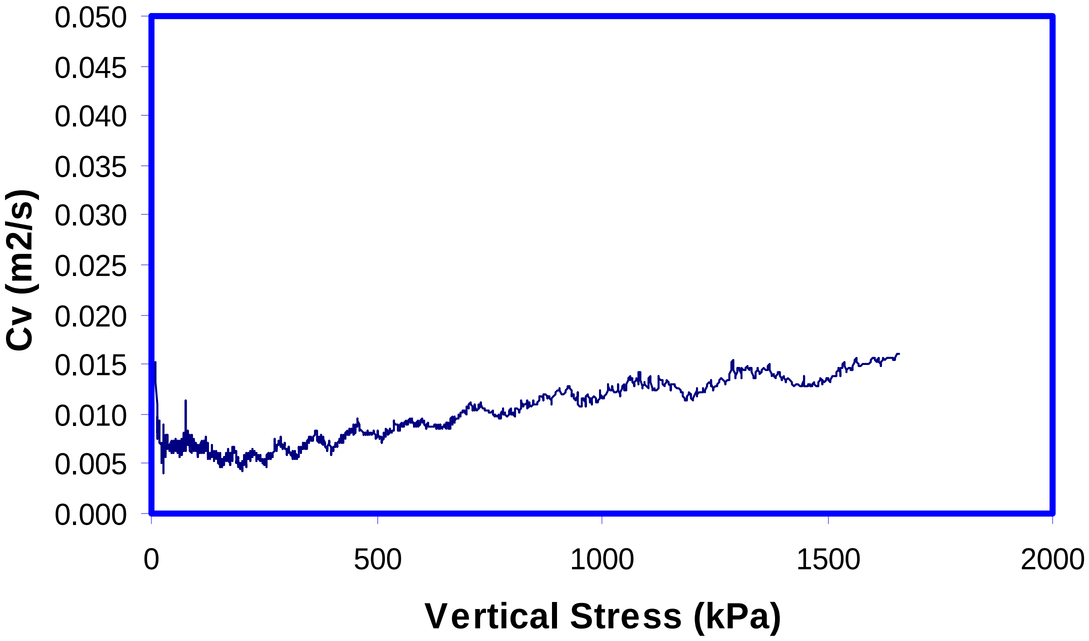

Figure 11-3: Coefficient of consolidation for the soil

Appendix IV

Aim: Performed numerical analysis to estimate development of dynamic pore pressures (controlled by the mean stress) in the subgrade during passage of the Acela train.

The railway track is represented by a three dimensional finite element model using Plaxis 3D foundation. The high speed Acela train loading is, in reality, a combination of static load (weight of the train at rest) and dynamic load (generated by motion). In the analysis, the train loading will be represented by quasi static load (i.e. static load multiplied by dynamic amplification).

Mesh and soil layers

The train signature at carrriages end (represented by two end bogies) are modeled. Significant reduction in computational effort and meshing can be achieved by modeling half the track and an end bogie (two wheels), as shown in Figure 11-4 and Figure 11-5. The mesh area is bounded by 13.5m x 8m (i.e. x = 13.5m and z = 8m) which is sufficiently large to avoid boundary effects. The depth of the three dimensional mesh is 7.5m (i.e. y = -7.5m) and corresponds to the rock / soil boundary.

The railtrack superstructure will be model as a two layer elastic continuum, consisting of stiff ballast (0.3m thick) overlying softer subgrade (7.2m thick). The elastic properties of the two layers are given in Table 11-1.

Table 11-1: Properties of the ballast and subgrade

Layer	*Poisson Ratio,* ν	*E (kPa)*
Ballast	0.3	140000
Subgrade	0.3	14000

Structural components and loading conditions

The structural components of the rail track are made of the rails, tie fasteners, ties and ballast. The rail spreads a large fraction of the wheel load onto the underlying and adjacent ties which is roughly in the proportion of 25%:50%:25% (i.e. 50% on the loaded tie, and 25% on adjacent ties on either side of the loaded tie). This widely used load transfer proportions recommended by AREA will be used to simply the structural components used in the model; the wheel load and rail action is represented by three point loads with the recommended proportions on three ties (Figure 11-4).

The static axle load of an Acela engine and passenger rolling stock is 250kN (wheel: 125kN) and 156kN (wheel: 78kN) respectively. The quasi static wheel load of the engine and rolling stock is 225kN and 140kN for dynamic amplification of 1.8[35]. For the passenger rolling stock, the wheel loading components on the three concrete ties are 35:70:35 kN. In the following analysis, only the passenger rolling stocks will be presented since the train is made up of mostly passenger rolling stocks. In addition, the contribution of the train engine can be scaled since this is an elastic analysis.

---

[35] measured by Mansfield Wheel Detector

The resulting wheel dynamic loading for the engine and rolling stock is 225kN and 140kN. Since this is an elastic analysis, the loads can easily be scaled from the passenger rolling stock onto the engine weight. And since the majority of the train loadings consist of passenger rolling stocks, only the passenger rolling stock will be shown in the following section. The loading components on three consecutive ties are 35:70:35 kN respectively.

Table 11-2: Properties of structural components

Name	*Area (m^2)*	*E (kPa)*	*I^3(m^4)*
Concrete Ties	0.038	20600000	0.000132

Results

In order to simulate the passage of Acela over the instrumented area, the applied mean and shear stresses along x = 0 to 13.5m at the two piezometers location are obtained. The first piezometer (top subgrade) is located at coordinates (x:y:z, 2.61:-0.45:1.3) and second (deep subgrade) at (2.61:-1.35:2.3). The mean and shear stresses for the two end bogies are shown in Figure 11-4 and Figure 11-5. The developed excess pore pressure is controlled by the mean stresses. The distance in the x axis is converted into time (based on Acela's speed of 220 kph) to better represent the time taken to generate the stress pulses.

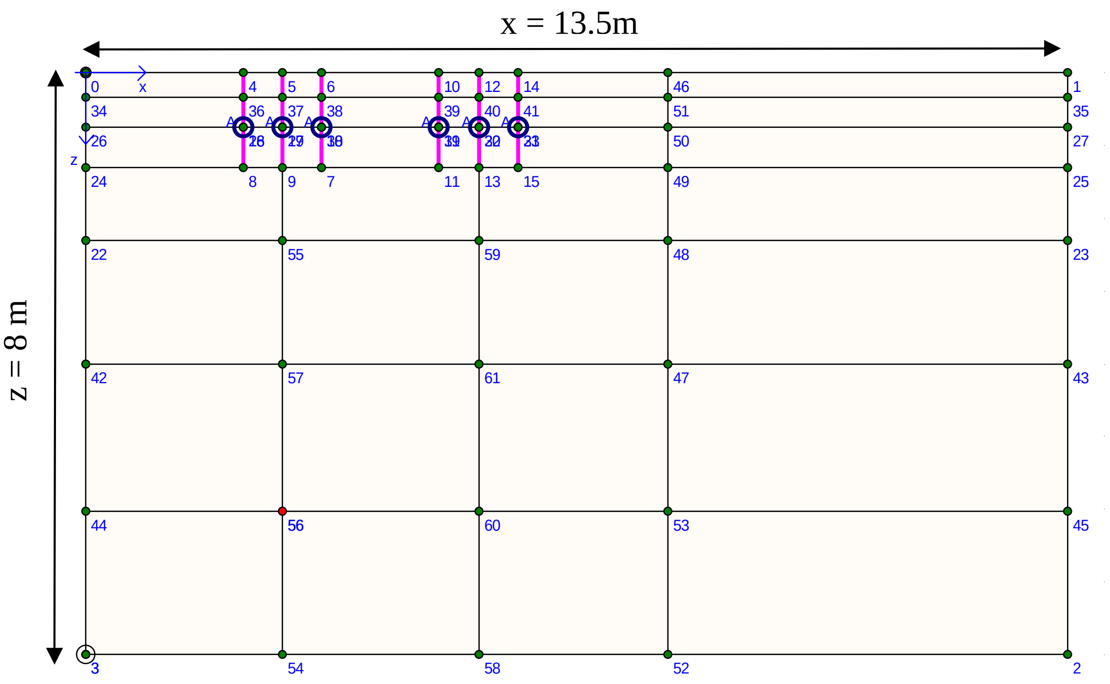

Figure 11-4: Plan view of the mesh. Due to symmetry, half the track (center line at z = 0) and one end bogie (center line at x = 0m) is modeled.

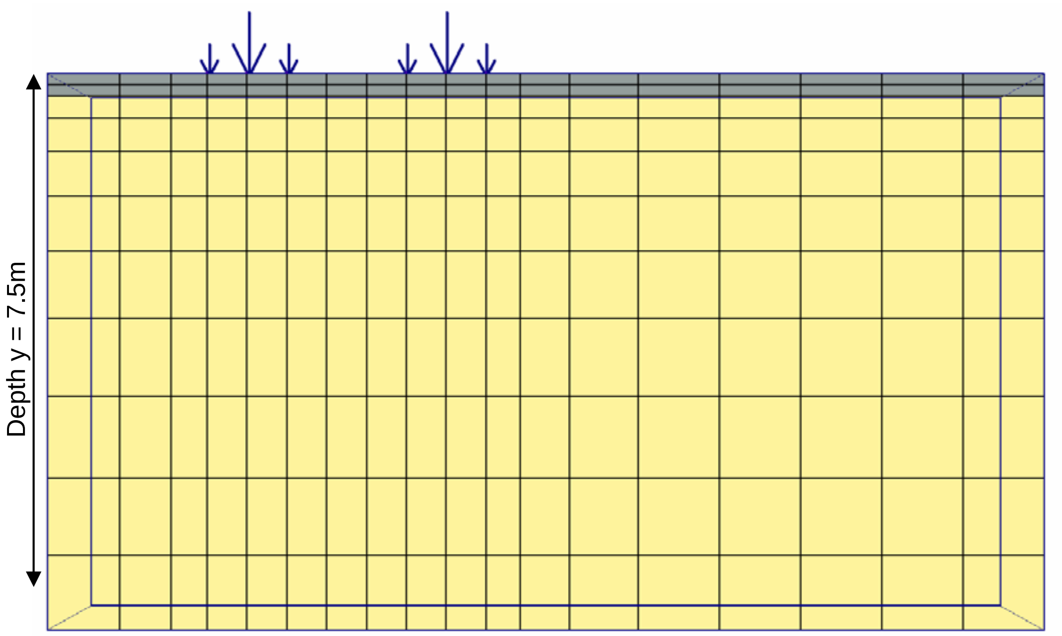

Figure 11-5: Side view of the mesh, viewed along the z-z axis.

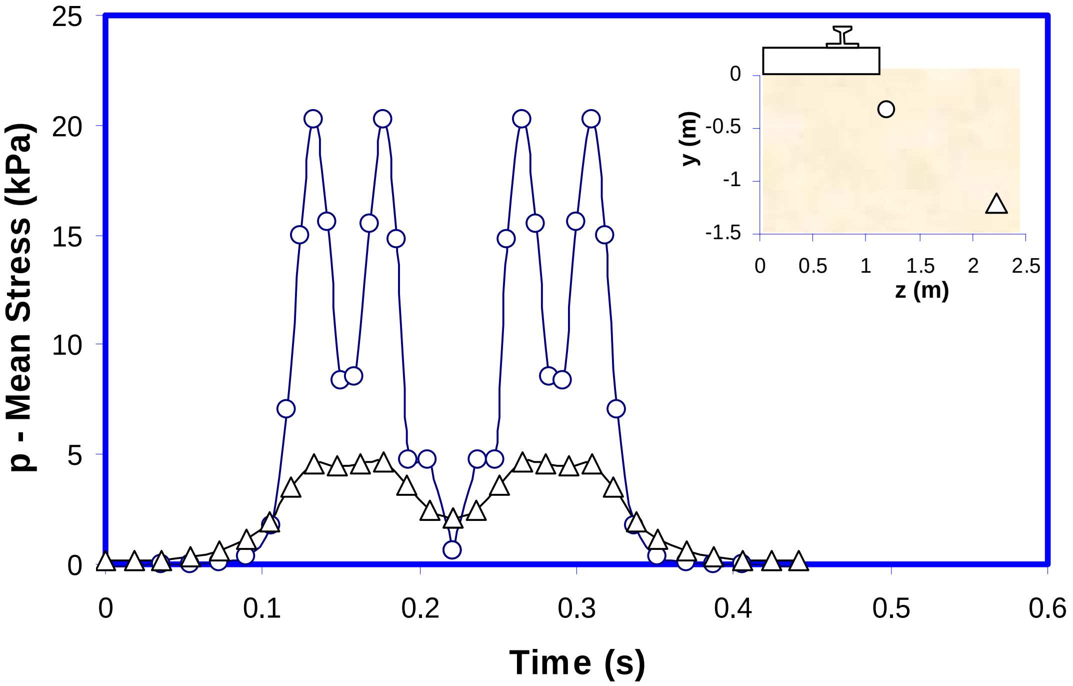

Figure 11-6: Theoretical mean stress pulses at the top (depth y = -0.45m, z = 1.3m) and deep (depth y = -1.35m, z = 2.3m) subgrade, as experienced by the reference top and deep subgrade piezometer during passage of the Acela. Result for two bogies are shown and is obtained by inverting the stresses over the center line x = 0 of the one-bogie-mesh.

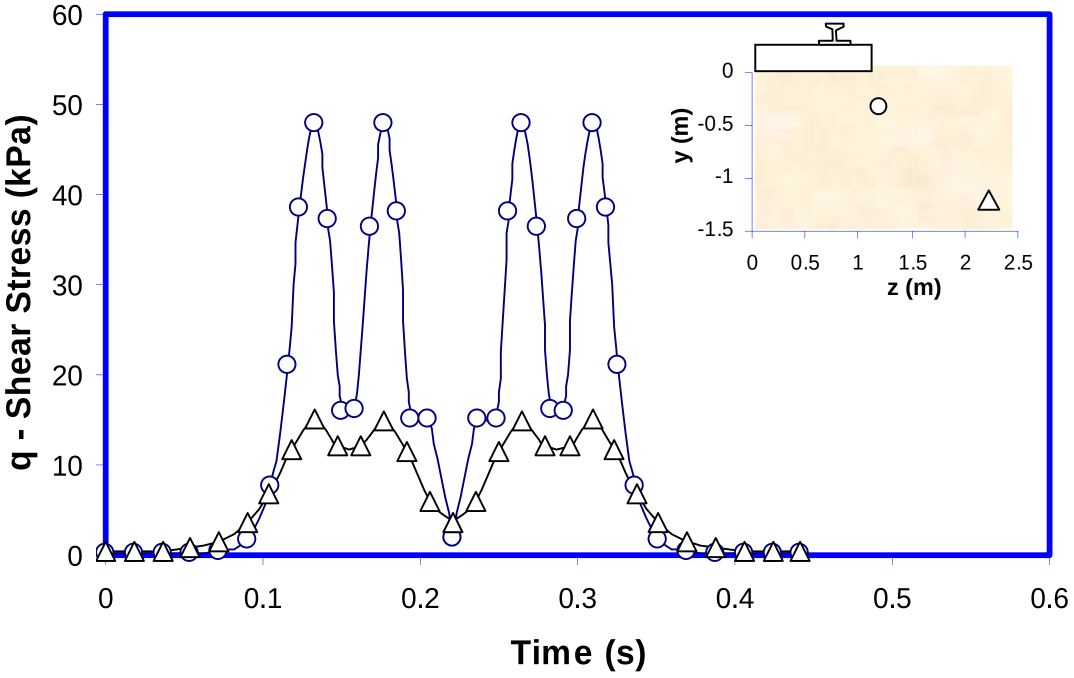

Figure 11-7: Theoretical shear stress pulses at the top (depth y = -0.45m, z = 1.3m) and deep (depth y = -1.35m, z = 2.3m) subgrade, as experienced by the reference top and deep subgrade piezometer

Appendix V

Matlab programming code for filter applications (from section 5.3.4).

```
uiimport         % import data file
time=data(1:end,1);
acc=data(1:end,2);
dt=time(2,1)-time(1,1); % determining the time steps in the data
f=(1/dt)*(0:length(acc)-1)/length(acc);
fsampling = 1/dt      % Sampling Frequency

NFFT = 2^nextpow2(length(acc));  % Next power of 2 from length of y
Y = fft(acc,NFFT)/length(acc);   % Perform fast fourier transform
fplot = fsampling/2*linspace(0,1,NFFT/2);

Yplot = 2*abs(Y(1:NFFT/2));  % Plot single-sided amplitude spectrum
plot(fplot,Yplot);
title('Single-Sided Amplitude Spectrum of y(t)')
xlabel('Frequency (Hz)')
ylabel('|Y(f)|')
[b,a] = butter(5, 10/(fsampling/2));  % 5th order, 10Hz Butterworth filter
fvtool(b,a);
filt = filter(b,a,acc);  %Filtering the data
plot(time, filt, time, acc);  %Plotting original and filtered data
```